High Fidelity Quantum Information Processing with Trapped Ions

by

Christopher E. Langer

B.S., Seattle Pacific University, 1999

M.S., University of Colorado at Boulder, 2005

A thesis submitted to the
Faculty of the Graduate School of the
University of Colorado in partial fulfillment
of the requirements for the degree of
Doctor of Philosophy
Department of Physics
2006

This thesis entitled:
High Fidelity Quantum Information Processing with Trapped Ions
written by Christopher E. Langer
has been approved for the Department of Physics

David Wineland

Eric Cornell

Date

The final copy of this thesis has been examined by the signatories, and we find that both the content and the form meet acceptable presentation standards of scholarly work in the above mentioned discipline.

Langer, Christopher E. (Ph.D., Physics)

High Fidelity Quantum Information Processing with Trapped Ions

Thesis directed by Dr. David Wineland

Quantum computing (QC) offers the ability to efficiently solve certain computational problems which are intractable classically. Recently, most of the requirements for QC have been demonstrated with ions, and the current focus in ion-trap QC is tackling problems of scalability. Large-scale QC, requiring error correction, is possible only if the error rates in the system are suppressed to very low levels. The focus of my thesis work has been to characterize the errors in our ion-trap system and reduce them to levels where fault tolerance may be achieved. Two areas were of primary focus: memory errors and errors due to the presence of laser light.

A dominant source of memory error is decoherence induced by fluctuating magnetic fields. We addressed this problem and created long-lived qubit memories using a first-order magnetic-field-independent hyperfine transition. Our results with ^{9}Be$^+$ qubits showed a coherence time of approximately 15 seconds, an improvement of over five orders of magnitude from previous experiments. Using pessimistic models for memory decoherence over time, the memory error for the duration of error correction is $\sim 10^{-5}$, below known fault-tolerance thresholds.

Errors during quantum gate operations must also be maintained to low levels to enable efficient error correction. In many atomic-ion based QC architectures, off-resonant laser light is used to perform quantum gate operations with stimulated-Raman transitions. In such schemes, spontaneous photon scattering is a fundamental source of decoherence. We experimentally studied decoherence of coherent superpositions of hyperfine states of ^{9}Be$^+$ in the presence of off-resonant laser light. Our results indicated that decoherence is dominated by inelastic Raman photon scattering which, for sufficient detunings from the excited states, occurs at a rate much smaller than the elastic Rayleigh scattering rate. For certain detunings, the measured decoherence rate is a factor of 19 below the calculated total scattering rate indicating that qubit coherence is maintained in the presence of photon scattering. Using the measured decoherence rate and experimental parameters from this experiment, the calculated error due to spontaneous scattering during a 2-qubit gate is also below known fault-tolerance thresholds.

Dedication

To my parents H. Arthur Langer and Gloria E. Langer

who inspired me to study the physical world,

to my daughter Maren E. Langer

who makes me laugh and loves to ride bicycles,

and most importantly to my wife Megan M. Langer

whose love and encouragement make life, even in graduate school, desirable.

Acknowledgements

Special thanks goes first and foremost to Dave Wineland, my research advisor, who not only taught me to perform experiments and understand the interaction of trapped ions with lasers, but who also rode his bike at a relaxed pace so that I could tag along. Thanks to Roee Ozeri with whom I spent many sleepless nights in attempts at collecting good data. Roee, thank you also for stimulating discussions which made the subject matter of this thesis understandable to me. Thanks to Didi Leibfried and Manny Knill for explaining the intricacies of quantum theory and to John Jost for his excellent contributions to the experiments. Special thanks goes to the many scientists with whom I have had the pleasure of working and who all contributed much to this work, namely: Till Rosenband, Piet Schmidt, John Chiaverini, Tobias Schaetz, Murray Barrett, Brian DeMarco, David Hume, Jim Bergquist, John Bollinger, Wayne Itano, Joe Britton, Brad Blakestad, Rainer Reichle, Janus Wesenberg, Seigne Seidelin, Ryan Epstein, David Keilpinski, Cass Sackett, Volker Meyer, Mary Rowe, Quentint Turchette, Amit Ben-Kish, Brana Jelenkovic, David Lucas, and Chris Monroe.

Contents

Chapter

Appendix

Tables

Table

Figures

Figure

Chapter 1

Introduction

In his famous 1982 paper, Richard Feynman pointed out that classical computer simulation of quantum mechanical systems was very difficult. [Feynman 82]. In the same work, however, he mentioned that it may be possible to simulate quantum systems with other quantum systems, namely a quantum computer, and writes, “It’s not a Turing machine, but a machine of a different kind.” Interest in the field of quantum information processing became very large when Peter Shor wrote his 1994 paper on the efficient factorization of large numbers [Shor 94] using a quantum computer, and since then, there has been an explosion of activity in the field. The efficient factorization of large numbers, if possible, would compromise public key cryptography.

An obstacle to implementation of Shor’s algorithm and hence factoring, of course, was the lack of a quantum computer. Although some of the earliest demonstrations of quantum algorithms were simulated using ensembles of nuclear spins in liquid state nuclear magnetic resonance [Jones 01] including factoring [Vandersypen 01], a deterministic quantum computer based on prepared pure quantum states remained a challenge. In 1995, Ignacio Cirac and Peter Zoller proposed an architecture of a quantum computer based on trapped ions [Cirac 95] which is the basis for most of the ion-trap based quantum computing experimental research efforts including this current work.

Cirac and Zoller’s proposal consisted of a linear array of trapped ions cooled to their ground state of motion. Using tightly focused laser beams, the states of individual ion qubits in the string could be rotated, and interactions between two ions in the string could be implemented by coupling the internal states of the individual ions with the collective motion of a particular mode. This satisfied the requirement of a universal gate set for universal quantum computation [Barenco 95], namely that any quantum algorithm could be constructed from a primitive set of gates. In particular, if an experimentalist had at his or her disposal arbitrary single qubit rotations and a single universal entangling gate between any two qubits, then an arbitrary quantum circuit could be constructed from these primitives. This is analogous to constructing classical logic circuits from a network of classical NAND (NOT AND) gates. In this sense, the set of single qubit rotations and the two-qubit entangling gate is “universal.” In addition to the universal gate set, other requirements exist for quantum computation [DiVincenzo 98], and most of these had already been developed and demonstrated in ions. Enumerating, the five DiVincenzo criteria are [DiVincenzo 98]:

(1) A scalable physical system with well characterized qubits.

(2) The ability to initialize the state of the qubits to a simple fiducial state, such as $|00\cdots 0\rangle$.

(3) Long qubit coherence times, much longer than the gate operation time.

(4) A universal set of quantum gates.

(5) A qubit specific measurement capability.

Item (2) was accomplished via optical pumping and laser cooling [Wineland 79]; item (3) had been demonstrated in experiments devoted to making highly stable atomic clocks [Bollinger 91]; item (5) was realized in resonance fluorescence and electron shelving experiments [Wineland 80, Nagourney 86, Bergquist 86]. Cirac and Zoller’s proposal filled the gaps of items (1) and (3). Many of the intermediate steps required by the Cirac-Zoller proposal were quickly demonstrated, namely ground state cooling [Monroe 95b] and conditioned two-qubit quantum gates between the internal state of a single ion and its motion [Monroe 95a]. It was quickly realized that the Cirac-Zoller proposal had some technical drawbacks, and it wasn't until 2003 that the original Cirac-Zoller two-qubit entangling gate was realized [Schmidt-Kaler 03].

Meanwhile, two-qubit entangling phase gates based on conditional displacements in the motional mode's phase space were proposed [Mølmer 99, Sørensen 99, Sørensen 00, Milburn 01] and implemented [Sackett 00, Leibfried 03]. These gates had the technical advantages that individual addressing was not required and that ground state cooling was not required so long as the ions were sufficiently cold to be in the Lamb-Dicke regime. Furthermore, the ion's motion was only excited in a transient fashion such that after the application of the gate, the ion's motional state returned to its original state. These gates appeared to be more robust than the Cirac-Zoller gate, and the highest fidelity deterministically generated two-qubit entangled states to date were generated by these gates [Leibfried 03].

As of a few years ago, all of the DiVincenzo requirements enumerated above have been demonstrated with ions by multiple groups, and some simple quantum algorithms have been demonstrated including: dense coding [Schaetz 04], quantum teleportation [Barrett 04, Riebe 04], quantum error correction [Chiaverini 04], quantum semiclassical Fourier transform [Chiaverini 05], Grover search [Brickman 05], and entanglement purification [Reichle 06]. In addition, entanglement of six [Leibfried 05] and eight [Haffner 05] ions has been demonstrated. As with all possible implementations of QIP, the current challenge in ion-trap quantum information processing was (and still is) contained in the second word of the first item in the above list, namely, "how do you build a *scalable* physical system which can perform quantum information processing?" Part of the technical challenge of the Cirac-Zoller proposal was just this; it was not scalable. As the number of ions in a single linear trap increased, the number of motional modes increased, and it would be very difficult to spectrally resolve a single mode of motion on which to perform quantum gates. Furthermore, for the number of ions needed to perform Shor's factorizing algorithm, a trap length of many tens of meters would be required with impractically high voltages. The current architecture which most of the ion-trap quantum information processing community has embraced is that of a multiplexed array of traps where ions are shuttled back and forth between different interconnected trapping regions and can interact in small numbers (say 2) in isolated traps such that the large number of motional modes is not problematic, and high trap frequencies can be used to implement fast quantum gates [Wineland 98, Kielpinski 02]. During transport, the ions would inevitably acquire kinetic energy which must be removed prior to performing two-qubit gates; this can be accomplished via sympathetic cooling with a different ion species. The current progress in this area is that ions have been shuttled and split in a linear trap array [Rowe 02, Barrett 04], sympathetic cooling has been demonstrated [Rohde 01, Blinov 02, Barrett 03], ion transport around a corner in a two-dimensional trap array has been realized [Hensinger 06], and new trap fabrication techniques have been developed [Stick 06, Seidelin 06, Britton 06]. In addition, two trap foundries, Lucent Bell Labs and Sandia National Labs, have been established to build even more complicated trap structures to support the ion-trap quantum information processing effort.

The idea of scalability in a physical system encompasses more than the architecture alone. For example, the number of qubits and the number of quantum gate operations required to factorize a number which would break public key cryptography is in the thousands of qubits and in the millions of operations. What about the errors? If the probability of error during a single operation is ϵ, then the probability that N operations will succeed without error is $(1-\epsilon)^N$, an exponentially small number. This is not scalable in any sense of the word. Fortunately, the theory of quantum error correction has been developed, and by encoding the quantum information into codes with redundancy, arbitrarily long computations can be performed with a constant predetermined probability of error for the entire computation so long as the errors per operation are below what is termed the "fault-tolerance threshold" (for a review, see [Preskill 97]). The fault-tolerance thresholds depend on the architecture, noise model, and the particular error-correcting code used. The current estimates for the thresholds are somewhere in the range of 10^{-4} to 10^{-2}. These numbers should be taken with caution. In some sense, they are too pessimistic. With a probability of error of 10^{-2}, a computation utilizing $\sim 10^2$ gates could be performed without error correction at all, and upon repetition of the experiment and averaging the results, we could obtain some confidence in the answer. However, we are concerned with scalable quantum computation, and for that, we require gate errors to be below threshold. In fact, when the errors are only slightly below threshold, the resource requirements for the error-correcting codes become very large; therefore, the errors should be well below the threshold, probably by an order of magnitude. The smaller are the errors, the simpler is the code. If a quantum computer is to be scalable, then its errors per operation at the most basic level must be suppressed below the fault-tolerance threshold. This is the focus of this thesis—to investigate ways to reduce the errors to the smallest possible levels in order to make fault-tolerant scalable quantum information processing with ions possible. We tackled this problem in two areas: (1) reducing memory errors below threshold and (2) demonstrating that spontaneous scattering of photons during quantum gate operations induces a probability of error less than the fault-tolerance threshold. Hence the title of this thesis is "High fidelity quantum information processing with ions."

I begin this thesis with a discussion of the $^9\mathrm{Be}^+$ qubit where I explain how to implement all of the DiVincenzo criteria for quantum computation with ions (Ch. 2). I then describe the experimental apparatus used (Ch. 3). In Ch. 4, the experimental demonstration of long coherence times (DiVincenzo criteria #3) is discussed, and the quantum memory is shown to have a probability of error below threshold. Finally, I discuss our results on the measurement of decoherence induced by the spontaneous scattering of photons. As all of the quantum gate operations involve the interaction of ions with off-resonant laser light, this is an important topic of study as it appears to be the most important fundamental source of decoherence. We demonstrate that the probability of decoherence induced by spontaneous scattering can be suppressed to very low levels, and at the levels demonstrated in Ch. 5, the probability of error during a two-qubit gate operation induced by spontaneous scattering is below the fault-tolerance threshold.

Chapter 2

The ^{9}Be$^+$ Qubit

Quantum information processing requires information to be stored and manipulated in quantum systems. In general, multilevel quantum systems can be used for processing; however, the simplest quantum system is the two-level system, namely the qubit. ^{9}Be$^+$ ions have multiple internal electronic levels, and we spectroscopically isolate two levels to form a qubit. In this chapter, I describe the relevant atomic structure of ^{9}Be$^+$. I derive the Breit-Rabi formula for $J = \frac{1}{2}$ hyperfine structure and show which transitions are suitable as “field-independent” qubits in the $S_{1/2}$ manifold. I then explain how we initialize the system to a well defined state and how we perform state-dependent measurements. A detailed analysis of measurement error is given. We find that ^{9}Be$^+$ qubit measurements can be fault-tolerant in principle. Finally, I discuss how we implement a universal gate set for ions, namely single qubit rotations and a single entangling two-qubit gate. Combined with the demonstration of long coherence times in Chapter 4, this list meets most of the DiVincenzo criteria for building a quantum computer [DiVincenzo 98] with the exception of a scalable architecture. As mentioned in the introduction (Ch. 1), work is in progress on building scalable architectures for ion traps [Kielpinski 02, Rowe 02, Barrett 04, Hensinger 06, Stick 06, Seidelin 06, Britton 06].

2.1 Atomic Structure

The ^{9}Be$^+$ ion, like the Alkali neutral atoms, has a single valence electron. Its gross structure has a ground S orbital with a P orbital as its lowest lying excited state. The $S \leftrightarrow P$ transition is accessible via electric dipole radiation at 313 nm, and the excited state has a radiative lifetime of 8.2 ns (19.4 MHz excited state line width). The spin-orbit interaction gives rise to the fine structure of the excited P orbital splitting this level into two manifolds of states with well defined electron angular momentum. In spectroscopic notation, these manifolds of states are labeled $2p\ ^2P_{3/2}$ and $2p\ ^2P_{1/2}$ or $P_{3/2}$ and $P_{1/2}$ for short. An energy level diagram is shown in Fig. 2.1. The fine structure splitting of the P orbital is 197.2 GHz [Bollinger 85]. There is no fine structure in the S orbital. Its spectroscopic notation is $2s\ ^2S_{1/2}$, or $S_{1/2}$ for short.

The nuclear spin of ^{9}Be$^+$ is $I = 3/2$ and couples to the electron angular momentum generating the hyperfine interaction. This interaction gives rise to a splitting of the levels into states with well defined total angular momentum described by the quantum number F at low magnetic field. In the ground S orbital, the hyperfine splitting is 1.25 GHz [Wineland 83]; in the excited $P_{1/2}$ manifold, the hyperfine splitting is 237 MHz [Bollinger 85]. The $P_{3/2}$ hyperfine splitting is less than 1 MHz [Poulsen 75]. The states in each hyperfine manifold are degenerate at zero magnetic field, and in the presence of a small magnetic field, this degeneracy is lifted by the linear Zeeman effect. The Zeeman energy shift is $-\mu_B g_F m_F B$ where the g-factor g_F is $-1/2$ and $+1/2$ for $F = 2$ and $F = 1$ respectively for $S_{1/2}$. The projection of the ion's total angular momentum on the magnetic field axis is $\hbar m_F$, μ_B is the Bohr magneton, $\hbar$ is Planck's constant divided by 2π, and B is the strength of the magnetic field. We use two hyperfine ground states in the $S_{1/2}$ manifold as the qubit. Any two states will do; however, as we will see in Section 2.2, certain states are better suited for quantum information processing than others. The $F = 1$ hyperfine manifold lies higher in energy than the $F = 2$ manifold,

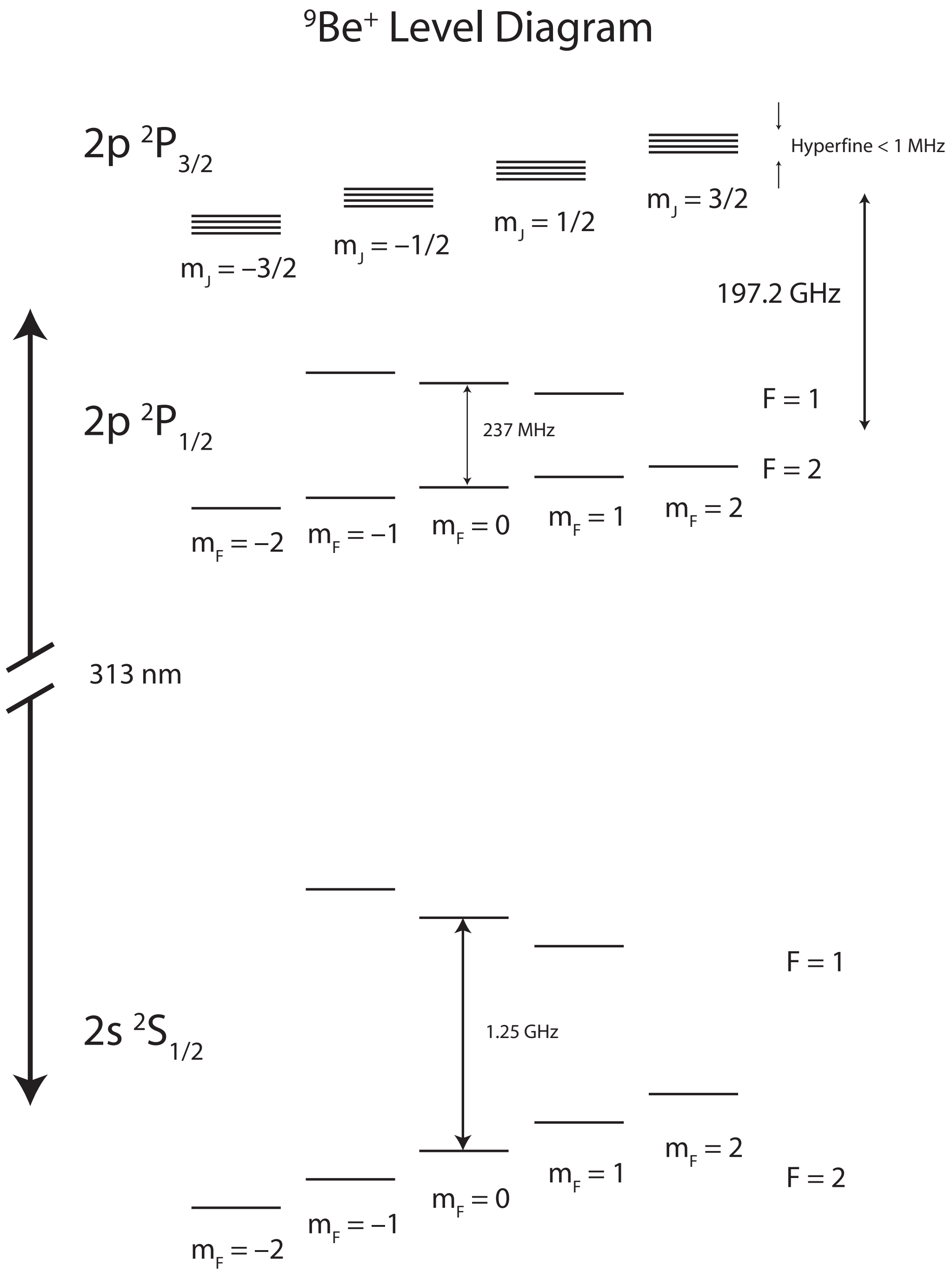

Figure 2.1: Energy level diagram of ^{9}Be$^+$. The fine structure splitting of the excited P orbital is 197.2 GHz. The hyperfine splitting is 237 MHz for the $P_{1/2}$ manifold and less than 1 MHz for the $P_{3/2}$ manifold. The hyperfine splitting of the ground $S_{1/2}$ states is 1.25 GHz. The $S \leftrightarrow P$ transition is electric dipole allowed at 313 nm.

and its radiative lifetime is estimated to be on the order of 10^{15} seconds [Wineland 98].

2.2 Hyperfine Structure and Magnetic Field—Breit-Rabi Solution

The Hamiltonian for the combined system including the hyperfine and Zeeman interactions is

$$\begin{aligned} H &= hA\mathbf{I}\cdot\mathbf{J} - \mu\cdot\mathbf{B} \\ &= hA\mathbf{I}\cdot\mathbf{J} - \mu_B(g_J\mathbf{J} + g_I\mathbf{I})\cdot\mathbf{B} \end{aligned} \tag{2.1}$$

where A is the hyperfine constant in units of Hz, h is Planck's constant, $\hbar\mathbf{J}$ and $\hbar\mathbf{I}$ are the electron and nuclear angular momentum operators respectively, and $g_{J/I}$ is the corresponding Landé g-factor. The operators $\mathbf{J}$ and $\mathbf{I}$ are dimensionless. In the following discussion, we take the magnetic field to be along the z-axis. The quantum numbers of interest are F, J, and I and their corresponding z-projections m_F, m_J, and m_I. The quantum number F represents the total angular momentum of the atom $\mathbf{F} \equiv \mathbf{J} + \mathbf{I}$. For $J = 1/2$, as is the case for alkali-like atoms in the ground $S_{1/2}$ state (including ${}^9\mathrm{Be}^+$), the hyperfine splitting (hfs) is $\Delta E_{\mathrm{hfs}} = hAF_+$, where $F_+ \equiv I + 1/2$; $F_+ = 2$ for ${}^9\mathrm{Be}^+$.

For magnetic fields where the Zeeman interaction is small compared to the hyperfine interaction, the eigenstates of the Hamiltonian are states with well defined total angular momentum. In this case, the Zeeman interaction can be treated as a perturbation in the $|F, m_F\rangle$ basis, and we obtain a shift linear in B with slope proportional to m_F as discussed in Section 2.1. This is the low-field regime. In the opposite high-field regime where the magnetic field is so large that the Zeeman interaction dominates, the eigenstates are described by the $|I, J, m_I, m_J\rangle$ basis (or $|m_I, m_J\rangle$ for short since I and J are constants in the $S_{1/2}$ manifold). In the high field regime, the hyperfine interaction can be treated as a perturbation in the $|m_I, m_J\rangle$ basis. The result is $\Delta E_{m_I,m_J} = hAm_Im_J$. The stretched states ($m_F = \pm F_+$ where $F_+ \equiv I + J$) are eigenstates of the Hamiltonian for all magnetic field strengths. The energy levels for these states are

$$\langle m_F = \pm F_+ | H | m_F = \pm F_+ \rangle = hAJI \mp \mu_B B(g_J J + g_I I). \tag{2.2}$$

In the intermediate field regime, the non-stretched eigenstates are neither $|F, m_F\rangle$ nor $|m_I, m_J\rangle$, but rather superpositions of these states. We must solve for the eigenstates by diagonalizing the Hamiltonian in Eq. (2.1). For $J = 1/2$, this system can be solved analytically, and its solution is termed the Breit-Rabi formula.

To solve the system described by Eq. (2.1), we take advantage of the fact that the total angular momentum projection $m_F \equiv m_J + m_I$ is a conserved quantity in either basis at all magnetic fields. As such, the problem is reduced to diagonalizing a family of two-dimensional matrices parameterized by m_F. We define the states

$$|\pm\rangle \equiv |m_J = \pm 1/2, m_I = m_F \mp 1/2\rangle \tag{2.3}$$

which conserve m_F. For a general angular momentum operator $\hbar\mathbf{L}$ with quantum numbers L and M_L describing its magnitude and z-projection, we define the ladder operators,

$$L_\pm \equiv L_x \pm iL_y. \tag{2.4}$$

They have the properties

$$L_\pm |L, M_L\rangle = \sqrt{(L \mp M_L)(L \pm M_L + 1)}\,|L, M_L \pm 1\rangle \tag{2.5}$$

so long as $M \pm 1$ lies within the range $\{-L, -L+1, .., L\}$. Using $J_\pm$ and $I_\pm$ based on Eq. (2.4), we can write the Hamiltonian [Eq. (2.1)] as

$$H = hAI_zJ_z + \frac{hA}{2}(J_+I_- + J_-I_+) - \mu_B B(g_J J_z + g_I I_z). \tag{2.6}$$

Using Eqs. (2.6) and (2.5), we calculate the matrix elements,

$$\begin{aligned} \langle \pm | H | \pm \rangle &= -\frac{1}{4}hA - \mu_B B g_I m_F \pm \frac{1}{2}(hAm_F - \mu_B B(g_J - g_I)) \\ \langle \pm | H | \mp \rangle &= \frac{1}{2}hA\sqrt{F_+^2 - m_F^2}. \end{aligned} \tag{2.7}$$

Diagonalizing H in the $|\pm\rangle$ basis yields the eigenvalues

$$E(F,m_F) = hA\left(-\frac{1}{4} + \frac{g'_I}{1-g'_I}m_F x \pm \sqrt{F_+^2 + 2m_F x + x^2}\right) \tag{2.8}$$

and (non-normalized) eigenvectors

$$\left(\frac{m_F + x \pm \sqrt{F_+^2 + 2m_F x + x^2}}{\sqrt{F_+^2 - m_F^2}}\right)|+\rangle + |-\rangle. \tag{2.9}$$

where $x \equiv -\frac{\mu_B B g_J (1-g'_I)}{hA}$ is a normalized dimensionless measure of the strength of the magnetic field, and $g'_I \equiv \frac{g_I}{g_J}$ is the ratio of nuclear to electron g-factors. The $\pm$ sign in Eqs. (2.8) and (2.9) correspond to the $F = I \pm 1/2$ states at low magnetic field. The energy spectrum in Eq. (2.8) is the well-known Breit-Rabi formula [Woodgate 92, § 9.6].

A nice feature of the physics of Breit-Rabi solution for quantum information processing is that in the intermediate field regime, the spectral lines exhibit curvature. The curvature of these lines allows us to identify transitions where the differential energy shift vs. magnetic field vanishes to first order. Using such a transition as a qubit is advantageous for quantum information processing because fluctuations in magnetic field couple negligibly to the qubit frequency. The use of field-independent qubits as robust quantum memories is discussed in Chapter 4.

The energy levels as a function of magnetic field for $^9\text{Be}^+$ are shown in Fig. 2.2a. Three of the "field-independent" transitions at non-zero field are indicated by arrows in Fig. 2.2a. The $|F=2, m_F=0\rangle \leftrightarrow |F'=1, m'_F=0\rangle$ transition is field-independent at zero magnetic field. However, due to the degeneracy of the magnetic sub-levels at zero field, a small finite field would be required to spectrally resolve these levels. This would induce a linear field dependence to the transition frequency and hence increase the coupling of magnetic field noise to the qubit frequency. The lowest non-zero field-independent point at $B = 2.54 \times 10^{-5}$ T between states $|F=2, m_F=1\rangle \leftrightarrow |F'=1, m'_F=-1\rangle$[1] is also less practical because performing rotations via optical

---

[1] This transition is similar to the $|F=1, m_F=-1\rangle \leftrightarrow |F'=2, m'_F=1\rangle$ transition in rubidium at 3.23×10^{-4} T [Harber 02, Treutlein 04].

stimulated Raman transitions (see § 2.5.2) would require four laser beams[2] . The two field-independent transitions near 0.0119 T occur at slightly different magnetic fields because of the $\frac{g_I'}{1-g_I'} m_F x$ term in Eq. (2.8). This term is on the order of $\sim 10^{-4}x$, thus the magnetic field at which these two field-independent points occur differ by roughly $\sim 10^{-4} \times 0.0119$ T. Data used for calculating Fig. 2.2 are the hyperfine constant $A = -625.008837048(10)$ MHz, electron g-factor $g_J = -2.00226206(42)$, and nuclear to electron g-factor ratio $g_I' \equiv \frac{g_I}{g_J} = 2.134779853(2) \times 10^{-4}$ [Wineland 83].

The energy difference between different F-levels $E(F = I + \frac{1}{2}, m_F) - E(F' = I - \frac{1}{2}, m_F')$ is given by

$$\frac{\Delta E}{hA} = \frac{g_I'}{1-g_I'} \Delta m_F x + \sqrt{F_+^2 + 2m_F x + x^2} + \sqrt{F_+^2 + 2m_F' x + x^2} \tag{2.10}$$

where $\Delta m_F \equiv m_F - m_F'$. Practical transitions utilizing optical stimulated Raman transitions for single qubit rotations require $\Delta m_F = 0, \pm 1$. For $\Delta m_F = 0$, differentiating Eq. (2.10) with respect to x and setting to zero yields a field independent point at $x = -m_F$. This is the condition for the $|F = 2, m_F = 0\rangle \leftrightarrow |F' = 1, m_F' = 0\rangle$ transition at $B = 0$ and the $|F = 2, m_F = 1\rangle \leftrightarrow |F' = 1, m_F' = 1\rangle$ transition at $B \simeq 0.02231$ T. The stretched states do not have a $\Delta m_F = 0$ transition. The most straight forward way to determine the locations of the $\Delta m_F = \pm 1$ field-independent points is to differentiate Eq. (2.10) with respect to x, set this to zero, and numerically solve for x. Examining Eq. (2.10), we notice that the $\frac{g_I'}{1-g_I'}$ is small; therefore, these transitions exist in pairs with different x locations differing on the order of $\sim g_I' x$ in the neighborhood of

$$x_0 = -\frac{F_+^2 + m + m^2 - \sqrt{F^4 + m^2(m+1)^2 - F^2(1 + 2m + 2m^2)}}{2m+1}, \tag{2.11}$$

the solution to $\frac{\partial \Delta E}{\partial x}|_{g_I'=0} = 0$ where $m = \min(m_F, m_F')$. The transitions $|F = 2, m_F = 1\rangle \leftrightarrow |F' = 1, m_F' = 0\rangle$ at $B = 0.01196$ T and $|F = 2, m_F = 0\rangle \leftrightarrow |F' = 1, m_F' = 1\rangle$ at $B = 0.01194$ T are examples of this duplicity.

---

[2] Because of nuclear spin selection rules, stimulated Raman transitions involving two laser beams can only change m_F by at most 1. Therefore, $\Delta m_F = 2$ transitions would require four laser beams.

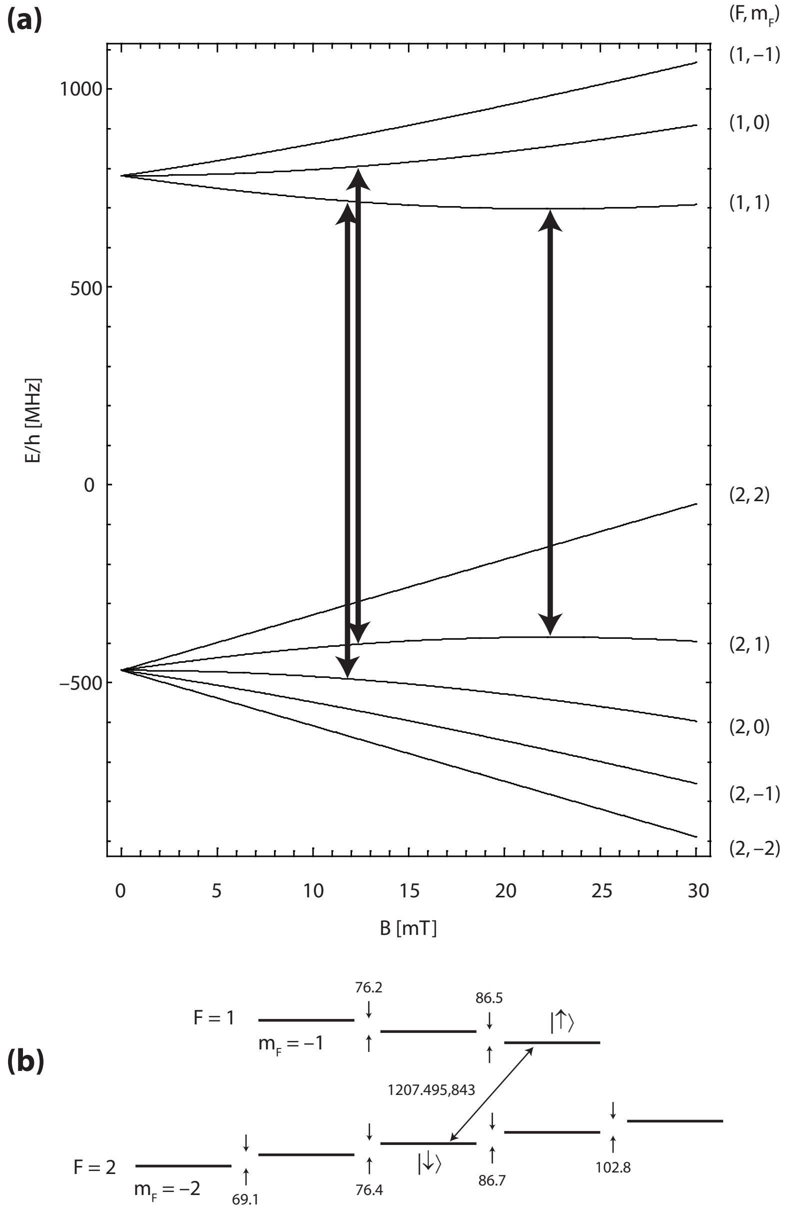

Figure 2.2: **(a)** Energy levels of the ground $S_{1/2}$ state in $^9\mathrm{Be}^+$ as a function of magnetic field calculated via the Breit-Rabi formula. The hyperfine constant $A = -625.008837048(10)$ MHz, electron g-factor $g_J = -2.00226206(42)$, and ratio of nuclear to electron g-factor $g_I' \equiv \frac{g_I}{g_J} = 2.134779853(2) \times 10^{-4}$ used in this calculation are taken from Ref. [Wineland 83]. The arrows indicate first-order magnetic field-independent transitions at 11.94 mT, 11.96 mT, and 22.31 mT. **(b)** Detailed transition frequencies of $S_{1/2}$ at 11.94 mT used in the experiments of Chapters 4 and 5. Frequencies are in MHz. The field-independent transition is indicated by the arrow. The states of the qubit are labeled as $|\downarrow\rangle$ and $|\uparrow\rangle$.

At very high magnetic fields, field-independent transitions exist between different nuclear hyperfine states (m_I) within an electron spin manifold (fixed m_J) due to the nuclear spin Zeeman effect. One such transition exists between states $|m_J = \frac{1}{2}, m_I = -\frac{3}{2}\rangle$ and $|m_J = \frac{1}{2}, m_I = -\frac{1}{2}\rangle$ at $x \simeq -36.73$ ($B \simeq 0.8194$ T). This particular transition was used as a 303 MHz frequency standard, and coherence times exceeding ten minutes were observed [Bollinger 91]. Other high-field field-independent transitions exist in $^9\text{Be}^+$ and are listed in Table 2.1.

When the coupling of magnetic field fluctuations to the transition frequency vanishes to first order, the second order coefficient determines the transition frequency's dependence on the field. At such extremum points, the transition frequency can be approximated by the following

$$\nu(B) \simeq \nu(B_0) + c_2(B - B_0)^2 \tag{2.12}$$

where ν is the transition frequency in Hz, B_0 is the magnetic field at which the field-independent transition occurs, and $c_2 \equiv \frac{1}{2h}\frac{\partial^2 \Delta E}{\partial B^2}|_{B=B_0}$. c_2 for the various field-independent points is tabulated in Table 2.1. Small values for c_2 are advantageous to reduce phase noise induced by ambient magnetic field fluctuations. As such, the 303 MHz frequency standard in Ref. [Bollinger 91] used the field-independent transition at $B_0 \simeq 0.8194$ T which has one of the smallest second order coefficient c_2 in $^9\text{Be}^+$. Unfortunately, optical stimulated Raman transitions (useful for individual qubit addressing in quantum information processors) between these states are inefficient because the nuclear spin is largely decoupled from the electron spin at such high magnetic fields. This, in addition to the relative ease it is to produce smaller magnetic field strengths, spurred us to pursue field-independent transitions near 0.0119 T for quantum information processing (see Chapter 4). The experiments in Chapters 4 and 5 used the $|F = 2, m_F = 0\rangle \leftrightarrow |F' = 1, m'_F = 1\rangle$ transition as the qubit. A detailed energy diagram of the $S_{1/2}$ manifold at 0.00194 T required for this qubit is shown in Fig. 2.2b.

Transition $\vert F, m_F\rangle \leftrightarrow \vert F', m'_F\rangle$	ν **[MHz]**	B_0 **[T]**	c_2 **[Hz/μT^2]**
$\vert 2,0\rangle \leftrightarrow \vert 1,0\rangle$	1250.01767410	0	$+3.140 \times 10^{-1}$
$\vert 2,1\rangle \leftrightarrow \vert 1,-1\rangle$	1250.01752212	2.5403×10^{-5}	$+2.355 \times 10^{-1}$
$\vert 2,0\rangle \leftrightarrow \vert 1,1\rangle$	1207.49584322	1.1945×10^{-2}	$+3.049 \times 10^{-1}$
$\vert 2,1\rangle \leftrightarrow \vert 1,0\rangle$	1207.35280753	1.1964×10^{-2}	$+3.049 \times 10^{-1}$
$\vert 2,1\rangle \leftrightarrow \vert 1,1\rangle$	1082.54706095	2.2307×10^{-2}	$+3.626 \times 10^{-1}$
$\vert 1,1\rangle \leftrightarrow \vert 1,0\rangle$	322.551896190	1.6018×10^{-1}	-5.293×10^{-4}
$\vert 2,0\rangle \leftrightarrow \vert 2,1\rangle$	324.547848987	1.7472×10^{-1}	-3.123×10^{-4}
$\vert 2,0\rangle \leftrightarrow \vert 2,1\rangle$	321.168429685	6.7740×10^{-1}	$+7.562 \times 10^{-6}$
$\vert 2,0\rangle \leftrightarrow \vert 1,0\rangle$	303.016377260	8.1944×10^{-1}	-7.749×10^{-6}

Table 2.1: Field-independent points in ^{9}Be$^+$

There are three parameters in the Breit-Rabi formula which determine the transition frequencies: A, g'_I, and x. The hyperfine constant A sets the y-scale. The x-locations of field-independent points in the intermediate field regime are determined by quantum numbers (F_+, m_F) with g'_I causing small variations in the x-positions. Field-independent x-locations in the high field regime (eigenstates approximated by $|m_I, m_J\rangle$) are determined solely by g'_I. In the limit $g'_I \to 0$, the high-field field-independent points tend toward $x \to \infty$. The magnetic field B can be determined from x given A and g_J. However, in practice, x is determined by measuring a transition frequency with non-zero first order dependence on changes in the magnetic field using knowledge of A and g'_I. Once x is measured, the energy levels of all other hyperfine states can be determined. In particular, the frequency of a field-independent transition can be calculated as a function of a field-dependent transition frequency. This calculation and corresponding measurement data are shown in Fig. 4.3.

The eigenvectors of the hyperfine Hamiltonian are described by Eq. (2.9). Writing the eigenvectors as $|0\rangle = \alpha_0|-\rangle + \beta_0|\rangle$ and $|1\rangle = \alpha_1|-\rangle + \beta_1|+\rangle$ for the two states of the field independent transition, we find that at any field-independent point, $\alpha_0 = -\alpha_1$ and $\beta_0 = \beta_1$ in the limit $g'_I \to 0$. Including g'_I causes a small correction on the order of 10^{-4}. This can be seen by optimizing Eq. (2.10) for x with $g'_I \to 0$ and substituting

x into Eq. (2.9). This has implications for quantum information processing because two-qubit gates relying on differential Stark shifts are less efficient (see § 2.6.2). The Stark shift of each qubit level is a function of $|\alpha|^2/\Delta$ where Δ is the detuning of the Raman laser from one of the exited $P_{1/2}$ or $P_{3/2}$ states. Therefore, the differential Stark shift for a field-independent qubit will have factors of the form $\frac{1}{\Delta} - \frac{1}{\Delta+\omega_0} \simeq \frac{\omega_0}{\Delta}\frac{1}{\Delta}$ where ω_0 is the qubit transition frequency. To reduce the effects of spontaneous scattering, we desire large detunings Δ, and the factor ω_0/Δ is typically 10^{-2} or less. A more detailed discussion of two-qubit gates based on differential Stark shifts can be found in § 2.6.2.

2.3 Initialization

One of the DiVincenzo criteria for quantum computation is the ability to initialize the system to a well defined state. We accomplish this via optical pumping. In the experiments, we use circularly polarized $\hat{\sigma}^+$ laser light propagating along the direction of the magnetic field to optically pump the state of the ions to the stretched $|F = 2, m_F = 2\rangle$ state. These laser beams consisted of the near resonant "Blue Doppler" (BD) beam tuned $\frac{1}{2}\gamma$ ($\gamma = 2\pi \times 19.4$ MHz, the natural linewidth) to the red of the cycling transition $|S_{1/2}, F = 2, m_F = 2\rangle \leftrightarrow |P_{3/2}, F' = 3, m'_F = 3\rangle$, the "BD Detuned" beam tuned 400 MHz to the red of the cycling transition, the "Red Doppler" (RD) beam tuned slightly to the red of the $|S_{1/2}, F = 1, m_F = 1\rangle \leftrightarrow |P_{1/2}, F' = 2, m'_F = 2\rangle$ transition, and the "Repumper" beam tuned on resonance with the $|S_{1/2}, F = 2, m_F = 1\rangle \leftrightarrow |P_{1/2}, F' = 2, m'_F = 2\rangle$ transition (see Fig. 2.3). The BD Detuned beam performs pre-cooling for very hot ions where the Doppler-broadened resonance makes the near-resonant BD cooling less efficient. This beam has approximately 500–1000 μW of laser power in a $\sim$30 μm waist. The near-resonant BD beam is responsible for fast Doppler cooling after the pre-cooling stage, and its intensity is set to approximately half of the saturation intensity ($\sim$0.5 μW in 25 μm waist). The RD beam assists in optically pumping the F=1 manifold when the polarization of BD is imperfect. However, for field-

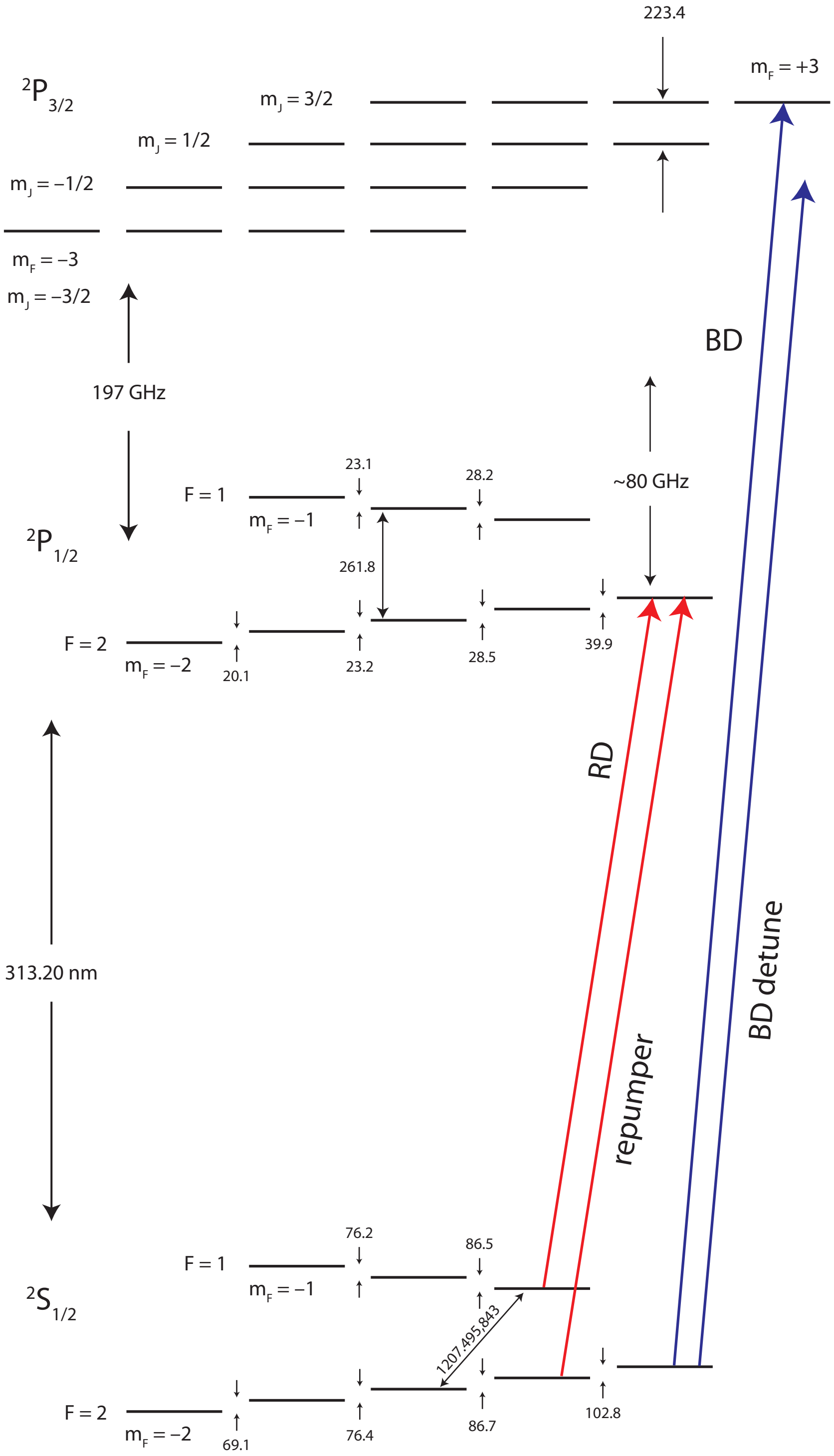

Figure 2.3: Laser frequencies and ^{9}Be$^+$ levels

independent qubits at 0.0119 T, imperfect BD polarization is less problematic than in the low field case (∼1 mT) because the depumping transition $|S_{1/2}, F = 2, m_F = 2\rangle \leftrightarrow |P_{3/2}, m_J = 1/2, m_I = 3/2\rangle$ is 223 MHz (11.5 γ) off-resonant. Furthermore, the high-power BD Detuned beam, even though it is ∼600 MHz off-resonant from the $|S_{1/2}, F = 1\rangle \leftrightarrow |P_{3/2}, m_J = 3/2\rangle$ transition, power broadens this transition to a ∼600 MHz width; therefore, BD Detuned is also efficient at optically pumping the $F = 1$ manifold. The Repumper beam optically pumps the $|F = 2, m_F = 1\rangle$ state during Raman side-band cooling (§ 2.5.4). Empirically we found that pre-cooling for a few hundred microseconds increased the ion lifetime in the trap. We suspect that ions became very hot occasionally after collisions with thermal background gas, and pre-cooling with an off-resonant beam would re-cool these hot ions after such an event.

After Doppler cooling and preparing the electronic state of the ion to the stretched state, the ion was further cooled to the motional ground state via resolved side-band cooling for some experiments (see § 2.5.4). Side-band cooling was performed on the $|F = 2, m_F = 2\rangle \leftrightarrow |F = 2, m_F = 1\rangle$ transition at 103 MHz. The final stage of side-band cooling involved repumping the ion back to the stretched $|F = 2, m_F = 2\rangle$ state, now in its motional ground state $|n = 0\rangle$. ($|n\rangle$ are Fock states of a harmonic oscillator potential, and n represents the phonon occupation number). Side-band cooling can prepare the ion in the motional ground state with 99% fidelity [Wineland 98]. However, the ion's motional state is only of importance prior to performing two-qubit logic gates. For the schemes outlined in this thesis (§ 2.6), the Lamb-Dicke criteria only need be satisfied. Therefore, a ground state preparation fidelity of 99% is sufficient for fault-tolerant quantum computation (see § 2.6 and Refs. [Sørensen 00, Steane 03]). To prepare the ion in the $|\uparrow\rangle$ in the qubit subspace, we performed a π-rotation on the $|F = 2, m_F = 2\rangle \leftrightarrow |\uparrow\rangle$ transition (see § 2.5.2). This is the starting point for computation.

The initialization infidelity of the ion's electronic state depends on the impurity of the RD laser-beam polarization since this is the last optical pumping operation prior to the start of the computation. This error, in principle, can be eliminated completely. However, it is instructive to calculate the preparation error given some impurity in the polarization. We consider the fidelity of preparing the stretched $|F = 2, m_F = 2\rangle$ state after optical pumping with RD and the Repumper, both $\hat{\sigma}^+$ polarized. We now consider the optical pumping rates away from $|F = 2, m_F = 2\rangle$ due to imperfect Repumper polarization since it is closest to resonance with the $|S_{1/2}, F = 2, m_F = 2\rangle \leftrightarrow |P_{1/2}\rangle$ transition. We assume for the present analysis that the Repumper beam has ϵ_{σ^+} admixture of $\hat{\sigma}^+$ polarization and ϵ_π admixture of $\hat{\pi}$ polarization.

The optical pumping rate from state i to state f through a single excited state is given by:

$$\Gamma_{i\to f} = \frac{\gamma}{2}\frac{s_0}{1 + s_0 + 4\frac{\delta^2}{\gamma^2}} c_{i\to f} \tag{2.13}$$

where γ is the natural line width, $s_0 \equiv I/I_s$ is the on-resonance saturation parameter, δ is the detuning of the laser from the excited state through which the scattering occurs, and $c_{i\to j}$ is a coupling coefficient[3] . I is the laser intensity, and I_s is the saturation intensity [Metcalf 99, § 2.4]. For scattering through either $|P_{1/2}, F = 2, m_F = 2\rangle$ via $\hat{\pi}$ polarized light or through $|P_{1/2}, F = 2, m_F = 1\rangle$ via $\hat{\sigma}^-$ polarized light, summing over coupling coefficients yields $\sum_j c_{i\to j} = 2/9$ (independent of the magnetic field). The optical pumping rate into the stretched state also has a coupling coefficient of 2/9. Therefore, the ratio of rates gives the steady state fraction and hence the error in initialization:

$$e_{\text{init}} = \frac{\epsilon_\pi}{1 + \delta_\pi^2/\gamma'^2} + \frac{\epsilon_{\sigma^-}}{1 + \delta_{\sigma^-}^2/\gamma'^2} \tag{2.14}$$

where $\gamma' \equiv \frac{1}{2}\sqrt{1 + s_0}$ is half of the power broadened line width. For ^{9}Be$^+$ at 0.0119 T, the field independent point, $\delta_\pi = 103$ MHz and $\delta_{\sigma^+} = 143$ MHz. With 0.1% admixture of both $\hat{\pi}$ and $\hat{\sigma}^+$ polarizations and an on-resonance saturation parameter of $s_0 = 1/2$, the

---

[3] The calculation of the coupling coefficient $c_{i\to j}$ is very similar to the calculation of $b_{ij}^{(k)}$ in § 2.4.3.

error in initialization is 2.0×10^{-5}, below the fault-tolerant limit [Steane 03, Knill 05].

2.4 Measurement

Qubit measurements are performed via state-dependent resonance fluorescence. Originally proposed by Dehmelt *et al.* [Dehmelt 75] and later demonstrated by Wineland *et al.* [Wineland 80], Nagourney *et al.* [Nagourney 86], Sauter *et al.* [Sauter 86], and Bergquist *et al.* [Bergquist 86], this technique takes advantage of a closed transition's ability to scatter many photons without optically pumping out of the closed transition. A resonant laser on a strong closed transition is applied to the ion causing a projective measurement of the atomic state collapsing the wave function of the ion into one of the ion's atomic eigenstates. If the collapsed ion state is found to be in one of the states participating in the closed transition, then strong fluorescence occurs. Conversely, if the ion's state collapses into a state that does not participate in the closed transition, then a very small amount of fluorescence occurs. For the $^9\mathrm{Be}^+$ qubit, we use the cycling transition $|S_{1/2}, F = 2, m_F = 2\rangle \leftrightarrow |P_{3/2}, F' = 3, m'_F = 3\rangle$ excited by $\hat{\sigma}_+$ light as the strong closed transition. We tune the BD laser on resonance with approximately half of the saturation intensity. If the ion collapses into the $|F = 2, m_F = 2\rangle$ state, the ion scatters approximately 20 million photons per second. The qubit states $|\uparrow\rangle$ and $|\downarrow\rangle$ (see Fig. 2.2b) are transferred to the states $|F = 2, m_F = 2\rangle$ ("bright") and $|\uparrow\rangle$ ("dark") respectively by a sequence of two π-pulses on their respective transitions prior to applying the resonant BD laser for fluorescence measurement. With a detector efficiency of 3×10^{-3}, we collected on average 12 photons on a photomultiplier tube (PMT) in a 200 μs detection interval if the ion was projected into the "bright" state. (The photon collection apparatus is described in detail in § 3.3.1). The "dark" state $|\uparrow\rangle$ scatters negligible photons since the detection laser is 1.2 GHz off resonance. The typical background photon count for the dark state was ~0.1 photon in the 200 μs detection interval.

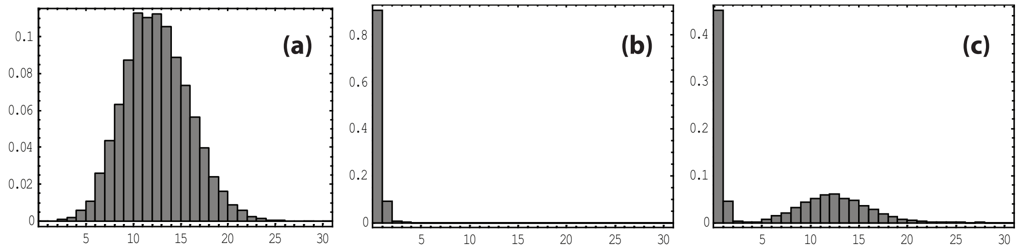

Figure 2.4: Typical histogram of qubit measurements for the qubit state prepared in **(a)** $|\uparrow\rangle$, **(b)** $|\downarrow\rangle$, and **(c)** equal superposition of $|\uparrow\rangle$ and $|\downarrow\rangle$. The histograms are normalized by the number of experiments, $N = 1000$ in this case.

The distribution of collected photons from the bright state ideally follows Poisson statistics with a mean given by the scattering rate, detection efficiency, and detection interval—12 photons in our case. If the ion does not scatter any photons, background light collected on the detection system generates a histogram of photon counts that also obeys Poisson statistics. The mean of the "dark" distribution was 0.1. We performed multiple repetitions of the experiments and generated a histogram of photon counts. Typical histograms for qubit states in $|\uparrow\rangle$, $|\downarrow\rangle$, and superpositions of these two are shown in Fig. 2.4. To determine the probability that the qubit state was in either $|\uparrow\rangle$ or $|\downarrow\rangle$, we fit the measurement histogram to a weighted sum of two Poisson distributions. The bright mean of the Poisson distribution used for fitting is extracted by fitting measurement data for a prepared $|F = 2, m_F = 2\rangle$ state. The dark mean is determined by fitting the background counts collected to a Poisson distribution when the detection laser was tuned far off resonance (∼1 GHz). The fitting procedure used was the method of maximum likelihood (see Appendix C and [Freund 92]).

2.4.1 Dark to Bright State Optical Pumping

One fundamental source of measurement error occurs due to off-resonant optical pumping of the dark state into the bright state. When this occurs, the dark state begins to participate in the cycling transition, and the collected photons obey Poisson statistics with a reduced mean. For the dark state $|\uparrow\rangle$, the probability of scattering into the bright state follows an exponential distribution assuming a two level system. We expect the distribution of collected photons then to be the convolution of an exponential distribution and the Poisson distribution [King 99, Acton 05]. We give the analysis following that of Acton *et al.* [Acton 05].

For an ion originally in the dark state at time $t = 0$, the probability that the ion will be found in the bright state at time t is given by

$$f(t) = 1 - e^{-\omega t} \tag{2.15}$$

where ω is the scattering rate into the bright state and is calculated from atomic parameters and the laser intensity at the ion. To a first approximation,

$$\omega = \frac{\gamma}{2} \frac{s_0}{1 + s_0 + \frac{4\delta^2}{\gamma^2}} c_{BR} \tag{2.16}$$

where γ is the natural line width, $s_0 \equiv I/I_s$ is the on-resonance saturation parameter, δ is the detuning of the detection laser from the dark state to $|P_{3/2}, m_J = 1/2\rangle$ state transition, and c_{BR} is the coupling coefficient for scattering through this state into the bright stretched state. Here, we have neglected scattering into $|F = 2, m_F = 1\rangle$ followed by scattering into the bright state. This is a second order off-resonant scattering process, and the above analysis still gives a conceptual view of the repumping error process. Later I will use a rate-equation treatment to show the repumping error in the case where the dark state is transferred (or "shelved") to an auxiliary state where multiple scattering events must occur in order for the dark state to participate in the cycling transition. In this more general treatment, all allowed scattering paths are taken into account; therefore, I will delay its discussion until then. Using field-independent qubits, c_{BR} is no longer a simple product of Clebsch-Gordon coefficients because the eigenstates are no longer states with well defined total angular momentum (see § 2.2). The eigenstates are more generally described by superpositions in the $|m_I, m_J\rangle$ basis:

$|\mathrm{dark}\rangle = \alpha|m_I = m_F + 1/2, m_J = -1/2\rangle + \beta|m_I = m_F - 1/2, m_J = +1/2\rangle$. Using this definition, $c_{BR} = \frac{2}{9}\alpha^2$. For $^9\mathrm{Be}^+$ at 0.0119 T, $\gamma = 2\pi \times 19.4\ \mu\mathrm{s}^{-1}$, $\frac{2\delta}{\gamma} = 128$, and $\alpha = -0.793$. At $s_0 = \frac{1}{2}$, the scattering rate from the dark state into the bright state is $\omega = 2.6 \times 10^{-4}\ \mu\mathrm{s}^{-1}$.

Eq. (2.15) describes the probability that the dark state will be found in the bright state at time t. The probability that the dark state will scatter into the bright state between t and $t + \mathrm{d}t$ is given by its derivative,

$$\dot{f}(t)\mathrm{d}t = \omega e^{-\omega t}\mathrm{d}t. \tag{2.17}$$

If the dark ion enters the bright state at time t, the collected photons will exhibit Poisson statistics with a mean given by

$$\lambda(t) = r_{bg}\gamma_c\tau_D + \gamma_c(\tau_D - t) \tag{2.18}$$

where τ_D is the detection interval, $\gamma_c = \eta\frac{\gamma}{2}\frac{s_0}{1+s_0}$ is the rate of *collected* photons from the cycling transition, η is the photon collection efficiency, and r_{bg} is the rate of background collected photons normalized by γ_c. The mean of the background distribution is $\lambda_{bg} = r_{bg}\gamma_c\tau_D$, and the mean of the bright distribution (in the absence of background) is $\lambda_0 = \gamma_c\tau_D$. Including background, the bright distribution has a mean of $\lambda_{bg} + \lambda_0 = (1 + r_{bg})\gamma_c\tau_D$. $\lambda(t)$ in Eq. (2.18) is a function of the random variable t. We desire the distribution of λ, and we are given $\lambda(t)$ and $\dot{f}(t)\mathrm{d}t$, the probability of the dark ion entering the bright state between t and $t + \mathrm{d}t$. The fundamental transformation law of probabilities states that for a probability distribution $p(x)\mathrm{d}x$ of the random variable x, the distribution for a function $y(x)$ of the random variable x follows the rule $|p(x)\mathrm{d}x| = |p(y)\mathrm{d}y|$. Using this transformation law for the function $\lambda(t)$, we find

$$g(\lambda)\mathrm{d}\lambda = \begin{cases} \frac{\omega}{\gamma_c}e^{-\frac{\omega}{\gamma_c}[\lambda_{bg}+\lambda_0-\lambda]}\mathrm{d}\lambda & \lambda_{bg} < \lambda \le \lambda_{bg} + \lambda_0 \\ e^{-\omega\tau_D} & \lambda = \lambda_{bg} \end{cases}, \tag{2.19}$$

the probability that the collected photons from a dark ion will exhibit Poisson statistics with mean λ. When the dark ion never optically pumps to the bright state, the mean of the photon distribution is simply the background mean λ_{bg}. The probability that the dark ion will exhibit Poisson statistics with mean λ_{bg} is $e^{-\omega\tau_D}$ which is the probability $1 - f(\tau_D)$ that the ion never optically pumps to the bright state.

The calculation of the dark state photon count distribution is now straight forward. Given the density of means $g(\lambda)$ and conditional probability of detecting n photons given λ (the Poisson distribution $P(n|\lambda) = \frac{e^{-\lambda}\lambda^n}{n!}$) the distribution of photon counts for an ion originally in the dark state is simply the convolution:

$$\begin{aligned} p_{\text{dark}}(n) &= e^{-\omega\tau_D}\left(P(n|\lambda_{bg}) + \frac{\omega e^{-\frac{\omega}{\gamma_c}\lambda_{bg}}}{\gamma_c n!}\int_{\lambda_{bg}}^{\lambda_{bg}+\lambda_0} e^{\omega\lambda/\gamma_c}e^{-\lambda}\lambda^n \mathrm{d}\lambda\right) \\ &= e^{-\omega\tau_D}\Bigg[P(n|r_{bg}\gamma_c\tau_D) + \frac{\omega\gamma_c^n e^{-\omega\tau_D r_{bg}}}{(\gamma_c-\omega)^{n+1}}\big\{P_2(n+1,(\gamma_c-\omega)(1+r_{bg})\tau_D) \\ &\quad - P_2(n+1,(\gamma_c-\omega)r_{bg}\tau_D)\big\}\Bigg] \end{aligned} \tag{2.20}$$

where $P_2(a,x) \equiv \frac{1}{(a-1)!}\int_0^x e^{-y}y^{a-1}\mathrm{d}y$ is the incomplete Gamma function normalized such that $P_2(a,\infty) = 1$. We have explicitly shown the τ_D dependence on the second line in Eq. (2.20).

2.4.2 Improving Dark to Bright State Leakage Through Shelving

Off-resonant repumping of the dark state can further be suppressed by transferring the dark state to a hyperfine state where multiple scattering events would be required before the dark state would be pumped into the bright state. Fig. 2.5 illustrates this basic idea. If the dark state is $|F=1, m_F=1\rangle$, even though scattering is suppressed because the detection beam is off resonance, only a single scattering event is required to pump this state into the bright $|F=2, m_F=2\rangle$ state. Conversely, if the dark state is $|F=2, m_F=-2\rangle$, a minimum of four scattering events would be required for this state to pump to the bright state[4] . Because scattering into the bright state is a

---

[4] The quantum number m_F can only change by 1 per scattered photon at most because the electron spin is largely decoupled from the nuclear spin in the $P_{3/2}$ state. This occurs because the hyperfine

multi-order off-resonant photon scattering process, we expect Eq. (2.15) to no longer be valid. Eq. (2.15) describes the probability of the electron to be in the $|F=2, m_F=2\rangle$ state at time t. Once we determine the correct $f(t)$, we can proceed as in the previous section to calculate the distribution of photon counts for the dark state.

The dynamics of the probability of the electron to be in state $|F=2, m_F=2\rangle$ can be calculated using a rate-equation treatment. Let the vector $\mathbf{v}$ represent the population in each of the hyperfine states. In $^9\mathrm{Be}^+$ the length of this vector is 8. We define the rate matrix $\mathbf{\Gamma}$ as the matrix whose elements Γ_{ij} are the optical pumping rates from state $j \rightarrow i$. Because the detection beam is $\hat{\sigma}^+$ polarized and population can only scatter into states with $\Delta m_F \in \{0, +1\}$, the columns of $\mathbf{\Gamma}$ have at most three entries. We ignore Rayleigh elastic scattering by letting $\Gamma_{ii} = 0$ as it does not affect the optical pumping process. The rate of population transfer is given by:

$$\frac{\partial v_i}{\partial t} = \sum_j \Gamma_{ij} v_j - v_i \sum_j \Gamma_{ji}. \tag{2.21}$$

In matrix notation, Eq. (2.21) can be written as

$$\frac{\partial \mathbf{v}}{\partial t} = \mathbf{M} \cdot \mathbf{v} \tag{2.22}$$

where $\mathbf{M} \equiv \mathbf{\Gamma} - \mathbf{D}(\mathbf{1}_v^{\mathrm{T}} \cdot \mathbf{\Gamma})$, $\mathbf{1}_v$ is a column vector of ones, and the operator $\mathbf{D}(\mathbf{x})$ is defined as a diagonal matrix whose diagonal elements are the elements of the vector $\mathbf{x}$. The matrix $\mathbf{M}$ has at most four entries per column or row with the diagonal elements dependent on the other three non-zero entries in the same column (the sum of each column is zero to conserve total population). Taking the Laplace transform of Eq. (2.22) yields:

$$s\mathbf{V}(s) - \mathbf{v}(0) = \mathbf{M} \cdot \mathbf{V}(s). \tag{2.23}$$

where $\mathbf{V}(s)$ is the Laplace transform of $\mathbf{v}(t)$, $\mathbf{v}(0)$ is the initial condition, and s is the Laplace transform variable. Eq. (2.23) is an algebraic linear system of equations which

---

splitting in the $P_{3/2}$ manifold (< 1 MHz) is small compared to the Zeeman splitting (223 MHz). The nuclear spin quantum number m_I is conserved through emission of a photon from the exited P state to the ground state.

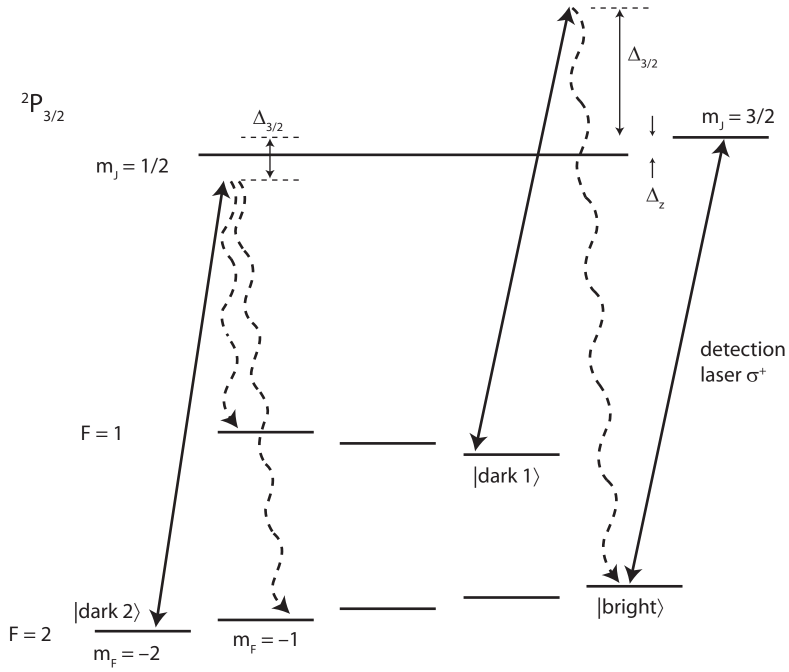

Figure 2.5: Shelving the dark state for increased detection efficiency. During the detection interval, the |dark 2⟩ state has a smaller probability of off-resonantly scattering into the |bright⟩ state than the |dark 1⟩ state. In the first case, a minimum of four scattering events must occur, whereas in the latter case, only 1 scattering event must occur. In the figure, $\Delta_{3/2}$ is the detuning of the detection laser from the $|P_{3/2}, m_J = 3/2\rangle$ manifold for different $S_{1/2}$ hyperfine states, and $\Delta_z = 233$ MHz is the $P_{3/2}$ excited state Zeeman splitting between the $m_J = 3/2$ and $m_J = 1/2$ manifolds at 0.0119 T. Not shown are four hyperfine sub-levels in each m_J manifold in the $P_{3/2}$ level all within 1 MHz.

is easily solved, and its solution is:

$$\mathbf{V}(s) = -(\mathbf{M} - s\mathbf{1})^{-1}\mathbf{v}(0) \tag{2.24}$$

where $\mathbf{1}$ is the identity matrix. The inverse Laplace transform of Eq. (2.24) gives the time domain solution for the state vector $\mathbf{v}(t)$ given the initial condition $\mathbf{v}(0)$.

Some comments on the solution Eq. (2.24) are in order. Firstly, we note that the columns of the matrix $-(\mathbf{M} - s\mathbf{1})^{-1}$ are the solutions for the initial conditions where 100% of the population starts in a particular hyperfine state. Secondly, the inverse of a matrix is proportional to the inverse of its determinant; therefore, each element is proportional to the inverse of the characteristic polynomial of $\mathbf{M}$. In terms of control theory, we can interpret $-(\mathbf{M}-s\mathbf{1})^{-1}$ as a transfer function, and the poles of the transfer function represent the characteristic frequencies of the system. These frequencies are independent of the initial conditions. Looking at a single term further, we can rearrange the term in to a sum of partial fractions:

$$\begin{aligned} [(\mathbf{M} - s\mathbf{1})^{-1}]_{ij} &= \frac{p_{ij}(s)}{q(s)} \\ &= \sum_k \frac{a_{ij}^{(k)}}{s + \omega_k} \end{aligned} \tag{2.25}$$

where $q(s)$ is the characteristic polynomial common to all terms, $p_{ij}(s)$ is a polynomial in s, $-\omega_k$ are the roots of $q(s)$ $[q(s) = \prod_k (s + \omega_k)]$, and

$$\begin{aligned} a_{ij}^{(k)} &= \lim_{s \to -\omega_k} \frac{(s + \omega_k)p_{ij}(s)}{q(s)} \\ &= \frac{p_{ij}(\omega_k)}{\prod_{l \neq k}(\omega_l - \omega_k)} \end{aligned} \tag{2.26}$$

are constants assuming $q(s)$ has no double roots. This is the case for our detection system. Thirdly, we know physically that $\hat{\sigma}^+$ polarized light optically pumps any initial state to the $|F = 2, m_F = 2\rangle$ stretched state, so we know the solution $\mathbf{v}(t \to \infty)$ approaches $|F = 2, m_F = 2\rangle$. As such, we can use the final value theorem for Laplace transforms, $\lim_{s\to 0} s\mathbf{V}(s) = \lim_{t\to\infty} v(t)$, to state that the characteristic polynomial

$q(s)$ must have a single zero at $s = 0$. Furthermore, the $1/s$ term in the partial fraction expansion of $(\mathbf{M} - s\mathbf{1})^{-1}$ has a coefficient of -1 for the $|F = 2, m_F = 2\rangle$ row and 0 for all other rows ($p_{ij}(s)$ has a zero at $s = 0$ for all rows other than $|F = 2, m_F = 2\rangle$). Since we are concerned with the probability of detecting the electron in state $|F = 2, m_F = 2\rangle$ with the electron starting in some other hyperfine state at $t = 0$, we are only concerned with the $|F = 2, m_F = 2\rangle$ row of $-(\mathbf{M} - s\mathbf{1})^{-1}$. Its elements represent different hyperfine states as initial conditions.

We are now prepared to give some insight into the time-domain solution. Taking the inverse Laplace transform of $-[(\mathbf{M} - s\mathbf{1})^{-1}]_{i=(2,2),j}$ gives the probability that the state $|j\rangle$ will have optically pumped into the bright state $|F = 2, m_F = 2\rangle$ by time t:

$$P(\text{bright}|j) = 1 - \sum_k a^{(k)}_{i=(2,2),j} e^{-\omega_k t}. \tag{2.27}$$

The frequencies $-\omega_k$ are the non-zero roots of the characteristic polynomial; the j index specifies the initial condition, and $a^{(k)}_{i=(2,2),j}$ are determined from Eq. (2.26). Comparing to $f(t)$ in Eq. (2.15), we can simply replace $e^{-\omega t}$ with the sum $\sum_k a^{(k)}_{i=(2,2),j} e^{-\omega_k t}$ and follow the analysis of the previous section to obtain the distribution of collected photons as:

$$\begin{aligned} p_{\text{dark}}(n|j) = \sum_k a^{(k)}_{i=(2,2),j} e^{-\omega_k \tau_D} \Bigg[& P(n|r_{bg}\gamma_c\tau_D) + \frac{\omega_k \gamma_c^n e^{-\omega_k \tau_D r_{bg}}}{(\gamma_c - \omega_k)^{n+1}} \\ & \times \big\{ P_2(n+1, (\gamma_c - \omega_k)(1 + r_{bg})\tau_D) \\ & - P_2(n+1, (\gamma_c - \omega_k) r_{bg} \tau_D) \big\} \Bigg]. \end{aligned} \tag{2.28}$$

Plots of the dark distribution Eq. (2.28) for different initial conditions are shown in Fig. 2.6. Parameters used in the calculation of the rate matrix are the following. The on-resonance saturation parameter for the cycling transition is $s_0 = 0.5$, and the frequency of the detection laser is on resonance with the cycling transition. The detunings and hyperfine state superposition amplitudes α and β are calculated from the Breit-Rabi formula (see § 2.2) at 0.0119 T, the field-independent point. For initial conditions where

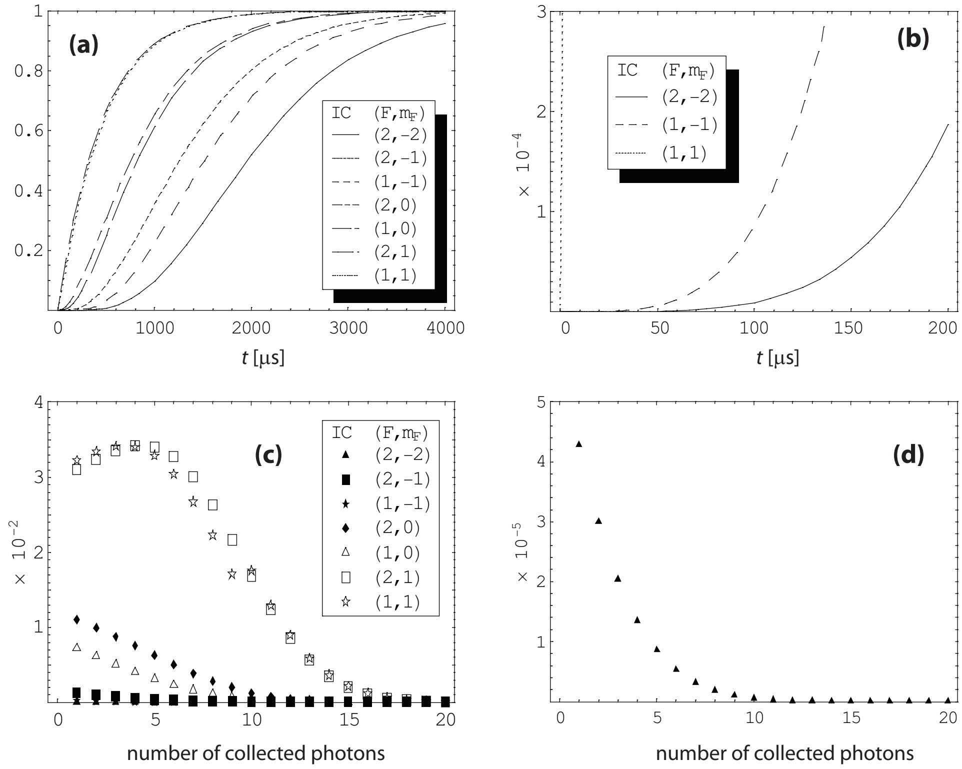

Figure 2.6: **(a)** Probability of a $^{9}\mathrm{Be}^{+}$ ion to be in state $|F = 2, m_F = 2\rangle$ at time t given different initial conditions (IC) at $t = 0$ calculated using Eq. (2.27). **(b)** Close up of probability of electron to be in state $|F = 2, m_f = 2\rangle$ for the two best states $|F = 2, m_F = -2\rangle$ and $|F = 1, m_F = -1\rangle$ and the $|F = 1, m_F = 1\rangle$ state for comparison. **(c)** Photon count distribution for the dark state for different initial conditions (IC). **(d)** Close up view of the photon count distribution for the state $|F = 2, m_F = -2\rangle$. In both **(c)** and **(d)** the probability of detecting 0 photons is off the y-scale and near 1. The mean of the bright distribution is $\lambda_0 = 10$ in $\tau_D = 200\ \mu$s ($\gamma_c = 5 \times 10^{-2}$). Background is zero ($r_{bg} = 0$).

$|j\rangle = |F=1, m_F=1\rangle$ or $|F=2, m_F=1\rangle$ such that a single scattered photon could optically pump the state $|j\rangle$ into the bright state, Eq. (2.28) has a single dominant term and approximates the simpler solution in Eq. (2.20). In this case, the dark distribution exhibits a bimodal feature (the first mode is at $n=0$ and off the y-scale near 1; the second mode is near $n=4$). The multi-order scattering processes do not exhibit this property.

2.4.3 Optical Pumping Rates—Kramers-Heisenberg Formula

The non-zero elements Γ_{ij} of the rate matrix in Eq. (2.21) can be calculated using the Kramers-Heisenberg formula [Ozeri 05, Loudon 00, §8.7]

$$\Gamma_{ij} = g^2\gamma \left| \sum_k \frac{b_{ij}^{(k)}}{\Delta_k} \right|^2 \tag{2.29}$$

where $g = \frac{E\mu}{2\hbar} = \frac{\gamma\sqrt{s_0}}{2\sqrt{2}}$, $E = \sqrt{2I/c\epsilon_0}$ is the laser-beam electric field amplitude, c is the speed of light, ϵ_0 is the vacuum dielectric constant, and $\mu = |\langle P_{3/2}, F=3, m_F = 3|\mathbf{d}\cdot\hat{\sigma}^+|S_{1/2}, F=2, m_F=2\rangle|$ is the magnitude of the cycling transition electric-dipole moment. Here, $\mathbf{d}$ is the electric dipole operator, I is the laser-beam intensity, γ is the natural line-width, and $s_0 \equiv I/I_s$ is the on-resonance saturation parameter. The amplitude $b_{ij}^{(k)} = \sum_q \langle i|\mathbf{d}\cdot\hat{\sigma}^q|k\rangle\langle k|\mathbf{d}\cdot\hat{\sigma}^+|j\rangle/\mu^2$ is the normalized second-order coupling from state $|j\rangle$ to state $|i\rangle$ through the excited state $|k\rangle$, and Δ_k is the detuning of the detection laser from the $|j\rangle \leftrightarrow |k\rangle$ transition frequency. The sum over k in Eq. (2.29) is over all intermediate excited states $|k\rangle$. For this case, we will only be concerned with $m_J \in \{1/2, 3/2\}$ manifolds in the $P_{3/2}$ level since the detection laser is $\hat{\sigma}^+$ polarized and near resonance with only these levels. Furthermore, we only consider Raman inelastic scattering where $i \neq j$ since only these events cause optical pumping.

States $|i\rangle$ and $|j\rangle$ can be written as $|l\rangle \equiv \alpha_l|m_I = m_F+1/2, m_J = -1/2\rangle + \beta_l|m_I = m_F - 1/2, m_J = +1/2\rangle$ for $l \in \{i, j\}$. We distinguish between two types of Raman scattering, namely $\Delta m_F = 0$ transitions where the scattered photon does not change the z-projection of total angular momentum, and $\Delta m_F = 1$ where the final total z-projection is increased by 1. For $\Delta m_F = 0$ transitions, Raman photon scattering occurs through two excited states, one in each of the $m_J = 3/2$ and $m_J = 1/2$ manifolds in the $P_{3/2}$ level. The result is:

$$\begin{aligned}\Gamma_{ij}^{\Delta m=0} &= g^2\gamma\left|\frac{1}{3}\frac{\alpha_i\alpha_j}{\Delta_{3/2}+\Delta_z}+\frac{\beta_i\beta_j}{\Delta_{3/2}}\right|^2 \\ &= g^2\gamma\frac{4}{9}|\alpha_j\beta_j|^2\left(\frac{1+\frac{3}{2}\frac{\Delta_z}{\Delta_{3/2}}}{\Delta_{3/2}+\Delta_z}\right)^2\end{aligned} \tag{2.30}$$

where we have used the orthonormality of the hyperfine states and the definitions of $\Delta_{3/2}$ and Δ_z in Fig. 2.5. Raman photon scattering for the $\Delta m_F = 1$ case only scatters through the $|P_{3/2}, m_I = m_F + 1/2, m_J = 1/2\rangle$ states. Its rate is:

$$\Gamma_{ij}^{\Delta m=1} = g^2\gamma\frac{2}{9}\frac{|\beta_i\alpha_j|^2}{(\Delta_{3/2}+\Delta_z)^2}. \tag{2.31}$$

Eqs. (2.30) and (2.31) break down when the detuning $\Delta_{3/2}$ is comparable to half of the power broadened line width. We can include radiative damping in Eqs. (2.30) and (2.31) by including an imaginary term in the detuning [Loudon 00, §8.8–8.9]. Letting $\Delta_{3/2} \to \Delta_{3/2} + i\gamma'$, we obtain the following result:

$$\begin{aligned}\Gamma_{ij}^{\Delta m=0} &= g^2\gamma\frac{4}{9}|\alpha_j\beta_j|^2\frac{1}{\Delta_{3/2}^2}\frac{\left(1+\frac{3}{2}\frac{\Delta_z}{\Delta_{3/2}}\right)^2+\left(\frac{\gamma'}{\Delta_{3/2}}\right)^2}{\left[1+\frac{\Delta_z}{\Delta_{3/2}}-\left(\frac{\gamma'}{\Delta_{3/2}}\right)^2\right]^2+\left(\frac{\gamma'}{\Delta_{3/2}}\right)^2\left(2+\frac{\Delta_z}{\Delta_{3/2}}\right)^2} \\ \Gamma_{ij}^{\Delta m=1} &= g^2\gamma\frac{2}{9}\frac{1}{\left(\Delta_{3/2}+\Delta_z\right)^2+\gamma'^2}\end{aligned} \tag{2.32}$$

where $\gamma' \equiv \frac{\gamma}{2}\sqrt{1+s_0}$ is half of the power broadened line width. This method of adding $i\gamma'$ to the detuning in the Kramers-Heisenberg formula on a 2-level atom reproduces the well known saturated scattering rate in Eq. (2.16). Letting $\gamma' \to 0$, Eq. (2.32) reduces to Eqs. (2.30) and (2.31).

The parameters α, β and $\Delta_{3/2}$ are calculated using the Breit-Rabi formula (see § 2.2). We use $g^2 = \gamma^2 s_0/8$ with $s_0 = 1/2$ to generate the $\mathbf{\Gamma}$ matrix used in the calculation of Fig. 2.6.

2.4.4 Optimizing Measurement Fidelity

The goal of a single qubit measurement is to determine whether the ion was projected into the bright $|F = 2, m_F = 2\rangle$ state or a dark state. As discussed in § 2.4, this is determined by observing the fluorescence of the ion. The bright state scatters many photons, whereas the dark state scatters a much smaller number of photons. Experimentally, we collect fluorescence for a fixed detection interval τ_D, and we establish a cut-off for the number of collected photons n_c such that if we collect more than n_c photons, we determine that the ion was projected into the bright state. Likewise, if we collect at most n_c photons, we claim that the ion was projected into a dark state. The optimum cut-off n_c is a function of τ_D, the background photon collection rate, the distribution of collected photons in the dark state $p_{\text{dark}}(n)$ [see Eq. (2.28)], and to which hyperfine state we choose to map the original $|\downarrow\rangle$ state. From § 2.4.2, we see that $|F = 2, m_F = -2\rangle$ is the optimum dark state. We now focus attention on optimizing τ_D and n_c.

The probability of falsely determining that a bright ion was dark is given by $\sum_{n=0}^{n_c} P(n|\gamma_c \tau_D(1 + r_{bg}))$ where $P(n|\lambda) \equiv e^{-\lambda}\lambda^n/n!$ is the Poisson distribution with mean λ (the bright-ion distribution). Likewise, the probability of falsely determining that an ion prepared in the dark state $|j\rangle$ was bright is given by $\sum_{n=n_c+1}^{\infty} p_{\text{dark}}(n|j) = 1 - \sum_{n=0}^{n_c} p_{\text{dark}}(n|j)$ [see Eq. (2.28)]. The total error in measuring a qubit is the average of these two (assuming a uniform prior distribution of states). We wish to minimize the total error by varying n_c and τ_D. It so happens that $n_c = 0$ is optimal independent of which dark is used if the background is zero ($r_{bg} = 0$). This can be physically understood by considering the knowledge acquired about the state once a single photon is detected. If there is no background and the photon collection efficiency is small such that we can neglect the probability of collecting one of the photons scattered by states other than the bright state, then the collected photon is generated by scattering on the cycling transition. That is, whether the original state was dark or bright, the detection of a photon implies that the state of the ion directly after the photon is collected is bright. This is because the cycling transition is closed, and once the ion is optically pumped to the bright state, it stays there. In the presence of background, this is not necessarily the case. The collected photon could have been generated by the cycling transition, or it could have been generated by the background. Depending on the background level, different n_c are optimal. We can include the probability of collecting any of the photons scattered by the dark states as they optically pump to the bright state similarly to including background. For collection efficiencies on the order of $\eta \sim 10^{-3}$, $n_c = 0$ is optimal. A straight forward way to determine n_c is to numerically calculate the optimal error by varying τ_D for different n_c.

Assuming zero background, the optimal cut-off is $n_c = 0$, and we can optimize the average error by varying τ_D. With a photon collection efficiency of 2.5×10^{-3} (this corresponds to collecting 10 photons in 200 μs), we find the optimal measurement interval to be $\tau_D = 196$ μs yielding an average measurement error of 8.6×10^{-5}. With an $f/1$ optical collection system and a PMT quantum efficiency of 20%, a detection efficiency of 5×10^{-3} is possible. Using such a system, we can collect 20 photons in 200 μs, and the optimal measurement interval is 121 μs in which we collect on average 12.1 photons for the bright state. In this case, the measurement error is 1.0×10^{-5}. High-finesse cavities can increase total photon collection efficiencies to as high as ∼30% [Keller 04, Acton 05]; however, using simple measurement optics and transferring the dark state to a "far-away" hyperfine state where multiple scattering events are required before the dark state can optically pump to the bright state, we obtain measurement errors below the fault-tolerance threshold [Steane 03, Knill 05].

It is interesting to compare the far-away hyperfine dark state measurement fidelity to an ion with a large hyperfine splitting and a dark state only $\Delta m_F = 1$ away from the bright state. In Ref. [Acton 05], the authors calculate the ideal measurement fidelity for such a case in $^{111}\mathrm{Cd}^+$. With a photon collection efficiency of $\eta = 1 \times 10^{-3}$ and a hyperfine splitting of 14.5 GHz, the minimum infidelity in $^{111}\mathrm{Cd}^+$ is 5×10^{-3}. The smallness of the infidelity is due solely to the relatively large hyperfine splitting in $^{111}\mathrm{Cd}^+$ decreasing the optical pumping rate. For comparison, in $^{9}\mathrm{Be}^+$ with a 1.2 GHz hyperfine splitting, photon collection efficiency of $\eta = 1 \times 10^{-3}$, and a far-away dark state $|F = 2, m_F = -2\rangle$, the minimum infidelity is 1.1×10^{-3}. However, the suppression of dark to bright optical pumping in the far-away dark state case shows its true power in the scaling of error rate with photon collection efficiency. At $\eta = 5 \times 10^{-3}$, the infidelity in $^{111}\mathrm{Cd}^+$ is 1.2×10^{-3}, whereas in $^{9}\mathrm{Be}^+$, it is 1.0×10^{-5}. Measurement errors could be suppressed even further using a different ion with larger nuclear spin such as $^{25}\mathrm{Mg}^+$. In addition, quantum logic operations may be used to increase measurement fidelity [Schaetz 05]. In Ref. [Acton 05] the authors optimize the worst case error calculated by taking the maximum of the errors in falsely inferring the bright or dark state. We calculate the average error (for reasons, see § 2.4.6) which are $\sim 2 - 6\%$ lower than the worst case error.

We note that these theoretical low error probabilities for measurement using far-away dark states have not been verified experimentally. Background light and imperfect transfer pulses limit the measurement error. However, without trying too hard, we can achieve measurement errors less than 1% day to day using the $|F = 2, m_F = -2\rangle$ dark state.

2.4.5 Bright to Dark State Optical Pumping

A similar source of measurement error is bright ions being optically pumped to a dark state during the detection interval due to imperfect BD polarization. If the BD polarization has a small admixture of $\hat{\pi}$ ($\hat{\sigma}^-$) polarization, the $|S_{1/2}, F = 2, m_F = 2\rangle$ state can couple to the $|P_{3/2}, m_J = 1/2\rangle$ ($|P_{3/2}, m_J = -1/2\rangle$) state and decay to a dark state. We reduced this source of error by tilting and rotating a $\lambda/4$ wave plate while monitoring the fraction of dark experiments for a prepared bright ion. We also apply smaller shimming magnetic fields orthogonal to the primary field to overlap the magnetic field axis with the BD beam direction. In practice, however, this was unnecessary since altering the $\lambda/4$ wave plate was sufficient for reducing this source of error to below 10^{-3}. In previous experiments with $^9\mathrm{Be}^+$ at magnetic fields near 1 mT, shimming fields were required [Barrett 03]. The moderate 0.0119 T magnetic field offers an advantage in this area in that the depumping $\hat{\pi}$ ($\widehat{\sigma^-}$) transitions are off-resonant by 223 (446) MHz due to the Zeeman shift of the excited $P_{3/2}$ states. The alignment procedure described above also improves state preparation because the RD and Repumper beams are co-propagating with BD. This source of error can be eliminated in principle.

The bright to dark optical pumping error during measurement can be quantified using analysis similar to § 2.4.1. We replace ω in Eq. (2.16) with $\epsilon_\pi\omega$ where ϵ_π is the fraction of the BD laser intensity in the $\hat{\pi}$ polarization component. Because the $\hat{\pi}$ polarized depumping transition through the $|P_{3/2}, m_J = 1/2\rangle$ state is closer to resonance than the $\hat{\sigma}^-$ polarized transition, we calculate the worst case error assuming all of the impure polarization is $\hat{\pi}$. $\epsilon_\pi\omega$ is the rate of depumping out of the bright state. Ideally the measurement laser propagates parallel to the magnetic field vector. The $\hat{\pi}$ polarization component results from misalignment of the measurement beam direction with respect to the magnetic field vector. The probability of collecting n photons for an ion initially in the bright state is the convolution of the Poisson distribution with the exponential distribution (see § 2.4.1 and Ref. [Acton 05]):

$$
\begin{aligned}
p_{\mathrm{bright}}(n) = e^{-\epsilon_\pi\omega\tau_D} P(n|(1+r_{bg})\gamma_c\tau_D) + \frac{\epsilon_\pi\omega\gamma_c^n e^{\epsilon_\pi\omega\tau_D r_{bg}}}{(\gamma_c+\epsilon_\pi\omega)^{n+1}} \\
\times \left\{P_2(n+1,(\gamma_c+\epsilon_\pi\omega)(1+r_{bg})\tau_D) - P_2(n+1,(\gamma_c+\epsilon_\pi\omega)r_{bg}\tau_D)\right\}. \quad (2.33)
\end{aligned}
$$

With $\epsilon_\pi = 10^{-3}$ and using the coupling coefficient $c_{BR} = 2/9$ for the total optical pumping to both $|F = 1, m_F = 1\rangle$ and $|F = 2, m_F = 1\rangle$ states, we calculate the probability of detecting zero photons in the 200 μs detection interval to be 3.0×10^{-4}.

With a collection efficiency of $\eta = 5 \times 10^{-3}$, the optimal infidelity is 1.3×10^{-4} at $\tau_D = 192\ \mu$s collecting on average 19.2 photons in the bright state. In principle, polarization errors can be as low as 10^{-5}. In this case, the error in falsely determining the bright state as dark is dominated by the Poisson distribution at $n = 0$, and the optimal error rates for measurement are those given in § 2.4.4.

2.4.6 Measurement via Photon Arrival Times

In the measurement scheme described earlier, one collects a number of photons for a fixed detection interval, and if the number of collected photons n is greater than the cut-off photon number n_c, then we infer that the qubit was projected into a particular state, $|\uparrow\rangle$ for example. We found that for zero background, $n_c = 0$ is optimal, and there exists an optimal detection interval τ_D which minimizes the probability of falsely inferring the quantum state. Alternatively, rather than count the number of photons collected in a fixed detection interval, we may record the arrival times of the photons $\{t_k\}$ into our measurement apparatus. Certainly there is more information in the set $\{t_k\}$ than in the number of photons collected, and we explore a method of qubit state inference based on $\{t_k\}$ in this section.

The problem is to determine whether the ion was projected into the bright state $|b\rangle$ or dark state $|d\rangle$ given the arrival times of N photons $\{t_k\}$ ($k \in \{1, 2, \cdots, N\}$) during the detection interval $\tau_D > t_N$. We calculate the likelihood that the set $\{t_k\}$ was generated by the state $|b\rangle$ or the state $|d\rangle$, and we infer the qubit state based on the method of maximum likelihood. The likelihood function $L(\{t_k\}; \alpha)$ is the conditional probability of generating the data set $\{t_k\}$ given the vector α. In our case, the vector α simply describes whether the ion was projected into $|b\rangle$ or $|d\rangle$ and is one dimensional and binary. Practically speaking, we calculate the likelihood function for $|b\rangle$ and $|d\rangle$ and choose the state which has the higher likelihood. We first consider the likelihood of the first photon arriving at time t_1 for the $|b\rangle$ and $|d\rangle$ states. In the analysis that follows, we assume zero background photons and no depumping from $|b\rangle$. The case where background photons exist will be handled later.

Once the first photon arrives at time t_1, independent of whether the ion was in the $|b\rangle$ or $|d\rangle$ state, the ion is in the fluorescing state $|F = 2, m_F = 2\rangle$ for the remainder of the measurement interval $(t > t_1)$. As such, the probability of detecting photons for the remaining collection times $\{t_2, t_3, \cdots, t_N\}$ is determined by the bright state distribution. Therefore, the likelihood of the remaining photon arrival times $\{t_2, t_3, \cdots, t_N\}$ is the same for both the $|b\rangle$ and $|d\rangle$ states. As such, we only need to consider the likelihood of the first photon arrival time t_1.

The conditional probability of collecting a photon between t and $t + \mathrm{d}t$ given the bright or dark state is given by the following:

$$\begin{aligned}
P_b(t)\mathrm{d}t &= \gamma_c e^{-\gamma_c t}\mathrm{d}t \\
P_d(t)\mathrm{d}t &= \left(\int_0^t \mathrm{d}t' \gamma_c e^{-\gamma_c (t-t')} \dot{f}(t')\right)\mathrm{d}t \\
&= M(t)\gamma_c e^{-\gamma_c t}\mathrm{d}t \\
&= M(t)P_b(t)\mathrm{d}t
\end{aligned} \tag{2.34}$$

where $M(t) \equiv \int_0^t \mathrm{d}t' e^{\gamma_c t'} \dot{f}(t')$. In the calculation of $P_d(t)$ in Eq. (2.34), the dark to bright state pumping event can occur any time between 0 and t_1 with probability $\dot{f}(t)$. Once the pumping event occurs, the ion can scatter photons at the rate γ_c into the collection system for the remainder of the interval. $P_b(t)$ and $P_d(t)$ are the probability densities of detecting the first photon at time t conditioned on the ion being in state $|b\rangle$ or $|d\rangle$ respectively. The likelihood that the bright state produced a photon between t_1 and $t_1 + \mathrm{d}t$ is $P_b(t_1)\mathrm{d}t$, and the likelihood that the dark state produced a photon between t_1 and $t_1 + \mathrm{d}t$ is $P_d(t_1)\mathrm{d}t$. Using the method of maximum likelihood, we conclude that the ion was in state $|d\rangle$ if $P_d(t)/P_b(t) = M(t) > 1$. Because $M(t)$ is an increasing function, this method of inference is equivalent to inferring the qubit state is $|d\rangle$ if and only if $t > t_c$ where t_c is defined by the relation $M(t_c) = 1$.

The method of state inference based on maximum likelihood optimizes the average error in false inference assuming a uniform prior distribution. The uniform prior distribution in this case is equal probability of $|b\rangle$ or $|d\rangle$ preparations. The average error, not the worst case error, is the relevant parameter for quantum error correction. Furthermore, the assumption of a uniform prior distribution actually closely resembles many of the measurements that occur in a quantum information processor[5] . This is the case for measurements during quantum teleportation and teleporting gate protocols. For the case of state preparation and verification where the actual prior distribution is very close to a single state, using a uniform prior distribution when calculating the average error is pessimistic. For this case, one may develop an inference method which takes the prior distribution into account in order to minimize the expected error when integrating the prior distribution of states over the posterior distribution of errors. Here we do not concern ourselves with prior distributions other than the uniform distribution.

As an example, we consider the system where only one scattering event is required to optically pump $|d\rangle$ into $|b\rangle$. In this case, $f(t) = 1 - e^{-\omega t}$ as in Eq. (2.15), which gives $M(t) = \frac{\omega}{\gamma_c - \omega}\left[e^{(\gamma_c - \omega)t} - 1\right]$. In the general case where $|d\rangle$ is some other dark hyperfine state, then $f(t) = 1 - \sum_k a_k e^{-\omega_k t}$ as in Eq. (2.27), and $M(t)$ has the form:

$$M(t) = \sum_k \frac{a_k \omega_k}{\gamma_c - \omega_k}\left[e^{(\gamma_c - \omega_k)t} - 1\right] \tag{2.35}$$

Solving for t_c using Eq. (2.35) is difficult analytically.

The measurement error for a particular t_1 is the probability of false inference for this point. In our inference method, we choose between two values (i.e. $|d\rangle$ or $|b\rangle$) based on whether $P_d(t_1) > P_b(t_1)$ or not[6] . Normalizing by the total probability that either $|b\rangle$ or $|d\rangle$ produced at photon at t_1, the probability that $|d\rangle$ is more likely is $P_d(t_1)/(P_b(t_1) + P_d(t_1))$. Our inference method then is to infer $|d\rangle$ if $P_d(t_1)/(P_b(t_1) + P_d(t_1)) > 0.5$. Using this definition, we can calculate the conditional probability of false

---

[5] E. Knill, private communication.

[6] This is equivalent to the condition $M(t_1) > 1$ which is equivalent to the condition $t_1 > t_c$.

inference given we were actually in state $|d\rangle$ or $|b\rangle$:

$$\begin{aligned} P(\text{falsely infer } b \text{ at } t|d) &= \begin{cases} \frac{P_d(t)}{P_b(t)+P_d(t)} & t \le t_c \\ 0 & t > t_c \end{cases} \\ P(\text{falsely infer } d \text{ at } t|b) &= \begin{cases} 0 & t < t_c \\ \frac{P_b(t)}{P_b(t)+P_d(t)} & t \ge t_c \end{cases} . \end{aligned} \tag{2.36}$$

The worst case error of 50% occurs if we collect the first photon at $t_1 = t_c$. At this point, we cannot identify which state produced t_1 as both states are equally likely. Given t_1, not only do we infer which state produced it based on the query $t_1 > t_c$, we know the error in false inference directly from Eq. (2.36). Therefore, we can reject certain measurements when the individual error becomes too large. The posterior distribution of errors [Eq. (2.36)] may be useful to certain error correcting protocols.

The expected error in falsely inferring $|b\rangle$ given $|d\rangle$ is:

$$\begin{aligned} \epsilon_b &= \int_0^{t_c} P_d(t)\mathrm{d}t \\ &= f(t_c) - e^{-\gamma_c t_c} \end{aligned} \tag{2.37}$$

where we have used Eq. (2.34) and the fact that $M(t_c) = 1$ and $f(0) = 0$. Similarly, the expected error in falsely inferring $|d\rangle$ given $|b\rangle$ is $\epsilon_d = 1 - \int_0^{t_c} P_b(t)\mathrm{d}t = e^{-\gamma_c t_c}$. Therefore, the average expected measurement error is the average of ϵ_d and ϵ_b, namely $\epsilon_{\text{ave}} = \frac{1}{2} f(t_c)$.

It is worth checking that the average error is optimal. We can calculate the probability of false inference for the bright and dark states as a function of a different cut-off time t'_c. In doing so, we obtain $\epsilon_{\text{ave}}(t'_c) = \frac{1}{2}\left[f(t'_c) + e^{-\gamma_c t'_c}(1 - M(t'_c))\right]$. Differentiating $\epsilon_{\text{ave}}(t'_c)$ with respect to t'_c and setting to zero yields $M(t'_c) = 1$, implying $t'_c = t_c$. Therefore, the maximum likelihood inference method gives the optimal average error.

For the case where $f(t) = 1 - e^{-\omega t}$, the maximum likelihood estimate for t_c is $t_c = \frac{1}{\gamma_c - \omega} \log\left(\frac{\gamma_c}{\omega}\right)$, and the average error is $\epsilon_{\text{ave}} = \frac{1}{2}\left[1 - \left(\frac{\omega}{\gamma_c}\right)^{\frac{\omega}{\gamma_c - \omega}}\right]$. With $|d\rangle = |F =$

$1, m_F = 1\rangle$, $s_0 = 0.5$, and $\eta = 2.5 \times 10^{-3}$, then $\omega = 2.6 \times 10^{-4}$, $\gamma_c = 5.0 \times 10^{-2}$, and we find $t_c = 106$ μs yielding an average error of $\epsilon_{\text{ave}} = 1.4 \times 10^{-2}$. For the far-away dark state $|d\rangle = |F = 2, m_F = -2\rangle$ and the same parameters, the cut-off time is $t_c = 196$ μs with an optimal average error of $\epsilon_{\text{ave}} = 8.6 \times 10^{-5}$. With a collection efficiency of 5×10^{-3} as in Fig. 2.6, $\epsilon_{\text{ave}} = 1.0 \times 10^{-5}$. These average errors are the same as those calculated in § 2.4.4, and the cut-off time t_c is the same as the optimal τ_D. This is expected because the inference methods are essentially the same. In the absence of background, the optimal cut-off photon number n_c is zero; therefore, inferring the state based on whether t_1 is greater or lesser than t_c is the same as detecting zero or more photons in τ_D. Knowing the time the first photon arrived t_1 does provide us with the posterior distribution of errors which may be useful to error correcting protocols. For example, in the three qubit redundancy code, three ancilla qubits entangled with the logical qubit are measured and are expected to yield the same result. The error correcting protocol takes a majority vote for these three ancilla measurements. However, if we know the time of the first photon arrivals, we can weight the measurements by the posterior probability of false inference and obtain more confidence in the ancilla measurements.

2.4.6.1 Background Photons

We saw in the previous section that in the absence of background, comparing the time of arrival of the first photon t_1 to a cut-off time t_c is equivalent to the optimal measurement scheme for counting photons in a fixed detection interval τ_D. We will show in this section that in the presence of background, using the full set of photon arrival times $\{t_k\}$ we can achieve lower average measurement errors than in the case of counting photons in a fixed detection interval. As an example of this point, if we detect photons for an interval longer than τ_D, the error in dark to bright repumping dominates and the average error increases. However, we loose nothing by detecting longer using the method of photon arrival times. These extra photons may hold no more useful information, but they can also easily be ignored.

We begin by calculating the likelihood that the bright or dark state produced the set $\{t_k\}$ in the interval $[0, \tau_D)$. We define the background photon collection rate as $\gamma_{bg} \equiv r_{bg}\gamma_c$, and the conditional probability that the background will produce a photon between t and $t + \mathrm{d}t$ after a time t of no photons is $P_{bg}(t)\mathrm{d}t = \gamma_{bg} e^{-\gamma_{bg} t}\mathrm{d}t$. In general, the conditional probability that a single event X will occur given that either distribution a or distribution b generated the event X is $P(X|a \text{ or } b) = P(X|a)P(\bar{X}|b) + P(\bar{X}|a)P(X|b)$ where $P(\bar{X}|c)$ is the conditional probability that event X will *not* occur given distribution c. This rule can be understood by realizing that we are examining the probability of a *single* event X. It can only be generated by a or b exclusively. Therefore, we must sum the probabilities that distribution a generated X AND distribution b did not OR distribution b generated X AND distribution a did not. Following this rule, the conditional probability that a photon will arrive at time t given the ion is in the bright state and there exists background at rate γ_{bg} is $P_{b+bg}(t)\mathrm{d}t = (\gamma_c + \gamma_{bg})e^{-(\gamma_c+\gamma_{bg})t}\mathrm{d}t$ which is expected. The probability distribution in time for two independent scattering mechanisms each with exponential distributions is an exponential distribution with rate equal to the sum of the individual rates. In more detail, the probability that a photon will not arrive by time t for an exponential distribution with rate γ is $1 - \int_0^t \gamma e^{-\gamma t'}\mathrm{d}t' = e^{-\gamma t}$. The probability that a photon will arrive at time t for an exponential distribution with rate γ is $\gamma e^{-\gamma t}\mathrm{d}t$. Using the rule above, we obtain our expression for $P_{b+bg}(t)\mathrm{d}t$. Generalizing to N photon arrival times, the likelihood function assuming the qubit is in the bright state is

$$\begin{aligned} L_b(\{t_k\}, \tau_D)\mathrm{d}t^N &= (\gamma_c + \gamma_{bg})^N e^{-(\gamma_c+\gamma_{bg})\sum_{k=1}^{N}\Delta t_k}\mathrm{d}t^N e^{-(\gamma_c+\gamma_{bg})(\tau_D - t_N)} \\ &= (\gamma_c + \gamma_{bg})^N e^{-(\gamma_c+\gamma_{bg})\tau_D}\mathrm{d}t^N \end{aligned} \tag{2.38}$$

where $\Delta t_k \equiv t_k - t_{k-1}$, $t_0 \equiv 0$, and N is the number of photons collected. The $e^{-(\gamma_c+\gamma_{bg})(\tau_D - t_N)}$ term is the probability that neither the bright state nor the background produced a photon in the interval from t_N to τ_D. The likelihood function for the dark state is

$$\begin{aligned}
L_d(\{t_k\},\tau_D)\mathrm{d}t^N = {} & P_d(t_1)\mathrm{d}t\left(1-\int_0^{\Delta t_1} P_{bg}(t')\mathrm{d}t'\right) \\
& \times(\gamma_c+\gamma_{bg})^{N-1}e^{-(\gamma_c+\gamma_{bg})(\tau_D-t_1)}e^{-\gamma_{bg}\Delta t_1}\mathrm{d}t^{N-1} \\
& +\left(1-\int_{t_0}^{t_1} P_d(t')\mathrm{d}t'\right)P_{bg}(\Delta t_1)\mathrm{d}t\biggl[P_d(t_2)\mathrm{d}t\left(1-\int_0^{\Delta t_2} P_{bg}(t')\mathrm{d}t'\right) \\
& \times(\gamma_c+\gamma_{bg})^{N-2}e^{-(\gamma_c+\gamma_{bg})(\tau_D-t_2)}e^{-\gamma_{bg}\Delta t_2}\mathrm{d}t^{N-2} \\
& +\left(1-\int_{t_1}^{t_2} P_d(t')\mathrm{d}t'\right)P_{bg}(\Delta t_2)\mathrm{d}t\biggl[P_d(t_3)\mathrm{d}t\left(1-\int_0^{\Delta t_3} P_{bg}(t')\mathrm{d}t'\right) \\
& \times(\gamma_c+\gamma_{bg})^{N-3}e^{-(\gamma_c+\gamma_{bg})(\tau_D-t_3)}e^{-\gamma_{bg}\Delta t_3}\mathrm{d}t^{N-3} \\
& +\cdots \\
& +\left(1-\int_{t_{N-2}}^{t_{N-1}} P_d(t')\mathrm{d}t'\right)P_{bg}(\Delta t_{N-1})\mathrm{d}t \\
& \times\biggl[P_d(t_N)\mathrm{d}t\left(1-\int_0^{\tau_D-t_{N-1}} P_{bg}(t')\mathrm{d}t'\right)e^{-\gamma_c(\tau_D-t_N)} \\
& +\left(1-\int_{t_{N-1}}^{\tau_D} P_d(t')\mathrm{d}t'\right)P_{bg}(\tau_D-t_{N-1})\mathrm{d}t\biggr]\cdots\biggr]\biggr].
\end{aligned} \tag{2.39}$$

Our inference method is to infer $|d\rangle$ if the likelihood ratio $L_r \equiv L_d/L_b$ is greater than 1, otherwise infer $|b\rangle$. After some simplification, this ratio is:

$$\begin{aligned}
L_r = {} & (1-\gamma_r)M_1 \\
& +\gamma_r f_1(1-\gamma_r)M_2 \\
& +\gamma_r^2 f_1 f_2(1-\gamma_r)M_3 \\
& +\cdots+\gamma_r^{N-1}f_1f_2\cdots f_{N-1}(1-\gamma_r)M_N \\
& +\gamma_r^N f_1 f_2\cdots f_N f_{N+1} \\
= {} & (1-\gamma_r)M_1+(1-\gamma_r)\sum_{k=2}^{N}\gamma_r^{k-1}M_k\prod_{l=1}^{k-1}f_l+\gamma_r^N\prod_{l=1}^{N+1}f_l
\end{aligned} \tag{2.40}$$

where

$$M_k \equiv M(t_k)e^{-\gamma_c t_{k-1}}e^{-\gamma_{bg}\Delta t_k} \text{ for } k < N, \tag{2.41}$$

$$M_N \equiv M(t_N)e^{-\gamma_c t_{N-1}}, \tag{2.42}$$

$$\begin{aligned} f_k \equiv\ & e^{\gamma_c \Delta t_k}[1 - f(t_k) + f(t_{k-1})] \\ & + e^{-\gamma_c t_{k-1}}[M(t_k) - e^{\gamma_c \Delta t_k}M(t_{k-1})] \text{ for } k \leq N, \end{aligned} \tag{2.43}$$

$$\begin{aligned} f_{N+1} \equiv\ & e^{\gamma_c(\tau_D - t_N)}[1 - f(\tau_D) + f(t_N)] \\ & + e^{-\gamma_c t_N}[M(\tau_D) - e^{\gamma_c(\tau_D - t_N)}M(t_N)], \text{ and} \end{aligned} \tag{2.44}$$

$$\gamma_r \equiv \frac{\gamma_{bg}}{\gamma_c + \gamma_{bg}}. \tag{2.45}$$

Notice that in the limit of no background $\gamma_r \to 0$, Eq. (2.40) reduces to $M(t_1)$ which is expected. The likelihood ratio L_r for the empty set of zero photons in the measurement interval τ_D is $L_r(\{\}, \tau_D) = f_1 = M(\tau_D) + e^{\gamma_c \tau_D}(1 - f(\tau_D))$. We note that $L_r(\{\}, \tau_D)$ is greater than 1 for systems where the repump rates are less than γ_c. Said another way, in the absence of photons, the maximum likelihood estimator for the state is the dark state with confidence exponentially approaching 1. Once a photon arrives, however, the state estimate may change depending on when the photon arrives.

We can calculate the measurement error for our inference method in a fashion similar to the previous section. We first calculate the probability of false inference given we perfectly prepared states $|b\rangle$ and $|d\rangle$ and take the average. The probability of falsely inferring $|b\rangle$ and $|d\rangle$ respectively is:

$$\begin{aligned} \epsilon_b &= \int_{L_r<1} L_d(\{t_k\}, \tau_D)\mathrm{d}t^N \\ \epsilon_d &= \int_{L_r\geq 1} L_b(\{t_k\}, \tau_D)\mathrm{d}t^N. \end{aligned} \tag{2.46}$$

Eq. (2.46) is difficult to calculate analytically due to the complex N-dimensional boundary defined by $L_r(\{t_k\}, \tau_D) = 1$. To determine the errors in Eq. (2.46), we simulated 10^7 data sets of photon arrival times $\{t_k\}$ of length at least $N = 35$ taken

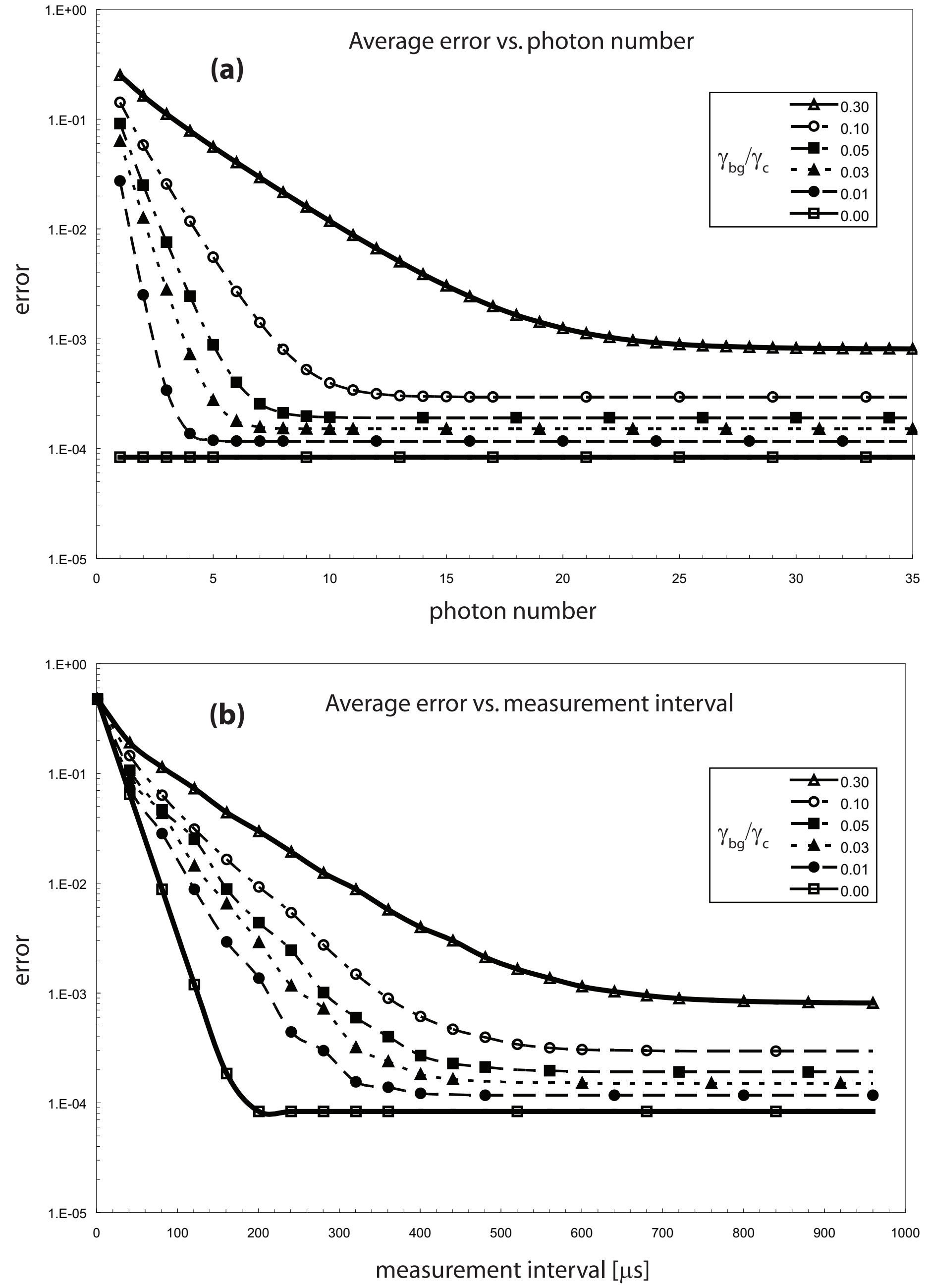

Figure 2.7: Simulated measurement error using photon arrival times. **(a)** Average measurement error as a function of the number of photons used for state inference. **(b)** Average measurement error as a function of the detection interval. The simulation used 10^7 data sets $\{t_k\}$ of length at least $N = 35$ photon arrival times of at least 1 ms total duration taken from the bright and dark distributions for each background level. The bright state scattering rate used was $\gamma_c = 5 \times 10^{-2}\ \mu\text{s}^{-1}$. The ratio of the background scattering rate to the bright state scattering rate γ_{bg}/γ_c is shown in the legend. The theoretical minimum error of 8.58×10^{-5} agrees with the zero background simulation within the statistical uncertainty. The dark state was $|d\rangle = |F = 2, m_F = -2\rangle$.

	(1) photon arrival method				(2) photon counting method				
γ_{bg}/γ_c	ϵ_{ave}	$n_{10\%}$	$t_{10\%}$ [μs]	t_{cnt} [μs]	ϵ_{ave}	n_c	τ_D [μs]	λ_0	λ_{bg}
0	8.58×10^{-5}	1	191	196	8.58×10^{-5}	0	196	9.80	0
0.01	$1.17(3) \times 10^{-4}$	5	383	278	2.82×10^{-4}	3	303	15.1	0.15
0.03	$1.51(4) \times 10^{-4}$	7	442	309	4.18×10^{-4}	4	323	16.2	0.48
0.05	$1.91(4) \times 10^{-4}$	9	483	336	5.19×10^{-4}	6	376	18.8	0.94
0.10	$2.95(5) \times 10^{-4}$	12	559	381	7.79×10^{-4}	9	434	21.7	2.2
0.30	$8.08(9) \times 10^{-4}$	25	719	456	2.45×10^{-3}	16	470	23.5	7.1

Table 2.2: Optimal measurement errors for the two methods: (1) maximum likelihood using the set of photon arrival times $\{t_k\}$ and (2) total photon counts in a fixed measurement period τ_D. The bright state scattering rate is 5×10^4 s^{-1}. The n_c cut-off photon number in method (2) is the number of photons required in the interval τ_D for the bright state to be inferred. In method (1), $n_{10\%}$ is the number of photons we should collect to achieve a measurement error within 10% of the optimal measurement error. Similarly, $t_{10\%}$ is the minimum measurement interval required to obtain measurement error within 10% of the optimal measurement error. For comparison, t_{cnt} is the measurement interval in method (1) where the measurement error equals the optimal measurement error in method (2). λ_0 is the mean of the bright distribution when collecting photons for τ_D in the absence of background. λ_{bg} is the mean of the background distribution.

from the bright and dark distributions with different background levels for a detection interval of at least $\tau_D = 1$ ms. For data sets where less than N photons arrived before τ_D, we extended the set to size N. We calculated the likelihood ratio L_r and the probability of falsely inferring dark given bright and vice versa using the first n of N photon arrival times $\{t_k\}$. In this fixed n method, we let the measurement interval τ_D equal the arrival time of the last photon t_n. We also inferred the state based on the likelihood ratio for variable sized sets $\{t_k\}$ with τ_D fixed and examined the average error as a function of τ_D. The results are shown in Fig. 2.7. The simulation used $\gamma_c = 5 \times 10^4$ s^{-1} and the shelved dark state $|d\rangle = |F = 2, m_F = -2\rangle$ with $s_0 = 0.5$. The fractional background scattering rates r_{bg} were between 0 and 0.3. We observe that the average measurement error drops exponentially with increasing photon number n until the error reaches a threshold above that of zero background. Similarly, the average error drops exponentially as a function of τ_D until it saturates at the same lower bound. The threshold for saturation is background dependent. In addition, the error for the zero background simulation agrees with the theoretical estimate within the statistical uncertainty after the first photon, and additional photons do not lower the error. This agrees with our theoretical hypothesis that in the absence of background, only the arrival time of the first photon carries useful information for state inference. More generally, there appears to be a background dependent critical photon number for which additional photons add negligible additional information useful for state inference. We quantify the critical photon number $n_{10\%}$ as the number of photons required to achieve a probability of measurement error within 10% of the optimal measurement error. For zero background, this critical photon number is 1; for 1% background, this critical photon number is 5. Practically, we expect that by collecting the arrival times of the first five photons, we can achieve average measurement errors in the presence of 1% background (typical in our experiments) very close to the zero background case. A similar critical measurement interval $t_{10\%}$ exists such that detecting photons for an interval longer than

$t_{10\%}$ yields a probability of measurement error within 10% of the optimal. Detecting longer adds negligible (only 10%) additional information useful for state inference. For the 1% background case, $t_{10\%} = 383\ \mu$s.

We compare the simulated average measurement errors in Fig. 2.7 to the calculated optimal average measurement errors using the cut-off photon number n_c method in the presence of background. The results are tabulated in Table 2.2. We observe that we can achieve approximately a factor of 3 improvement in the average error using the photon arrival times vs. counting the number of photons arriving in a fixed detection interval τ_D. The parameters $t_{10\%}$ and $n_{10\%}$ are the minimal measurement time and photon number respectively required to achieve a measurement error probability within 10% of the optimal measurement error probability. For comparison, we also tabulate t_{cnt}, the measurement interval in the photon counting method where the probability of measurement error equals that of the optimal measurement error in the photon counting method. We observe that for the same probability of measurement error, the photon counting method using maximum likelihood can be performed in approximately 10% less time.

2.5 Quantum Gates

As discussed in the introduction, a sufficient gate set for universal quantum computation consists of arbitrary single qubit rotations and a single entangling quantum gate [Barenco 95]. All gates in this thesis involve the interaction of one or more ions with laser beams. We acknowledge that there exist alternate methods for performing gates [Mintert 01, Schrader 04] including spin rotations using resonant magnetic fields. However, laser-ion interactions have the advantage that closely spaced ion qubits can be individually addressed with laser beams [Wineland 98, Riebe 04], and strong magnetic field gradients required for some two-qubit entangling gates are easily generated [Cirac 95, Wineland 98].

2.5.1 Single-Qubit Quantum Gates

The single qubit gates are implemented using stimulated Raman transition with co-propagating laser beams (see § 2.5.2 below). Co-propagating laser beams have the advantage that the phase as a function of space of the effective field driving the qubit transition is given by $\vec{\Delta k} \cdot \vec{x}$ where $|\vec{\Delta k}| \sim \frac{2\pi}{30cm}$ is the difference in the two k-vectors of the two co-propagating laser beams and $\vec{x}$ is the ion position (there is no need to quantize the ion position in this treatment since the coupling to the motional states is negligible). Therefore, interferometric stability of the laser fields is not required for single-qubit rotations. However, for high-fidelity single-qubit rotations where the phase error should be kept below 10^{-4}, the total optical path from the location where the two Raman beams are generated to the ion should not fluctuate by more than 5 μm. To reach this level of phase stability, the modulator frequency may need to be phase-locked to the optical heterodyne beat frequency measured close to the trap. We did not implement such a feedback loop in the experiments of this thesis. In addition, electronic state changing transitions with co-propagating Raman laser beams can occur independent of the motional state (the Lamb-Dicke parameter is $\eta \sim 10^{-7}$ for ^{9}Be$^+$). In the section that follows, I show how the phase of the single qubit rotation can be controlled by the differential phase between the two Raman lasers generated by stable microwave sources. Given rotations about any axis in the $x - y$ plane of the Bloch sphere, we can generate arbitrary rotations about any axis on the Bloch sphere.

2.5.2 Stimulated Raman Transitions

The basic building blocks of our gates are two-photon stimulated Raman transitions. Two states which do not couple directly through an applied radiation field can obtain an effective coupling mediated via the radiation field coupling these states to an auxiliary level. A diagram of such a situation is shown in Fig. 2.8. The qubit

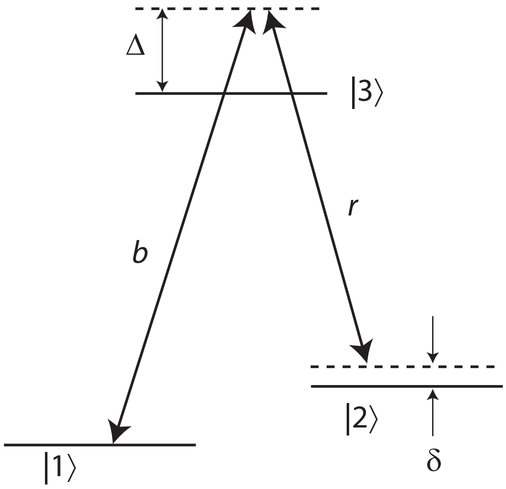

Figure 2.8: Energy level diagram for two-photon stimulated Raman transitions. The symbols b and r represent the "blue" and "red" lasers respectively. The electric field of laser beam i has the form $\vec{E}_i = \hat{\epsilon}_i E_i \cos(\vec{k}_i \cdot \vec{x} - \omega_i t + \phi_i)$ where $i \in \{b, r\}$. The detuning of the blue laser from the $|1\rangle \leftrightarrow |3\rangle$ transition frequency is Δ, and the detuning of the difference frequency $\omega_b - \omega_r$ from the $|1\rangle \leftrightarrow |2\rangle$ transition frequency is δ.

states are levels $|1\rangle$ and $|2\rangle$, and the auxiliary state is level $|3\rangle$. These states have energies $\hbar\omega_1$, $\hbar\omega_2$, and $\hbar\omega_3$ respectively corresponding to a base Hamiltonian $H_0 = \hbar\omega_1|1\rangle\langle 1| + \hbar\omega_2|2\rangle\langle 2| + \hbar\omega_3|3\rangle\langle 3|$. For ions commonly used in QIP, level $|3\rangle$ is typically one of the lowest P states, and the $|1\rangle$ and $|2\rangle$ levels are hyperfine ground states. We apply two lasers labeled by the indices b and r for "blue" and "red" respectively each having an oscillating electric field of the form $\vec{E}_i = \hat{\epsilon}_i E_i \cos(\vec{k}_i\cdot\vec{x} - \omega_i t + \phi_i)$ for $i \in \{b, r\}$. Here, E_i is the amplitude of the electric field, $\hat{\epsilon}_i$ is its polarization, $\vec{k}_i$ is the wave vector, $\vec{x}$ is the position of the ion, ω_i is the frequency of the laser, and ϕ_i is the phase of the laser. The interaction Hamiltonian for this system is given by the electric-dipole interaction $H_I = -\vec{\mu}\cdot(\vec{E}_b + \vec{E}_r)$ where $\vec{\mu}$ is the electric-dipole operator. Writing an arbitrary state as $|\Psi\rangle = \sum_{k=1}^{3} c_k e^{-i\omega_k t}|k\rangle$ and applying Schrödinger's equation, we obtain a system of differential equations for the coefficients c_k:

$$\begin{aligned} i\dot{c}_1 &= g_b^* e^{i\Delta t} c_3 \\ i\dot{c}_2 &= g_r^* e^{i(\Delta-\delta)t} c_3 \\ i\dot{c}_3 &= g_b e^{-i\Delta t} c_1 + g_r e^{-i(\Delta-\delta)t} c_2 \end{aligned} \tag{2.47}$$

where $g_b \equiv -\frac{E_b e^{i(\vec{k}_b\cdot\vec{x}+\phi_b)}}{2\hbar}\langle 3|\vec{\mu}\cdot\hat{\epsilon}_b|1\rangle$ and $g_r \equiv -\frac{E_r e^{i(\vec{k}_r\cdot\vec{x}+\phi_r)}}{2\hbar}\langle 3|\vec{\mu}\cdot\hat{\epsilon}_r|2\rangle$ are the on-resonance Rabi frequencies between states $|1\rangle \leftrightarrow |3\rangle$ and $|2\rangle \leftrightarrow |3\rangle$, and we have ignored terms oscillating near $2\omega_{b,r}$ by the rotating wave approximation. There is no direct coupling between c_1 and c_2 in Eq. (2.47); however, as we will see below, the coupling of each of these coefficients to c_3 mediates an effective coupling between c_1 and c_2.

c_3 can be removed from Eq. (2.47) by adiabatic elimination. We separate the fast phase evolution in c_3 from the slower envelop by letting $c_3' = e^{i\Delta t}c_3$. Upon taking its derivative and substituting into the last equation in Eq. (2.47), we find

$$\Delta c_3' + i\dot{c}_3' = g_b c_1 + g_r e^{i\delta t} c_2. \tag{2.48}$$

We now make the assumption that the majority of c_3's time dependence comes from the fast phase evolution induced by the large detuning Δ, namely that $|\Delta c_3'| \gg |\dot{c}_3'|$. This is valid as long as the two-photon Rabi frequency, which we are in the process of deriving, is small compared to Δ, which can be verified at the end of the calculation. Using this assumption to ignore the $i\dot{c}'_3$ term in favor of $\Delta c'_3$ in Eq. (2.48) and substituting it into Eq. (2.47) yields

$$
\begin{aligned}
i\dot{c}_1 &= \delta_{s1} c_1 + \Omega^* e^{i\delta t} c_2 \\
i\dot{c}_2 &= \Omega e^{-i\delta t} c_1 + \delta_{s2} c_2
\end{aligned}
\tag{2.49}
$$

where $\delta_{s1} \equiv |g_b|^2/\Delta$ and $\delta_{s2} \equiv |g_r|^2/\Delta$ are the AC Stark shifts of levels $|1\rangle$ and $|2\rangle$ respectively and $\Omega \equiv g_b g_r^*/\Delta$ is the two-photon Rabi frequency between states $|1\rangle$ and $|2\rangle$. We note that the two-photon Rabi frequency is proportional to $\exp[i(\vec{k}_b - \vec{k}_r) \cdot \vec{x} + (\phi_b - \phi_r)]$; therefore, we can control the phase of rotations by controlling the differential optical phase between the two laser beams. The Stark shifts can be removed from the problem by a redefinition of the $|1\rangle \leftrightarrow |2\rangle$ transition frequency, or alternatively absorbing the differential Stark shift into the definition of the Raman beam difference frequency detuning δ. We move to a frame rotating with the Stark shifts by letting $c_k \equiv c'_k e^{i\delta_{sk}}$ for $k \in \{1, 2\}$. Eq. (2.49) is transformed then to the following:

$$
\begin{aligned}
i\dot{c}'_1 &= \Omega^* e^{i\delta' t} c'_2 \\
i\dot{c}'_2 &= \Omega e^{-i\delta' t} c'_1
\end{aligned}
\tag{2.50}
$$

where $\delta' \equiv \delta + \delta_{s1} - \delta_{s2}$.

Eq. (2.50) are the equations for the standard 2-level problem. Its solution and many other aspects are discussed at length in a variety of works, not the least of which include [Allen 87, Sakurai 94, Metcalf 99]. The time dependence can be removed from Eq. (2.50) by moving to another rotating frame with the transformation $c'_1 \equiv c''_1 e^{i\delta' t/2}$ and $c'_2 \equiv c''_2 e^{-i\delta' t/2}$. The new coefficients obey the equation

$$
i\dot{\mathbf{c}} = \mathbf{M} \cdot \mathbf{c} \tag{2.51}
$$

where

$$\mathbf{M} \equiv \begin{pmatrix} -\delta'/2 & \Omega \\ \Omega^* & \delta'/2 \end{pmatrix} \text{ and } \mathbf{c} \equiv \begin{pmatrix} c_2'' \\ c_1'' \end{pmatrix}.$$

Taking the Laplace transform of Eq. (2.51) and solving for the Laplace transformed vector $\mathbf{C}(s)$ yields:

$$\begin{aligned} \mathbf{C}(s) &= (i\mathbf{M} + s\mathbf{1})^{-1} \cdot \mathbf{c}(0) \\ &= \frac{1}{s^2 + \Omega'^2} \begin{pmatrix} s + i\frac{\delta}{2} & -i\Omega \\ -i\Omega^* & s - i\frac{\delta}{2} \end{pmatrix} \cdot \mathbf{c}(0) \end{aligned} \tag{2.52}$$

where $\mathbf{C}(s)$ is the Laplace transform of the time-domain vector $\mathbf{c}(t)$, $\mathbf{c}(0)$ is the initial condition, $\mathbf{1}$ is the identity matrix, s is the Laplace transform variable, and $\Omega' \equiv \sqrt{|\Omega|^2 + \delta^2/4}$. The time-domain solution is obtained by taking the inverse Laplace transform of Eq. (2.52):

$$\begin{pmatrix} c_2''(t) \\ c_1''(t) \end{pmatrix} = \begin{pmatrix} \cos(\Omega' t) + i\frac{\delta}{2\Omega'}\sin(\Omega' t) & -i\frac{\Omega}{\Omega'}\sin(\Omega' t) \\ -i\frac{\Omega^*}{\Omega'}\sin(\Omega' t) & \cos(\Omega' t) - i\frac{\delta}{2\Omega'}\sin(\Omega' t) \end{pmatrix} \cdot \begin{pmatrix} c_2''(0) \\ c_1''(0) \end{pmatrix}. \tag{2.53}$$

The time-domain solution Eq. (2.53) is the general solution to the two-level problem. On resonance, the population of the two levels flops back and forth at a rate given by the on-resonance Rabi frequency $|\Omega|$, and the axis about which the Bloch vector rotates is given by $\arg(\Omega)$.

2.5.3 Coupling Electronic States to Motional States

In the previous section we showed how we can obtain an effective coupling between two ground internal states of an ion (qubit states) by using two laser beams detuned from an excited state with a difference frequency near resonance with the qubit transition frequency. The evolution of the state amplitudes [Eq. (2.50)] can be equivalently described by a single two-level quantum system driven with a near resonant field. We make the identification $|1\rangle \rightarrow |\downarrow\rangle$ and $|2\rangle \rightarrow |\uparrow\rangle$ with the qubit transition frequency defined as ω_0. The base Hamiltonian is $H_0 = H_{\text{int}}$ where $H_{\text{int}} = \hbar\frac{\omega_0}{2}\sigma_z$ and σ_z is the Pauli-z operator. The interaction Hamiltonian in the interaction picture with respect to H_{int} can be written as $H_I = \Omega_0 e^{i\vec{\Delta k}\cdot\vec{x}} e^{-i\delta t}\sigma_+ + h.c.$ [see Eq. (2.50)] where we have explicitly showed the $e^{i\vec{\Delta k}\cdot\vec{x}}$ factor imbedded in the Rabi frequency definition in the previous section. Here, $\Omega_0 \equiv \frac{E_b E_r}{4\hbar^2\Delta}\langle\uparrow|\vec{\mu}\cdot\hat{\epsilon}_r|3\rangle\langle 3|\vec{\mu}\cdot\hat{\epsilon}_b|\downarrow\rangle e^{i\Delta\phi}$, $\vec{\Delta k} \equiv \vec{k}_b - \vec{k}_r$, $\Delta\phi \equiv \phi_b - \phi_r$, and $\sigma_\pm = \frac{1}{2}(\sigma_x \pm i\sigma_y)$ are raising ($|\uparrow\rangle\langle\downarrow|$) and lowering ($|\downarrow\rangle\langle\uparrow|$) operators for the effective 2-level system ($\sigma_{x,y}$ are Pauli matrices). Writing a general state in the interaction picture as $|\Psi\rangle = c_\uparrow|\uparrow\rangle + c_\downarrow|\downarrow\rangle$ and applying Schrödinger's equation $i\hbar\frac{\partial}{\partial t}|\Psi\rangle = H_I|\Psi\rangle$, one can readily verify the evolution of the amplitudes is exactly that of Eq. (2.50).

The ion's quantized motion can be taken into account by including the harmonic oscillator Hamiltonian $H_{\text{osc}} = \hbar\omega_z a^\dagger a$ (neglecting the zero-point energy $\frac{1}{2}\hbar\omega_z$) in the base Hamiltonian $H_0 = H_{\text{int}} + H_{\text{osc}}$ where ω_z is the oscillation frequency. The interaction Hamiltonian is modified by replacing the x vector with its operator equivalent: $\vec{\Delta k}\cdot\vec{x} \rightarrow \eta(a^\dagger + a)$ where $\eta \equiv \Delta k_z z_0$ is the Lamb-Dicke parameter. The phase due to the mean position of the ion $\vec{\Delta k}\cdot\vec{x}$ ($\vec{x}$ a real vector) can be included in the definition of $\Delta\phi$ contained in Ω_0. Here, $z_0 \equiv \sqrt{\hbar/2m\omega_z}$ is the spread of the motional ground-state wave function, Δk_z is the projection of $\vec{\Delta k}$ onto the mode direction z, and m is the ion mass. Writing the general state of the ion including its motion as

$$|\Psi\rangle = \sum_{s\in\{\downarrow,\uparrow\}} \sum_{n=0}^{\infty} c_{s,n}(t)|s\rangle|n\rangle, \tag{2.54}$$

the interaction Hamiltonian in the interaction picture can be obtained by the transformation $H_I' = e^{iH_{\text{osc}}t/\hbar} H_I e^{-iH_{\text{osc}}t/\hbar}$:

$$H_I' = \hbar\Omega_0\sigma_+ \exp(i[\eta(a^\dagger e^{i\omega_z t} + a e^{-i\omega_z t}) - \delta t]) + h.c.. \tag{2.55}$$

Schrödinger's equation $i\hbar\frac{\partial}{\partial t}|\Psi\rangle = H_I'|\Psi\rangle$ then gives the evolution of the state $|\Psi\rangle$.

We are primarily concerned with near resonant transitions where the detuning is near an integer multiple of the motional mode frequency, namely $\delta = (n' - n)\omega_z + \Delta$

where n' and n are integers and $\Delta \ll \omega_z, \Omega_0$. When this is the case, the two states $|\uparrow, n'\rangle$ and $|\downarrow, n\rangle$ form a two-level system and evolve according to:

$$\begin{aligned}
\dot{c}_{\uparrow,n'} &= -i^{1+|n'-n|}e^{-i\Delta t}\Omega_{n',n}c_{\downarrow,n} \\
\dot{c}_{\downarrow,n} &= -i^{1-|n'-n|}e^{i\Delta t}\Omega_{n',n}c_{\uparrow,n'}
\end{aligned} \tag{2.56}$$

where $\Omega_{n',n}$ is given by [Wineland 98, Cahill 69, Wineland 79]

$$\begin{aligned}
\Omega_{n',n} &\equiv \Omega_0|\langle n'|e^{i\eta(a^\dagger+a)}|n\rangle| \\
&= \Omega_0 e^{-\eta^2/2}\left(\frac{n_<!}{n_>!}\right)^{1/2}\eta^{|n'-n|}L_{n_<}^{|n'-n|}(\eta^2)
\end{aligned} \tag{2.57}$$

and $n_<$ ($n_>$) is the lesser (greater) of n' and n; L_n^α is the generalized Laguerre polynomial

$$L_n^\alpha(x) = \sum_{m=0}^{n}(-1)^m\binom{n+\alpha}{n-m}\frac{x^m}{m!}. \tag{2.58}$$

For tightly confining traps and relatively cold ions, the ion's amplitude of motion is small compared to the wavelength of radiation, and the Lamb-Dicke criteria $\langle\Psi_{\text{motion}}|\Delta k_z^2 z^2|\Psi_{\text{motion}}\rangle^{1/2} \ll 1$ is satisfied. The Lamb-Dicke criteria should not be confused with the less restrictive condition $\eta \ll 1$ [Wineland 98] as ion motion with large amplitude can sample different portions of the wavefront even though η may be small. For Fock states with motional occupation number n, the Lamb-Dicke criteria is satisfied when $\eta\sqrt{2n+1} \ll 1$. In this limit, Eq. (2.57) can be expanded to the lowest order in η, and the Rabi frequency has the simpler form

$$\Omega_{n',n} \simeq \Omega_0\eta^{|n'-n|}\left(\frac{n_>!}{n_<!}\right)^{1/2}\frac{1}{|n'-n|!}. \tag{2.59}$$

In the Lamb-Dicke limit, the interaction Hamiltonian also takes on a simpler form. We can expand the exponential in Eq. (2.55) to lowest order in η to obtain:

$$H_I' \simeq \hbar\Omega_0\sigma_+e^{-i\delta t}[1 + i\eta(ae^{-i\omega_z t} + a^\dagger e^{i\omega_z t})] + h.c.. \tag{2.60}$$

With this approximation, spin flip transitions simultaneous with the creation or annihilation of motional quanta is apparent. If the laser field is resonant with the spin

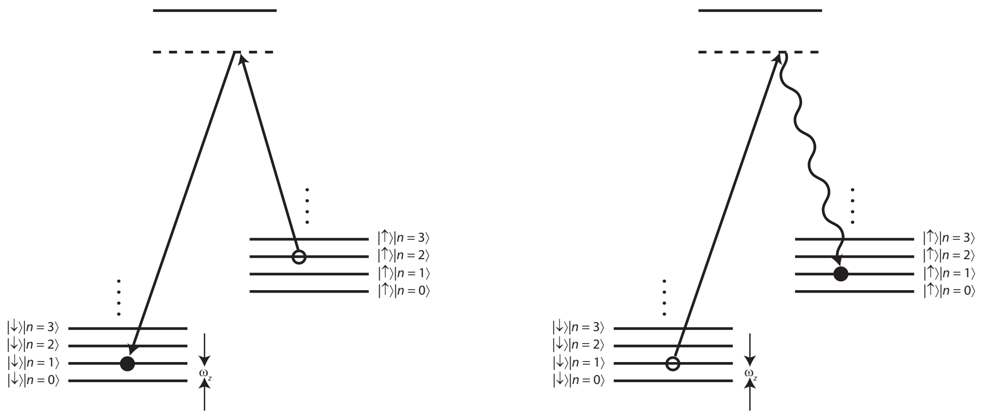

(a) stimulated Raman (Δn = −1)

(b) spontaneous Raman (Δn = 0)

Figure 2.9: Raman sideband cooling is a two-step process. **(a)** Step 1: starting in the higher-energy $|\uparrow\rangle$ state, perform a blue sideband π-pulse to remove one phonon of motional energy. **(b)** Step 2: optically pump back to the $|\uparrow\rangle$ via spontaneous Raman scattering. Repeat this processes until the ground motional state $|n = 0\rangle$ is reached.

flip transition frequency *plus* one motional quanta ($\delta = \omega_z$, the "blue" sideband) and we neglect oscillating terms, the Hamiltonian reduces to $H_I' = \eta\hbar(i\Omega_0\sigma_+a^\dagger - i\Omega_0^*\sigma_-a)$. Similarly, if the laser difference frequency is tuned to the qubit frequency *minus* the oscillation frequency ($\delta = -\omega_z$, the "red" sideband), the Hamiltonian has the Jaynes Cummings form [Jaynes 63] $H_I' = \eta\hbar(i\Omega_0\sigma_+a - i\Omega_0^*\sigma_-a^\dagger)$. The expansion of the Hamiltonian in Eq. (2.60) does not allow for the annihilation or creation of more than one phonon simultaneous with a spin flip transition, nor does it include the Debye-Waller factor $e^{-\eta^2/2}$ [Wineland 98, Wineland 79]. The multiple phonon creation/annihilation terms can be obtained by examining higher order terms in Eq. (2.55) or using the Rabi frequencies calculated in Eqs. (2.57) or (2.59).

2.5.4 Ground State Cooling

After initialization, the ions are Doppler cooled to their Doppler temperature. For typical trap frequencies in the few MHz region, the ions' motion is in a thermal state with average occupation number $\langle n\rangle \simeq 2 - 3$. The ions can be further cooled to their ground motional state $|n = 0\rangle$ via Raman sideband cooling [Wineland 79, Diedrich 89, Monroe 95b]. Cooling to the ground state and hence preparing a pure motional state is a requirement for some two-qubit gates [Cirac 95] and increases the fidelity of other two-qubit gates which are less restrictive in this regard [Leibfried 03, Sørensen 00]. A diagram of the stimulated Raman sideband cooling process is shown in Fig. 2.9. For an ion in the $|\uparrow\rangle|n = 2\rangle$ state, we can apply a π-pulse on the blue sideband to remove one motional quanta from the ion simultaneous with a spin-flip transition. The ion spin state can be reset to $|\uparrow\rangle$ via optical pumping. In the Lamb-Dicke limit, recoil heating is suppressed during the optical pumping process [Dicke 53, Bergquist 87]. The process to remove one motional quanta is repeated until the ion reaches the ground state. Even though the heating of the system on average is equal to the recoil energy after scattering of a photon, the increase in the motional occupation number is suppressed in the Lamb-Dicke limit. The probability of increasing the phonon number by one through the repump process is $\eta^2(n+1)$. There is still a small probability of increasing the phonon number through repumping. However, because the cooling process repeats, this additional heat can be removed by succeeding cooling cycles. Once in the ground state, additional cooling cycles become inactive. Because the optical pumping process resets the ion to the $|\uparrow\rangle$ state, if the ion is in the motional ground state $|\uparrow\rangle|n = 0\rangle$, the blue sideband drive is off resonance with any transition to the $|\downarrow\rangle$ state as there is no $|n = -1\rangle$ motional state. Furthermore, the $|\uparrow\rangle$ is a dark state for the optical pumping laser; therefore the ion will not scatter any photons once in the $|\uparrow\rangle$ state and hence does not recoil heat back to the Doppler temperature. The fact that additional cooling cycles do not affect ions in the ground state implies some robustness to the cooling process.

Because the ion's motion is in a thermal distribution after Doppler cooling, there is a significant fraction of experiments where the ion's motional occupation number is greater than that corresponding to the Doppler temperature. Furthermore, the pulse duration required to perform a π-pulse on the blue sideband differs based on the starting motional state $|n\rangle$ (see Eq. (2.57) in § 2.5.3). We can cool all experiments where the ion has at most L phonons by the following procedure. We first apply a blue sideband pulse for the duration required to induce the transition $|\uparrow\rangle|n = L\rangle \rightarrow |\downarrow\rangle|n = L-1\rangle$ followed by optical pumping to the $|\uparrow\rangle|n = L-1\rangle$ state. This is accomplished by choosing the duration of the pulse τ_L to be such that $\Omega_{L,L-1}\tau_L = \pi/2$. The population of the $|n = L\rangle$ state is now completely transferred to the $|n = L-1\rangle$ state. The population in the other states make only partial transitions reducing their phonon number by one because the Rabi frequencies for these transitions are different. However, next we apply a blue sideband pulse for $\tau_{L-1} = \pi/(2\Omega_{L-1,L-2})$ followed by the optical pumping step completely clearing out the $|n = L-1\rangle$ motional state. This processes is repeated clearing out motional states $|n = L-2\rangle, |n = L-3\rangle, \cdots, |n = 1\rangle$ until the final pulse transfers perfectly all of the remaining population in the $|n = 1\rangle$ state to the $|n = 0\rangle$ state. For a thermal (Boltzmann) distribution with $\langle n\rangle = 3$, 15 cooling cycles of this form is sufficient to successfully cool to the ground $|n = 0\rangle$ state 99.5% of the time. Additional cooling cycles will increase this percentage.

Using a sequence of π-pulses for perfectly transferring population from motional states $|n\rangle \rightarrow |n-1\rangle$ for n from L to 1 is analogous to frequency chirping a red-detuned Doppler cooling laser for weakly bound neutral atoms. As the frequency of the Doppler laser is chirped from the red of the Doppler broadened atomic linewidth closer to resonance, different velocity classes of atoms are cooled and redistributed closer to zero velocity. In this manner, the population of atoms in different velocity classes piles up near zero velocity. Similarly in Raman sideband cooling, as the cooling process progresses, the population of different motional states of the ion is cleared out and piles up near $|n = 0\rangle$.

The temperature of a cold harmonically-bound ion near the ground state can be measured by examining its motional spectra [Diedrich 89, Monroe 95b]. For an ion in electronic state $|\uparrow\rangle$ and a thermal state with average motional occupation number

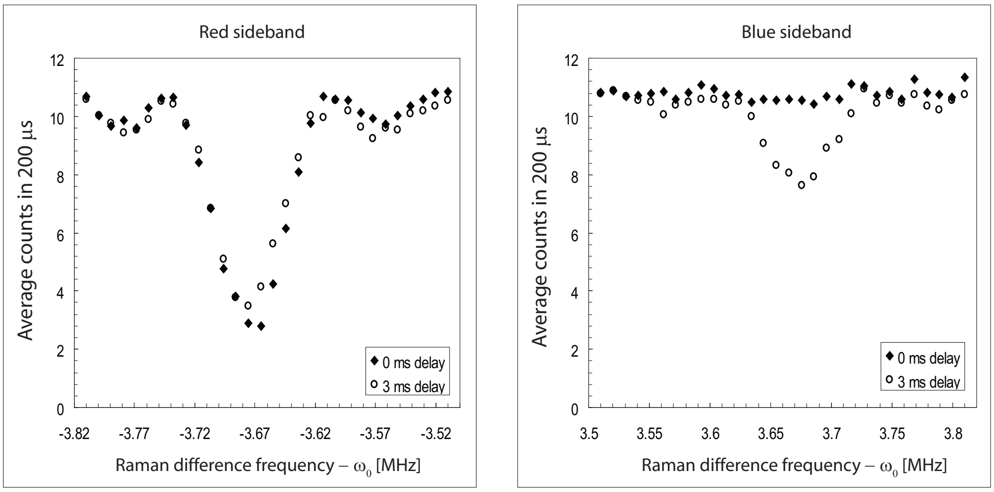

Figure 2.10: The temperature of an ion after Raman sideband cooling can be determined by measuring the transition probabilities on the red and blue sidebands. The y-axis measures the average number of photons collected in a 200 μs measurement interval λ. An ion in the $|\uparrow\rangle = |F = 2, m_F = 2\rangle$ gives the baseline fluorescence ($\lambda_\uparrow \sim$11 photons/200 μs). The transition probability to the $|\downarrow\rangle = |F = 2, m_F = 1\rangle$ is proportional to $\lambda_\uparrow - \lambda$. The filled diamonds are data for a temperature measurement taken directly after Raman sideband cooling and give $\langle n\rangle = 0.06$. The open circles are data for a temperature measurement taken 3 ms after Raman sideband cooling giving $\langle n\rangle = 0.88$. Data was taken on 2005-04-25 in John Jost's trap. Similar measurements of the ion temperature for various delays gives a heating rate of approximately 0.19 quanta/ms.

$\langle n \rangle$, the ratio of transition probabilities to $|\downarrow\rangle$ for the blue and red sidebands is $\frac{\langle n \rangle}{\langle n \rangle + 1}$ independent of the laser intensity, pulse duration, and trap frequency in the Lamb-Dicke limit [Turchette 00]. Therefore, we can determine $\langle n \rangle$ by making measurements of the ratio of the transition probabilities on the red and blue sidebands. A simple example of this measurement is when the ion is in the ground state. Here, the blue sideband transition probability vanishes indicating that $\langle n \rangle = 0$. Fig. 2.10. shows temperature measurement data immediately after cooling to the ground state and 3 ms there after. The blue sideband vanishes for the filled diamonds indicating that ground state cooling is achieved. After cooling to the ground state and waiting for a delay (3 ms in Fig. 2.10), the temperature can be probed again to measure the heating rate of the ion. Repeating the temperature measurement for multiple delays gave a heating rate of 0.19 quanta/ms in John Jost's trap on 2005-04-25.

2.6 Two-Qubit Quantum Gates

To complete the universal gate set for ions, we desire an entangling gate between the spin states (more specifically, the subsystem of two hyperfine ground states of $^9\mathrm{Be}^+$) of two ions. The direct interaction between two ions' internal states is negligible in our systems; however, an effective interaction is obtained by coupling the internal states of the ions to their collective motion. The original proposal to generate a universal two-qubit entangling gate in this manner was given by Cirac and Zoller [Cirac 95], and its experimental realization was recently demonstrated by Schmidt-Kaler *et al.* [Schmidt-Kaler 03]. Since Cirac's original proposal, schemes for generating entangling two-qubit gates for ions based on spin dependent motional displacements have been proposed [Mølmer 99, Solano 99, Milburn 01, García-Ripoll 03] and implemented [Sackett 00, Leibfried 03, Haljan 05b][7] . Such gates have the advantage that the ions

---

[7] A. M. Steane *et al.* have reported demonstration of two-qubit z-basis gates as well in private communication.

do not need to be cooled to the ground state so long as they remain in the Lamb-Dicke limit, and individual ion addressing is not required. These technical advantages can make these type of gates desirable over the original Cirac and Zoller gate, and entangled states created with these methods have been realized with fidelities as high as 97% [Leibfried 03].

Two gates are discussed in this section, and both operate in essentially the same manner. A mode of a two-ion crystal is displaced around a closed path in phase space conditioned on its two-qubit state and obtains a phase proportional to the area enclosed by the path taken in phase space. The differences between the two gates are the basis on which the phases are conditioned and the methods for generating the conditional displacements. I begin this section by explaining the theory of operation of conditional phase gates in the *xy*-basis, namely the Mølmer-Sørensen (MS) gate. I then discuss phase gates in the *z*-basis, namely the "Z-phase gate". We have experimentally realized both of these gates [Sackett 00, Leibfried 03]. Our published fidelities are higher for the Z-phase gate; however, direct application of the Z-phase gate on field-independent qubits is very inefficient. The work arounds to this problem are discussed.

2.6.1 Phase Gate in xy-Basis

The Mølmer-Sørensen gate generates conditional displacements in phase space by application of a bichromatic field to the ions. We recall from § 2.5.3 Eq. (2.55) that the interaction Hamiltonian of a single effective field which couples the spin state of a single ion to its motional state (non-negligible Lamb-Dicke parameter η) in the interaction picture is given by:

$$H_I' = \hbar\Omega\sigma_+ \exp(i[\eta(a^\dagger e^{i\omega_z t} + a e^{-i\omega_z t}) - \delta t + \phi]) + h.c. \tag{2.61}$$

where $\delta \equiv \omega - \omega_0$ is the detuning of the effective field from the qubit transition frequency (generated by two lasers with a difference frequency ω, see § 2.5.2), $\sigma_+ \equiv |\uparrow\rangle\langle\downarrow|$

($\sigma_- \equiv |\downarrow\rangle\langle\uparrow|$) is the qubit raising (lowering) operator, and we have explicitly shown the phase ϕ of the effective field previously contained in the definition of Ω (see § 2.5.2 and 2.5.3). We assume Ω is real and that all of its complex phase is contained in ϕ. In the Lamb-Dicke limit ($\eta\sqrt{\langle n\rangle + 1} \ll 1$, $\langle n\rangle$ the average phonon number), the exponential in Eq. (2.61) can be expanded to lowest order in η to obtain:

$$H_I' \simeq \hbar\Omega\sigma_+ e^{-i(\delta t-\phi)}[1 + i\eta(a^\dagger e^{i\omega_z t} + ae^{-i\omega_z t})] + h.c.. \tag{2.62}$$

The gate scheme by Mølmer and Sørensen is to apply two effective fields at equal and opposite detunings $\pm\delta$ of equal strengths near the blue and red sidebands [$\Omega_b = \Omega_r = \Omega$; subscript '$b$' and '$r$' represent "blue" (+) and "red" (−) detunings and phases $\phi_{b,r}$ respectively]. For a single ion, the application of a bichromatic field results in the transformation $e^{-i(\delta t-\phi)} \to e^{-i(\delta t-\phi_b)} + e^{i(\delta t+\phi_r)} = e^{i\phi_s}(e^{-i(\delta t-\phi_m)} + e^{i(\delta t-\phi_m)})$ in Eq. (2.62) where we have replaced ϕ_b and ϕ_r with the more symmetric definitions $\phi_s \equiv \frac{1}{2}(\phi_b + \phi_r)$ and $\phi_m \equiv \frac{1}{2}(\phi_b - \phi_r)$. The resulting Hamiltonian is:

$$\begin{aligned} H_I' = {} & 2\hbar\Omega\cos(\delta t - \phi_m)\sigma_{-\phi_s} \\ & - \hbar\eta\Omega\sigma_{\frac{\pi}{2}-\phi_s}(a^\dagger e^{i[(\omega_z-\delta)t+\phi_m]} + ae^{-i[(\omega_z-\delta)t+\phi_m]}) \\ & - \hbar\eta\Omega\sigma_{\frac{\pi}{2}-\phi_s}(a^\dagger e^{i[(\omega_z+\delta)t-\phi_m]} + ae^{-i[(\omega_z+\delta)t-\phi_m]}) \end{aligned} \tag{2.63}$$

where $\sigma_\phi \equiv \cos(\phi)\sigma_x + \sin(\phi)\sigma_y$ is a rotated Pauli matrix in the xy-plane [$\sigma_\pm = \frac{1}{2}(\sigma_x \pm i\sigma_y)$], and η is the Lamb-Dicke parameter for the selected mode of the two-ion crystal (the center of mass mode of two ions has a Lamb-Dicke parameter $1/\sqrt{2}$ times the Lamb-Dicke parameter for a single ion). The first term and last two terms are off-resonance, and we neglect them in the remainder of this treatment. Their contribution to the gate error is discussed in [Sørensen 00]. The first term, called the "direct" term by Sørensen, is an off-resonant drive of the carrier transition and is absent in the analogous Z-phase gate. However, with special control of the field intensities, its contribution can be made to vanish exactly [Sørensen 00]. Its presence should not be taken lightly because its resonant coupling strength is $1/\eta$ stronger than the gate drive strength.

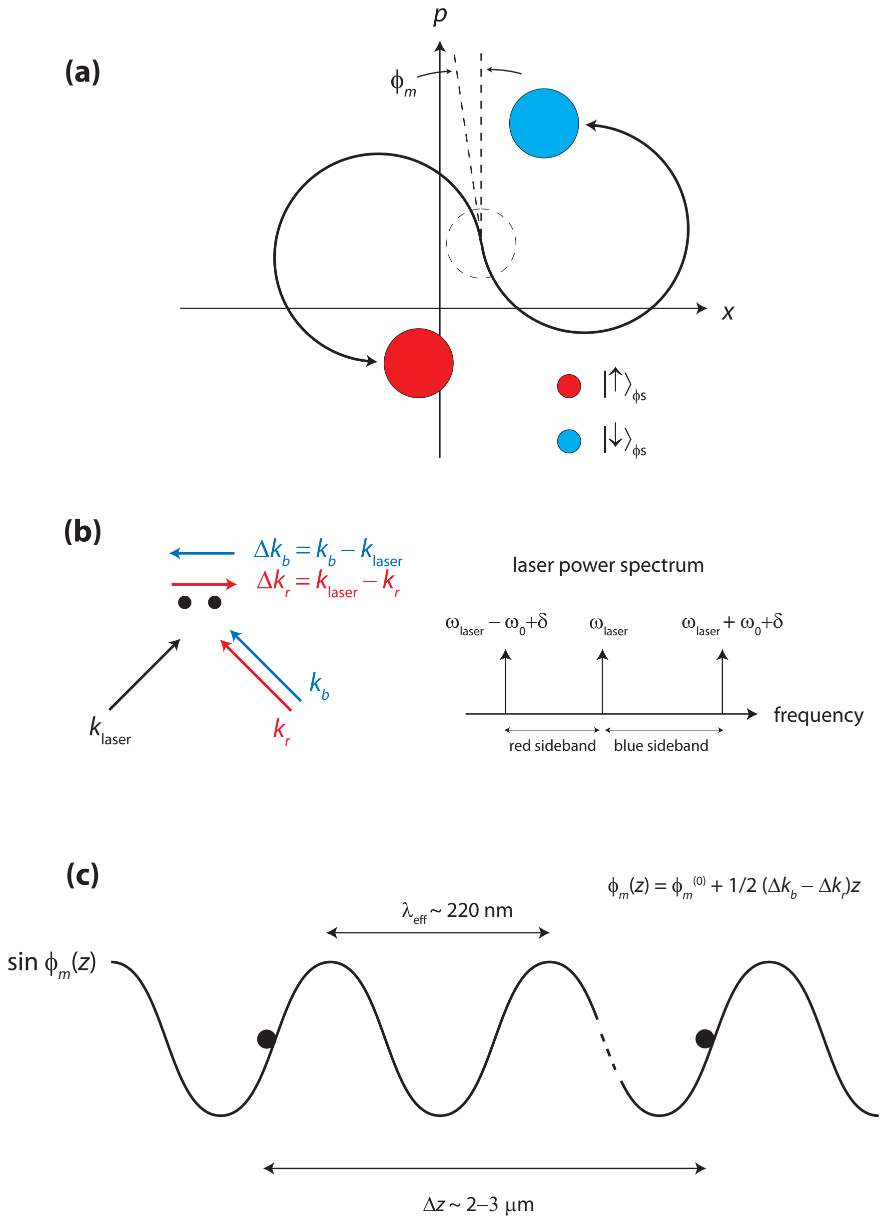

Figure 2.11: **(a)** Phase space displacement trajectory. The different states in the $\sigma_{\pi/2-\phi_s}$ basis follow different paths in phase space. Both paths are circular, and the motional state returns to its starting location after the period $2\pi/(\omega_z - \delta)$ independent of the spin state. Both paths circumscribe the same area with the same sense of rotation. The starting direction is given by the phase ϕ_m, and as long as it remains stable, the area circumscribed is independent of this phase. **(b)** Laser configuration for the Mølmer-Sørensen gate. By arranging the $\Delta k_{b,r}$ vectors in opposite directions, the ϕ_s phase dependence becomes negligible (see text and Ref. [Haljan 05a]). **(c)** The ϕ_m phase front oscillates in space with an effective wavelength $\lambda_{\text{eff}} = \lambda/\sqrt{2}$ in the optical regime. By controlling the trap strength, two ions can be spaced an integer number of effective wavelengths (~ 10) causing both ions to see the same ϕ_m phase.

We can gain an intuitive picture of state evolution under the Hamiltonian in Eq. (2.63) by examining the propagator for infinitesimal durations dt. At time t, the infinitesimal propagator has the form $e^{-iH_I'(t)dt/\hbar} = \exp(d\alpha(t)a^\dagger - d\alpha^*(t)a) = \mathcal{D}(d\alpha(t))$ where $\mathcal{D}(\alpha)$ is the displacement operator of complex displacement α, and $d\alpha(t) = 2i\eta\Omega\sigma_{\frac{\pi}{2}-\phi_s}e^{i[(\omega_z-\delta)t+\phi_m]}dt$ is the infinitesimal displacement for the MS gate. The strength of the infinitesimal displacement is proportional to the $|n=0\rangle \leftrightarrow |n=1\rangle$ sideband Rabi frequency $\eta\Omega$ and is conditioned on the qubit state in the $\sigma_{\pi/2-\phi_s}$ basis. The direction of the displacement at time t is given by $\arg(d\alpha(t)) = \pm[\pi/2 + (\omega_z - \delta)t + \phi_m]$ where the $\pm$ signs are taken for the $\pm$ qubit states in the $\sigma_{\pi/2-\phi_s}$ basis. We observe that the direction of the displacement in xp phase space in the interaction picture[8] rotates linearly in time with a rate given by the detuning of the effective field from the first sideband frequency. Assuming the gate drive strength $\eta\Omega$ is constant during the gate, the resulting path taken in phase space is a circle, and the motional state of the ion returns to its starting location after the period $2\pi/(\omega_z - \delta)$ (see Fig. 2.11).

Application of the MS gate drive to two or more ions can be examined by summing over the individual Hamiltonians for each ion [Eq. (2.63)] and noting that the motional mode is common to all ions[9] . When taking this sum, it is important to remember that the ions have different phases ϕ_s and ϕ_m due to their different locations [$\phi_{r,b}^{(i)} = \phi_{r,b}^{(0)} + (\Delta\vec{k}_{r,b} \cdot \hat{z})z_i$ where z_i is the location on the axis of the i^{th} ion]. By arranging the effective k-vectors $\vec{\Delta k}_r$ and $\vec{\Delta k}_b$ in opposite directions (see Fig. 2.11b), the difference in ϕ_s for the two ions $\phi_s^{(1)} - \phi_s^{(2)} \simeq \frac{1}{2}\frac{\omega_0}{c}\Delta z \sim 10^{-4}$ is essentially zero[10] [Haljan 05a], and for convenience, we choose $\phi_s = 0$. The small difference in basis between the two ions can be compensated by conjugating the gate by a small z-rotation on one of the qubits. More importantly, fluctuations in ion position or equivalent fluctuations in the laser

---

[8] The interaction picture phase space has xp coordinates which rotate at the trap frequency with respect to the lab frame xp coordinates.

[9] We neglect coupling to the other axial modes as they are off resonant. Coupling to the other modes is further suppressed by poor mode matching of the driving effective field to the auxiliary modes.

[10] We have $\Delta\phi_s = \frac{1}{2}(\Delta\phi_b + \Delta\phi_r) = \frac{1}{2}[\Delta k_b\Delta z + \Delta k_r\Delta z] = \frac{1}{2}(\Delta k_b + \Delta k_r)\Delta z$, and if Δk_b and Δk_r are in opposite directions, $\Delta k_b + \Delta k_r \to \omega_0/c$, and $\Delta\phi_s \simeq \frac{1}{2}\frac{\omega_0}{c}\Delta z$.

beam optical path will cause minimal fluctuations in the differential ϕ_s phase seen by the ions. Therefore, the Pauli-matrix $\sigma_{\pi/2-\phi_s} \rightarrow \sigma_y$ in Eq. (2.63) is common to all ions when we take the sum. The optical arrangement which makes ϕ_s common to all ions is also responsible for making ϕ_m position dependent ($\phi_m^{(i)} = \phi_m^{(0)} + \frac{1}{2}[(\Delta\vec{k}_b - \Delta\vec{k}_r) \cdot \hat{z}]z_i$, see Fig. 2.11c). We see from Fig. 2.11c that the ϕ_m phase front oscillates with a length scale given by the effective wavelength λ_{eff} of the laser field ($2\pi/\lambda_{\text{eff}} = |\Delta\vec{k}_b - \Delta\vec{k}_r|$). By tuning the trap strength appropriately, we can space the two ions by an integer of effective wavelengths of the ϕ_m phase front such that each ion sees the same ϕ_m. For more than three ions, the ions are not equally spaced; however, an ion spacing arrangement can be found for which the ions see the same ϕ_m to within a reasonable approximation [Leibfried 05]. It is notable that the laser configuration in Fig. 2.11b provides stability for the ϕ_s for long periods whereas the ϕ_m phase may change between applications of the gate within a single quantum algorithm due to lack of interferometric stability. However, the area circumscribed by the displacements of a closed trajectory is independent of this phase. What is important is that the relative ϕ_m phase between two ions does not change and that ϕ_m does not change during the application of the gate. This puts constraints on the spectrum of noise of relative beam positions and on DC electrode voltage stability. We don't expect fluctuations in ϕ_m to cause problems at the 1% error level. However, these error sources should be examined more closely when attempting gates at the 10^{-4} error level or below. With these considerations, the interaction picture Hamiltonian for N ions can be constructed by making the replacement $\sigma_{\pi/2-\phi_s} \rightarrow 2J_y/\hbar$ in Eq. (2.63) where $J_\xi = \hbar \sum_i^N \sigma_{\xi i}/2$ is the ξ^{th} component of the collective spin operator for the N-ion string ($\xi \in \{x, y, z\}$). The N ion interaction picture interaction Hamiltonian becomes:

$$H_I' \simeq -2\eta\Omega J_y(a^\dagger e^{i[(\omega_z-\delta)t+\phi_m]} + ae^{-i[(\omega_z-\delta)t+\phi_m]}) \tag{2.64}$$

We note that the Hamiltonian [Eq. (2.64)] has the form

$$H_I'/\hbar = i\dot{\alpha}(t)a^\dagger - i\dot{\alpha}^*(t)a \tag{2.65}$$

where $\dot{\alpha}(t) = 2i\eta\Omega(J_y/\hbar)e^{i\phi_m}e^{i(\omega_z-\delta)t}$. The propagator for Eq. (2.64) can be constructed by repeated application of the infinitesimal propagator $dU(t) = e^{-i(H_I'/\hbar)dt} = \mathcal{D}(\dot{\alpha}(t)dt)$ and the relation $\mathcal{D}(\alpha)\mathcal{D}(\beta) = \mathcal{D}(\alpha+\beta)e^{i\mathrm{Im}(\alpha\beta^*)}$ [Walls 94] such that the full propagator has the form

$$\begin{aligned} U(t) &= \prod_{i=1}^{M} \mathcal{D}(\dot{\alpha}(t_{M+1-i})dt) \\ &= \mathcal{D}(\sum_{i=1}^{M} \dot{\alpha}(t_i)dt) \prod_{i=1}^{M} e^{i\mathrm{Im}(\dot{\alpha}(t_i)dt \sum_{j=1}^{i-1} \dot{\alpha}^*(t_j')dt')} \\ &= \mathcal{D}(\alpha(t)) \exp\left(i \int_0^t \mathrm{Im}[\alpha^*(t')\dot{\alpha}(t')]dt'\right) \end{aligned} \tag{2.66}$$

where

$$\alpha(t) = \int_0^t \dot{\alpha}(t')dt' = \frac{2\eta\Omega J_y e^{i\phi_m}}{\hbar(\omega_z-\delta)}\left(e^{i(\omega_z-\delta)t} - 1\right) \tag{2.67}$$

is the total displacement at time t. Here, we have broken up the time evolution into M infinitesimal displacements of size $\dot{\alpha}(t_i)dt$ for $i \in \{1, \cdots, M\}$. We convert back to the continuum with the introduction of the integrals in Eqs. (2.66) and (2.67). The integral in Eq. (2.66) is straight forward, and the resulting propagator is

$$U(t) = \mathcal{D}(\alpha(t)) \exp\left[i\frac{4\eta^2\Omega^2J_y^2}{\hbar^2(\omega_z-\delta)}\left(t - \frac{\sin[(\omega_z-\delta)t]}{\omega_z-\delta}\right)\right]. \tag{2.68}$$

We can verify that the propagator $U(t)$ in Eq. (2.68) satisfies Schrödinger's equation $i\hbar\frac{\partial}{\partial t}U(t) = H_I'U(t)$ by using the alternate definition $\mathcal{D}(\alpha) = e^{-|\alpha|^2/2}e^{\alpha a^\dagger}e^{-\alpha^* a}$ [Walls 94] and assuming the form $U(t) = \mathcal{D}(\alpha(t))e^{if(t)}$. As an intermediate step, we calculate

$$\begin{aligned} \dot{\mathcal{D}}(\alpha)\mathcal{D}^\dagger(\alpha) &= -\frac{1}{2}(\dot{\alpha}\alpha^* + \alpha\dot{\alpha}^*) + \dot{\alpha}a^\dagger - \dot{\alpha}^*\mathcal{D}(\alpha)a\mathcal{D}^\dagger(\alpha) \\ &= -\frac{1}{2}(\dot{\alpha}\alpha^* - \dot{\alpha}^*\alpha) + \dot{\alpha}a^\dagger - \dot{\alpha}^*a \\ &= -i\mathrm{Im}(\alpha^*\dot{\alpha}) - iH_I'/\hbar \end{aligned} \tag{2.69}$$

where we have used $\mathcal{D}(\alpha)a\mathcal{D}^\dagger(\alpha) = a - \alpha$ [Walls 94] and the definition of the Hamiltonian in Eq. (2.65). From Schrödinger's equation, we have $-iH_I'/\hbar = \dot{U}U^\dagger = \dot{\mathcal{D}}\mathcal{D}^\dagger + i\dot{f}$. Substituting Eq. (2.69) and integrating yields $f(t) = \int_0^t \mathrm{Im}[\alpha^*(t')\dot{\alpha}(t')]dt'$. Substituting

$f(t)$ into the assumed propagator $\mathcal{D}(\alpha(t))e^{if(t)}$ gives Eq. (2.66), and hence $U(t)$ in Eqs. (2.66) and (2.68) satisfies Schrödinger's equation.

The phase factor $e^{if(t)}$ has a nice geometric interpretation. At time t, we can close the path taken in phase space by displacing the motional state back to the starting location without altering the phase of the motional state. The total unitary transform is then $\mathcal{D}^{\dagger}(\alpha(t))U(t) = e^{if(t)}$. We define the massless position and momentum operators $x = (a^{\dagger} + a)/\sqrt{2}$ and $p = i(a^{\dagger} - a)/\sqrt{2}$ to convert the phase integral $f(t) = \int_P \mathrm{Im}(\alpha^* d\alpha) = 1/\hbar \int_A dxdp = A/\hbar$ [Leibfried 03]. The phase acquired by the motional state as it traverses the path P is equal to the area A circumvented in phase space divided by $\hbar$.

For $\tau = 2\pi/(\omega_z - \delta)$, the motional mode in phase space has completed a full circle, $\alpha(\tau) = 0$, and $U(\tau) = \exp(i4\eta^2\Omega^2(J_y/\hbar)^2\tau/(\omega_z - \delta))$. We note that $U(\tau)$ is independent of ϕ_m as expected. The gate time τ and the corresponding detuning $\omega_z - \delta$ are chosen such that $4\eta^2\Omega^2\tau/(\omega_z - \delta) = \pi/2$, and the gate operator becomes $U_{\mathrm{MS}} = e^{i(J_y/\hbar)^2\pi/2}$. We note that the rate at which the motional state is driven around a circle in phase space $(2\eta\Omega)^2/(\omega_z - \delta)$ is the two-photon Rabi frequency for making transitions from $|\downarrow\downarrow\rangle|n = 0\rangle \rightarrow |\uparrow\uparrow\rangle|n = 0\rangle$ through the two degenerate states $|\downarrow\uparrow\rangle|n = 1\rangle$ and $|\uparrow\downarrow\rangle|n = 1\rangle$ (see Ref. [Sørensen 99]).

The gate operator $U_{MS} = e^{i(J_y/\hbar)^2\pi/2}$ derived above is valid when driving the gate on the center of mass (COM) mode because each ion in the chain is driven equally and in the same direction. However, axial modes other than the COM mode and all axial modes for ion strings containing different masses do not exhibit this property. For two ions, the stretch mode where the ions oscillate out of phase, heats more slowly than the COM mode where the ions oscillate in phase [King 98]. As such, the stretch mode is preferable for driving two qubit gates. Therefore, we must modify the previous analysis slightly to take this into account.

The motion of the ions in the Lamb-Dicke limit is best described using the method of normal modes [Goldstein 80]. The amplitude and phase of each ion's motion in the crystal for a particular mode is proportional to the eigenvector for that mode. The mode frequencies and mode vectors have been calculated for small numbers of ions [James 98, Kielpinski 00] including different masses [Morigi 01]. The eigenvectors for the normal modes form a complete orthogonal set. Therefore, we can decompose the displacement vector (formed out of the displacement of each ion at the different ion positions) driving the ions into components driving each of the modes. Since we isolate a particular mode on which to drive the gate (by tuning the difference frequencies of the Raman lasers close to a particular mode sideband), we are concerned with this particular component of the displacement vector, and we ignore the off-resonant drive of the other modes. For the mode in question, we are given the normal mode vector $\vec{v}$ normalized such that $||\vec{v}|| = N$ where N is the number of logic ions in the string. We are also given the equilibrium position of the ions in the string which results in different phases $\phi_m^{(i)}$ for each i^{th} ion. For two logic ions, ϕ_m can be made the same for each ion by tuning the ion spacing (see Fig. 2.11). In the previous analysis, we made the transformation $\sum_i \sigma_y^{(i)} e^{i\phi_m^{(i)}} \to 2(J_y/\hbar)e^{i\phi_m}$. The direction of the force driving the harmonic motion on each ion is proportional to $\sigma_y^{(i)} e^{i\phi_m^{(i)}}$. Here, we modify this transformation by taking the projection of the driving force vector for the ions onto the mode vector and let $\sum_i \sigma_y^{(i)} e^{i\phi_m^{(i)}} \to \sum_i \sigma_y^{(i)} e^{i\phi_m^{(i)}} v_i$. For the two-ion stretch mode with mode vector $\vec{v} = (1, -1)$ and the ions spaced such that $\phi_m^{(i)} = \phi_m$ is the same for both ions, $\sum_i \sigma_y^{(i)} e^{i\phi_m^{(i)}} v_i = e^{i\phi_m}(\sigma_y^{(1)} - \sigma_y^{(2)})$, and we can make the replacement $4(J_y/\hbar)^2 \to (\sigma_y^{(1)} - \sigma_y^{(2)})^2$ such that the gate operator becomes $U_{MS} = e^{i(\pi/2)(\sigma_y^{(1)} - \sigma_y^{(2)})^2}$. This has the consequence that when the ions are spaced by an integer number of effective wavelengths of the ϕ_m phase front (see Fig. 2.11c), the stretch mode is driven when the two ions are in different states in the σ_y-basis (i.e. $|\uparrow\downarrow\rangle_y$ or $|\downarrow\uparrow\rangle_y$). Opposing driving forces on the two ions couples to the stretch mode whereas common-mode driving forces do not. The resulting transformation of the U_{MS} gate on the stretch mode in the y-basis is

$$\begin{aligned} U_{MS}|\uparrow\uparrow\rangle_y &= |\uparrow\uparrow\rangle_y \\ U_{MS}|\uparrow\downarrow\rangle_y &= |\uparrow\downarrow\rangle_y e^{i\pi/2} \\ U_{MS}|\downarrow\uparrow\rangle_y &= |\downarrow\uparrow\rangle_y e^{i\pi/2} \\ U_{MS}|\downarrow\downarrow\rangle_y &= |\downarrow\downarrow\rangle_y. \end{aligned} \tag{2.70}$$

2.6.2 Phase Gate in z-Basis

The Z-phase gate closely resembles the xy-basis Mølmer-Sørensen gate except for a change of basis. The frequencies of the two Raman lasers are tuned such that the difference frequency between the two beams $\omega \equiv \omega_b - \omega_r$ is near a particular motional mode frequency ω_z. We can safely ignore any qubit state couplings as the effective field frequency ω is off resonance from the qubit transition frequency ω_0. We can follow an analysis analogous to that in § 2.5.2 to obtain an effective field which couples different motional states within the same qubit-state manifold. The two Raman laser fields couple the states $|m_S\rangle|n\rangle$ and $|m_S\rangle|n'\rangle$ to a set of excited states which mediate an effective coupling between $|m_S\rangle|n\rangle$ and $|m_S\rangle|n'\rangle$ resulting in the matrix elements [Wineland 98, Wineland 03]:

$$\langle m_S, n'|H_I|m_S, n\rangle = \hbar\Omega(m_S)e^{i\phi}e^{-i\omega t}\langle n'|e^{i\eta(a^\dagger+a)}|n\rangle + \delta_S(m_S) \tag{2.71}$$

where

$$\Omega(m_S) = \frac{E_b E_r}{4\hbar^2}\sum_i \frac{\langle m_S|\vec{\mu}\cdot\hat{\epsilon}_r|i\rangle\langle i|\vec{\mu}\cdot\hat{\epsilon}_b|m_S\rangle}{\Delta_i}, \tag{2.72}$$

and

$$\delta_S(m_S) = \sum_{j\in\{b,r\}}\frac{E_j^2}{4\hbar^2}\sum_i \frac{|\langle m_S|\vec{\mu}\cdot\hat{\epsilon}_j|i\rangle|^2}{\Delta_i} \tag{2.73}$$

is the Stark shift of qubit state $|m_S\rangle$ ($m_S \in \{\uparrow,\downarrow\}$). The sums in Eqs. (2.72) and (2.73) are over all intermediate excited states i, and Δ_i is the detuning of the Raman laser from the excited state i ($\Delta \gg \omega, \omega_z$). The phase of the effective field $\phi = \phi_b - \phi_r$ is the differential phase between the two Raman beams.

We desire a strong coupling $\Omega(m_S)$ and a small differential Stark shift $\delta_S(\uparrow) - \delta_S(\downarrow)$. Using orthogonal linearly polarized light for the two Raman lasers, the differential Stark shift is of order $(\omega_0/\Delta)\Omega(m_S)$ [Wineland 03], and with a small elliptical polarization on one of the Raman beams, depending on the choice of the qubit states, the differential Stark shift can be made to vanish exactly [Wineland 03]. Alternatively, the differential Stark shift can be absorbed into the definition of the qubit transition frequency ω_0, and we therefore ignore it in the remainder of this treatment.

The excited states are adiabatically eliminated to obtain the effective Hamiltonian (in the Schrödinger picture) for the motional states in the $|m_S\rangle$ subspace

$$H_I(m_S) = \hbar\Omega(m_S)e^{i\phi}e^{-i\omega t}e^{i\eta(a^\dagger+a)} + h.c.. \tag{2.74}$$

Transforming to the interaction picture $H_I' = e^{iH_{\text{osc}}t/\hbar}H_I e^{-iH_{\text{osc}}t/\hbar}$ where $H_{\text{osc}} = \hbar\omega_z a^\dagger a$ yields:

$$H_I'(m_S) = \hbar\Omega(m_S)e^{i\phi}e^{-i\omega t}\exp\left[i\eta(a^\dagger e^{i\omega_z t} + ae^{-i\omega_z t})\right] + h.c., \tag{2.75}$$

and upon expanding Eq. (2.75) to lowest order in η, we obtain a Hamiltonian similar to Eq. (2.63):

$$\begin{aligned} H_I'(m_S) &\simeq \hbar\Omega(m_S)e^{i\phi}e^{-i\omega t}\left[1 + i\eta(a^\dagger e^{i\omega_z t} + ae^{-i\omega_z t})\right] + h.c. \\ &= 2\hbar\Omega(m_S)\cos(\omega t - \phi) \\ &\quad + \eta\hbar\Omega(m_S)\left(ia^\dagger e^{i[(\omega_z-\omega)t+\phi]} - iae^{-i[(\omega_z-\omega)t+\phi]}\right) \\ &\quad + \eta\hbar\Omega(m_S)\left(ia^\dagger e^{i[(\omega_z+\omega)t-\phi]} - iae^{-i[(\omega_z+\omega)t-\phi]}\right). \end{aligned} \tag{2.76}$$

There are three differences between the Z-phase gate Hamiltonian [Eq. (2.76)] and the MS Hamiltonian [Eq. (2.63)]. The first difference lies in the first term. In the Mølmer-Sørensen gate, the first term is an off-resonant drive of the carrier transition; in the Z-phase gate, the first term acts as a Stark shift modulated at the frequency of the effective field. In both cases, the duration of the gate can be chosen such that this term has no effect [for the Z-phase (MS) gate, this corresponds to $\omega t = 2\pi n$ ($\delta t = 2\pi n$), n an integer]. The resonant strength of this error term is $\sim 1/\eta$ times the gate drive strength in both cases. The second difference is that for the MS gate, the gate drive strength is proportional to $\pm\Omega$ for states in the $\pm\sigma_y$ basis ($\phi_s = 0$ in Eq. (2.63)) and is proportional to $\Omega(m_S)$ for the different $|m_S\rangle$ states in the Z-phase gate. We see that in the MS gate, the strength of the gate drive is equal and in opposite directions for the two qubit states in the $\pm\sigma_y$ basis. This is not necessarily the case for the Z-phase gate. The strength $\Omega(m_S)$ is a function of the qubit states and laser polarization. We desire a large state dependence to the gate drive strength; that is, we would like $|\Omega(\uparrow) - \Omega(\downarrow)|$ as large as possible. The third difference is that there is no ϕ_s phase in the Z-phase gate. That is, the basis on which the displacements in phase space are conditioned is *always* the σ_z basis. Similarly, the ϕ_m phase in the MS gate is duplicated by the phase $\phi + \pi/2$ in the Z-phase gate. In both cases, this phase oscillates in space with a length scale set by the effective wavelength of the effective field along the trap axis (see Fig. 2.11c). The last terms in these Hamiltonians are ignored in both cases by the rotating wave approximation.

Similar to the end of the previous section, we must project the displacement drive strength vector onto the mode vector $\vec{v}$. Summing over all ions in the string, we can write the Hamiltonian [Eq. (2.76)] in the form of Eq. (2.65) (ignoring the first and last error terms) where

$$\dot{\alpha}(m_S^{\{i\}}, t) = \eta e^{i(\omega_z - \omega)t} \sum_i \Omega(m_S^{(i)}) e^{i\phi_i} v_i \qquad (2.77)$$

and v_i is the component of the mode vector for the i^{th} ion. The notation $m_S^{\{i\}}$ indicates the qubit configuration in the σ_z basis for the set of ions. For the qubit states $|\downarrow\rangle = |F = 2, m_F = -2\rangle$ and $|\uparrow\rangle = |F = 1, m_F = -1\rangle$ used in the Leibfried *et al.* [Leibfried 03] experiment, $\Omega(\downarrow) = -2\Omega(\uparrow)$ [Wineland 03]. As indicated in the previous section, the mode vector for the two-ion stretch mode is $\vec{v} = (1, -1)$; upon spacing the ions such that the phase ϕ is the same for two ions, the strength of the displacement drive for the different two-qubit configurations becomes $\dot{\alpha}(\downarrow\uparrow, t) = -\dot{\alpha}(\uparrow\downarrow, t) = 3\eta e^{i(\omega_z-\omega)t}\Omega(\uparrow)e^{i\phi}$ and $\dot{\alpha}(\downarrow\downarrow, t) = \dot{\alpha}(\uparrow\uparrow, t) = 0$. Following the analysis of the previous section, we can choose the detuning of the effective field from the mode frequency $\omega - \omega_z$ such that after the period $\tau = 2\pi/(\omega_z - \omega)$ we obtain the gate operator $U_L = e^{i(\pi/2)(\sigma_z^{(1)}-\sigma_z^{(2)})^2}$. The period τ and the detuning $\omega - \omega_z$ are calculated using the relation $9\eta^2\Omega(\uparrow)^2\tau/(\omega_z - \omega) = \pi/2$.

The duration τ for the stretch mode two-ion Z-phase gate satisfies the relation $\eta^2|\Omega(\uparrow) - \Omega(\downarrow)|^2\tau/(\omega_z - \omega) = \pi/2$ where $\tau = 2\pi/(\omega_z - \omega)$. Substituting for $\omega_z - \omega$ in favor of τ yields the relation

$$\eta|\Omega(\uparrow) - \Omega(\downarrow)|\tau = \pi. \tag{2.78}$$

Therefore, the speed of the gate is directly proportional to $|\Omega(\uparrow) - \Omega(\downarrow)|$, and as such, we would like to maximize this rate. $\Omega(m_S)$ is calculated using Eq. (2.72). We write the qubit eigenstates as ($m_S \in \{\uparrow, \downarrow\}$)

$$\begin{aligned} |m_S\rangle = \alpha_{m_S}|m_J = -1/2, m_I = m_F(m_S) + 1/2\rangle \\ + \beta_{m_S}|m_J = +1/2, m_I = m_F(m_S) - 1/2\rangle \end{aligned} \tag{2.79}$$

where α_{m_S} and β_{m_S} are calculated from the Breit-Rabi formula (see § 2.2), and at low magnetic fields, α_{m_S} and β_{m_S} are Clebsch-Gordan coefficients. Because the detuning of the Raman lasers is large compared to the hyperfine splitting of the $P_{1/2}$ and $P_{3/2}$ manifolds, we can sum over all excited states in the $P_{1/2}$ manifold separately from those in the $P_{3/2}$ manifold when calculating $\Omega(m_S)$ in Eq. (2.72). We define the polarizations according to their left circular ($\hat{\sigma}^-$), right circular ($\hat{\sigma}^+$), and linear ($\hat{\pi}$) components such that $\hat{\epsilon}_l = l_+\hat{\sigma}^+ + l_-\hat{\sigma}^- + l_0\hat{\pi}$ and $l_+^2 + l_-^2 + l_0^2 = 1$ for $l \in \{b, r\}$. For the $P_{1/2}$ manifold,

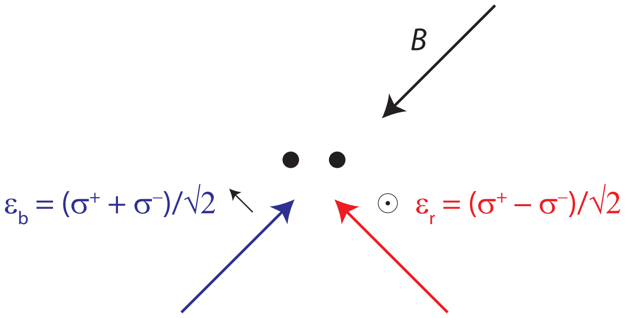

Figure 2.12: Raman laser configuration for the Z-phase gate. The blue and red Raman lasers propagate such that the difference in their k-vectors lies along the trap z-axis. The polarizations are both linear and orthogonal to each other and to the magnetic field $\vec{B}$.

we obtain

$$\begin{aligned}\sum_{i\in P_{1/2}} \frac{\langle m_S|\vec{\mu}\cdot\hat{\epsilon}_r|i\rangle\langle i|\vec{\mu}\cdot\hat{\epsilon}_b|m_S\rangle}{\Delta_i} &= \frac{|\mu|^2}{\Delta_{1/2}}\left\{|\alpha_{m_S}|^2\left(\frac{2}{3}b_+r_+^* + \frac{1}{3}b_0r_0^*\right)\right. \\ &\qquad \left. + |\beta_{m_S}|^2\left(\frac{2}{3}b_-r_-^* + \frac{1}{3}b_0r_0^*\right)\right\} \\ &= \frac{|\mu|^2}{3\Delta_{1/2}}\left[(b_0r_0^* + b_+r_+^* + b_-r_-^*) + \left(|\alpha_{m_S}|^2 - |\beta_{m_S}|^2\right)(b_+r_+^* - b_-r_-^*)\right], \end{aligned} \tag{2.80}$$

and similarly for the $P_{3/2}$ manifold,

$$\begin{aligned}\sum_{i\in P_{3/2}} \frac{\langle m_S\vec{\mu}\cdot\hat{\epsilon}_r|i\rangle\langle i|\vec{\mu}\cdot\hat{\epsilon}_b|m_S\rangle}{\Delta_i} &= \frac{|\mu|^2}{3\Delta_{3/2}}\left\{2(b_0r_0^* + b_+r_+^* + b_-r_-^*)\right. \\ &\qquad \left. - \left(|\alpha_{m_S}|^2 - |\beta_{m_S}|^2\right)(b_+r_+^* - b_-r_-^*)\right\} \end{aligned} \tag{2.81}$$

where $\mu = \langle P_{3/2}, F=3, m_F=3|\vec{\mu}\cdot\hat{\sigma}^+|S_{1/2}, F=2, m_F=2\rangle$ is the cycling transition electric dipole moment, and $\Delta_{1/2}$ ($\Delta_{3/2}$) is the detuning of the Raman lasers from the $P_{1/2}$ ($P_{3/2}$) state.

A few observations on Eqs. (2.80) and (2.81) are in order. Firstly, the state dependence enters two places: (1) the term $|\alpha_{m_S}|^2 - |\beta_{m_S}|^2$ and (2) the detunings $\Delta_{1/2}$ and $\Delta_{3/2}$. The relative detuning for the two qubit states is ω_0/Δ_j for $j\in\{\frac{1}{2},\frac{3}{2}\}$ where the qubit frequency is ~1 GHz and the detunings are of order ~100 GHz. Therefore, the different detunings for the different qubit eigenstates only modify the gate speed slightly if $|\alpha_{m_S}|^2 - |\beta_{m_S}|^2$ differs by order unity for the qubit eigenstates. Secondly, the gate speed is optimized when $b_+ r_+^* - b_- r_-^*$ is maximized. We are constrained to the use of linearly polarized light to minimize the differential Stark shift [Wineland 03]. However, we can maximize $b_+ r_+^* - b_- r_-^*$ while maintaining linearly polarized light by letting $b_- = b_+ = 1/\sqrt{2}$ and $r_- = -r_+ = 1/\sqrt{2}$. This polarization configuration is obtained with the laser beam geometry in Fig. 2.12. The third observation is that for fast gates, we require qubit eigenstates such that $\left||\alpha_\uparrow|^2 - |\alpha_\downarrow|^2\right|$ is large[11] . Unfortunately, field independent qubits have the property that $\alpha_\uparrow \simeq -\alpha_\downarrow + \mathcal{O}(10^{-4})$ (see § 2.2); therefore, direct application of the Z-phase gate to field independent qubits is inefficient. In order to efficiently use the Z-phase gate on field independent qubits, we must temporarily transfer out of the field independent subspace, perform the gate, and transfer back to the field independent subspace. If errors induced by magnetic field noise are small over the duration of these steps, this may be a viable option. Alternatively, we could perform the Mølmer-Sørensen gate directly. Because $|\alpha_\uparrow|^2 - |\alpha_\downarrow|^2 \sim 10^{-4}$ for field independent qubits, we might consider using the difference in detuning to drive the gate, particularly for ions where the hyperfine splitting is large (such as Cd$^+$ where the hyperfine splitting is 14.7 GHz). However, it is desirable to have large detunings from the excited states to reduce the error due to Raman inelastic spontaneous scattering (see [Ozeri 05] and Ch. 5). Therefore, given the availability of other equivalent gates (namely the Mølmer-Sørensen gate), the Z-phase gate is not the gate of choice for field independent qubits.

Using the approximation $\omega_0/\Delta_j \ll 1$ for $j \in \{\frac{1}{2}, \frac{3}{2}\}$, the differential displacement drive between the qubit eigenstates is

$$\Omega(\uparrow) - \Omega(\downarrow) = -\frac{E_b E_r |\mu|^2}{6\hbar^2} \frac{\Delta_F}{\Delta_{1/2}(\Delta_{1/2} - \Delta_F)} (b_+ r_+^* - b_- r_-^*)(|\alpha_\uparrow|^2 - |\alpha_\downarrow|^2) \tag{2.82}$$

where Δ_F is the fine structure splitting between $P_{3/2}$ and $P_{1/2}$. The duration of the

---

[11] By normalization, $|\alpha_{m_S}|^2 - |\beta_{m_S}|^2 = 2|\alpha_{m_S}|^2 - 1$; therefore, the speed of the gate is proportional to $\left||\alpha_\uparrow|^2 - |\alpha_\downarrow|^2\right|$.

stretch mode two-ion Z-phase gate satisfies Eq. (2.78).

2.6.3 Entanglement Verification

Both the Z-phase gate and the Mølmer-Søresen gate have been used to generate maximally entangled Schrödinger "cat" states of N ions of the form $|\Psi\rangle = |\uparrow\cdots\uparrow\rangle + e^{i\phi_0}|\downarrow\cdots\downarrow\rangle$ [Sackett 00, Leibfried 03, Leibfried 05]. In general, multi-qubit quantum states are characterized by quantum state tomography [Haffner 05]. However, for the case of "cat" states, the target density matrix $\rho_{\text{cat}} = |\Psi\rangle\langle\Psi|$ has only four non-zero elements, and the fidelity $F \equiv \langle\Psi|\rho|\Psi\rangle = \frac{1}{2}(P_{(\uparrow)} + P_{(\downarrow)}) + \rho_{(\uparrow\downarrow)}$ of an arbitrary density matrix ρ is characterized by the three experimentally measurable quantities: $P_{(\uparrow)}$ — the population of the $|\uparrow\cdots\uparrow\rangle$ state, $P_{(\downarrow)}$ — the population of the $|\downarrow\cdots\downarrow\rangle$ state, and the far off-diagonal element of the density matrix $\rho_{(\uparrow\downarrow)} \equiv \rho_{\uparrow\cdots\uparrow,\downarrow\cdots\downarrow}$ [Sackett 00]. In this section, I discuss how these three parameters are measured following the method of Sackett *et al.* [Sackett 00]. Fidelities greater than 0.5 are sufficient to prove N-particle entanglement [Sackett 00].

The populations $P_{(\uparrow)}$ and $P_{(\downarrow)}$ are determined by state dependent resonance fluorescence (see § 2.4 and Appendix C). After preparing the "cat" state and measuring all qubits in the z-basis, we obtain a histogram of collected photon counts upon repeated preparations and measurements. This histogram is fit to a sum of $N+1$ reference histograms for 0-ions bright, 1-ion bright, up to N ions bright to obtain the probability that N and 0 ions are bright and hence the populations $P_{(\uparrow)}$ and $P_{(\downarrow)}$ respectively. Measurement of the $\rho_{(\uparrow\downarrow)}$ requires the probabilities P_j that j ions are bright for $j \in \{0, 1, \cdots, N\}$, and these are extracted using the same histogram analysis.

The coherence term $\rho_{(\uparrow\downarrow)}$ is determined by performing an additional $\pi/2$ interrogation pulse with a variable phase ϕ to all the qubits prior to measuring P_j. That is, we perform the unitary rotation $U(\phi) = \frac{1}{\sqrt{2}}\sum_{i=1}^{N}\left[\mathbf{1} - i\left(\sigma_x^{(i)}\cos\phi + \sigma_y^{(i)}\sin\phi\right)\right]$ transforming the state into

$$\begin{aligned}|\Psi_1\rangle = U(\phi)|\Psi\rangle &= 2^{-(N+1)/2}\big[(|0\rangle - ie^{i\phi}|1\rangle)\cdots(|0\rangle - ie^{i\phi}|1\rangle) \\ &\qquad + e^{i\phi_0}(-ie^{-i\phi})^N(|0\rangle + ie^{i\phi}|1\rangle)\cdots(|0\rangle + ie^{i\phi}|1\rangle)\big] \\ &= \sum_{k=0}^{2^N} c_k|k\rangle\end{aligned} \tag{2.83}$$

where

$$c_k = 2^{-(N+1)/2}(-ie^{i\phi})^{n_1(k)}\left[1 + (-1)^{n_1(k)}e^{i(\phi_0 - N\phi - N\pi/2)}\right] \tag{2.84}$$

$$|c_k|^2 = 2^{-N}[1 + (-1)^{n_1(k)}\cos(\phi_0 - N\phi - N\pi/2)]. \tag{2.85}$$

We have made the associations $|\uparrow\rangle \to |0\rangle$, $|\downarrow\rangle \to |1\rangle$, and the binary number k labels the state $|k\rangle$. The function $n_1(k)$ is the number of 1's in the binary number k. From histogram analysis (see Appendix C), we extract P_j, the probability of measuring j ions in the $|1\rangle$ state. Using Eq. (2.85), P_j for the N-ion "cat" state is

$$P_j = \sum_{\{k:n_1(k)=j\}} |c_k|^2 = 2^{-N}\binom{N}{j}\left[1 + (-1)^j\cos(\phi_0 - N\phi - N\pi/2)\right]. \tag{2.86}$$

From P_j we can construct the parity[12]

$$\Pi(\phi) \equiv \sum_{j=0}^{N}(-1)^j P_j = \cos(\phi_0 - N\phi - N\pi/2). \tag{2.87}$$

We measure the parity as a function of ϕ which oscillates N times in 2π, and the amplitude of this oscillation is in fact $2\rho_{(\uparrow\downarrow)}$ [Bollinger 96].

An alternative method for measuring the coherence term $\rho_{(\uparrow\downarrow)}$ other than parity oscillations is to transform the cat state into a superposition of $|\uparrow\cdots\uparrow\rangle$ and $|\downarrow\cdots\downarrow\rangle$ with respective populations that are a function of the phase ϕ of the transformation pulse [Leibfried 04, Leibfried 05]. The populations of $|\uparrow\cdots\uparrow\rangle$ and $|\downarrow\cdots\downarrow\rangle$ oscillate back and forth N times in 2π as a function of ϕ. Because the fluorescence of the ions is proportional to the number of ions in the $\uparrow$ state, the fluorescence data can be used

---

[12] The factors $2^{-N}\sum_{j=0}^{N}\binom{N}{j}(-1)^j = 0$ and $2^{-N}\sum_{j=0}^{N}\binom{N}{j} = 1$ by the binomial theorem $(1+x)^N = \sum_{j=0}^{N}\binom{N}{j}x^j$ for $x = -1$ and $x = 1$.

directly without the need to fit the histograms to obtain the populations of 0 up to N ions bright. This method has been used to verify entanglement for N-ion Schrödinger cat states up to $N = 6$ ions [Leibfried 05]. Fluorescence oscillations as a function of the phase ϕ of the decoding pulse are shown in Fig. 2.13 [Leibfried 05]. We observe that fidelity drops considerably as the number of ions is increased verifying the need for higher-fidelity operations and/or quantum error correction and hence very low error rates for quantum memory (see Ch. 4) and quantum gates (see Ch. 5).

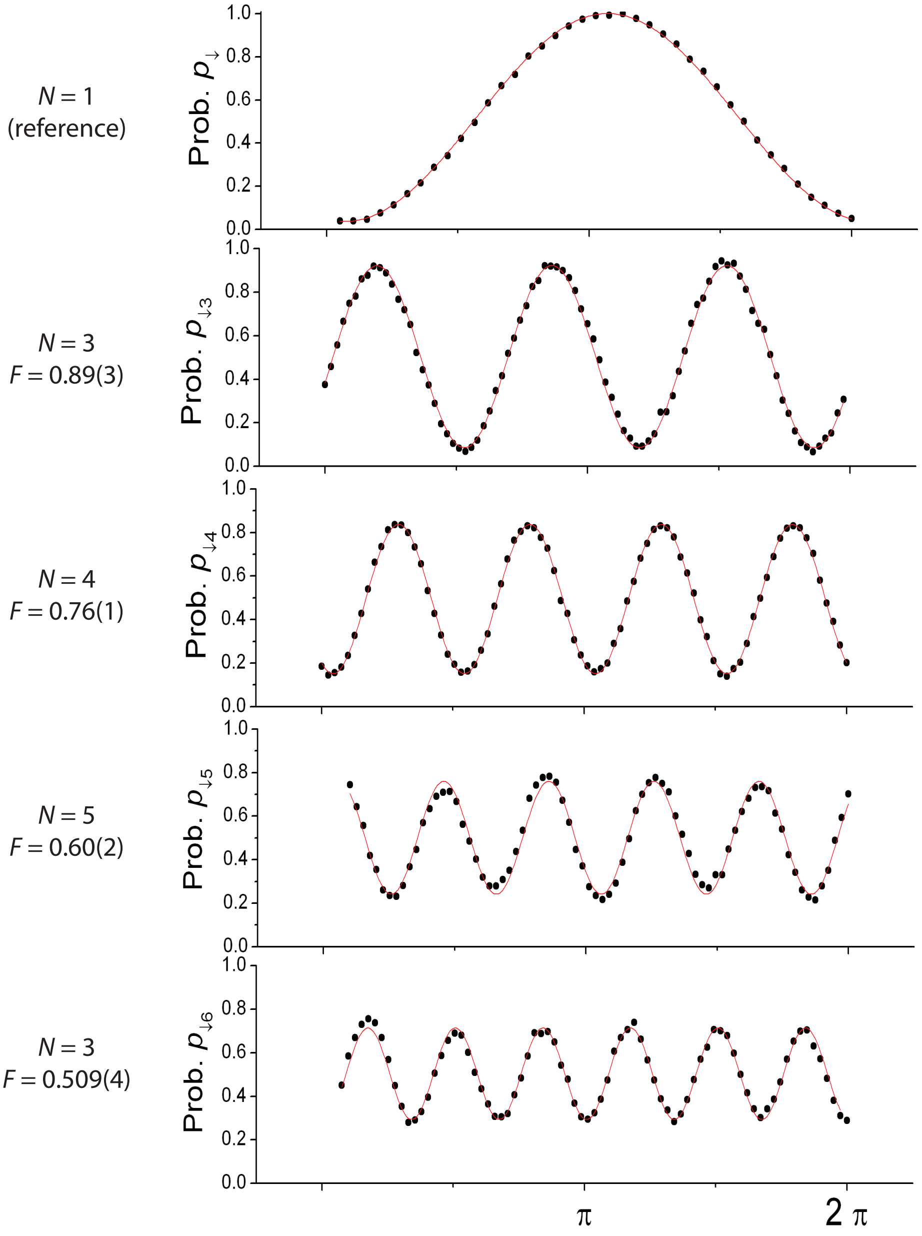

Figure 2.13: Fluorescence oscillation for “cat” states up to six ions [Leibfried 05]. In the figure, N is the number of ions entangled, and F is the fidelity (see text).

Chapter 3

Apparatus

3.1 Ion Traps

In order to perform quantum information processing experiments, our qubits must be well isolated from the environment. This is accomplished by trapping ion qubits in ultra high vacuum using linear Paul traps. In this section, I will describe the theory of linear Paul traps followed by descriptions of the trap apparatuses used in the experiments. Because the trapping electric fields couple strongly to the ion's net charge and only weakly to the internal states, the ion's internal states are left nearly unperturbed and well isolated from the environment leaving them available for use as robust quantum information carriers.

3.1.1 Ion Trap Theory

Due to their net charge, ions can be confined in free space with an appropriate arrangement of electric fields. It is interesting to note that static electric fields cannot confine charged particles by Earnshaw's theorem. A simple explanation of why this is the case is contained in Gauss's law which states that the divergence of the electric field at a point in space is proportional to the charge density at that point. Trapping of positive (negative) charge from static external fields requires negative (positive) divergence of the electric field, and in empty space, the charge density for the external field is zero. From a slightly different perspective, we can consider the potential energy of a positive charge in the static quadratic electric potential $\Phi(x, y, z) = \Phi_0(Ax^2 + By^2 + Cz^2)$. By Laplace's equation $\nabla^2\Phi = 0$, we must have $A + B + C = 0$; therefore, although it may be possible to trap in two directions (say $A, B > 0$ for $Q > 0$), the third direction will be anti-trapping ($C = -A - B < 0$).

Although static electric fields cannot confine charge, time-varying fields can. There are a number of works describing the theory of charged particle traps including two books [Major 05, Ghosh 95]. I refer the reader interested in primary sources to the references contained in [Major 05]. The traps used in the research of this thesis are linear RF Paul traps. The linear Paul trap is a Paul mass filter plugged at the ends with static potentials. A schematic diagram of a linear Paul trap [Raizen 93] similar to those used in this thesis is shown in Fig. 3.1. A potential of the form $V_0 \cos \Omega_T t + U_r$ is applied to the white diagonally opposing RF electrodes placed a distance R away from the trap z axis. The segmented control electrodes, also placed a distance R from the trap axis, are held at RF ground. This produces a potential near the axis of the form

$$\Phi_{RF} \simeq \frac{1}{2}\kappa_{RF}(V_0 \cos \Omega_T t + U_r)\left(1 + \frac{x^2 - y^2}{R^2}\right) \tag{3.1}$$

where κ_{RF} is a geometry factor on the order of unity resulting from the fact that the rods are not equipotential surfaces for the electric quadrupole field. As I will show later, this potential provides radial confinement of the ions. The ions are confined along the axis by applying a static potential U_0 to the end cap electrodes while holding the middle segmented electrodes at DC ground. Taylor expanding the static potential along the axis results in a static potential of the form:

$$\Phi_s \simeq \frac{\kappa_{DC} U_0}{Z_0^2}\left[z^2 - \frac{1}{2}\epsilon_{DC}x^2 - \frac{1}{2}(2 - \epsilon_{DC})y^2\right] \tag{3.2}$$

where Z_0 is the length of the middle segmented electrode and κ_{DC} and ϵ_{DC} are geometry factors on the order of unity similar to κ_{RF}. The potentials in Eqs. (3.1) and (3.2) are the lowest order terms in the multipole expansion of the potentials about the axis where

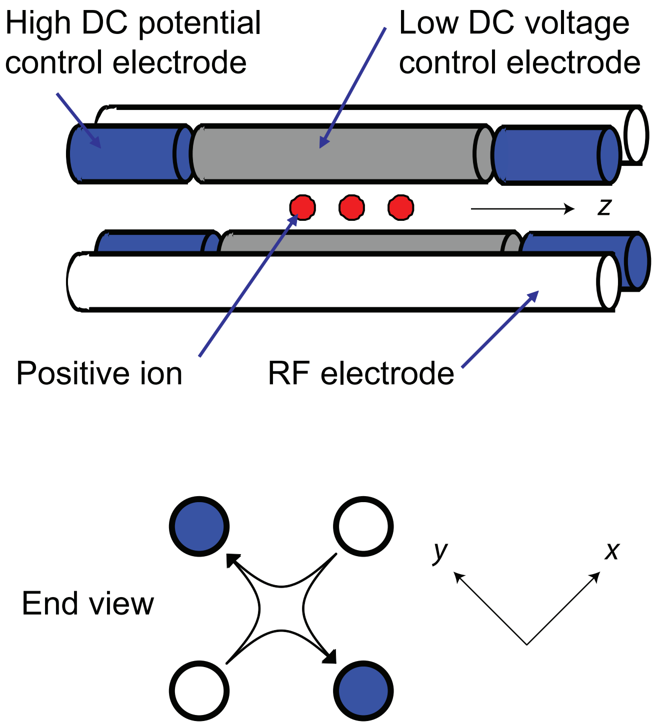

Figure 3.1: Schematic diagram of a linear RF Paul trap. An oscillating potential is applied to the white RF electrodes producing an approximate quadrupole electric field pattern in the xy plane (see end view). This provides radial confinement of the ions to the RF electric field null along the z axis. Axial confinement is provided by the segmented control electrodes. Applying higher DC potential to the end caps relative to the middle DC electrode provides a potential minimum along the axis for the ions. If axial confinement is weaker than radial confinement, multiple ions will configure into a linear chain along the axis.

the ions will be trapped. For laser cooled ions in typical traps with strengths of a few MHz, the extent of the ions' motion about their equilibrium positions is on the order of a few tens of nanometers. Given trap dimensions on the order of $R \sim 100\ \mu$m, higher order terms in the multipole expansion of the potential are negligible.

The equations of motion for an ion with mass m and charge q are given by $\ddot{x}_j = -\frac{q}{m}\frac{\partial}{\partial x_j}(\Phi_{RF} + \Phi_s)$ for $j \in \{x, y, z\}$. Motion in the z-direction is simple harmonic motion with frequency $\omega_z = \sqrt{2q\kappa_{DC}U_0/(mZ_0^2)}$. In the x and y directions, the equations of motion are homogenous differential equations of the Mathieu type ($i \in \{x, y\}$):

$$\frac{d^2 x_i}{d\tau^2} + (a_i + 2q_i \cos 2\tau)x_i = 0 \tag{3.3}$$

where $\tau = \Omega_T t/2$ is a dimensionless time, $a_x = -\frac{4q}{m\Omega_T^2}\left(\frac{\kappa_{DC}U_0}{Z_0^2}\epsilon_{DC} - \frac{\kappa_{RF}U_r}{R^2}\right)$, $a_y = -\frac{4q}{m\Omega_T^2}\left(\frac{\kappa_{DC}U_0}{Z_0^2}(2 - \epsilon_{DC}) + \frac{\kappa_{RF}U_r}{R^2}\right)$ quantify the static potentials, and $q_x = -q_y = \frac{2q\kappa_{RF}V_0}{m\Omega_T^2 R^2}$ is a measure of the strength of the RF potential. The Mathieu equation can be solved using Floquet solutions, and for an in-depth treatment in the context of ion traps, I refer the reader to [Major 05]. However, in practice, we work in the regime where $|a_i| < q_i^2 \ll 1$, and we can invoke the pseudopotential approximation.

Under the conditions $|a_i| < q_i^2 \ll 1$, we can separate the motion of a single coordinate x_i into two parts $x_i = u + \epsilon$ where $u \gg \epsilon$ is a slowly varying function representing the slow time scale position of the ion and ϵ is a small amplitude high frequency motion. We further assume that $\frac{d^2\epsilon}{d\tau^2} \gg \frac{d^2 u}{d\tau^2}$ which we will verify later. (In what follows, we drop the subscript i on the parameters a_i, q_i, and x_i to simplify the notation). Using these approximations, we can rewrite the Mathieu equation as

$$\begin{aligned} \frac{d^2\epsilon}{d\tau^2} + 2q\cos(2\tau)u = 0 \\ \Rightarrow \epsilon = \frac{q}{2}\cos(2\tau)u. \end{aligned} \tag{3.4}$$

We now back substitute ϵ in Eq. (3.4) into the Mathieu equation (3.3) to obtain the equation

$$\frac{d^2 u}{d\tau^2} + (a + q^2\cos^2 2\tau)u + \frac{1}{2}aq\cos(2\tau)u = 0. \tag{3.5}$$

Averaging Eq. (3.5) over one period of the RF cycle yields harmonic motion in u with frequency $\beta = \sqrt{a + q^2/2}$. The resulting x_i coordinate of the ion's position has then the approximate form:

$$x_i = u + \epsilon = A_i \cos(\beta_i \frac{\Omega_T}{2} t + \phi_i)(1 + \frac{q_i}{2} \cos \Omega_T t) \tag{3.6}$$

where A_i and ϕ_i are determined by initial conditions and $\beta_i \equiv \sqrt{a_i + q_i^2/2}$ $(i \in \{x, y\})$. We observe that under the conditions $a < q^2 \ll 1$, the frequency $\beta\Omega_T/2 \ll \Omega_T$ and hence $\frac{d^2\epsilon}{d\tau^2} \gg \frac{d^2u}{d\tau^2}$ is satisfied. Furthermore, because $q \ll 1$, the assumption $u \gg \epsilon$ is also verified. The large amplitude slower motion of the ion at frequency $\beta_i\Omega_T/2$ is termed the "secular" motion, and the smaller amplitude faster motion at the RF drive frequency Ω_T is termed the "micromotion". The micromotion amplitude is proportional to the instantaneous secular position.

Ignoring the micromotion, we see that the ion's secular motion in the xy directions can be equivalently determined by a harmonic pseudopotential Φ_p of the form

$$q\Phi_p = \frac{1}{2} m(\omega_x^2 x^2 + \omega_y^2 y^2) \tag{3.7}$$

where $\omega_i = \frac{\Omega_T}{2}\sqrt{a_i + \frac{q_i^2}{2}}$ for $i \in \{x, y\}$. When the radial confinement is much stronger than the axial confinement, the secular frequency is approximated by $\omega_i \simeq \frac{|q_i|}{2\sqrt{2}}\Omega_T = \frac{q\kappa_{RF}V_0}{\sqrt{2}m\Omega_T R^2}$.

The approximate solutions (3.6) are the lowest order terms of the more general Floquet solution (see [Major 05]). The pseudopotential approximation gives insight into the frequency of secular motion, and the motion is stable so long as $0 < \beta_i < 1$ for $i \in \{x, y\}$ [Major 05]. In the pseudopotential approximation, $\beta_i = \sqrt{a_i + q_i^2/2}$; however, this is an approximation valid only in the small a, q^2 limit. Therefore, higher order terms in the expansion of β_i become important when examining the stability diagram near

$\beta_i \lesssim 1$. Taken from [Major 05], β_i is given by the continued fraction expression:

$$\beta_i^2 = a_i + f_i(\beta_i) + f_i(-\beta_i)$$
$$f_i(\beta_i) = \frac{q_i^2}{(2+\beta_i)^2 - a_i - \frac{q_i^2}{(4+\beta_i)^2 - a_i - \cdots}}. \tag{3.8}$$

One can plot stability diagrams in the $a - q$ plane for which motion in both the x and y directions is stable simultaneously. In practice, however, having the axial trap frequency ω_z less than the radial trap frequencies ω_x and ω_y and having the radial trap frequencies much less than $\Omega_T/2$ results in stable ion motion. Furthermore, under these conditions, the micromotion amplitude is small (small q_i), and chains of ions will align along the axis of the trap ($\omega_z \ll \omega_{x,y}$).

Examining Eq. (3.6), the radial motion (say x motion) of the ion is slow secular motion at a frequency ω_x modulated at the RF drive frequency Ω_T. Consequently, the motional frequency spectrum contains frequencies ω_x and $\Omega_T \pm \omega_x$. The higher order terms in the Floquet solution have frequencies at $n\Omega_T \pm \omega_x$, n an integer. Therefore, noise at the RF drive frequency will not drive the ions motion. However, electrical noise at $\Omega_T \pm \omega_x$ will parametrically drive the ions motion. The situation changes when a stray electric field in the radial direction exists. The ion finds a new equilibrium position where the force from the stray field is balanced by the force induced by the pseudopotential. The motion of the ion in the x direction is modified to the following:

$$x = [A_x \cos(\omega_x t + \phi_x) + \Delta x_{\text{stray}}](1 + \frac{q_i}{2}\cos\Omega_T t) \tag{3.9}$$

where $\Delta x_{\text{stray}} = \frac{qE_x^{\text{stray}}}{m\omega_x^2}$ is the displacement induced by the stray field. Here, we see that the ion has motion at the RF drive frequency. Fortunately, this motion is separable from the secular motion, and coupling of the RF drive energy into the secular motion should not occur except when mediated by collisions.

Micromotion reduces the efficiency of Doppler cooling and state dependent resonance fluorescence. Consider resonance fluorescence of an ion with micromotion momentarily. In the ion's reference frame, the resonant laser will appear to be modulated at the RF drive frequency Ω_T and will consequently have sidebands at Ω_T due the Doppler effect. For typical RF drive frequencies near 100 MHz, these sidebands are outside of the natural line width of the cycling transition (19.4 MHz) and negligibly contribute to the scattering rate. Therefore, the intensity on resonance in the ion's reference frame is reduced limiting the efficiency of resonance fluorescence. Furthermore, when using state-dependent resonance fluorescence for qubit measurement (a transition involving one qubit eigenstate is on-resonance hence the state is "bright", whereas transitions involving the other qubit eigenstate are off-resonance hence the state is "dark"), some of the sidebands are closer to resonance to optical pumping transitions out of the dark state increasing the probability of repump error (see § 2.4). Micromotion can be minimized by applying external static fields to compensate for stray fields. Because the resonant scattering rate decreases with micromotion, we can use measurements of the scattering rate to minimize micromotion.

Another novel technique for minimizing micromotion exists when trapping two ions of different mass [Barrett 03]. Because the pseudopotential is mass dependent, the displacement from the RF null along the axis is also mass dependent. In the presence of a stray electric fields, a two-ion crystal of different masses will tilt with respect to the trap z-axis. This couples the radial and axial modes, and the axial mode spectrum is modified. By observing the axial mode spectrum while applying compensating electric fields, the stray fields and the micromotion can be eliminated.

The analysis of the ion motion so far has been for a classical charged particle. The quantum dynamics can be included in the pseudopotential approximation by simply transforming to the quantum harmonic oscillator with Hamiltonian $H_{\text{osc}} = (a^\dagger a + \frac{1}{2})\hbar\omega_i$ for $i \in \{x, y, z\}$ where a and $a^\dagger$ are the quantum harmonic oscillator annihilation and creation operators respectively. The ion's position and momentum operators for a particular mode i with frequency ω are expressed as $x = x_0(a^\dagger + a)$ and $p = p_0(a^\dagger - a)$ where $x_0 \equiv \sqrt{\hbar/(2m\omega)}$ and $p_0 \equiv i\sqrt{\hbar m\omega/2}$. In the z-direction, the potential is harmonic to a very good approximation, and transforming the quantum harmonic oscillator is well substantiated. However, transforming to the quantum harmonic oscillator for the ion's radial motion which classically is described by Floquet solutions is less clear. This problem has been extensively studied theoretically [Major 05, Leibfried 03, Ghosh 95, Brown 91, Stenholm 92, Gheorghe 92, Schrade 95, Nieto 00, Gheorghe 00, Bardroff 96]. In the small a and q limit (a here is the parameter in the Mathieu equation and *not* the harmonic oscillator annihilation operator), Bardroff [Bardroff 96] and Kielpinski [Kielpinski 01] show that the ion's motion can be described by a quantum harmonic oscillator with oscillating squeezing at the RF drive frequency. In practice, this "breathing" motion changes somewhat an ion's interaction with laser beam electric fields; this effect can be compensated in the determination of Rabi rates, etc.

In the context of quantum information processing, we isolate a single axial mode along the z-axis which is well described by the quantum harmonic oscillator. The motion is only involved during two-qubit gates (see § 2.6) which involves coherently displacing the ion wave packet around in phase space conditioned on the ions' internal states. After the completion of the gate, the motional mode's wave packet is restored to its original location in phase space. Because the z-axis motion is not affected by the RF motion, we neglect the full quantum dynamics of the Mathieu equation. The interested reader is referred to the references.

3.1.2 Gold Plated Alumina Wafer Trap

The ion trap used for the experiments of this thesis is shown in Fig. 3.2. It was constructed from two identical gold plated alumina wafers. The lower wafer is rotated about the trap axis by 180° such that the RF electrodes reside at two opposite corners of the four-rod quadrupole configuration in Fig. 3.1. The wafers are spaced by 200 μm thick alumina wafers. A "bias" board with a 0.6×4.4 mm slot to allow laser beam access is placed 400 μm from the back trap wafer using alumina spacers. Application of a DC potential to the bias board gives the experimenter control over the principle axes of the radial modes. To eliminate Be plating of the experimental trap zones, a “mask” board with two holes cut in it to allow laser beam access to all trapping regions and neutral Be access to the load trap is placed 1.5 mm from the bias board using alumina spacers. The eight control electrodes provide six different trapping regions, and ions can be shuttled between these regions by application of time-varying potentials to the control electrodes. The larger volume trap residing over electrode 2 (trap 2) is used for loading and hence is termed the load trap. Experiments where shuttling was not required typically used the trap residing over electrode 5. Separation of ions occurs over electrode 6 as its small width of 100 μm provided the narrowest potential wedge for separation, and thereby minimized heating of the ions during the separation process.

The RF filter board provides low pass filtering for the control electrodes from their source voltages using a first order RC circuit. The 820 pF capacitors also serve as RF shorting capacitors to ground, and consequently, the control electrodes serve as an RF ground.

The RF potential is provided by a quarter wave cylindrical unterminated transmission line which acts as a step-up transformer for the RF input. The RF input is coupled into the resonator inductively [Jefferts 95]. With a resonator Q in the few hundreds, we obtain RF potentials of a few hundred volts with input RF powers of a few watts. This provides radial confinement of the ions with trap frequencies $\sim$ 15 MHz. The control electrode potentials are provided by digital to analog converters in the few volts range which provides axial confinement of the ions with trap frequencies in the 3—5 MHz range.

The trap is loaded from a neutral ^{9}Be source via electron-bombardment. Neutral ^{9}Be wire is wrapped around a tungsten filament which when heated sublimates neutral ^{9}Be. The ^{9}Be source, termed the “Be oven”, is resistively heated with $\sim$ 1 A of electrical current. The neutral Be is ionized in the trapping region by electron bombardment with

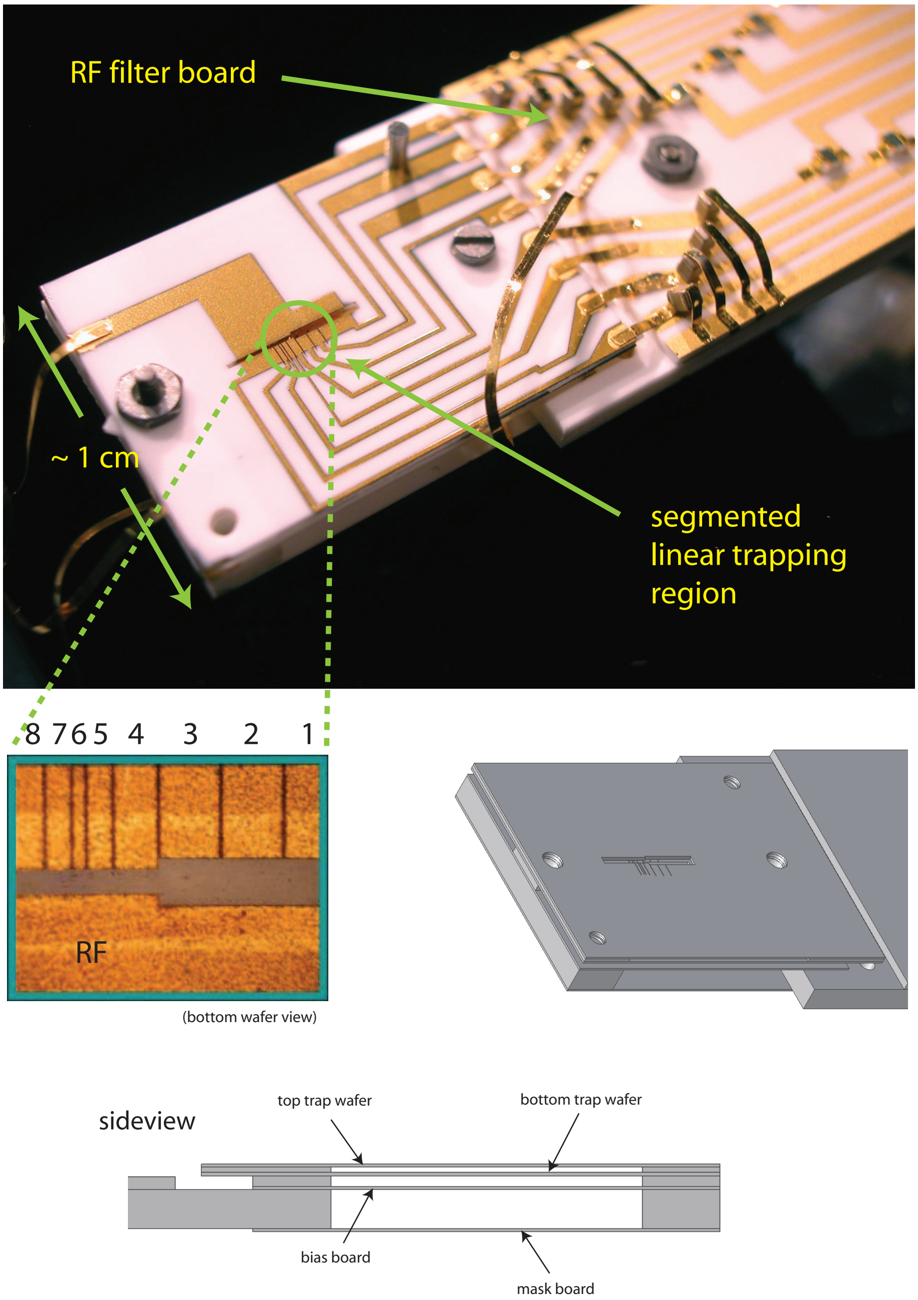

Figure 3.2: Gold plated alumina wafer trap. The trap has 8 control electrodes and 1 RF electrode per wafer. The control electrodes are numbered from left to right from 1 to 8. Trapping over electrode 2 (trap 2) is termed the load trap, and trap 5 is typically termed the experiment trap. The width of the (j^{th}) control electrode is: (2) 500 μm, (3) 500 μm, (4) 360 μm, (5) 200 μm, (6) 100 μm, (7) 200 μm. The spacing between the nearby edges of adjacent electrodes is 20 μm.

the "electron gun." The electron gun is constructed out of a thorated tungsten filament which is biased at −80 V with respect to ground. Applying ~ 1 A electrical current to the electron gun resistively heats the filament until the thermal energy of the electrons surpasses the work function and ejects electrons from the surface. Once free from the filament, the electrons are accelerated through the 80 V potential towards the trapping region bombarding the neutral Be atoms creating ions. When ions are created within the capture range of the trap, they become trapped. Upon Doppler cooling, the ions form cold crystals which are easily seen with the imaging system.

3.2 Magnetic Field Coils

A schematic of the trap apparatus, nearby optics, and the magnetic field coils are shown in Fig. 3.3. The magnetic field coils shown in Fig. 3.3 provide the 0.01194 T magnetic field required for field-independent qubits (see § 2.2 and Ch. 4). Nine turns of hollow 1/8 inch outer diameter copper refrigerator tubing are wound around a cylindrical aluminum coil form of 3.725 inch radius. The planes of two coils of this type are placed 0.5 inches away from the ion position and placed symmetrically about the ion. Because the coils require ~ 100 A of current to generate the 0.01194 T magnetic field generating ~ 500 W of heat, the coils were water cooled. The turns of the coils were insulated from each other by wrapping the copper tubing in heat shrink tubing prior to winding it on the mount.

3.3 Optics

There are three laser systems used for quantum information processing with $^9\mathrm{Be}^+$. These generate light for the three beam lines: (1) the "blue Doppler (BD) line", (2) the "red Doppler (RD) line", and (3) the "Raman line". The wavelength of these lasers is 313 nm. We generate the 313 nm radiation using three ring dye lasers at 626 nm and frequency double the light to 313 nm using resonant BBO doubling cavities. The

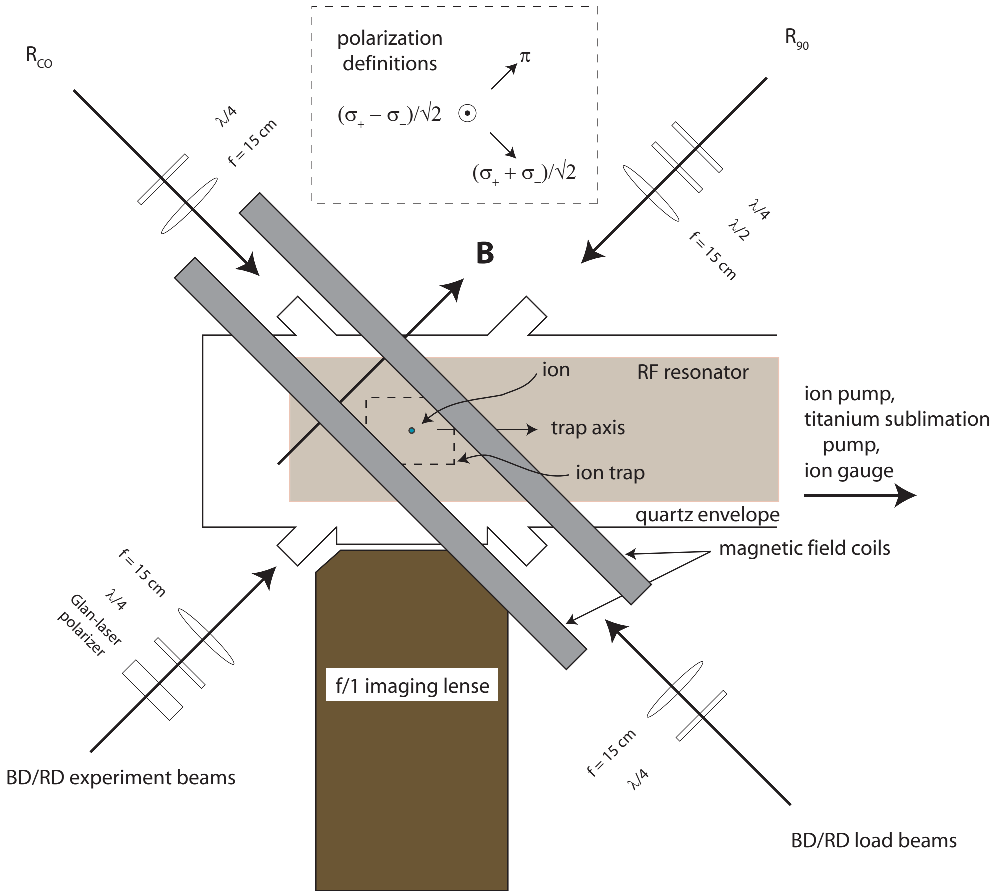

Figure 3.3: Optical system near the ion trap. Ion fluorescence is collected by the $f/1$ imaging lens. Magnetic field coils provide the 0.01194 T field required for field-independent qubits. The Raman beams R_{CO} and R_{90} propagate perpendicular and anti-parallel to the magnetic field such that the difference $\vec{k}$-vector $\overrightarrow{\Delta k}$ lies along the trap axis. The BD and RD beam lines propagate along the magnetic field and are polarized $\hat{\sigma}_+$. R_{CO} is circularly polarized such that its polarization is $\hat{\epsilon}_{\mathrm{CO}} = \frac{1}{2}(\hat{\sigma}_+ - \hat{\sigma}_-) + \frac{i}{\sqrt{2}}\hat{\pi}$. The R_{90} beam is horizontally linearly polarized, namely $\hat{\epsilon}_{90} = \frac{1}{\sqrt{2}}(\hat{\sigma}_+ + \hat{\sigma}_-)$. The BD load beam is circularly polarized.

frequencies of the three lasers are depicted in Fig. 3.4. The "BD line" consists of the "BD" and "BD detune" beams which are near resonant with the $S_{1/2} \leftrightarrow P_{3/2}$ transition frequency (D2 line, wavelength 313.13 nm). The "RD line" consists of the "RD" and "repumper" beams which are near resonant with the $S_{1/2} \leftrightarrow P_{1/2}$ transition frequency (D1 line, wavelength 313.20 nm). The "Raman line" beams are off-resonant from both the $S_{1/2} \leftrightarrow P_{3/2}$ and $S_{1/2} \leftrightarrow P_{1/2}$ transition frequencies and typically are detuned $\sim$ 80 GHz blue of the D1 line. The detuning of the Raman laser from the $P_{1/2}$ and $P_{3/2}$ levels affects the speed of gate operations as well as the probability of spontaneous scattering (see Ch. 5). Because the BD and RD lines are resonant with the D2 and D1 lines in $^9\text{Be}^+$, their absolute frequencies are stabilized to molecular absorption lines in I_2 using saturated absorption spectroscopy [Preston 96]. The Raman laser, however, is not stabilized to an atomic reference as its relatively small slow frequency drift[1] only affects the detuning of the laser and not the difference frequency between the Raman beam pairs. All of the dye lasers are frequency stabilized to external optical reference cavities by measuring polarization changes of the laser reflected from the cavity [Hansch 80]. In addition, the resonant BBO doubling cavities are locked to resonance with the laser frequencies using the same technique [Hansch 80].

3.3.1 Imaging System

A schematic of the trap apparatus and nearby optics is shown in Fig. 3.3. During qubit measurement (see § 2.4), ion fluorescence is collected through an $f/1$ imaging lens and projected onto either a photon counting camera or a photo-multiplier tube as selected by an electronic flipper mirror. When imaged on the camera, the ion fluorescence is shown as a picture on an oscilloscope. When imaged on the PMT, the photons are counted by the FPGA-based experiment controller (see § 3.4). The optics of the imaging system consists of an $f/1$ objective lens placed approximately 40 mm

---

[1] The Raman laser frequency is stable to within a few hundred MHz over many hours.

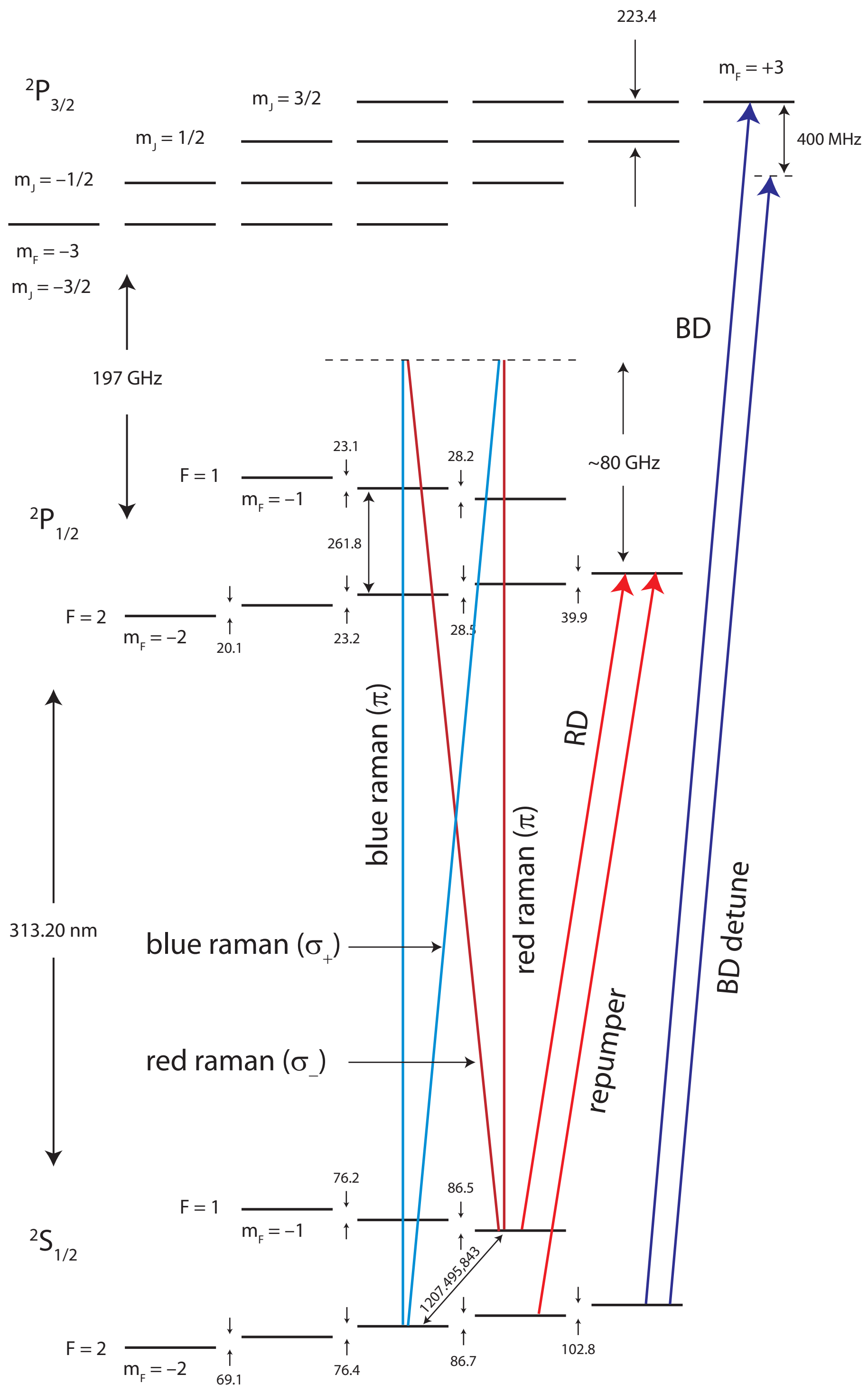

Figure 3.4: Laser frequencies and $^9\mathrm{Be}^+$ levels. Numbers are in units of MHz except where marked.

from the ion which provides $\sim 5\times$ magnification. The objective images the ion at the location of a 600 μm diameter aperture after which a second-stage lens provides another $\sim 25\times$ magnification of the first image. The total magnification of the imaging system is ~ 125. The 600 μm aperture at the location of the first image reduces stray light since, to a high degree, only light originating from the object plane passes through the aperture. In addition, another iris is used as a second aperture at the second image near the PMT/camera to mask stray light other than the ion signal, particularly light scattered from nearby ion trap electrode surfaces. With this system, we typically could achieve ion fluorescence signal to background ratios of over 100.

3.3.2 Blue/Red Doppler Beam Lines

The beam lines enter the ion trapping region through four optical ports in the trap apparatus (see Fig. 3.3). The BD/RD experiment beams propagate along the magnetic field direction and are circularly polarized $\hat{\sigma}_+$. This allows BD to perform Doppler cooling and state-dependent resonance fluorescence on the cycling transition $|^2S_{1/2}, F = 2, m_F = 2\rangle \leftrightarrow |^2P_{3/2}, F = 3, m_F = 3\rangle$. The BD laser power is set such that the intensity at the ion is half of the saturation intensity. With a beam waist of ~ 30 μm, the BD laser power is ~ 0.5 μW. The BD detune beam is a higher power laser beam (~ 500 μW) tuned to the red of the BD beam by ~ 400 MHz. This provides efficient Doppler cooling of very hot ions whereas the relatively small detuning and intensity of the BD beam provides little cooling for hot ions. The BD detune beam is also used for loading for the same reason. During the loading process, the ions are created via electron bombardment of hot neutral atoms, and a red-detuned high power laser beam assists in cooling these ions considerably. For this reason, the BD detuned beam is detuned by another 500–1000 MHz to the red during loading. Because the trap's loading region and experimental region reside in different locations, we found it useful to send the BD detuned beam through another optical port into the loading region such that the experiment beam and loading beam did not have to be moved every time we needed to load another ion (see "BD/RD load beams" in Fig. 3.3). The load beam is circularly polarized. During the loading process, the magnetic field is turned off such that the load beam's $\vec{k}$-vector provides the quantization axis. This establishes a cycling transition when the load beam is circularly polarized.

The BD beam line is shown in Fig. 3.5. The BD dye laser at 626 nm is doubled in a resonant BBO doubling cavity where the UV light exits vertically polarized. The beam is split using the "BD split" AOM establishing the separate "BD" and "BD detune" beams of the BD beam line. The $+1^{\text{st}}$ order of the BD split AOM is sent to the "BD SW" (BD switch) double-pass AOM after which it is recombined with the BD detuned beam at the "BD detuned SW" (BD detuned switch) AOM. The BD and RD lines are then combined on a 50/50 beam splitter prior to the combined BD/RD beam lines being split into the "BD/RD load beams" and the "BD/RD experiment beams" which enter the trapping regions from the lower two optical ports in Fig. 3.3. This optical configuration allows for a frequency scannable resonant BD beam and a non-frequency scannable 400 MHz red detuned BD detune beam. The double-pass BD SW AOM allows for the BD beam to have its frequency changed during a single experiment from on resonance for state-dependent resonance fluorescence (see § 2.4) to red detuned by half of the excited state line width for optimum Doppler cooling. Furthermore, the optical system allows for the BD and BD detuned beams to be applied individually or together independently. Alternate optical configurations exist. For example, the BD detuned SW could be rotated such that the -1^{st} order was used rather than the $+1^{\text{st}}$ order. This would create an 800 MHz frequency difference between the resonant BD beam and the BD detuned beam which may help even more in cooling very hot ions after collisions with thermal background gas. Furthermore, because the optical power of the BD beam is a few orders of magnitude lower than the BD detuned beam, the BD split AOM could be replaced with a 90/10 beam splitter or a piece of glass with 4%

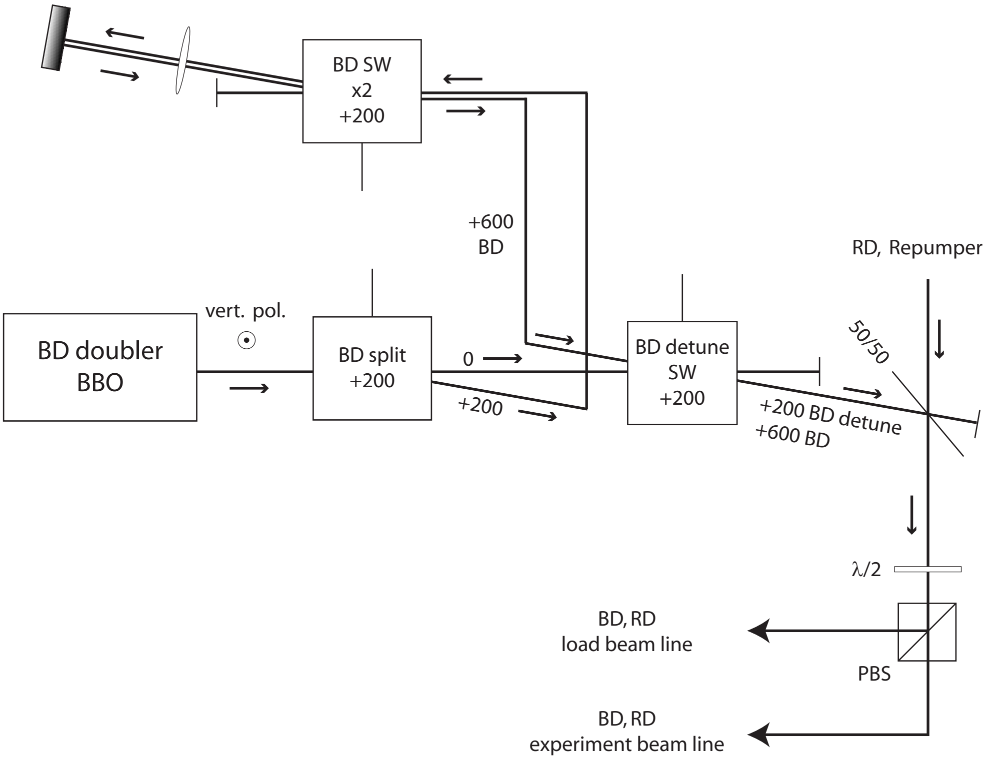

Figure 3.5: Blue Doppler (BD) beam line. The two beams in the BD beam line ("BD" and "BD detune") are generated with three AOMs. The "BD split" AOM sends light to the "BD SW" double pass AOM setup. The BD beam is combined with the BD detune beam on the "BD detune SW" AOM forming the "BD beam line". The beam line is combined with the Red Doppler (RD) beam line prior to being sent to the trap at two different optical ports (see Fig. 3.3).

reflectivity. Combining these two alterations would establish a BD detuned beam with a frequency 600 MHz red of the BD beam frequency. Lastly, we found in the robust quantum memory experiment (Ch. 4) that BD detuned leakage light caused a systematic Stark shift of the qubit transition. Optical shutters were used for the long-coherence time measurement; however, the BD detuned SW AOM could be double-passed to reduce scattered light. For long experiments such as measuring a 15 second coherence time, optical shutters are appropriate. However, for quantum information processing experiments where the entire experiment may last only a few milliseconds, the long delays and slow repetition rates of optical shutters are a limiting factor, and configuring the BD detune SW as a double-pass AOM may be advantageous. Removing the BD split AOM and converting the BD detune SW into a double-pass using the -1^{st} order creates two beams separated in frequency by 800 MHz.

The RD beam line optical setup is shown in Fig. 3.6. The two beams of the RD beam line are the "RD" beam and the "repumper" beam. These two beams are separated in frequency by the $|^2S_{1/2}, F = 2, m_F = 1\rangle \leftrightarrow |^2S_{1/2}, F = 1, m_F = 1\rangle$ transition frequency of 1120 MHz. The RD beam is resonant with the $|^2S_{1/2}, F = 1, m_F = 1\rangle \leftrightarrow |^2P_{1/2}, F = 2, m_F = 2\rangle$ transition frequency, and the repumper beam is resonant with the $|^2S_{1/2}, F = 2, m_F = 1\rangle \leftrightarrow |^2P_{1/2}, F = 2, m_F = 2\rangle$ transition frequency. The frequency different of 1120 MHz is generated with two 636 MHz AOMs and another 152 MHz AOM. The reason the 1120 MHz frequency difference is not generated by two AOMs at 560 MHz is for compatibility of the optical system with the $^{27}\mathrm{Al}^+$ clock experiment sharing the same laser systems. The $^{27}\mathrm{Al}^+$ clock experiment uses a $^9\mathrm{Be}^+$ ion as a refrigerant at near zero magnetic field and requires the RD and repumper beams to be separated by 1272 MHz, corresponding to the difference frequency between the $|^2S_{1/2}, F = 2, m_F = -1\rangle$ and $|^2S_{1/2}, F = 1, m_F = -1\rangle$ states of $^9\mathrm{Be}^+$ at low magnetic field. The dashed lines in Fig. 3.6 show the $^{27}\mathrm{Al}^+$ clock experiment RD beam line; removable mirrors are inserted between the two 636 MHz AOMs to route the beam through the 152 MHz AOM such that our experiment has the correct difference frequency. The repumper and RD beams are combined on the +636 MHz AOM. The "RD SW" double-pass AOM provides a global frequency scannable offset and acts as an optical switch. The RD and repumper beams are combined with the BD beam line on a 50/50 beam splitter prior to being sent to the BD/RD experiment beams and BD/RD load beams (see also Figs. 3.5 and 3.3).

The RD beam line polarization at the position of the ions is $\hat{\sigma}_+$ similar to the BD line (see Fig. 3.3). This polarization allows the RD and repumper beams to perform near recoilless optical pumping of the ion to the stretched $|^2S_{1/2}, F = 2, m_F = 2\rangle$ state through the $^2P_{1/2}$ manifold. The optical pumping is recoilless (in the Lamb-Dicke limit) in the sense that the stretched $|^2S_{1/2}, F = 2, m_F = 2\rangle$ state is a dark state for the optical pumping process and the probability of scattering from $|F, m = 1\rangle$ with motional Fock state $|n = 0\rangle$ to $|F = 2, m_F = 2\rangle|n = 1\rangle$ is η^2 where η is the Lamb-Dicke parameter (see § 2.5.4). In contrast, if BD was used for optical pumping out of the $|F, m_F = 1\rangle$ states, after scattering into the stretched $|F = 2, m_F = 2\rangle$, the ion would scatter many photons on the cycling transition and equilibrate back to the Doppler temperature ($\langle n\rangle \simeq 3$).

3.3.3 Raman Beam Line

The Raman beam line is shown in Fig. 3.7. After exiting the doubler, the beam passes through a spatial filter of diameter 75 μm which is used more as an alignment tool rather than an optical mode filter due to the presence of the optical fibers later in the beam line. At the magnetic field-independent point (0.01194 T), the transition frequencies between different m_F states within the same F manifold are not degenerate and span the range of 69—103 MHz. We generate two beams with difference frequencies in this range by using two high-bandwidth deflector AOMs in a double-pass configuration which operate in the frequency range of 160—240 MHz ("R-90" and "R-CO" in Fig. 3.7). The difference frequency between these two beams can be set to any fre-

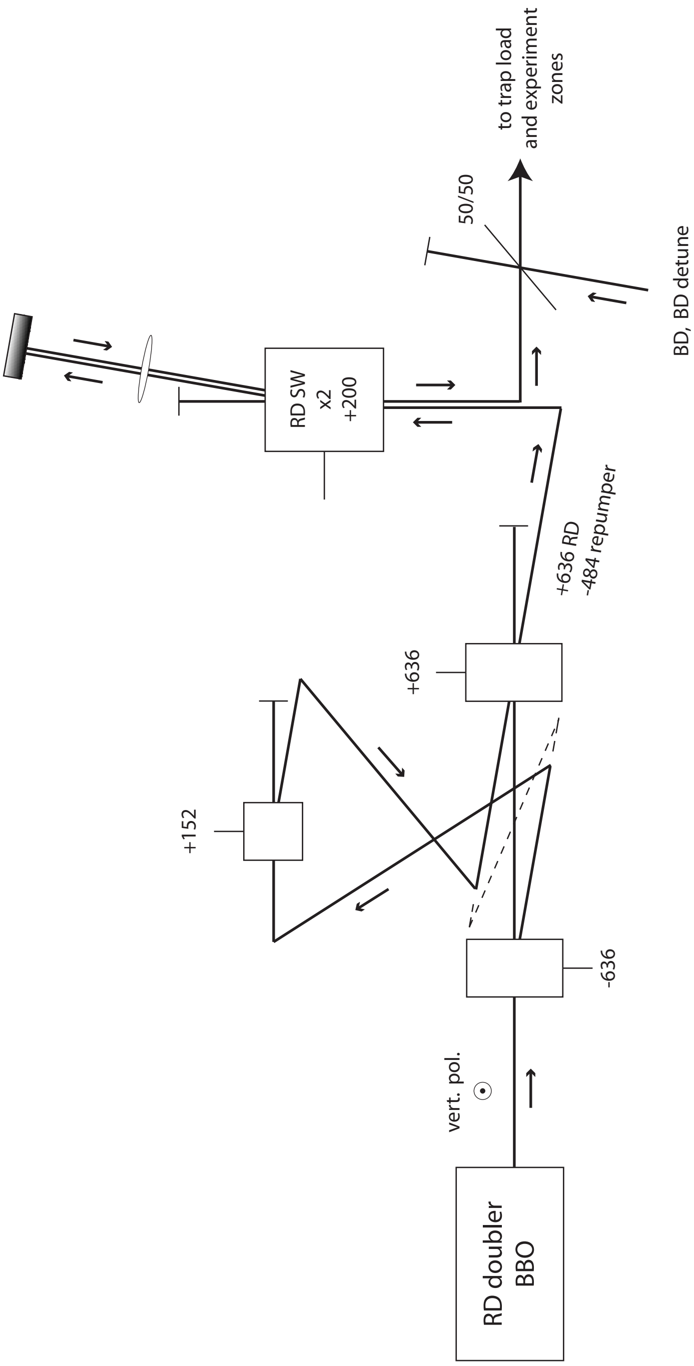

Figure 3.6: Red Doppler (RD) beam line. The RD beam line consists of the “RD” beam and the “repumper” beam separated by 1120 MHz. The dashed line shows the beam path used by the ^{27}Al^{+} clock experiment. Removable mirrors direct the beam through the 152 MHz AOM such that we have the frequency difference needed at 0.01194 T. The RD SW AOM is frequency scannable. The beam line is combined with the Blue Doppler (BD) beam line prior to being sent to the trap at two different optical ports (see Figs. 3.3 and 3.3).

quency in the range from 0 to 160 MHz. The outputs of these two AOMs form the R_{CO} and the R_{90} beam lines entering the trap from the upper two optical ports in Fig. 3.3. Using just these two AOMs, we can perform co-carrier rotations, 90°-carrier rotations, sideband cooling, and Z-phase two-qubit gates between pairs of states within the same F manifold (see § 2.5). Co-propagating carrier (co-carrier) rotations are performed by sending two frequency components to the R-CO AOM. For example, sending 175 MHz and 226.4 MHz to the R-CO AOM will generate two laser beams with a difference frequency of 102.8 MHz co-propagating at 90° to the magnetic field vector and can drive the $|F=2, m_F=2\rangle \leftrightarrow |F=2, m_F=1\rangle$ transition.

The two AOMs R-CO and R-90 are not sufficient to drive F-changing transitions, however. In particular, the field-independent qubit transition $|F=2, m_F=0\rangle \leftrightarrow |F=1, m_F=1\rangle$ at 1207 MHz is of this type. To generate frequency differences spanning the F-changing transition frequency range of 1018—1516 MHz, we use the ΔF AOM which operates over the range of 500—740 MHz[2] . The ΔF AOM configuration double-passes both the 0^{th} order and the $+1^{\mathrm{st}}$ order such that after the double-pass, there exist two co-propagating laser beams with a difference frequency twice that of the AOM frequency. The lens makes both beam paths after the first pass through the AOM parallel such that they can reflect off a common retro reflecting two-mirror apparatus. The two-mirror vertical retro reflector serves to provide a vertical displacement of the retro reflected beam relative to the incoming beam. After the retro reflected beam passes through the lens, the vertical displacement is converted into an angular change such that the returning beam intersects the original beam directly at the acoustic wave focus of the AOM maximizing the diffraction efficiency through the second pass of the AOM. This is a common optical arrangement for a double-pass AOM. All of the 200 MHz double-pass

---

[2] The largest F-changing transition $|F=2, m_F=-2\rangle \leftrightarrow |F=1, m_F=-1\rangle$ near 1516 MHz falls outside the double-passed range of the ΔF AOM; however, we may be able to drive this transition at the expense of less AOM efficiency. We have not tried this in the lab, and in practice, there is no foreseeable need.

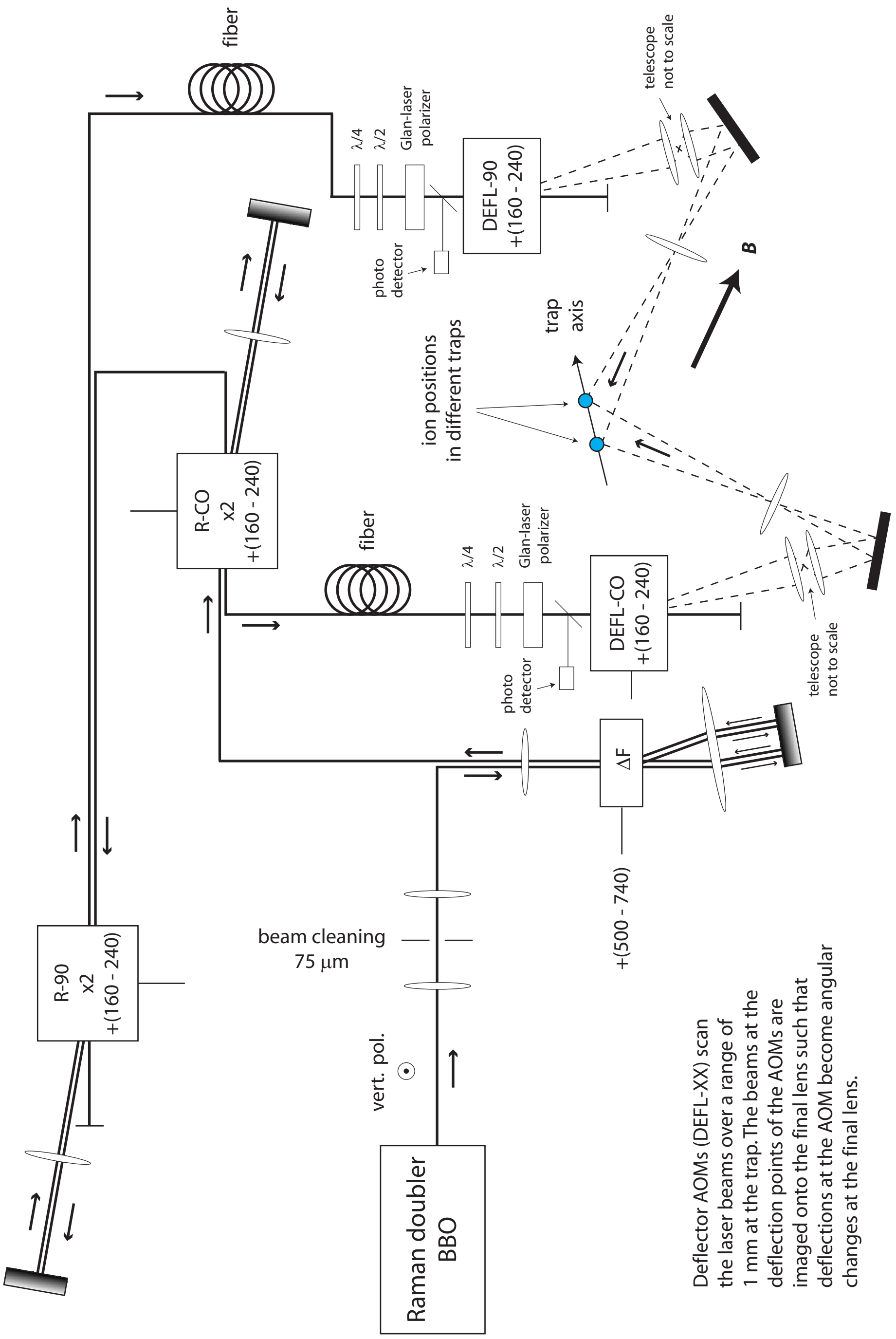

Deflector AOMs (DEFL-XX) scan the laser beams over a range of 1 mm at the trap. The beams at the deflection points of the AOMs are imaged onto the final lens such that deflections at the AOM become angular changes at the final lens.

Figure 3.7: Raman beam line. Both the 0^{th} and the $+1^{\text{st}}$ orders of the ΔF AOM are double-passed generating two laser frequencies differing by 1000 — 1480 MHz spanning the large range of F-changing transition frequencies in $^9\text{Be}^+$ at 0.00194 T. The deflector AOMs (DEFL-CO and DEFL-90) move the beams across a range of 1 mm at the trap. The wide bandwidth of the R-CO and R-90 AOMs allow a difference frequency between the two beams from 0 up to 160 MHz spanning all m_F changing transition frequencies within the same F manifold.

AOM configurations use right angle prisms to provide vertical retro reflection. Because we require very good overlap of the second pass 0^{th} order with the second pass $+1^{\text{st}}$ order in the ΔF AOM, we used two separate mirrors mounted at $\pm 45^\circ$ with respect to the horizontal with their normal vectors in the plane of laser beam travel. This provided the additional degrees of freedom to simultaneously maximize the second pass diffraction efficiency and 0^{th} order/$+1^{\text{st}}$ order beam overlap. The lens on the incoming beam to the ΔF AOM focuses the laser to ~ 80 μm at the AOM such that the beam fits within the AOM's acoustic focus of 100 μm. When performing rotations or two-qubit z-basis gates, the ΔF AOM is off, and the double-passed 0^{th} order propagates to the R-90 and R-CO AOMs. The insertion loss of the double-passed 0^{th} order beam when the ΔF AOM is off is less than 20%. When performing F-changing rotations or two-qubit Mølmer-Sørensen gates, the ΔF AOM is on.

Fibers are used on both R_{CO} and R_{90} beam lines to clean the optical spatial mode as well as provide some passive beam pointing stability. Because the polarization of the light exiting the fiber drifts over time, the polarization optics $\lambda/2$, $\lambda/4$ and a Glan-laser polarizer are placed at the exit of the fiber. Small bending of the fibers increases the optical loss, hence paddles could not be used to adjust the polarization. Instead, the $\lambda/4$ and $\lambda/2$ plates are rotated to optimize the laser power transmitted through the Glan-laser polarizer. Both polarization drift and beam pointing fluctuations at the entrance of the fiber translate into intensity fluctuations after the polarizer at the exit of the fiber. The intensities of the beams are sampled on photo detectors and fed back on the RF power of the R-90 and R-CO beams to stabilize the intensity after the fiber. The broadband deflector AOMs DEFL-CO and DEFL-90 provide beam steering capability. The deflection point of each of the deflector AOMs is imaged onto the center of the corresponding final lens using a telescope (not to scale in Fig. 3.7) such that beam steering operations with the AOMs translates into angular deviations at the corresponding final lens. The beams can span over 1 mm distance covering multiple trapping regions in the trap.

The polarizations of the R_{CO} and R_{90} beams is shown in Fig. 3.3. The co-propagating Raman beam line (R_{CO}) enters the trap from the upper-left optical port in Fig. 3.3, and its polarization is $\hat{\epsilon}_{\mathrm{CO}} = \frac{1}{2}(\hat{\sigma}_+ - \hat{\sigma}_-) + \frac{i}{\sqrt{2}}\hat{\pi}$. Because the two co-propagating Raman beams have the same polarization, the two beams are equivalent to a single laser beam with amplitude modulation. We require both $\hat{\pi}$ and $\hat{\sigma}_+/\hat{\sigma}_-$ polarization components to drive transitions with $\Delta m_F = 1$. For linear polarized amplitude modulated light with both $\hat{\pi}$ and $\hat{\sigma}_+/\hat{\sigma}_-$ components (generated, for example, by a linear polarization at 45° with respect to the vertical), the Rabi frequency contains two terms which destructively interfere suppressing the Rabi frequency. However, by adding a phase shift of $\pi/2$ to the $\hat{\pi}$-polarized beam with respect to the $(\hat{\sigma}_+ - \hat{\sigma}_-)/\sqrt{2}$ component, the two terms in the calculation of the Rabi frequency constructively interfere. We establish this polarization scheme by introducing the $\lambda/4$ plate in the R_{CO} beam path. The polarization of the R_{90} beam is nominally horizontally linearly polarized; the $\lambda/2$ plate is used to rotate the vertical polarized beam to this configuration. The differential Stark shift of non-field-independent transitions induced by linear polarized light, although suppressed, is not zero. We can tune the differential Stark shift to zero by adding a small elipticity to the beam. The $\lambda/4$ plate is used for this purpose.

Because the phase of qubit superpositions is measured relative to the difference phase between the two Raman beams, it is important to have good relative phase stability between the two beams in the co-propagating Raman pair. In the Raman beam line depicted in Fig. 3.7, the Raman beam pair for the field-independent qubit is generated at the ΔF AOM. After the ΔF AOM, the beams are co-propagating; therefore, any phase noise such as index of refraction changes in air or optical path fluctuations, is common to both beams, and the differential phase is unaffected to a high degree. However, the path of the two beams is not co-propagating between the ΔF AOM and the retro reflecting mirror setup. To reduce differential phase fluctuations, the beam paths where the two beams are physically separated is kept as small as possible. In our setup, the beams traverse different paths for only 20 cm. Throughout these paths, the two beams are separated horizontally by approximately 1 mm and travel through the same optical elements in the hopes that vibrations in the optical elements and index changes in the air will be mostly common mode. In addition, a box is placed over the AOM/lens/mirror setup to reduce air currents and differential beam pointing fluctuations. We measured the phase noise between the two beams by optical heterodyne detection followed by rf homodyne measurement to obtain a signal proportional to the phase difference between the two beams. The phase was passively stable to within 0.05 radians rms for minutes with zero detectable drift. In principle, the optical heterodyne/rf homodyne measurement scheme could be used to feedback on the phase of the ΔF AOM and achieve even lower phase noise.

3.3.4 Electro-Optic Raman Beam Line

The long coherence time measurements in Ch. 4 used a different Raman beam line. There was no need for sideband cooling or coupling the internal states of the ion to its motion. Therefore, a single laser beam was used entering the trap through the R_{CO} port (see Fig. 3.3). As discussed in the previous paragraph, the two beams of a co-propagating Raman beam pair can cause phase noise on qubit superpositions if the beams are physically separated over a finite distance. For the long coherence-time experiment, we required very high phase stability between the Raman beam pairs, and we accomplished this by using the electro-optic modulator (EOM) based Raman beam line shown in Fig. 3.8. The two radio-frequency (RF) EOMs at 1.018 GHz and 1.207 GHz respectively phase modulate the horizontal polarization component while leaving the vertical polarization component free of modulation. These frequencies drive the $|F = 2, m_F = 2\rangle \leftrightarrow |F = 1, m_F = 1\rangle$ and $|F = 2, m_F = 0\rangle \leftrightarrow |F = 1, m_F = 1\rangle$ transitions in $^9\mathrm{Be}^+$. The 45° Z-cut KD*P crystal orientation which allows this type of modulation also has static birefringence which gives a relative phase retardation between the horizontal and vertical polarization components of a few thousand π. The Rabi frequency with this scheme is proportional to $\sin\phi$ where ϕ is the retardation between the two polarization components. We compensated the static birefringence by measuring the retardation ϕ with a polarization analyzer similar to that in [Hansch 80] and fed back on the temperature of the birefringent KD*P crystal in the DC EOM (see Fig. 3.8). This stabilized the retardation ϕ to its optimal value of $\pi/2 \mod 2\pi$.

Even though the EOM scheme in Fig. 3.8 has the advantage that the two Raman beams (generated by the two polarization components of a single laser beam) are co-propagating and hence have a very small susceptibility to differential phase noise, we eventually switched to the AOM based scheme in Fig. 3.7 due to a number of problems with the EOM scheme. Because of the large capacitance of the KD*P crystal in the RF EOM (the dielectric constant of KD*P is $\sim 50\epsilon_0$), we could only achieve an oscillator Q of ~ 50 at the same resonance frequency. Consequently, over 10 W of RF power was required to achieve a phase modulation index high enough maximize the optical power in the first sideband. Our RF amplifiers which had a saturated output power of 7 W could not achieve this. Nevertheless, with 7 W RF power, we could not operate the EOMs at a duty cycle larger than 1.5% without suffering thermal lensing of the beam as it passed through the KD*P crystal. Because temperature changes in the KD*P crystal modified the birefringence of the crystal, such large impulses of energy deposited on the crystal made locking the retardation using temperature controllers very difficult. The only way we could operate these EOMs was to maintain a constant duty cycle throughout the experiment. We accomplished this with sophisticated software which would automatically insert extra EOM pulses during wait times and extra delays to maintain the constant duty cycle requirement. In practice, this was quite problematic, and after the long coherence time experiment was finished, we switched the optical setup to that in Fig. 3.7.

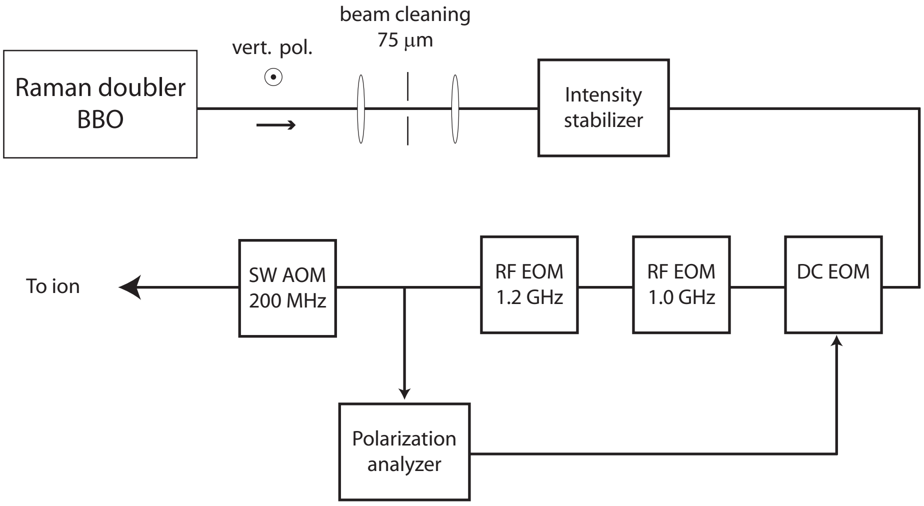

Figure 3.8: Raman beam line used in long coherence time measurement in Ch. 4. Two radio-frequency (RF) electro-optic modulators (EOMs) at 1.018 GHz and 1.207 GHz respectively phase modulate the horizontal polarization component while leaving the vertical polarization component free of modulation. The static birefringence of the EOMs is compensated with a polarization detector and feedback on the temperature of an additional birefringent KD*P crystal (DC EOM).

3.4 Experiment Control

Quantum information processing with trapped ions as described in this thesis requires the controllable interaction of modulated laser sources with the ions. The experimenter must control the frequency and phase of the modulation source as well as the duration of the laser pulse. In addition, a minimum of one measurement is performed every experiment as described in section 2.4. Some experiments require the application of classically conditioned quantum gates based on measurement outcomes [Barrett 04, Riebe 04, Chiaverini 04, Chiaverini 05]. This is particularly true for quantum error correction schemes where measurements of ancilla qubits yields information about what error, if any, occurred on the computational logic qubits. Such schemes are required for large-scale quantum information processing. To accommodate all of these necessary capabilities, I designed and built a field programmable gate array (FPGA) based experiment controller for use in quantum information processing experiments with trapped ions.

Throughout this section, many acronyms are used. The acronyms are defined at first use in the text as well as in Appendix A.

3.4.1 Introduction to Field Programmable Gate Arrays

Field programmable gate arrays (FPGAs) are reconfigurable digital logic devices. They consist of primitive components capable of generating arbitrary logic functions. The primitive components vary from device to device and may include logic blocks such as registers, look-up tables, shift registers, memory, buffer drivers, adders, multipliers, counters, multiplexers, and in some cases processors. It is possible to create an entire system on a chip including processor, memory, and input/output functionality. Because the designer has access to hardware-level components, the designs can be very fast (few nanoseconds delay) as compared to software running on a computer. FPGAs are completely reconfigurable. If the experimenter needs more functionality, he or she can implement the functionality by reprogramming the FPGA. At the time of this thesis, the two largest manufacturers of FPGAs are Xilinx and Altera.

Each of these manufacturers sell software tools to assist in the design and configuration of their FPGAs. For simpler designs, the designer can use schematic capture tools; however, for larger designs, this method becomes very cumbersome. Schematic capture tools allow the designer to draw the schematic in block diagram format interconnecting different modules with wires. More complicated designs are written using a Hardware Description Language (HDL). Using an HDL, the designer can write the design in a top-down modular format making the management of larger designs less complicated. The two most common HDLs are Verilog and VHDL[3] . I focus on VHDL in this work. The software tools sold by the FPGA manufacturers typically have both schematic capture and HDL design tools built into one integrated development environment.

VHDL is a high level text-based hardware description language. It was originally developed for hardware description and simulation and was later used for synthesis [Perry 02]. VHDL is a modular language allowing for top-down design with components. There are two types of statements in VHDL—concurrent statements and sequential statements. The designer uses concurrent statements to describe combinatorial logic (i.e. AND gates, multiplexers, etc.) and uses sequential statements to describe synchronous logic (i.e. counters, state-machines). I refer the reader to [Perry 02] for a VHDL tutorial and reference.

FPGA manufacturers and third party companies sell development and evaluation boards for FPGAs at a very reasonable price (few hundreds of dollars to few thousands of dollars). Typically included on these boards is external memory, input/output ports (i.e. RS-232, Ethernet, USB), and plug-in connectors for user daughter boards with

---

[3] VHSIC (Very High Speed Integrated Circuit) Hardware Description Language

general purpose I/O. Some boards have multiple fast high resolution analog-to-digital and digital-to-analog converters (ADCs, DACs) for use in digital feedback controllers. Such boards are in use in the experiments of Hideo Mabuchi at Caltech [Geremia 04, Stockton 02].

The design process consists of writing a hardware description in VHDL and verifying the design. This process is illustrated in Fig. 3.9. All of these steps can be performed using the software tools provided by the FPGA manufacturer. After describing the design in VHDL, the designer performs a behavioral simulation to verify the design's functionality. This is where the designer spends most of his or her effort. The behavioral simulator allows the designer to view all intermediate logic signals given some input logic stimulus. Separate components can be simulated independently allowing the designer to build large logic systems in a modular fashion. After the functionality is verified, the design is synthesized and implemented. During this phase, the hardware description written in VHDL is compiled into an optimized gate-level description using the primitive components of the particular device (multiplexers, look-up tables, etc.). The synthesis tool provides timing information and constraints such as gate delays and input setup time for the primitive components to be used during timing simulation. The designer, after timing simulation, may choose to rewrite parts of the hardware description in an attempt to optimize the speed and/or area of the design. All of these processes can occur without access to the physical hardware. After the timing simulation results are satisfactory, the final step is testing the design on actual hardware.

3.4.2 Introduction to Direct Digital Synthesis

Direct Digital Synthesis (DDS) is a technique for generating an analog signal source derived from a stable reference clock given a digital frequency input. Schematically, the DDS is broken up into two sections—the digital part and the analog part (see Fig. 3.10). The digital section consists of a digital phase accumulator and a sine

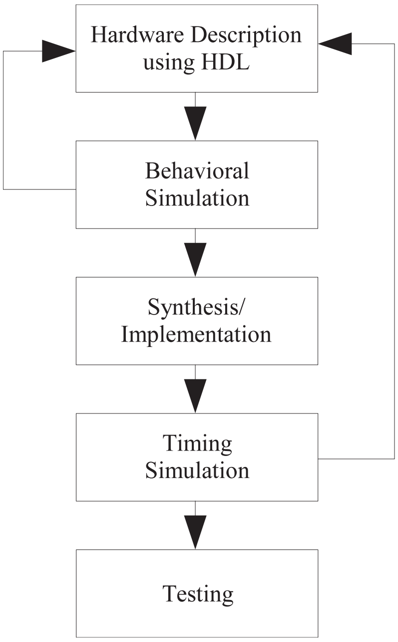

Figure 3.9: FPGA Design Flow.

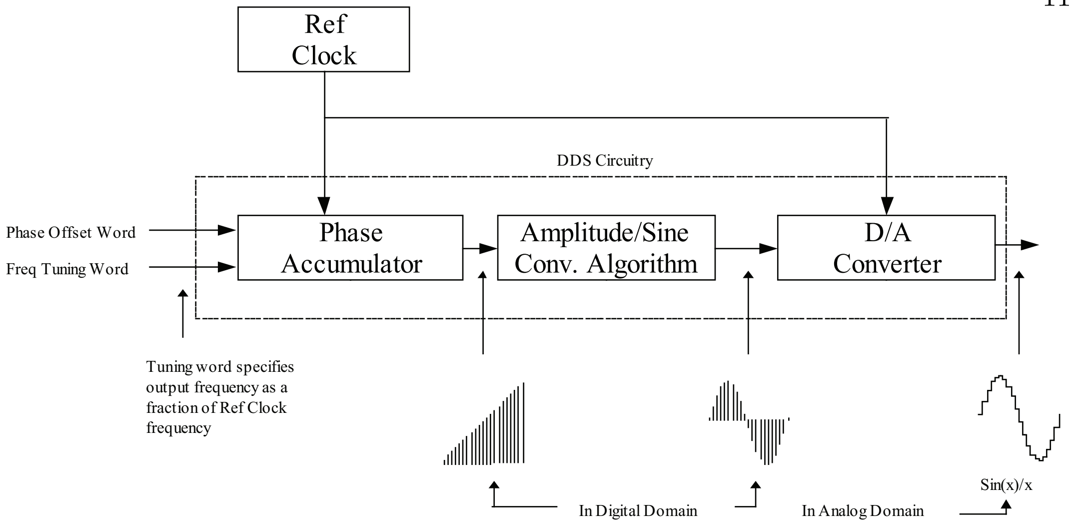

Figure 3.10: Block Diagram of a DDS. Figure taken from Analog Devices, *A Technical Tutorial on Digital Synthesis*, (1999).

look-up table. The phase accumulator simply ramps a digital phase word modulo its range (interpreted as 2π) at a rate proportional to the frequency tuning word input. The digital phase word is the phase written in binary, and the digital phase word range is 0 to $2^n - 1$ where n is the number of bits in the digital phase word. The phase offset word input is summed into the phase accumulator as well allowing the user to make fast phase changes. The output of the phase accumulator feeds the sine look-up table where the phase is converted into a digital amplitude. The digital amplitude is converted into an analog signal with a fast digital-to-analog converter (DAC) in the analog section. The output of the DDS is a sampled sinusoid, and with proper low-pass filtering, frequencies up to the Nyquist frequency (1/2 reference clock frequency) can be generated. DDS synthesizers are stand-alone integrated circuits and can easily be controlled by an FPGA.

DDS technology offers many advantages over more traditional frequency synthesis techniques such as phase locked loops (PLL). The DDS frequency is digitally tuned; therefore, the DDS has high accuracy, low frequency drift, low phase drift, and large frequency dynamic range. 32 bits of frequency resolution is common, and some devices have up to 48 bits. Furthermore, phase continuous frequency switching can be performed in a few reference clock cycles (tens of nanoseconds). Disadvantages of DDS technology are limited spectral purity, quantized DAC noise (equal to one least-significant bit), and the existence of image frequencies. (It is notable, however, that it is possible to band-pass filter the frequency images for higher frequency applications). At the time of this writing, devices with reference clock frequencies up to 1 GHz exist[4] , and agile frequency synthesis at higher frequencies can be achieved with the integration of PLL translation loop or divider loop circuits. However, frequency switching time for PLL circuits will be limited to the rise time of the loop filter. For fast frequency switching at high frequencies, single side band (SSB) modulation can be used.

3.4.3 Experiment Controller Design

The FPGA based experiment controller was designed to have variable duration digital output pulses, fast (sub-microsecond) frequency/phase switching, integrated photon counting input from a photo-multiplier tube (PMT), and the ability to branch the pulse sequence conditioned on measurement. To reduce memory requirements, support was added for subroutines and loops. The fast frequency/phase switching was accomplished by the FPGA controlling a shared communications bus (DDS Bus) used to program individual DDS modules. Each DDS module contained one Analog Devices AD9858 DDS.

The FPGA card used was the Xilinx XtremeDSP Kit. It contained one user programmable Virtex IV FPGA, 42 general purpose I/O pins, 2 14-bit 65 MSPS[5] ADCs, 2 14-bit 160 MSPS DACs, 512 kB[6] of off-chip memory, and an external clock

---

[4] Analog Devices AD9858. This device also has a 2 GHz analog mixer and 400 MHz phase-frequency detector with charge pump functional blocks for versatile PLL integration.

[5] Mega-samples per second

[6] kilobyte

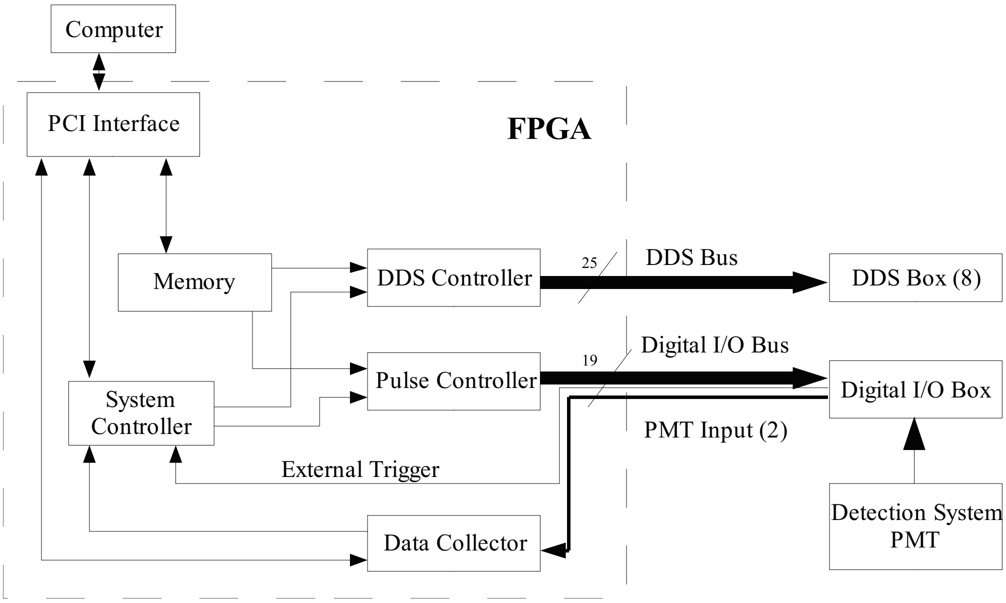

Figure 3.11: Block diagram of the experiment controller.

input. This card interfaces to a computer through the PCI[7] bus. The FPGA is programmed to interface to the Digital I/O Box and the DDS Box through the Digital I/O Bus and the DDS Bus respectively (see Section. 3.4.3.2). The Digital I/O Box has 16 digital output channels, 2 digital counter input channels, and 1 external triggering digital input. The DDS Box has 8 DDS modules, each of which can be individually controlled by the FPGA through the DDS Bus using module select addressing logic circuitry. Although the DDS Box contained only 8 modules, the DDS Bus was designed to control up to 32 DDS modules.

3.4.3.1 FPGA Design

A block diagram of the FPGA design is illustrated in Figs. 3.12, 3.13, and 3.14. The PCI_IFACE block coordinates communication between the computer and the FPGA. The FPGA card ships with software drivers (Nallatech FUSE library) which allows the programmer to perform simple operations on the FPGA such as resetting and reconfiguring the FPGA and performing read/write operations over the PCI bus. The FPGA card provides other digital circuitry (a smaller dedicated FPGA) to handle the PCI communications according to the PCI specifications and transfer the read/write information to the user FPGA in a well defined format (see [Nallatech 03] for details). The FPGA design must contain logic to handle this communication.

The FPGA is configured once writing the hardware description into the FPGA. The hardware description is written in such a way so as to allow different experimental sequences or “program sequences” to be downloaded into the FPGA’s internal memory. When the experimenter desires to run a different program sequence, it is downloaded to the FPGA memory without reconfiguring the FPGA.

After the FPGA is configured, all computer interactions with the FPGA are implemented with read/write cycles. For example, after the program sequence is down-

---

[7] Peripheral Component Interconnect

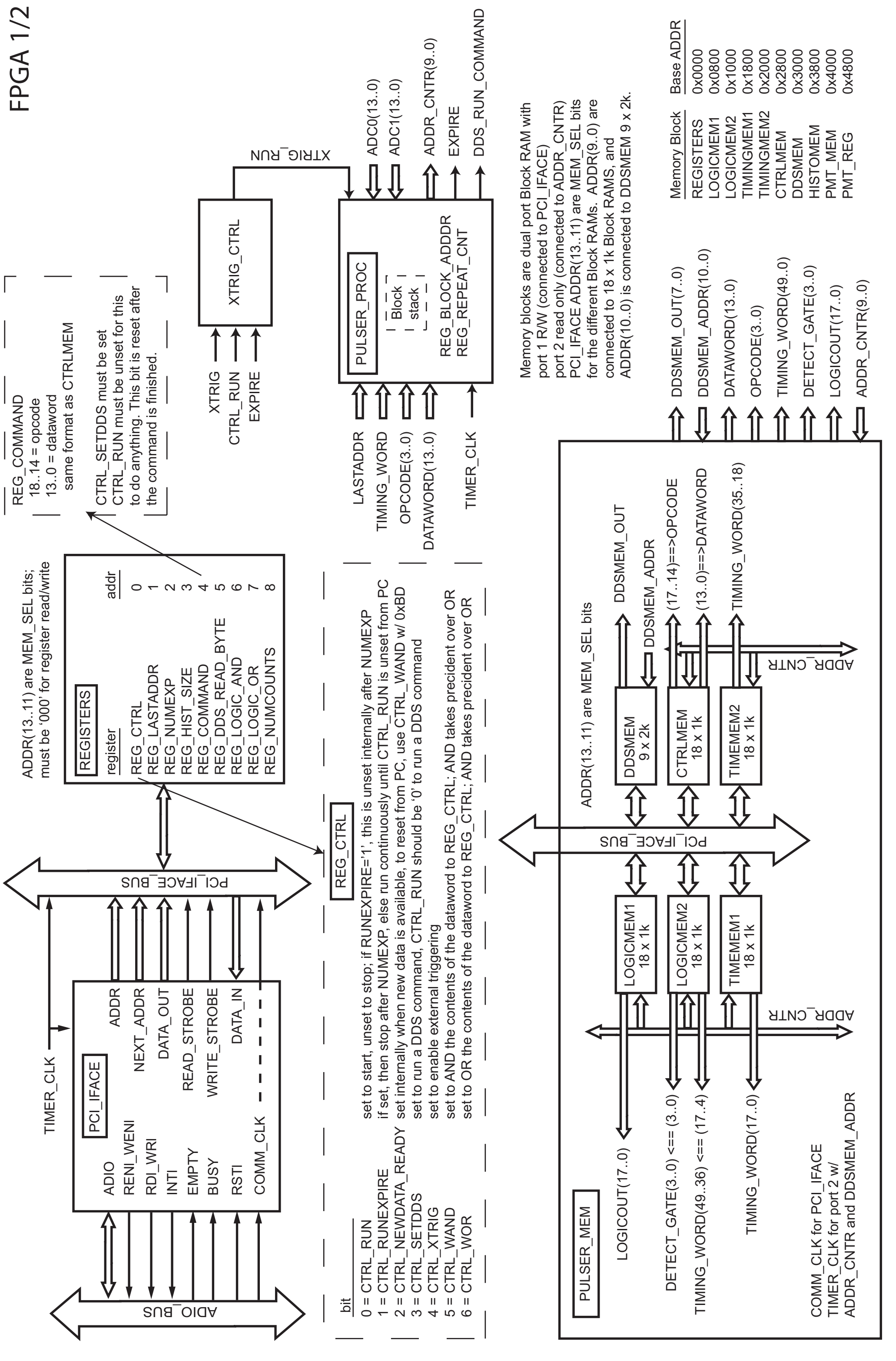

ADDR(13..11) are MEM_SEL bits; must be '000' for register read/write

register	addr
REG_CTRL	0
REG_LASTADDR	1
REG_NUMEXP	2
REG_HIST_SIZE	3
REG_COMMAND	4
REG_DDS_READ_BYTE	5
REG_LOGIC_AND	6
REG_LOGIC_OR	7
REG_NUMCOUNTS	8

REG_COMMAND
18..14 = opcode
13..0 = dataword
same format as CTRLMEM

CTRL_SETDDS must be set
CTRL_RUN must be unset for this
to do anything. This bit is reset after
the command is finished.

bit	
0 = CTRL_RUN	set to start, unset to stop; if RUNEXPIRE='1', this is unset internally after NUMEXP
1 = CTRL_RUNEXPIRE	if set, then stop after NUMEXP, else run continuously until CTRL_RUN is unset from PC
2 = CTRL_NEWDATA_READY	set internally when new data is available, to reset from PC, use CTRL_WAND w/ 0xBD
3 = CTRL_SETDDS	set to run a DDS command, CTRL_RUN should be '0' to run a DDS command
4 = CTRL_XTRIG	set to enable external triggering
5 = CTRL_WAND	set to AND the contents of the dataword to REG_CTRL; AND takes precident over OR
6 = CTRL_WOR	set to OR the contents of the dataword to REG_CTRL; AND takes precident over OR

Memory blocks are dual port Block RAM with
port 1 R/W (connected to PCI_IFACE)
port 2 read only (connected to ADDR_CNTR)
PCI_IFACE ADDR(13..11) are MEM_SEL bits
for the different Block RAMs. ADDR(9..0) are
connected to 18 x 1k Block RAMS, and
ADDR(10..0) is connected to DDSMEM 9 x 2k.

Memory Block	Base ADDR
REGISTERS	0x0000
LOGICMEM1	0x0800
LOGICMEM2	0x1000
TIMINGMEM1	0x1800
TIMINGMEM2	0x2000
CTRLMEM	0x2800
DDSMEM	0x3000
HISTOMEM	0x3800
PMT_MEM	0x4000
PMT_REG	0x4800

ADDR(13..11) are MEM_SEL bits

COMM_CLK for PCI_IFACE
TIMER_CLK for port 2 w/
ADDR_CNTR and DDSMEM_ADDR

Figure 3.12: Block diagram of the FPGA design part 1/2. Thick arrows are multi-bit logic signals (or buses); thin arrows are single-bit signals. Direction of arrow indicates direction of data flow.

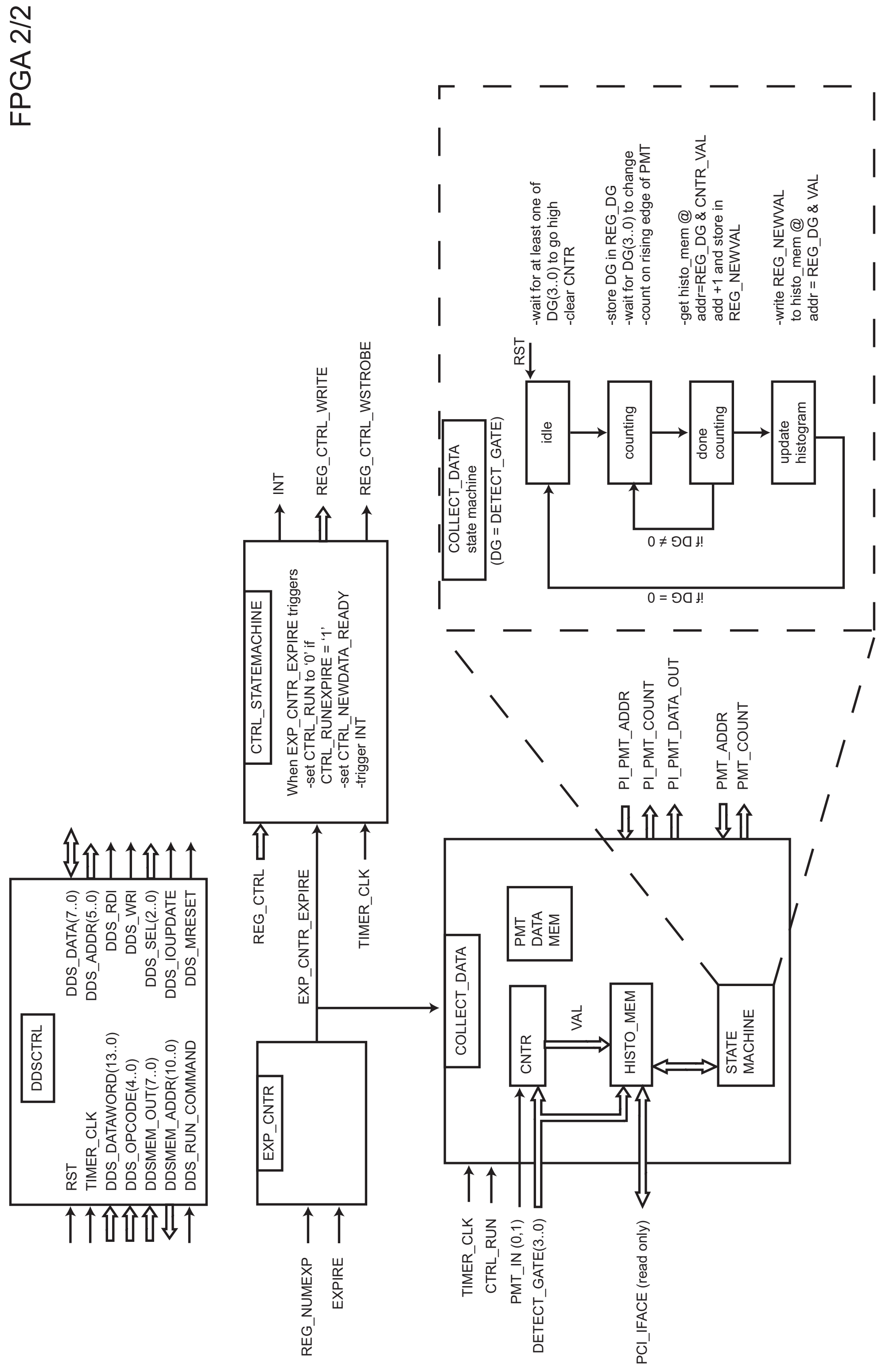

Figure 3.13: Block diagram of the FPGA design part 2/2.

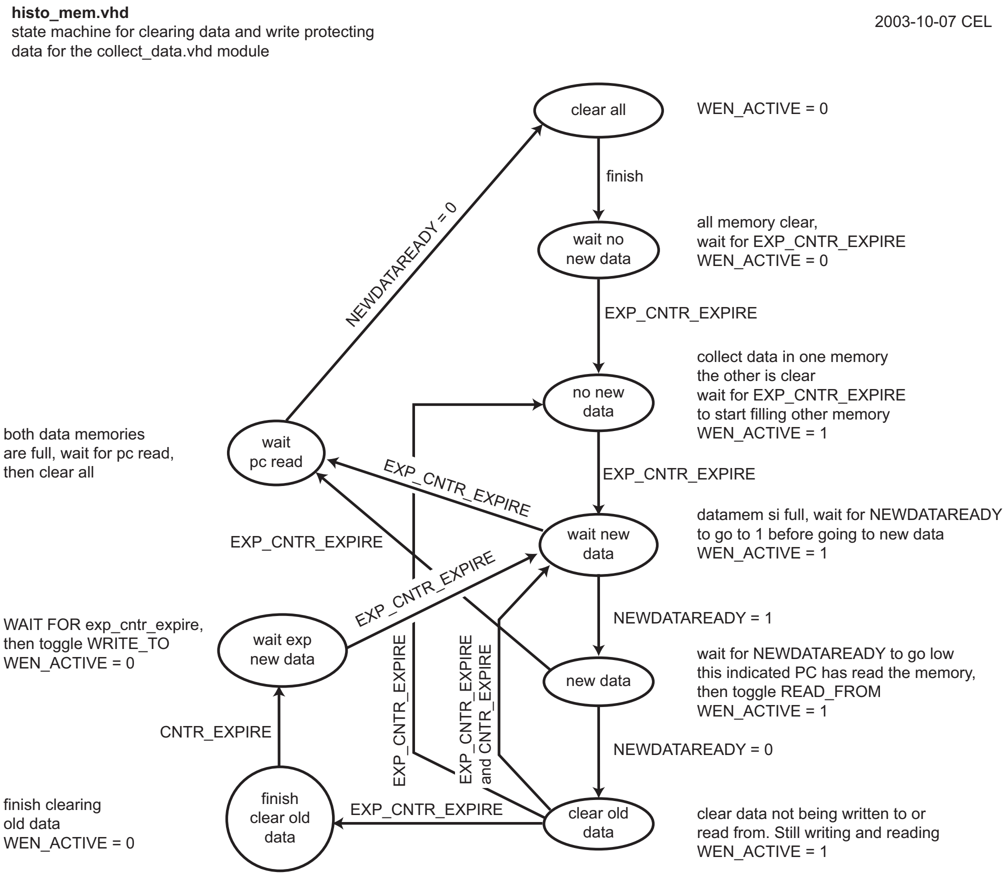

Figure 3.14: Histogram memory state machine for COLLECT_DATA module in Fig. 3.13.

loaded to the FPGA through a sequence of write cycles, the pulse sequence is “started” by writing the value ‘1’ to the control register (REG_CTRL). Similarly, the FPGA can be stopped by writing the value ‘0’ to the control register. Data (fluorescence counts) is retrieved through a sequence of read cycles. Consequently, the PCI_IFACE module was the first block that I designed, and its success was paramount to getting the rest of the design working. It transforms the ADIO bus signals (ADIO(31..0), RENl_WENl, RDl_WRl, INTl, EMPTY, BUSY, RSTl, see [Nallatech 03]) into the PCI_IFACE_BUS signals used to read/write the PULSER_MEM block and the registers (see Fig. 3.12).

The PULSER_MEM module contains the memory for the pulse sequencer. There are four blocks of memory in the PULSER_MEM module: (1) LOGICMEM, (2) TIMEMEM, (3) CTRLMEM, and (4) DDSMEM. The LOGICMEM stores the digital logic channels which are output for variable lengths of time. The duration of these pulses is stored in TIMEMEM. The design allows for a limited set of control flow, and the commands and data associated with this are stored in CTRLMEM. Finally, the DDSMEM stores frequency and phase data used to program the DDS modules over the DDS Bus. The PULSER_MEM LOGICOUT bus is routed off the chip to the Digital I/O Box (see Fig. 3.11). The memory modules in PULSER_MEM are dual port Xilinx Block RAMs. Port 1 is read/write and connected to the PCI_IFACE bus, and port 2 is read only and addressed by ADDR_CNTR. Port 1 allows the computer to write to and read from the contents of memory to load new pulse sequences and read them back for verification. Port 2 is used by the remainder of the FPGA design for operation. The Block RAMs output the data at address ADDR_CNTR within one TIMER_CLK cycle after ADDR_CNTR changes. ADDR_CNTR is driven by the PULSER_PROC module.

The PULSER_PROC module controls the address counter ADDR_CNTR and the address into the DDS memory, DDSMEM_ADDR. When the CTRL_RUN bit of the REG_CTRL register is ‘0’, PULSER_PROC sets ADDR_CNTR to zero, and the first pulse is output on the LOGICOUT bus. This is the non-running state. When

CTRL_RUN is '1', PULSER_PROC is running. The simplest operation is as follows. When running, PULSER_PROC loads the TIMING_WORD located at ADDR_CNTR (starting at zero, the first pulse) into a decrementing counter. Upon counter expiration, ADDR_CNTR is incremented, the next LOGICOUT pulse is output, the next TIMING_WORD is loaded into the counter, and the process repeats. When ADDR_CNTR reaches REG_LASTADDR, PULSER_PROC triggers the EXPIRE signal, sets ADDR_CNTR to zero, and the next experiment begins. The EXPIRE pulses are counted by the EXP_CNTR module, and when the count of experiments matches REG_NUMEXP, the EXP_CNTR_EXPIRE signal triggers an interrupt for the host computer. At this point, if the CTRL_RUNEXPIRE bit is set to '1' in the REG_CTRL register, the CTRL_RUN bit is reset to '0', and the PULSER_PROC enters the non-running state. If the CTRL_RUNEXPIRE bit is '0', the PULSER_PROC module remains in the running state and continues to run the next experiment starting at ADDR_CNTR = 0.

In addition to the linearly incrementing ADDR_CNTR run mode described above, the PULSER_PROC module also supports branching the ADDR_CNTR. It does so by processing a limited set of OPCODEs (see Table 3.1). The CTRLMEM block of the PULSER_MEM module outputs the OPCODE and the DATAWORD addressed by ADDR_CNTR for processing. The DATAWORD takes on different meanings based on the OPCODE being processed. For example, when the PULSER_PROC encounters the OPCODE OP_ENTER_BLOCK, it interprets the DATAWORD to be the number of times the following block should be repeated. In contrast, if the OPCODE is OP_CALL_SR, the DATAWORD represents the address to which to branch for a subroutine call. The OPCODEs and the meaning of the corresponding DATAWORDs are shown in Table 3.1.

The OPCODEs listed in Table 3.1 represent two types: (1) ADDR_CNTR control flow and (2) DDS control. ADDR_CNTR control flow OPCODEs are processed by PULSER_PROC, whereas the DDS control OPCODEs (value 0xB and above) are

OPCODE	**Value**	**DATAWORD Meaning**
OP_NOP	0x0	Bit 0 = ADC accumulate mode(1), normal mode (0), bit 8 = ADC channel in ADC accumulate mode
OP_ENTER_BLOCK	0x1	Block repeat count
OP_EXIT_BLOCK	0x2	N/A
OP_BRANCH	0x3	Branch address
OP_BRANCH_GREATER	0x4	Bits 9..0 branch address, bits 13..0 register address to compare; Register data: bits 13..10 detect gate, bits 9..0 value to compare.
OP_BRANCH_LESS	0x5	
OP_BRANCH_EQUAL	0x6	
OP_BRANCH_NOT_EQUAL	0x7	
OP_CALL_SR	0x8	Subroutine branch address
OP_RETURN_SR	0x9	N/A
OP_SET_REG	0xA	Bits 13..10 register address, bits 9..0 register value to write
DDS Opcodes		
OP_SETFREQ	0x0B	Address of 4 byte frequency in DDSMEM
OP_SETPHASE	0x0C	14 bit phase
OP_SETRF	0x0D	Address in DDSMEM of 4 byte frequency followed by 2 byte phase (low byte first on both frequency and phase)
OP_SET_SEL	0x0E	DDS selection value
OP_DDS_WRITE_BYTE	0x11	Bits 13..8 address of DDS register, bits 7..0 data to write
OP_DDS_READ_BYTE	0x12	DDS register address to read
OP_DDS_MRESET	0x13	N/A

Table 3.1: FPGA opcodes.

processed by the DDSCTRL module (see Fig. 3.13). The DDSCTRL module is responsible for communicating with the DDS modules on the DDS Bus, and it uses DDSMEM as a resource. For example, if a certain pulse has the OPCODE OP_SET_FREQ, the DDSCTRL module interprets the DATAWORD as the address in DDSMEM where the frequency is stored. It then sets the DDSMEM_ADDR to this value, reads the first byte of the frequency tuning word from DDSMEM_OUT and routes this to the DDS_DATA bus while setting the DDS_ADDR to 0xA[8] . A few clock cycles later[9] , DDSCTRL increments DDSMEM_ADDR, retrieves the next byte of the frequency tuning word from DDSMEM_OUT and sends this out the DDS_DATA bus at DDS_ADDR 0xB. This process is repeated until all of the bytes of the frequency tuning word are written to the DDS Bus. Next, the frequency update signal is pulsed on the DDS Bus to write the new frequency tuning word to the internal registers of the DDS. Consequently, there is a minimum pulse duration for each DDS OPCODE. The minimum pulse duration varies as a function of the DDS OPCODE because certain OPCODEs must transfer more information to the DDS than others. In the case of OP_SETFREQ, the minimum time is 23 TIMER_CLK cycles[10] and transfers four bytes of information to the DDS (32 bits of the frequency tuning word). In contrast, the minimum pulse duration for OP_SETPHASE is shorter because only two bytes of information is transferred to the DDS (14 bits of the phase offset word). The minimum pulse duration for all of the DDS OPCODEs is shown in Table 3.2.

The DDS Bus supports individual addressing of different DDS modules. This is accomplished via the DDS selection address (or DDS board address). Each DDS module has a 5-bit DIP[11] switch which is set to a unique binary value. This identifies each DDS module from the others. The FPGA interfaces to an individual DDS module by first

---

[8] This is the register address on the Analog Devices AD9858 DDS of bits 7..0 of the 32-bit frequency tuning word. See the AD9858 datasheet for further details.

[9] The communications clock for the DDS is intentionally divided down by a factor of three to make DDS Bus communications more robust.

[10] At the TIMER_CLK frequency of 62.5 MHz, this corresponds to 368 ns.

[11] Dual inline package

DDS OPCODE	**Minimum TIMER_CLK Cycles**	**Minimum Duration at 62.5 MHz (ns)**
OP_SETFREQ	23	368
OP_SETPHASE	10	160
OP_SETRF	29	464
OP_SET_SEL	3	48

Table 3.2: DDS OPCODEs minimum durations.

setting the DDS selection bits prior to executing a DDS OPCODE. This is accomplished in two steps: (1) execute OP_SETSEL to set the DDS selection bits to the DDS module you wish to address, and (2) execute the DDS OPCODE of interest (OP_SETFREQ, OP_SETPHASE, or OP_SETRF).

The OPCODEs for both control flow and DDS operations are stored in CTRLMEM to allow these OPCODEs to be processed synchronously with the experiment. However, there are other operations that we desired which did not require intra- experiment operation. These include DDS reset and the ability to write and read a single byte to any address on the DDS. CTRLMEM is only 18 bits wide and stores a 14 bit DATAWORD and a 4 bit OPCODE. The extra OPCODEs are 5 bits wide and processed via the register REG_COMMAND. The FPGA must be in the non-running state (CTRL_RUN set to '0') for these commands to be processed. The user first writes a command to REG_COMMAND including a 5 bit opcode and 14 bit dataword. Next, the user sets the CTRL_SETDDS bit in the REG_CTRL register to initiate the command. The OPCODE and DATAWORD are routed to the DDSCTRL module, and the DDS command is executed. In the case of OP_DDS_READ_BYTE, the byte read from the DDS is stored in REG_DDS_READ_BYTE. The user can then read the REG_DDS_READ_BYTE from the computer.

Experimental measurements are performed by counting photons on a photomultiplier tube, and the experiment controller has 2 counter inputs to accommodate this: PMT1 and PMT2. Management of PMT counts occurs in the COLLECT_DATA module in Fig. 3.13. Even though there are two only PMT inputs, counts are stored in 14 different sections of memory based on the DETECT_GATE signal bus. The DETECT_GATE signal bus is 4 bits wide, and the most significant bit indicates the PMT input. If the 3 least significant bits of DETECT_GATE are all zero, then the COLLECT_DATA state machine is in the non-counting state. Therefore, each PMT input has 7 different DETECT_GATE sections of memory where the counts are collected into a histogram and stored.

At the beginning of an experiment, the COLLECT_DATA state machine is in the idle state waiting for DETECT_GATE(2..0) to be non-zero. When DETECT_GATE changes, the COLLECT_DATA module begins counting rising edges from the PMT input. Counting continues until DETECT_GATE changes. If DETECT_GATE(2..0) changes to a non-zero value, counting continues for the new DETECT_GATE. After DETECT_GATE returns to zero, the count is used to update the histogram at the location in memory associated with both the DETECT_GATE(2..0) and the count.

In addition to maintaining a histogram of photon counts, the COLLECT_DATA block also stores the raw counts in the PMT data memory in succession. Because the actual pulse sequence can change from experiment to experiment based on intra-experiment measurements and conditional branch instructions, then number of measurements during each experiment is not known a priori. However, this information can be extracted from the raw counts (see Table 3.3). The most significant bit, termed the “successive detect bit,” is ‘0’ for the first count in an experiment and ‘1’ for each additional count. This labels the first count in an experiment so that the user can reconstruct which pulse sequence occurred. The DETECT_GATE is stored in bits 16–13, and the actual count value is stored in bits 12–0. The maximum count value which can be stored is 8192.

During an experiment, the most recent count for each DETECT_GATE is stored

PMT Memory Bit Map			
Bit	17	16..13	12..0
Meaning	Successive detect bit	DETECT_GATE	Count value

Table 3.3: PMT memory bit map.

in a register such that the PULSER_PROC module can compare the PMT count to threshold values when processing conditional branch OPCODEs such as OP_BRANCH_LESS.

3.4.3.2 DDS Bus and Digital I/O Bus

The FPGA communicates to the DDS modules and the Digital I/O box via 2 buses—the DDS Bus and the Digital I/O Bus. The bus signals are listed in Table 3.5 and Table 3.7. Each bus uses low voltage differential signaling (LVDS) over 100 Ω twisted pair transmission lines. Because the FPGA only provides 42 general purpose logic I/O pins, I designed a daughter interface board to the FPGA board which converts the LVTTL[12] logic levels of the FPGA to LVDS signals. The daughter board schematic and board layout can be found in Appendix B.

LVDS adds many advantages to digital communications over LVTTL. Since it is a differential signal standard, it is less susceptible to interference. This allows it to use lower voltages and hence lower currents. It uses terminated transmission lines which reduces transients. This all sums up to faster communications speeds. My first attempt to communicate with DDS modules using fanned-out LVTTL had many problems including cross-talk induced DDS resets even at low communication speeds.

Each DDS module uses an unterminated LVDS transceiver as a "drop" on the transmission line (see Fig. 3.15). The transmission line is terminated into 100 Ω on each end with one end residing at the FPGA. The "drop" is an unterminated LVDS transceiver residing on the transmission line with short electrical traces to reduce the alterations to the transmission line's characteristic impedance. When the FPGA drives the bus, the signal propagates down the transmission line until it is terminated into 100 Ω. Because the load impedance is matched to the transmission line, there is minimal reflection. When one of the DDS modules drive the bus, it drives two 100 Ω transmission

---

[12] Low voltage transistor-transistor logic

DDS Bus 50-Pin Header			
Name	**Pin**	**Pin**	**Name**
DDS_PROF_SEL_H0	50	49	DDS_PROF_SEL_L0
DDS_PROF_SEL_H1	48	47	DDS_PROF_SEL_L1
DDS_MRESET_H	46	45	DDS_MRESET_L
DDS_RDL_H	44	43	DDS_RDL_L
DDS_SEL_H0	42	41	DDS_SEL_L0
DDS_SEL_H1	40	39	DDS_SEL_L1
DDS_SEL_H2	38	37	DDS_SEL_L2
DDS_SEL_H3	36	35	DDS_SEL_L3
DDS_SEL_H4	34	33	DDS_SEL_L4
DDS_WRL_H	32	31	DDS_WRL_L
DDS_IOUPDATEL_H	30	29	DDS_IOUPDATEL_L
DDS_ADDR_H0	28	27	DDS_ADDR_L0
DDS_ADDR_H1	26	25	DDS_ADDR_L1
DDS_ADDR_H2	24	23	DDS_ADDR_L2
DDS_ADDR_H3	22	21	DDS_ADDR_L3
DDS_ADDR_H4	20	19	DDS_ADDR_L4
DDS_ADDR_H5	18	17	DDS_ADDR_L5
DDS_DATA_H0	16	15	DDS_DATA_L0
DDS_DATA_H1	14	13	DDS_DATA_L1
DDS_DATA_H2	12	11	DDS_DATA_L2
DDS_DATA_H3	10	9	DDS_DATA_L3
DDS_DATA_H4	8	7	DDS_DATA_L4
DDS_DATA_H5	6	5	DDS_DATA_L5
DDS_DATA_H6	4	3	DDS_DATA_L6
DDS_DATA_H7	2	1	DDS_DATA_L7

Table 3.5: DDS Bus

Logic Bus 40-Pin Header			
Name	**Pin**	**Pin**	**Name**
NC	40	39	NC
LOGIC_OUT_H15	38	37	LOGIC_OUT_L15
LOGIC_OUT_H14	36	35	LOGIC_OUT_L14
LOGIC_OUT_H13	34	33	LOGIC_OUT_L13
LOGIC_OUT_H12	32	31	LOGIC_OUT_L12
LOGIC_OUT_H11	30	29	LOGIC_OUT_L11
LOGIC_OUT_H10	28	27	LOGIC_OUT_L10
LOGIC_OUT_H9	26	25	LOGIC_OUT_L9
LOGIC_OUT_H8	24	23	LOGIC_OUT_L8
LOGIC_OUT_H7	22	21	LOGIC_OUT_L7
LOGIC_OUT_H6	20	19	LOGIC_OUT_L6
LOGIC_OUT_H5	18	17	LOGIC_OUT_L5
LOGIC_OUT_H4	16	15	LOGIC_OUT_L4
LOGIC_OUT_H3	14	13	LOGIC_OUT_L3
LOGIC_OUT_H2	12	11	LOGIC_OUT_L2
LOGIC_OUT_H1	10	9	LOGIC_OUT_L1
LOGIC_OUT_H0	8	7	LOGIC_OUT_L0
XTRIG_H	6	5	XTRIG_L
PMT_IN_H0	4	3	PMT_IN_L0
PMT_IN_H1	2	1	PMT_IN_L1

Table 3.7: Logic Bus

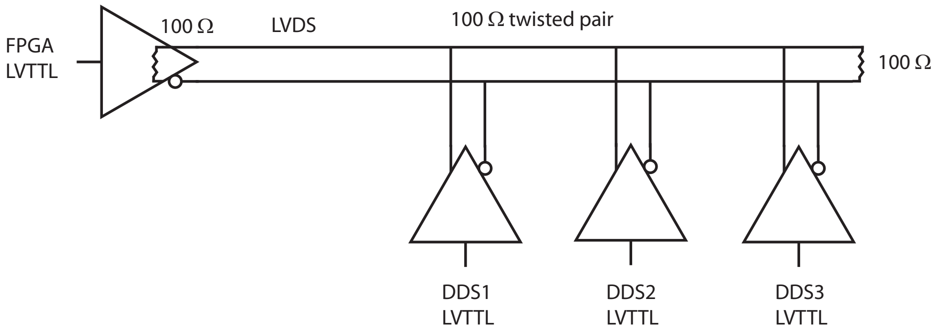

Figure 3.15: LVDS transmission line with multiple transceiver "drops"

lines in parallel—one transmission line terminating at the FPGA and the other at the opposing end. We use the Texas Instruments LVDM series LVDS transceivers for this task as they can source twice the normal current required to drive 100 Ω loads; these chips are designed specifically for this purpose.

3.4.3.3 DDS Module

The DDS module consists of an Analog Devices AD9858/PCB evaluation board containing the AD9858 DDS chip and an interface daughter board. The evaluation board provides an LVTTL header to program the DDS. Our daughter board interfaces to this header by converting the LVDS signals to LVTTL in the appropriate fashion. The daughter board also provides board addressing with a 5-pin DIP switch. When the FPGA desires to communicate with a particular DDS, it first sets the DDS selection bits to the desired DDS board address. The DDS daughter board compares the DDS selection bits to the board address set by the DIP switch. If they match, the bus signals are routed to the DDS; otherwise, the signals are ignored. This allows multiple DDS modules to share the same bus. The schematics for the DDS daughter board are shown in Appendix B. A picture of the DDS Box containing 8 DDS modules is shown in Fig. 3.16. The clock source for each DDS module is a 1 GHz synthesized source referenced to the NIST Hydrogen maser.

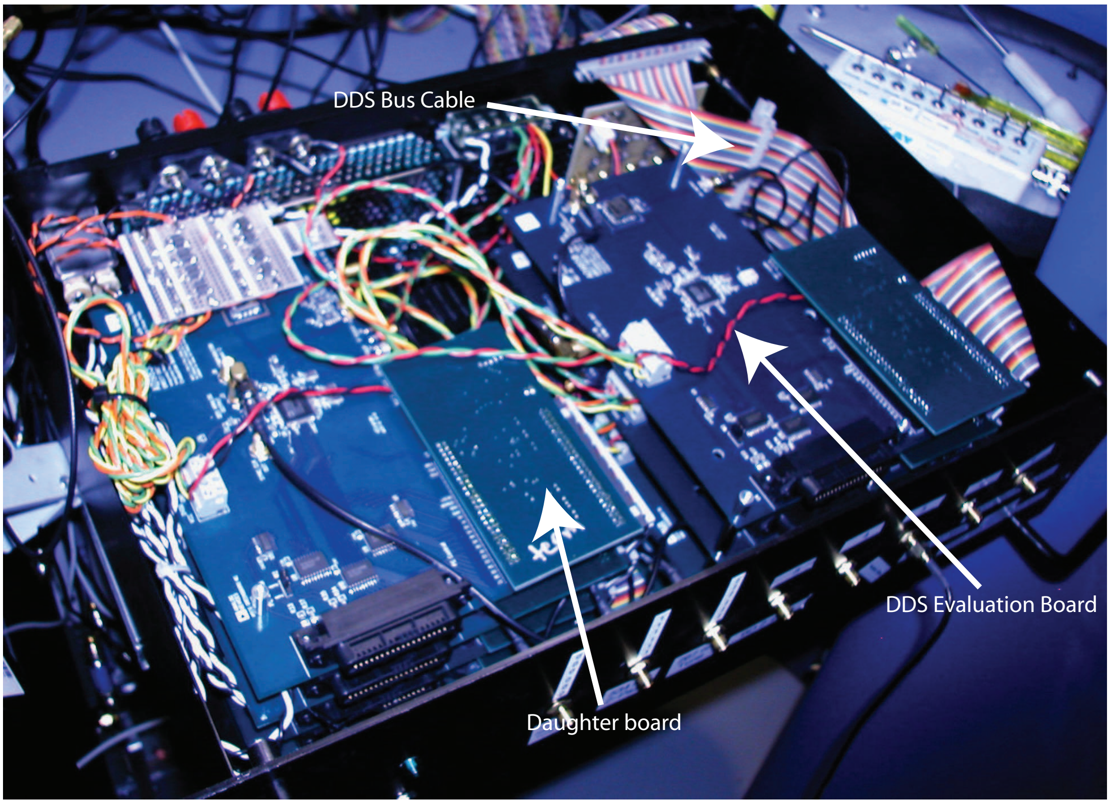

Figure 3.16: Picture of DDS Box containing 8 DDS modules. Each module consists of an Analog Devices AD9858/PCB evaluation board with the AD9858 DDS and a daughter interface board. The daughter boards are "drops" on the LVDS transmission line (flat cable) with the last daughter board on the cable terminated (top left).

3.4.3.4 Software Interface

The FPGA experiment controller as described in the previous sections, though very functional, provides a very low-level interface with which to program experiments. The Nallatech FUSE software library exports all of the necessary functions to download and run experiments on the controller. As we discussed above, all computer interactions with the FPGA are either read or write statements. However, writing an experimental pulse sequence requires converting the duration of pulses into a number of clock cycles, setting the control memory to handle appropriate commands to set DDS frequencies and phases, and setting the control memory to handle program execution flow. This process can become very complicated even for simple experiments.

To facilitate simpler pulse sequence design, I developed a pulse-programming language and a corresponding parser for the language. The experimenter defines names of pulses corresponding to a set of logic channels which should be asserted high when the pulse is active. Variables can also be defined. The pulse sequence is described by a list of “pulse” statements containing the name of the pulse followed by its duration (see Fig. 3.17; language keywords are highlighted in blue). The pulse statement can have an optional DDS command such as “setfreq” or “setphase.” Pulses also have optional labels marked by the keywords “tscan” and “fscan.” These labels alert the parser to remember the addresses where these pulses reside in the FPGA memory such that changes to the duration and/or frequency/phase of the individual pulses can be made quickly. The language provides some simple control flow statements such as the “if” statement, “block repeat” statement (simpler version of the “for” loop in most programming languages), and subroutine calls. The language takes advantage of the branching capabilities of the FPGA design to accomplish this.

The parser is only one part of the interface library (fpgart.dll) to the experiment controller. The software library maintains a memory map of the parsed file, maps of

```
//experiment to flop on the carrier

name bd = 3,10;
name rd = 4;
name cool      = bd,rd;
name wait      = none;
name detect    = bd,pmt(1);
name raman     = 7,8;

var ddsRaman   = 2;
var tpi        = 2.34;        //durations are in microseconds
var fCar       = 201.65;      //frequencies are in MHz

pulse cool 200.0;             //durations are in microseconds
pulse wait 1   setsel(ddsRaman);
pulse wait 1   setfreq(fCar)          fscan(fsRaman);
pulse raman tpi                       tscan(tsRaman);
pulse wait 1;

pulse detect;
pulse wait 1;

if(pmt(1) < 4) {
        pulse cool 1000;
}

pulse wait 1;
```

Figure 3.17: Sample pulse sequence script

the pulse names, variables, and tscan/fscan identifiers. It exports functions which allow the user to make changes to the pulse information associated with tscan and fscan identifiers. It allows the user to set the number of experiments and histogram size, and it provides functionality to download the measurement data stored on the FPGA.

I also developed a graphical user interface (pulser_ui.exe) which consumes the fpgart.dll library. This interface gives the experimenter tools to perform scans of the time, frequency, and phase. The data for each scan parameter is stored in a file, and the results are displayed on plot. This software is particularly useful for quick test experiments that scan over experimental parameters. For example, a simple Rabi flopping experiment requires scanning the duration of a laser pulse at a fixed frequency after the ion has been initialized. The experimenter would write a pulse sequence script file, parse and download it to the FPGA, select the tscan identifier associated with the flopping duration, and scan it over the desired range. The pulser_ui would then display the measurement results as a function of the duration of the pulse on a plot, and if the experiment was successful, sinusoidal flopping data would result.

3.4.3.5 Concluding Remarks

In the previous sections I tried to give an overview of the design of the FPGA based experiment controller we used in the experiments described in this thesis. After its first few years of use, many of the bugs have been worked out, and the controller has become quite reliable. However, looking back, there are a few things which I would improve in a second generation of such a device. I will outline these thoughts here.

The first limitation we have encountered are the small number of pins. The XtremeDSP Kit only provides 42 general purpose I/O pins for the user's design. We use 23 pins for the DDS Bus and 19 for the Digital I/O Box. This can be further broken down. Of the 19 pin group, 16 are TTL output, 2 counter inputs, and 1 external triggering input. For small experiments, 16 TTL channels is sufficient, but as the experiments get more complicated, this number is too small. The obvious solution to this problem is to use a different FPGA card which has more pins. Many commercial FPGA cards have as many as 100 general purpose pins, so this would certainly solve this problem. These boards have other features as well. For example, some boards give access to the Virtex IV's high speed serial ports which can communicate at over 1 gigabit per second. A new design could use such a serial port for the DDS bus by modifying the DDS daughter board to interface to a serial communications protocol. This would free up pins and reduce cross talk between signals on the parallel bus.

Choosing a new FPGA card should not be taken lightly. The current design takes advantage of PCI interrupts that the XtremeDSP kit provides. After the set number of experiments expires, the computer is interrupted allowing it to modify scan parameters and restart the experiment. Many of the alternate cards do not generate interrupts for the computer; therefore, an alternate scheme for alerting the computer that data is available must be used. Changing the DDS Bus to a serial bus rather than a parallel bus would free up some pins, so changing the FPGA card may not be necessary. Using an alternate FPGA card should be considered, however.

The current design also uses on-chip memory to store the pulse sequence, DDS data, and measurement data. Because of the size of the original FPGA on the first version of the XtremeDSP kit[13] , I only allocated enough memory for 1024 pulses. Granted, the experimenter's requirements are heavily reduced because of variable length pulses, subroutines, and loops; however, we are currently running into the limits of such a small amount of program memory. The newer Virtex IV FPGAs have more on-chip memory, so extending this amount should be trivial. This has not been done yet, however. In addition to expanding on-chip memory, the design could utilize the 512 kB of off-chip memory. This is an excellent location to store the measurement data. Alternate FPGA cards may have a larger size of external memory as well.

---

[13] Virtex II XC2V2000

The opcode processing also suffers from a flawed design. The CTRLMEM block is 18 bits wide due to the size of the original Block RAMS. Because I wanted to make phase changes as fast as possible, I made the DATAWORD 14 bits such that the entire phase word could fit in the DATAWORD. Consequently, the DDS_CTRL block did not have to query the DDSMEM for the phase word reducing the latency between the DDS_CTRL block and the DDS module in question. This forced the OPCODE size to be 4 bits. Unfortunately, we desired more OPCODEs than 2^4, so I developed the following work around. Certain DDS commands (reset, read byte, and write byte) did not need to be executed during an experiment. I made the DDS opcode 5 bits wide and substituted a '0' for the most significant bit when the card was running. When the card was stopped, however, the full 5-bit OPCODE from the REG_DDS_COMMAND register was routed to the DDS_CTRL block. This is obviously a bad design, and a future design should plan for a larger OPCODE space from the beginning, even if it means using a smaller DATAWORD and addressing the phase word in the DDSMEM.

The last modification I would make in a future version is to convert the DDS Bus into a more general purpose bus. This would allow different peripheral modules like fast DACs to interface to the same bus. It is important to note that the bus definition is one of the most important aspects of the design. Once the bus is defined, the peripheral modules can be designed and redesigned at will as long as the bus specifications do not change. Similarly, the FPGA design can change as long as it communicates with the bus in the same fashion. Good bus design allows for modularity and expansibility. One of the successes of the current design is that the DDS Bus has board addressing functionality that allowed it to be expanded to address up to 32 DDS modules. Future redesigns of the bus should be carefully thought out. In a future version, I would give a strong thought to using a fast serial bus with shift registers on the daughter boards converting the signals back into parallel words.

Chapter 4

Robust Quantum Memory

In section § 2.2 we calculated the energy spectrum of the ground $S_{1/2}$ hyperfine states of ^{9}Be$^+$. We found that at certain magnetic fields there exists transitions whose frequency has no first order dependence on the magnetic field. In this chapter, we use the particular field-independent transition $|F = 2, m_F = 0\rangle \equiv |\downarrow\rangle \leftrightarrow |F = 1, m_F = 1\rangle \equiv |\uparrow\rangle$ as our qubit and investigate its properties. In particular, we measure the location where the transition is field-independent and measure the coherence time of the qubit. Our results indicate that the coherence time of this qubit is approximately 15 seconds. I develop a simple model of memory decoherence based on random magnetic field changes every fixed sample interval. Exponential memory coherence decay models indicate that the memory error per measurement interval is $\sim 10^{-5}$. More sophisticated models indicate that the memory error per measurement interval may be $\sim 10^{-7}$. With such a long coherence time, this qubit is suitable for use in a fault-tolerant quantum computing architecture [Knill 05, Steane 03, Kielpinski 02].

In the later half of the chapter, I discuss some experimental challenges to measuring long coherence times. Some of these include magnetic field drift, detection loss due to ion heating, and systematic frequency shifts. In general, many of the characteristics of a good qubit memory are common to atomic clocks, such as transition frequency stability. In particular, the ^{9}Be$^+$ field independent qubit is a relatively stable radio frequency clock near 1.2 GHz. We do note, however, that the requirements for good atomic clocks, and their performance characteristics, far exceed the $^9\mathrm{Be}^+$ qubit discussed in this thesis. Nevertheless, we performed a systematic study of frequency shifts so that we could be reasonably confident that long coherence times were attainable.

4.1 Field-Independent Qubits

Atomic systems have proven themselves as good candidates for quantum information storage through their use in highly stable atomic clocks [Diddams 04]. Here, the principle of using first-order magnetic-field-independent transitions is well established. A typical clock transition $|F, m_F = 0\rangle \leftrightarrow |F', m_{F'} = 0\rangle$ between hyperfine states of angular momentum F and F' in alkali atoms has no linear Zeeman shift at zero magnetic field, and coherence times exceeding 10 minutes have been observed [Fisk 95]. Unfortunately, the degeneracy of magnetic sublevels at zero magnetic field makes it more advantageous to operate at a nonzero field in order to spectrally resolve the levels, thereby inducing a linear field dependence of the transition frequency. However, field-independent transitions between hyperfine states also exist at nonzero magnetic field. For example, coherence times exceeding 10 minutes have been observed in $^9\mathrm{Be}^+$ ions at a magnetic field $B = 0.8194$ T [Bollinger 91].

In neutral-atom systems suitable for quantum information processing (QIP), field-independent transitions at nonzero magnetic field have been investigated in rubidium [Harber 02, Treutlein 04]. The radio-frequency (RF)/microwave two-photon hyperfine transition $|F = 1, m_F = -1\rangle \leftrightarrow |F' = 2, m_{F'} = 1\rangle$ is field-independent at approximately 3.23×10^{-4} T , and coherence times of 2.8 s have been observed [Treutlein 04]. In these and the clock experiments, transitions were driven by microwave fields on large numbers of atoms. Using microwaves, it may be difficult to localize the fields well enough to drive individual qubits unless a means (e.g., a magnetic-field gradient or Stark-shift gradient) is employed to provide spectral selection [Mintert 01, Schrader 04], a technique that has the additional overhead of keeping track of the phases induced by these

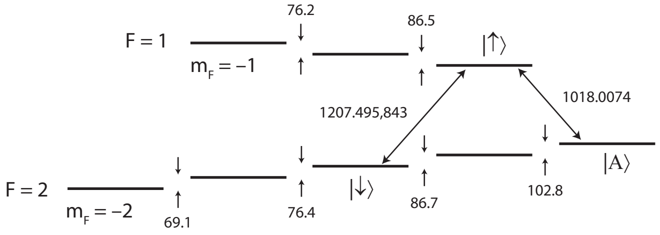

Figure 4.1: Frequencies of transitions relevant to experiments in the text. The qubit states are indicated by $|\downarrow\rangle$ and $|\uparrow\rangle$. The state $|A\rangle$ is the starting state for the experiments as it is easily initialized via optical pumping (see § 2.3). $|A\rangle$ is also used for detection. The transition $|A\rangle \leftrightarrow |\uparrow\rangle$ is linearly dependent on the magnetic field. We use frequency measurements of this transition as a probe of the magnetic field. Units are in MHz.

shifts. With transitions induced by laser beams, the addressing can be accomplished by strong focusing [Riebe 04] or by weaker focusing and inducing transitions in separate trap zones [Barrett 04]. In contrast to microwave fields, optical fields (using appropriate geometry [Cirac 95, Monroe 95b]) provide stronger field gradients that are desirable for coupling ion motional states with internal states, a requirement for certain universal multi-qubit logic gates [Cirac 95, Wineland 98]. Here, we explore the coherence time of a single atomic ion qubit in a scalable QIP architecture using laser beam addressing.

In recent ^{9}Be$^+$ QIP experiments utilizing 2s $^2S_{1/2}$ hyperfine states: $|F = 2, m_F = -2\rangle$ and $|F = 1, m_F = -1\rangle$ as qubit levels, fluctuating ambient magnetic fields caused significant decoherence [Barrett 04, Chiaverini 04]. There, the qubit transition depended linearly on the magnetic field with a coefficient of approximately 21 kHz/μT (see Fig. 2.2 in § 2.2). Thus, random magnetic field changes of 0.1 μT (typical in our laboratories) would dephase qubit superpositions (to a phase uncertainty of 1 rad) in 80 μs. To mitigate this decoherence, refocussing spin-echo π-pulses were inserted in the experimental sequences [Barrett 04, Chiaverini 04] to limit the bandwidth of noise to which the qubits were susceptible. However, these effects could not be eliminated completely, and fluctuating fields remained a major source of error in these experiments.

The energy spectrum of the ground hyperfine states of $^9\mathrm{Be}^+$ as a function of magnetic field is calculated in § 2.2 and shown in Fig. 2.2 and repeated in Fig. 4.1. At $B_0 \simeq 0.01194$ T, the transition $|F = 2, m_F = 0\rangle \equiv |{\downarrow}\rangle \leftrightarrow |F = 1, m_F = 1\rangle \equiv |{\uparrow}\rangle$ (frequency $\nu_{\uparrow\downarrow} \simeq 1.2$ GHz) is first-order field-independent with second-order dependence given by $(0.305\ \mathrm{Hz}/\mu\mathrm{T}^2)(B - B_0)^2$ (see Table 2.1). Given random magnetic field changes of 0.1 μT, we expect superpositions of $|{\downarrow}\rangle$ and $|{\uparrow}\rangle$ to dephase in approximately 50 s. The transition $|F = 2, m_F = 2\rangle \equiv |A\rangle \leftrightarrow |{\uparrow}\rangle$ (frequency $\nu_{\uparrow A} \simeq 1.0$ GHz) is first-order field sensitive with linear dependence of 17.6 kHz/μT for $B = B_0$. We use frequency measurements of this transition as a probe of the magnetic field.

In the experiment, a single $^9\mathrm{Be}^+$ ion is confined to a zone of the trap described in § 3.1. The ion is optically pumped to the state $|A\rangle$, and its motion is Doppler cooled by use of the cycling transition $|A\rangle \leftrightarrow |2p\ ^2P_{3/2}, F' = 3, m_{F'} = 3\rangle$ (see § 2.3). We detect the state of the $^9\mathrm{Be}^+$ ion through state-dependent resonance fluorescence on the cycling transition (see § 2.4). Using coherent rotations described below, we measure the $|{\downarrow}\rangle$, $|{\uparrow}\rangle$ "qubit" level populations by mapping the states $|{\uparrow}\rangle$ and $|{\downarrow}\rangle$ to $|A\rangle$ and $|{\uparrow}\rangle$ respectively and measuring the state $|A\rangle$.

Coherent rotations between states $|A\rangle \leftrightarrow |{\uparrow}\rangle$ and $|{\uparrow}\rangle \leftrightarrow |{\downarrow}\rangle$ can be represented by (in the Bloch sphere representation)

$$R(\theta, \phi) = \cos\frac{\theta}{2}\ I - i\sin\frac{\theta}{2}\cos\phi\ \sigma_x - i\sin\frac{\theta}{2}\sin\phi\ \sigma_y, \tag{4.1}$$

where I is the identity matrix, σ_i are Pauli operators, θ is the rotation angle, and ϕ is the angle from the x-axis to the rotation axis (here, assumed to be in the x-y plane). These rotations are driven by two-photon stimulated Raman transitions using focused laser beams (see § 2.5.2). We modulate one polarization component of a single laser beam with an electro-optic modulator. This technique simplifies the stabilization of differential optical path length fluctuations between the two Raman beams (generated by the two polarizations). The difference in optical path, due to the static birefringence of the modulator, is stabilized to its optimal value of $\lambda/4$ by measuring the retardation with an optical phase detector and feeding back on the temperature of an additional birefringent crystal in the beam path (see § 3.3.4).

The use of co-propagating Raman beams for rotations was important for these experiments because any differential path-dependent phase fluctuations between the Raman beam pair would manifest itself as phase error on the qubit superposition. We took great care to make sure that the Raman beam pair was co-propagating for the entire beam path. This ensured that any phase fluctuations in the laser beams would be common mode, and the differential phase fluctuations would be negligible. The electro-optic phase modulation scheme for Raman transitions proved very useful for the long coherence time measurement even though there were many technical drawbacks to its implementation (see § 3.3.4).

We perform two different types of Ramsey experiments in this chapter, the Ramsey frequency scan and the Ramsey phase scan. The Ramsey frequency scan is more useful for frequency measurements as in Fig. 4.3, whereas the phase scan is useful for determining the contrast of Ramsey fringes alone as in Fig. 4.4. The Ramsey frequency scan description is as follows. To measure the frequency of a two-level system with states labeled $|0\rangle$ and $|1\rangle$[1] , the Ramsey frequency scan experiment begins by preparing the system in a superposition state $|\Psi_1\rangle = \frac{1}{\sqrt{2}}(|1\rangle - i|0\rangle)$ by first preparing $|1\rangle$ followed by application of the rotation $R(\frac{\pi}{2}, 0)$. After a delay T_R, the system evolves to $|\Psi_2\rangle = \frac{1}{\sqrt{2}}(e^{i\delta T_R}|1\rangle - i|0\rangle)$ where δ is the detuning of the local oscillator frequency driving the transition from the qubit frequency (we assume T_R is much greater than the duration of the $\pi/2$ pulses). In our case, the local oscillator frequency is the Raman laser beam pair difference frequency. Here, we assume the detuning δ is fixed. In general, the phase factor δT_R is the integrated detuning over the Ramsey interval T_R. Application of a second rotation $R(\frac{\pi}{2}, 0)$ and making multiple projective measurements

---

[1] We assume state $|1\rangle$ lies higher in energy than state $|0\rangle$.

of identically prepared systems yields the probability of detecting the $|1\rangle$ state:

$$P_{\text{1-fscan}} = \frac{1}{2}[1 - \cos(\delta T_R)]. \tag{4.2}$$

Repeating the experiment for different δ and fitting to the form $a - \frac{b}{2}\cos(\delta T_R)$ allows us to extract the frequency of the qubit transition. The fit parameter a allows for a bias in the measurement signal which may occur from background light during the measurement operation for example. The fit parameter b is responsible for the contrast of the scan. Any frequency fluctuations in the detuning (either generated by an unstable local oscillator or an unstable qubit frequency) will reduce the contrast b. For frequency measurements of transitions which are first-order sensitive to the magnetic field such as the $|A\rangle \leftrightarrow |\uparrow\rangle$ transition in Fig. 4.1, the Ramsey interval T_R is limited to values on the order of 100 μs due to the drop in contrast b from magnetic field noise in the laboratory. However, frequency measurements of the field-independent qubit can be much longer as indicated in Fig. 4.4.

The Ramsey frequency scan experiment is used to measure the qubit transition frequency to high accuracy. It is also used to measure the differential Stark shift. By applying the Stark shifting laser during the Ramsey interval T_R, the phase of the qubit superposition will evolve at a rate given by the difference between the local oscillator frequency and the Stark shifted qubit transition frequency. Performing Ramsey frequency scan experiments with and without the Stark shifting beam yields frequency measurements with a difference frequency equal to the differential Stark shift.

In units of frequency, Eq. (4.2) is periodic in $2\pi/T_R$. Therefore, care must be taken to make sure we are measuring the detuning about the central Ramsey fringe. For example, measurements about $\omega_0 + 2\pi n/T_R$ will yield the same results where n is an integer and ω_0 is the qubit frequency. We ensure we are examining detunings about the central fringe ($n = 0$) by performing frequency scans at different T_R. Data for frequency scans of the field-independent qubit transition at different Ramsey intervals

T_R is shown in Fig. 4.2. The fringe shown in Fig. 4.2 is the central fringe because the minima of multiple frequency scans at different T_R overlap. We observe that the minima in Fig. 4.2 do not overlap perfectly. The small shift of the minimum is due to the AC stark shift of the Raman laser during the $\pi/2$ pulses. The central frequency is shifted by $\Delta\omega_{ss} = \omega_{ss}(1 + \frac{\pi}{4}\frac{T_R}{\tau_{\pi/2}})^{-1}$ where ω_{ss} is the differential AC stark shift of the qubit transition frequency induced by the Raman laser, $\tau_{\pi/2}$ is the duration of the $\pi/2$ pulse, and T_R is the Ramsey interval measured between the end of the first $\pi/2$ pulse to the beginning of the last $\pi/2$ pulse. In the calculation for $\Delta\omega_{ss}$, we assume ω_{ss} is much smaller than the Rabi frequency with no assumption on the size of T_R as compared to $\tau_{\pi/2}$.

To characterize the field-independent transition, we perform Ramsey spectroscopy [Ramsey 63] on the two transitions $|A\rangle \leftrightarrow |\uparrow\rangle$ and $|\downarrow\rangle \leftrightarrow |\uparrow\rangle$ for different magnetic fields using the Ramsey frequency scan method. The data is shown in Fig. 4.3. The magnetic field is determined from the $\nu_{\uparrow A}$ measurement. By measuring $\nu_{\uparrow\downarrow}$ at $B = B_0$ for different RF trapping strengths and extrapolating to zero, we can determine the corresponding AC Zeeman shift produced by the trap's RF currents. This shift [1.81(2) Hz] was removed from the data in Fig. 4.3. The solid curve in Fig. 4.3 is calculated using the Breit-Rabi formula (see § 2.2).

We measure the qubit coherence time by adjusting the magnetic field to the minimum of Fig. 4.3 and performing Ramsey phase scans on the $|\downarrow\rangle \leftrightarrow |\uparrow\rangle$ transition for different Ramsey intervals T_R. The $^9\text{Be}^+$ ion is first Doppler cooled and prepared in the state $|\uparrow\rangle$. We then apply the rotation $R(\frac{\pi}{2}, 0)$, creating the superposition state $|\Psi_1\rangle = \frac{1}{\sqrt{2}}(|\uparrow\rangle - i|\downarrow\rangle)$ and wait for the Ramsey interval T_R during which the state evolves to $|\Psi_2\rangle = \frac{1}{\sqrt{2}}(e^{i\phi_D}|\uparrow\rangle - i|\downarrow\rangle)$. The phase ϕ_D is given by the integrated detuning of the Raman beams' frequency difference from the qubit transition frequency over the Ramsey interval T_R. The Raman beam's difference frequency is derived from a stable hydrogen maser based local oscillator which is itself periodically calibrated to the NIST

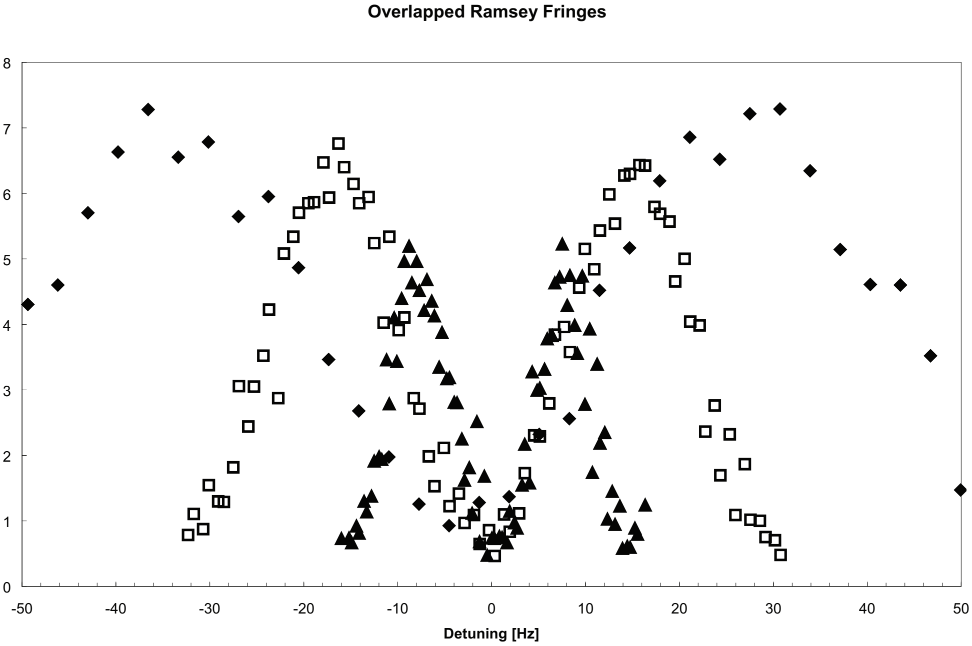

Figure 4.2: Frequency scans of the field-independent transition $|\downarrow\rangle \leftrightarrow |\uparrow\rangle$ for different Ramsey intervals T_R. The filled diamonds have $T_R \simeq 16$ ms; the open squares have $T_R \simeq 32$ ms; the filled triangles have $T_R \simeq 64$ ms.

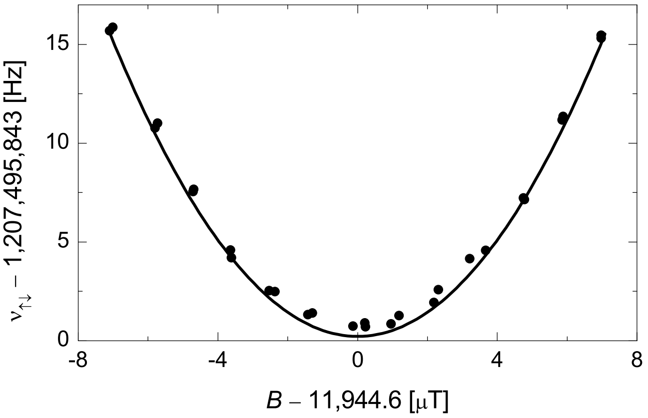

Figure 4.3: Field-independent transition frequency vs. magnetic field. The field-independent transition frequency (y-axis) is for the $|F = 2, m_F = 0\rangle$ ($|\downarrow\rangle$) $\leftrightarrow$ $|F = 1, m_F = 1\rangle$ ($|\uparrow\rangle$ transition). The x-axis is determined via frequency measurements of the field-dependent transition $|F = 2, m_F = 2\rangle \leftrightarrow |F = 1, m_F = 1\rangle$ near 1018 MHz. Circles are measured data; the solid curve is a theoretical prediction from the Breit-Rabi formula (see § 2.2). The statistical uncertainty in each datum is $\Delta B \lesssim 3$ nT and $\Delta\nu_{\uparrow\downarrow} \lesssim 0.3$ Hz. Figure taken from Ref. [Langer 05].

F1 cesium fountain clock. A second rotation $R(\frac{\pi}{2},\phi)$ is then applied with ϕ variable. Repeating the experiment many times and performing a projective measurement of the state $|\uparrow\rangle$ as described in § 2.4 ideally yields

$$P_\uparrow = \frac{1}{2}(1 - \cos{(\phi_D + \phi)}), \tag{4.3}$$

the probability of measuring the state $|\uparrow\rangle$. The measurement sequence is repeated for different phases ϕ, and the detected probability $P_\uparrow$ is fit to the function $f = a - \frac{b}{2}\cos{(d\phi + \phi_D)}$. The fit parameter d allows for magnetic-field drift in time as successive phase points are recorded sequentially; d is close to unity for all scans in this data set. Phase scans for $T_R = 4$ ms and 4 s are shown in Fig. 4.4a. Any fluctuation in ϕ_D during the Ramsey interval T_R will reduce the contrast b. The form of contrast decay vs. T_R is dependent on the spectrum of magnetic field noise which has components corresponding to times both long and short compared to T_R. The coherence time is limited in part by slow drift of the magnetic field over the measurement time scale of a single point. For the $T_R = 4$ s data in Fig. 4.4a, this time scale is 400 s. Moreover, since the measurement of the contrast can take many hours for the longer Ramsey intervals, the magnetic noise environment can vary over different points in Fig. 4.4b. As a benchmark, we fit the contrast b for different T_R to the exponential $b(T_R) = b_0 e^{-T_R/\tau}$ (Fig. 4.4b) and find $\tau = 14.7 \pm 1.6$ s. In principle, if the magnetic-field drift is small for the period of a single measurement, we can interrupt data collection to measure (via $\nu_{\uparrow A}$) and correct for magnetic-field deviations from B_0.

4.2 Magnetic Field Noise Model

Fitting the contrast to exponential decay, although useful as a bench marking tool, is somewhat naive. We can calculate the expected contrast as a function of time using the following simple model. Suppose we perform a Ramsey phase scan experiment with Ramsey interval T_R where the measurement after the final phase-scanned $\pi/2$

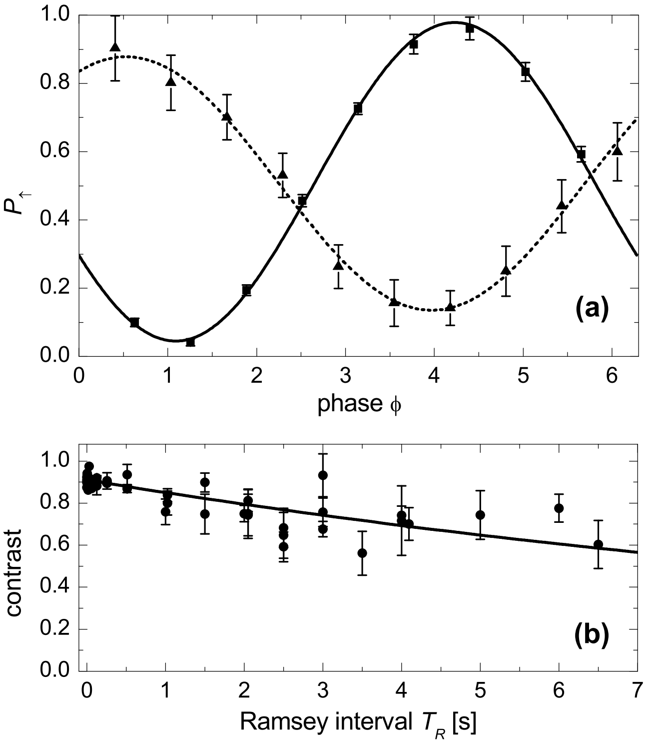

Figure 4.4: **(a)** Ramsey data at $T_R = 4$ ms (squares) and 4 s (triangles). The y-axis represents the probability of measuring the state $|\uparrow\rangle$. The contrast b for the 4 ms data is 0.933 ± 0.014 and for the 4 s data is 0.742 ± 0.043. The $\phi_D \simeq 1$ rad phase shift in the 4 ms data is due to detuning the local oscillator by the differential Stark shift (∼4.2 kHz) such that the Ramsey $\pi/2$-pulses are resonant. **(b)** Contrast vs. Ramsey interval T_R. Each datum represents the fitted contrast b for a phase scan with Ramsey interval T_R. The solid curve is a weighted least-squares fit to the data with reduced $\chi^2 \simeq 1.16$. Figure taken from Ref. [Langer 05].

pulse, averaged over many experiments, yields $A\cos(\phi+\phi_0) = 1 - 2P_\uparrow$ where $P_\uparrow$ is the probability of measuring $|\uparrow\rangle$ (see e.g. Eq. 4.3). Here, ϕ is the phase scan variable, and ϕ_0 is some constant offset phase arising from skewness the phase noise distribution, for example. We further assume that the local oscillator is tuned exactly to resonance and any bias in the measurement signal has been removed. Perfect contrast is defined by $A = 1$. Suppose that the accumulated phase noise is distributed according to some probability density function $p(x)$ which is responsible for the decrease in contrast A from the ideal $A = 1$. In the absence of phase noise (and hence perfect contrast), the final phase-scanned signal is given by $\cos\phi$. Given phase noise distributed according to $p(x)$, the actual measured signal is the expectation value of $\cos(\phi+x-\mu_x)$ with respect to the density function $p(x)$ where $\mu_x \equiv \langle x\rangle$ is the mean of the phase noise distribution. The phase noise with respect to its mean $x-\mu_x$ rather than x is added to ϕ because we assume that the local oscillator is tuned on resonance with the qubit transition frequency including the systematic frequency shift μ_x/T_R. Therefore, the actual measured signal is given by $A\cos(\phi+\phi_0) = \int p(x)\cos(\phi+x-\mu_x)\mathrm{d}x$ from which we can solve for A. Using the trigonometric identity $\cos(\alpha+\beta) = \cos(\alpha)\cos(\beta) - \sin(\alpha)\sin(\beta)$ and equating the coefficients of $\cos\phi$ and $\sin\phi$, we obtain the system of equations

$$\begin{aligned} A\cos(\phi_0) &= \langle\cos(x-\mu_x)\rangle \\ A\sin(\phi_0) &= \langle\sin(x-\mu_x)\rangle \end{aligned} \tag{4.4}$$

where $\langle f(x)\rangle$ is the expectation value of $f(x)$ according to the density function $p(x)$. The contrast can be calculated from $A^2 = \langle\cos(x-\mu_x)\rangle^2 + \langle\sin(x-\mu_x)\rangle^2$. For density functions symmetric about the mean where $p(\mu_x+x) = p(\mu_x-x)$, then $\langle\sin(x-\mu_x)\rangle = 0$, and $A = \langle\cos(x-\mu_x)\rangle$. For asymmetric density functions about the mean, $\langle\cos(x-\mu_x)\rangle$ gives a lower bound for the contrast. Therefore, the study of coherence decay induced by symmetric density functions is useful as it gives a lower bound to the contrast. In addition, in many practical situations such as transition frequencies which have a linear dependence on changes in the magnetic field, the phase probability density function is symmetric about the mean, and the contrast is given by $\langle\cos(x-\mu_x)\rangle$. As mentioned above, asymmetric density functions will have a non-zero phase offset ϕ_0.

For the remainder of this section, we assume, without loss of generality, that the density function $p(x)$ has mean 0. In practice, if the mean of the phase noise density function is not zero, we can simply redefine the qubit frequency to take this systematic phase shift over the Ramsey interval into account. As a simple example, suppose the phase noise is distributed by the gaussian distribution: $p(x) = \exp(-x^2/2\sigma_x^2)/\sqrt(2\pi)\sigma_x$ where σ_x^2 is the variance in the phase probability density. Because $p(-x) = p(x)$, the equation for the contrast simplifies to:

$$\begin{aligned} A &= \int_{-\infty}^{\infty} p(x)\cos(x)\mathrm{d}x \\ &= e^{-\sigma_x^2/2}. \end{aligned} \tag{4.5}$$

For symmetric phase probability density functions, the contrast is $A = \langle\cos(x)\rangle = \langle 1 - x^2/2! + x^4/4! - \cdots\rangle \simeq \exp(-\sigma_x^2/2)$ for any symmetric probability density function with negligible probability density for $x > 1$. For gaussian distributed phase noise, Eq. (4.5) is exact. For other density functions, as long as the standard deviation σ_x is small compared to 1 and higher moments are also small, Eq. (4.5) is a valid approximation. In particular, for asymmetric distributions, the contrast is given as in Eq. (4.5) with the variance σ_x^2 modified by a factor $1 - \frac{1}{36}\frac{\mu_3^2}{\sigma_x^2}$ where $\mu_3 \equiv \langle(x-\mu_x)^3\rangle$ is the third moment about the mean. To determine how the contrast A decays with time, we must determine how the variance σ_x^2 changes with Ramsey interval T_R and substitute it into Eq. (4.5).

We assume the magnetic field deviation ΔB is distributed according to the probability density function $p_B(\Delta B)$ and the qubit transition frequency has zero first order dependence on changes in the magnetic field. This in turn will distribute the frequency shifts from resonance $\omega = c_2\Delta B^2$ according to $p(\omega) = p_B(\Delta B(\omega))/\frac{d\omega}{d\Delta B} \times$

(multiplicity of $\Delta B(\omega)$) $= p_B(\sqrt(\omega/c_2))/\sqrt(c_2\omega)$ by the fundamental transformation law of probabilities [Freund 92, Press 03]. This density function has a non-zero mean, and we tune the local oscillator to account for this such that we have an effective asymmetric density function $p(\omega)$ centered at $\omega = 0$. The constant $c_2 \simeq 2\pi \times 0.3$ rad s^{-1} μT^{-1} is taken from Table 2.1.

As a model, we let the frequency shifts from resonance ω induced by fluctuating magnetic fields randomly change every sample interval T_s according to the distribution $p(\omega)$. The k^{th} sample taken from $p(\omega)$ is ω_k, and the frequency ω_k is held constant over the T_s interval. Here, the amplitude of phase fluctuations is described by $p(x)$, and the spectrum is described by T_s (i.e. the frequency of noise in this model is $1/T_s$). For T_s much less than the Ramsey interval T_R, the phase x is approximated by

$$x = T_s \sum_{k=1}^{N} \omega_k \tag{4.6}$$

where $N \equiv \text{floor}(T_R/T_s)$,[2] and we have neglected the remaining time interval $T_R - T_s N$. (Because $\frac{T_R}{T_s} - 1 < N \leq \frac{T_R}{T_s}$, the remaining interval $T_R - T_s N$ is less than T_s which we assume is much less than the Ramsey interval T_R.) The phase x as a random variable is well described by the random walk problem with variable step size [Reif 65, §1.9] where the step size ω_k is taken from the distribution of frequency shifts from resonance $p(\omega)$. Frequency noise modeled in this manner is termed "random walk frequency modulation" (RWFM) in the time metrology literature. Phase noise generated by RWFM is an integrated Wiener noise. Solutions to this problem in terms of stochastic differential equations are given in [Galleani 03].

Independent of the density function $p(\omega)$, the variance in the phase x is

$$\sigma_x^2 = N T_s^2 \sigma_\omega^2 \simeq T_R T_S \sigma_\omega^2 \tag{4.7}$$

where σ_ω^2 is the variance of $p(\omega)$. To see this, we simply take the expectation value of the square of Eq. (4.6) and note that factors of the form $\langle \omega_j \omega_k \rangle = \langle \omega_j \rangle \langle \omega_k \rangle = 0$ for $j \neq k$

---

[2] The function floor(x) is defined as the largest integer less than or equal to the real number x.

because different random frequencies drawn from $p(\omega)$ are independent. Therefore, the only non-zero terms in $\langle x^2\rangle$ are the N terms of the form $T_s^2\langle\omega_k^2\rangle$, and hence we arrive at Eq. (4.7) (remember, $\langle x\rangle = 0$). For $T_s \ll T_R$, the variance in the phase is linear in the Ramsey interval T_R, and the contrast decays exponentially with time constant $\tau = 2/(T_s\sigma_\omega^2)$. We note that for field independent transitions, the frequency probability density function is not symmetric, and the approximation of Eq. (4.5) is a lower bound valid only for small σ_x^2.

We now consider the general case with no restrictions on the size of T_s. We first consider the case where $T_R \geq T_s$ ($N \geq 1$). The time of the first frequency change t_1 occurs randomly within the interval $[0, T_s)$[3] after which successive frequency changes occur every T_s interval after t_1. The last interval is in general less than T_s. We let the t_1 random variable be uniformly distributed over the first T_s interval. There are two cases to consider (see Fig. 4.5). First, if $t_1 < T_R - NT_s$, then there are N intervals of length T_s and two intervals shorter than T_s, namely t_1 and the last interval t_L which make up the entire Ramsey interval T_R. The last interval is never independent. In this first case, it is $t_L = T_R - NT_s - t_1$. The second case occurs when $t_1 \geq T_R - NT_s$. Here there are $N-1$ intervals of length T_s, and the final interval is $t_L = T_R - (N-1)T_s - t_1$. The Ramsey interval T_R only has enough duration to allow N steps of size T_s if the first interval is less than the remainder $T_R - NT_s$; therefore, if t_1 is greater than this value, the last T_s interval vanishes.

We wish to calculate the variance in the phase $\sigma_x^2 = \langle x^2\rangle$. For $T_R \geq T_s$, the phase random variable is given by:

$$x = \begin{cases} \omega_1 t_1 + \omega_L(T_R - NT_s - t_1) + \sum_{k=2}^{N+1}\omega_k & \text{for } t_1 < T_R - NT_s \\ \omega_1 t_1 + \omega_L[T_R - (N-1)T_s - t_1] + \sum_{k=2}^{N}\omega_k & \text{for } t_1 \geq T_R - NT_s \end{cases}, \tag{4.8}$$

where ω_k for $k \in \{1, 2, .., N+1, L\}$ are all independent. We can simplify this equation

---

[3] The notation $[a, c)$ defines an interval such that $b \in [a, c)$ is equivalent to ($\Leftrightarrow$) $a \leq b < c$. Similarly, $b \in (a, c) \Leftrightarrow a < b < c$ and $b \in (a, c] \Leftrightarrow a < b \leq c$.

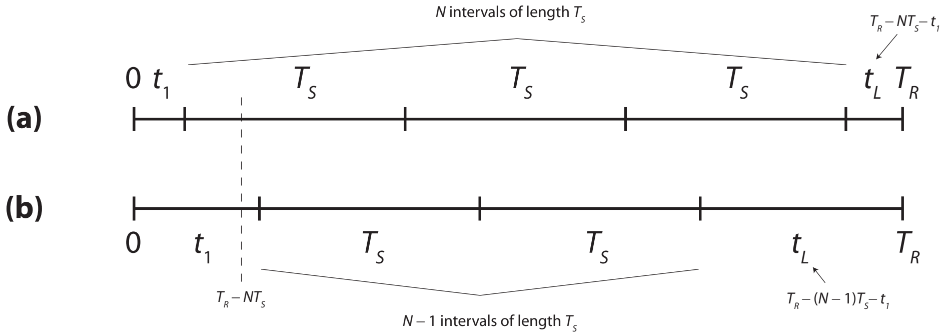

Figure 4.5: Sample magnetic field change intervals for $N \equiv \text{floor}(T_R/T_s) = 3$. The first interval t_1 is uniformly distributed in the interval $[0, T_s)$. **(a)** $t_1 < T_R - NT_s$ case: there are N intervals of size T_s. **(b)** $t_1 \geq T_R - NT_s$ case: there are $N-1$ intervals of size T_s. In all cases, the last interval t_L is dependent on t_1.

by introducing $g_1(t_1) \equiv 1$ if $t_1 \in [0, T_R - NT_s)$, otherwise $g_1(t_1) = 0$. Eq. (4.8) can now be rewritten as:

$$x = t_1\omega_1 + [T_R - (N-1)T_s - (t_1 + T_s g_1)]\omega_L + g_1 T_s \omega_{N+1} + T_s \sum_{k=2}^{N} \omega_k. \tag{4.9}$$

The phase variance is calculated by evaluating $\langle x^2 \rangle$ using Eq. (4.9) and the fact that different ω_k are independent. As such, the phase variance is the sum of the variances of each term with a different ω_k, and all terms are proportional to σ_ω^2. The result is:

$$\frac{\langle x^2 \rangle}{\sigma_\omega^2} = \langle t_1^2 \rangle + \langle [T_R - (N-1)T_s - (t_1 + T_s g_1)]^2 \rangle + T_s^2 \langle g^2 \rangle + (N-1)T_s^2. \tag{4.10}$$

We observe that we must evaluate expectation values of g_1, g_1^2, t_1, t_1^2, and $g_1 t_1$. Since t_1 is uniformly distributed over the $[0, T_s)$ interval, these are easily calculated. After evaluation, substitution, and simplification, the phase variance simplifies a great deal to:

$$\langle x^2 \rangle = \left(\frac{T_R}{T_s} - \frac{1}{3} \right) T_s^2 \sigma_\omega^2 \tag{4.11}$$

for $T_R \geq T_s$.

For $T_R < T_s$ ($N = 0$), the Ramsey interval T_R has either two intervals both less than T_R or a single interval equal to T_R. The probability of having two intervals with different frequency deviations is T_R/T_s. This can be understood by thinking about many repetitions of the experiment performed sequentially. If the frequency deviation changes every T_s, then floor(T_s/T_R) experiments will all have the same frequency, and the frequency will change in the middle of the next experiment. Therefore, the probability of having a frequency change in a single experiment is T_R/T_s. We model this by letting the random variable t_1 be uniformly distributed over the $[0, T_s)$ interval, and if a particular sample t_1 happens to lie in the interval $[0, T_R)$, we let the frequency change at t_1. In this case, the phase is $x = t_1\omega_1 + (T_R - t_1)\omega_2$. If t_1 happens to be within the interval $[0, T_R)$, the Ramsey interval experiences only a single frequency, and $x = T_R\omega_2$. We can introduce the function $g_2(t_1) = t_1$ if $t_1 \in [0, T_R)$, otherwise $g_2(t_1) = 0$, similar to before, to rewrite the phase as $x = g_2\omega_1 + (T_R - g_2)\omega_2$. After calculating the intermediate expectation values $\langle g_2 \rangle$ and $\langle g_2^2 \rangle$, the phase variance simplifies to

$$\langle x^2 \rangle = \left(1 - \frac{1}{3}\frac{T_R}{T_s}\right) T_R^2 \sigma_\omega^2 \tag{4.12}$$

for $T_R < T_s$. Summarizing, the phase variance as a function of the Ramsey interval T_R is:

$$\sigma_x^2 = \begin{cases} \left(1 - \frac{1}{3}\frac{T_R}{T_s}\right) T_R^2 \sigma_\omega^2 & \text{for } T_R < T_s \\ \left(\frac{T_R}{T_s} - \frac{1}{3}\right) T_s^2 \sigma_\omega^2 & \text{for } T_R \geq T_s \end{cases} . \tag{4.13}$$

A few remarks on Eq. (4.13) are in order. First, σ_x^2 and its first two derivatives with respect to T_R are continuous across the $T_R = T_s$ boundary. Furthermore, the discrete function $N = \text{floor}(T_R/T_s)$ has dropped out of the equation, and σ_x^2 is a smooth function of T_R. Finally, as before, for long Ramsey intervals $T_R \gg T_s$, the decay is exponential, and for short Ramsey intervals $T_R \ll T_s$, the decay is gaussian. This is the best of both worlds. The long time behavior has decaying contrast which is slower than gaussian, namely exponential, and the short time behavior has decaying contrast which is slower than exponential, namely gaussian. We might suspect that the 14.7 s coherence time measured in the previous section might have short term errors during the measurement interval quadratically smaller than the 10^{-5} level proclaimed in [Langer 05].

The coherence time is defined as the Ramsey interval T_R where the contrast decays to the e^{-1} level. In this model, this occurs when $\sigma_x^2 = 2$. Defining $y = T_R/T_s$ and $a = T_s\sigma_\omega$, we must solve $(1 - \frac{y}{3})y^2a^2$ for $y < 1$ and $(y - \frac{1}{3})a^2$ for $y \geq 1$. For $y \geq 1$, the solution is $y_0 = \frac{2}{a^2} + \frac{1}{3}$ requiring $a^2 \leq 3$. That is, for low noise levels and fast modulation frequencies, the coherence time lies in the exponential decay section. Solving $\sigma_x^2 = 2$ for $y < 1$ gives the equation $y^3 - 3y^2 + b = 0$ where $b = \frac{6}{a^2} \in (0, 2)$ because $a^2 > 3$. This cubic equation only has one solution which is physically viable, namely $y_0 = 1 + 2\cos(\frac{\theta - 2\pi}{3})$ where $\theta = \tan^{-1}(\frac{\sqrt{3(2a^2-3)}}{a^2-3})$. Summarizing, the coherence

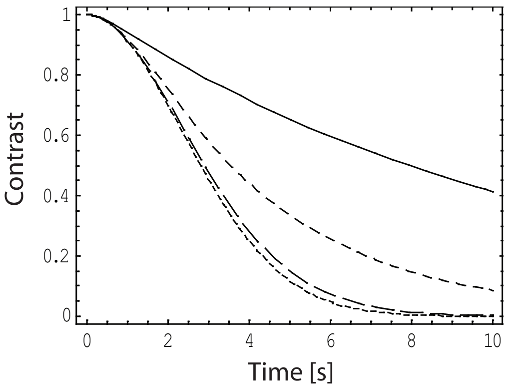

Figure 4.6: Theoretical contrast decay vs. Ramsey interval. The curves are the contrast vs. T_R for different sample intervals T_s. T_s in the figure (top down) is: 1 s, 3 s, 10 s, and 30 s. The magnetic field uncertainty is $\sigma_B = 0.4$ μT.

time τ in this model is given by:

$$\tau = \begin{cases} \frac{1}{3} + \frac{2}{T_s^2\sigma_\omega^2} & T_s^2\sigma_\omega^2 \leq 3 \\ 1 + 2\cos\left(\frac{\theta - 2\pi}{3}\right) & T_s^2\sigma_\omega^2 > 3 \end{cases} \tag{4.14}$$

where $\theta \equiv \tan^{-1}\left(\frac{\sqrt{3(2T_s^2\sigma_\omega^2 - 3)}}{T_s^2\sigma_\omega^2 - 3}\right)$. We note that there exists continuity of the coherence time across the $T_s^2\sigma_\omega^2 = 3$ boundary.

Sample contrast decay curves are shown in Fig. 4.6. The quadratic decay at short times is indicative of the gaussian decay in this section. In the laboratory, a dominant source of magnetic field noise occurs at 60 Hz due to noise in AC line currents in the walls and electronic instruments. Using the model with $T_s = 0.0167$ s (the period of 60 Hz) and the measured $\tau = 14.7$ s coherence time, we find the uncertainty in the magnetic field at 60 Hz to be $\sigma_B = 1.0$ μT. This is approximately an order of magnitude higher than we measure in the laboratory indicating that 60 Hz noise is not the limiting factor in the 14.7 s coherence time. Rather, slow magnetic field drift with $T_s \gg T_R$ is more likely the cause. Nevertheless, assuming that all of noise is in the 60 Hz spectral line, we can calculate the memory errors during 1-qubit and 2-qubit gates as well as the measurement interval. Remember, the contrast is a function of the $T_s\sigma_\omega$ product;

therefore, even though the 1 μT noise field at 60 Hz is artificially high, the product $T_s\sigma_\omega$ is in agreement with the measured 14.7 s coherence time. Using the model, the error during a 1-qubit gate (1 μs) is 4×10^{-12}, 2-qubit gate (10 μs) is 4×10^{-10}, and measurement interval (100 μs) is 4×10^{-8}, all much below the fault-tolerance threshold of 10^{-4} for the Steane code [Steane 03]. We note that the region of validity where Eq. (4.5) represents a lower bound to the contrast is when σ_x^2 is small, which is definitely the case here.

In summary, for short times, memory errors are quadratic in the time interval, and at all times, memory errors scale as the magnetic noise amplitude to the fourth power. Therefore, with minimal speed and minimal shielding, the memory errors induced by magnetic field noise can be suppressed to very low levels. We note that such small memory errors are extremely difficult to measure and these arguments are estimates only. We also point out that slow magnetic field drift ($T_s \gg T_R$) plays a strong role in the decoherence. However, slow drift is relatively easy to correct using slow feedback control. The next section addresses this issue.

4.3 Magnetic Field Drift

Slow magnetic field drift, as seen in the previous section, can cause significant memory decoherence. Fortunately, slow time scale drift can be controlled via feedback. For the measurements in § 4.1, no feedback was implemented. As seen in Fig. 4.7a, the magnetic field drift can vary from day to day. The drift on Jan. 21, 2005 in Fig. 4.7a is tolerable, whereas the drift on Jan. 28, 2005 is not. We remove drift by periodically interrupting the experimental sequence to measure the magnetic field via Ramsey spectroscopy on an auxiliary transition which depends linearly on the magnetic field deviation. The measurement is then used to null the field deviation with separate feedback coils. The stabilized magnetic field is shown in Fig. 4.7b. The transition used to interrogate the magnetic field was $|F=2, m_F=2\rangle \leftrightarrow |F=2, m_F=1\rangle$ at 0.01196 T (transition frequency is 103 MHz).

The inset in Fig. 4.7b indicates that our magnetic field servo system stabilizes the slow magnetic field drift to zero offset from the set point. The scatter in the data is due to statistical uncertainty in the frequency measurements of the $|F = 2, m_F = 2\rangle \leftrightarrow |F = 2, m_F = 1\rangle$ transition frequency. For the measurements in Fig. 4.7b, Ramsey frequency measurements were performed with a Ramsey interval of $T_R = 100$ μs and averaging for $N = 100$ experiments on each side of the Ramsey fringe. With perfect contrast, we would expect statistical uncertainty in the measured magnetic field to be 0.015 μT. The sample standard deviation in the data of the inset in Fig. 4.7b is 0.017 μT, consistent with statistical measurement uncertainty assuming Ramsey fringe contrast of 88%.

4.4 Heating Induced Measurement Degradation

One challenge we faced while taking the measurements of § 4.1 was detection degradation induced by ion heating. The experiments inherently required leaving the ion in the dark for periods on the order of seconds, and consequently, the ion would acquire kinetic energy. The mechanisms responsible for ion heating are not well understood, and this is still an active area of research [Deslauriers 06, Wineland 98, Turchette 00]. The most likely candidate is fluctuating patch potentials on electrode surfaces. Measurements of the heating rate for short intervals are described in § 2.5.4.

The measurement prescription described in § 2.4 is immune to small amounts of heating. However, when left in the dark for many seconds, the ion's kinetic energy is large enough to reduce the scattering of the detection beam due to Doppler broadening. We performed the following experiment to measure the detection loss due to heating. A single ion was Doppler cooled and prepared in the bright $|F = 2, m_F = 2\rangle$ state. The ion was then left in the dark in the absence of cooling for a variable duration after which the ion was detected. Data are shown in shown in Fig. 4.8. Detection loss for John Jost's trap is better than that of Brian DeMarco's trap by approximately an order

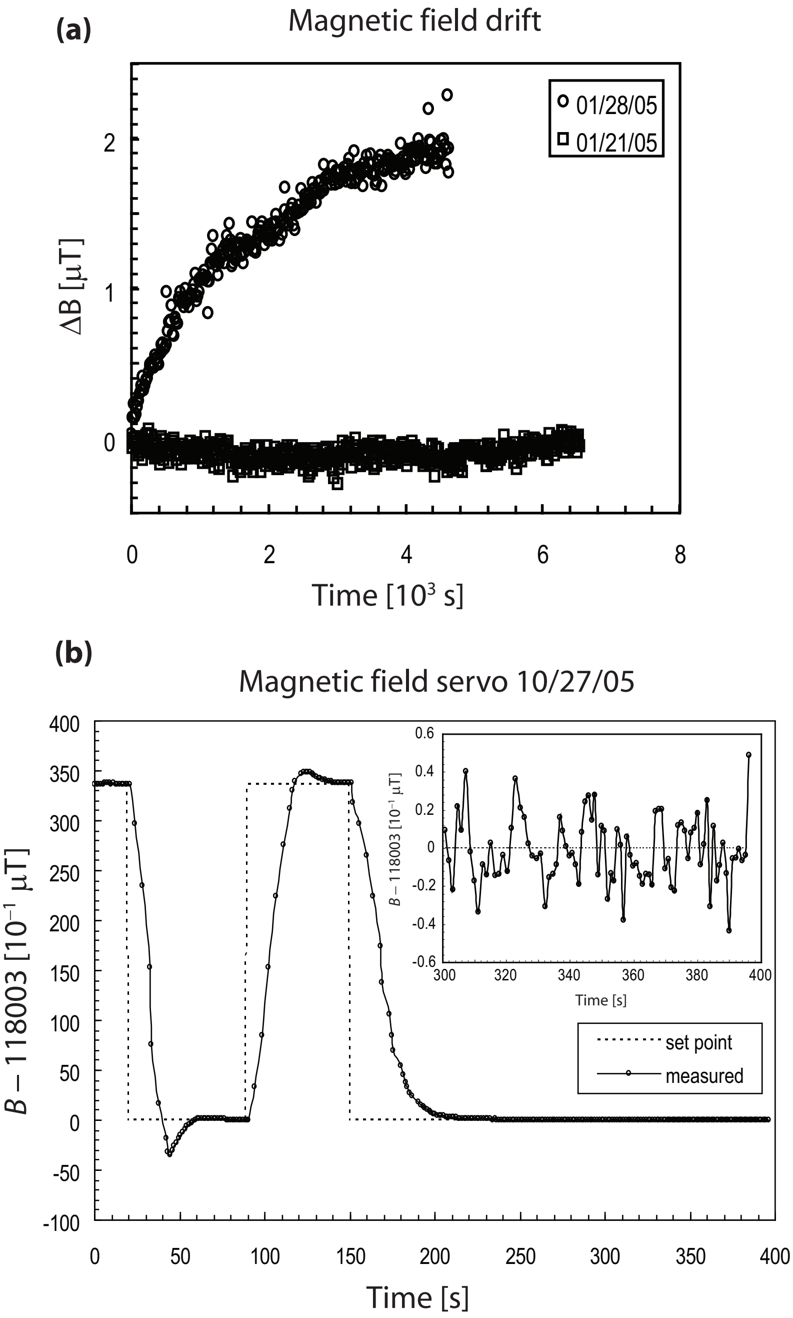

Figure 4.7: Magnetic field drift and servo. **(a)** Typical magnetic field drift for two different days without feedback. **(b)** Stabilized magnetic field drift via slow feedback. The dashed line is the magnetic field set point. The open circles are measurements of the magnetic field via frequency measurements of the $|F = 2, m_F = 2\rangle \leftrightarrow |F = 2, m_F = 1\rangle$ transition. The inset in **(b)** is a close up view of the measured magnetic field data for times 300 − 400 s after the start of the graph. The magnetic field is stabilized at this point, and the scatter in the data is due to statistical uncertainty in the frequency measurements.

of magnitude. In John Jost's trap, the amount of Doppler cooling during initialization did not appear to play a role.

We model the detection loss induced by heating using the following simple model. First, assume the momentum p of the ion is gaussian distributed with mean zero and width $\sqrt(\langle p^2\rangle)$. If the mean were not zero, the ion would fail to be trapped. Here, $\langle p^2\rangle$ is expectation value of p^2 and is equal to the variance of p given that the mean is zero. We further assume that the trap frequency is small compared to the natural line width of the excited ${}^2P_{3/2}$ state. The photon scattering rate of the detection laser detuned by δ from the cycling transition resonance ($|{}^2S_{1/2}, F = 2, m_F = 2\rangle \leftrightarrow |{}^2P_{3/2}, F = 3, m_F = 3\rangle$) for an ion originally prepared in the bright state $|F = 2, m_F = 2\rangle$ is given by

$$f(\delta) = \frac{\gamma}{2}\frac{s_0}{1 + s_0 + \frac{4\delta^2}{\gamma^2}} \tag{4.15}$$

where γ is the natural line width of the $|{}^2P_{3/2}, F = 3, m_F = 3\rangle$ state, and s_0 is the on-resonance saturation parameter. With the detection laser tuned on resonance, an ion with momentum p along the trap axis $\hat{z}$ will see the detection laser Doppler shifted from resonance by an amount $\delta = k_{\text{eff}}p/m$ where $k_{\text{eff}} = \vec{k} \cdot \hat{z}$ is the projection of the detection laser's wave vector along the trap axis. We can now write the on-resonance photon scattering rate as a function of the ion's momentum as

$$f(p) = \frac{b}{1 + \frac{4p^2}{\Delta p^2}} \tag{4.16}$$

where $b \equiv \frac{\gamma}{2}\frac{s_0}{1+s_0}$, and $\Delta p \equiv \frac{m\gamma'}{k_{\text{eff}}}$ is the Lorentzian width of the scattering rate measured in units of momentum. Here, m is the mass of the ion, and $\gamma' \equiv \gamma\sqrt(1 + s_0)$ is the power broadened line width. We let

$$g(p|\langle p^2\rangle) = \frac{1}{\sqrt{2\pi\langle p^2\rangle}}e^{-\frac{1}{2}\frac{p^2}{\langle p^2\rangle}} \tag{4.17}$$

be the conditional probability density for the ion's momentum given the variance in the momentum distribution is $\langle p^2\rangle$. For an ion in the ground state of a harmonic oscillator,

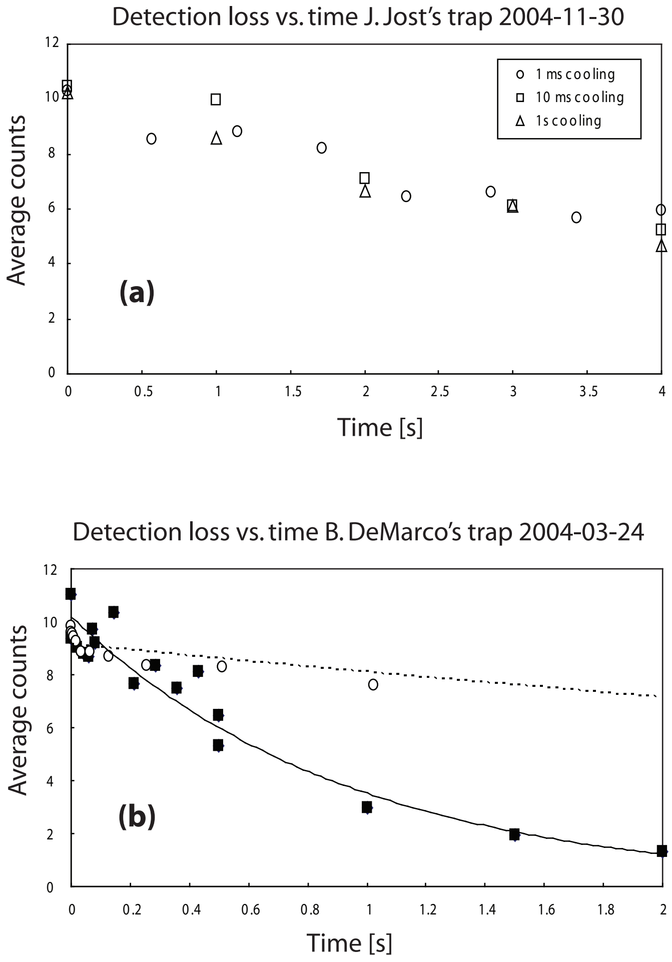

Figure 4.8: Detection loss induced by ion heating. **(a)** Measurements in John Jost's trap on Nov. 30, 2004. **(b)** Filled squared are measurements in Brian DeMarco's trap on Mar. 24, 2004. The open circles with the dashed trend line are the fitted means of the bright distribution from Ramsey phase scan data as a function of Ramsey interval T_R. Data was taken on August 10, 2004 on a single ^{9}Be$^+$ ion with sympathetic Doppler cooling being performed on a simultaneously stored ^{24}Mg$^+$ ion in the same trap. We observe that the detection loss induced by ion heating is reduced in this case.

Eq. (4.17) is an exact description of the probability of measuring the ion's momentum with the variance given by $\langle p^2 \rangle = \frac{1}{2} p_0^2 = \frac{1}{2}\hbar m\omega$, half of the square of the momentum wave function spread p_0. Here, ω is the harmonic oscillation frequency. At low thermal energies where the ion's momentum state is a statistical mixture of the lowest momentum Fock states, Eq. (4.17) is a rather poor description. However, as we will see below, in terms of calculating the detection laser scattering rate, it is sufficient. In addition, for large energies on the order of a few hundred or more, the ion's momentum distribution in thermal equilibrium is gaussian, and Eq. (4.17) is a good approximation.

The variance in the momentum can be calculated using the Virial theorem which states that for a system of harmonic oscillators in thermal equilibrium, the total energy of the system is equally divided between the kinetic energy and the potential energy [Pathria 96]. For the quantum harmonic oscillator, we find $\langle \frac{p^2}{2m} \rangle = \frac{1}{2}\langle E \rangle = \frac{1}{2}(\langle n \rangle + \frac{1}{2})\hbar\omega$. Therefore, the momentum variance can be expressed in terms of the average harmonic oscillator occupation number $\langle n \rangle$ as $\langle p^2 \rangle = (\langle n \rangle + \frac{1}{2}) p_0^2$.

The thermal average scattering rate for an ion in a thermal average occupation number $\langle n \rangle$ can be expressed as

$$\begin{aligned} h(\langle n \rangle) &= \int_{-\infty}^{\infty} f(p) g(p|\langle p^2 \rangle) \mathrm{d}p \\ &= \frac{b}{\sqrt{2\pi(\langle n \rangle + \frac{1}{2})p_0}} \int_{-\infty}^{\infty} \frac{1}{1 + 4\frac{p^2}{\Delta p^2}} e^{-\frac{1}{2}\frac{p^2}{(\langle n \rangle + \frac{1}{2})p_0^2}} \mathrm{d}p \qquad (4.18) \\ &= \frac{b}{\sqrt{\pi}} e^{\Delta y^2} \pi \Delta y \ \mathrm{erfc}(\Delta y) \end{aligned}$$

where $\Delta y = \frac{\Delta p}{2p_0\sqrt{2\langle n \rangle + 1}} = \frac{\gamma'}{2k_{\mathrm{eff}}}\sqrt{\frac{m}{\hbar\omega(2\langle n \rangle + 1)}}$, and $\mathrm{erfc}(x) \equiv 1 - \frac{2}{\sqrt{\pi}} \int_0^x e^{-t^2} \mathrm{d}t$ is the complimentary error function of x. The integral in Eq. (4.18) is similar to the integral in the Voigt profile, a spectral line shape common in many branches of spectroscopy which arises from Doppler broadening of a Lorentzian profile. The Voigt profile is the convolution of a gaussian distribution with the Lorentzian distribution. In Eq. (4.18) we integrated over these two distributions and did not take the convolution resulting in the

Voigt profile evaluated at line center. This is a consequence of the fact that we tuned the detection laser on resonance. If we would have left the detuning of the detection laser as a free parameter, h would have been a Voigt profile function of the detuning.

A plot of Eq. (4.18) is shown in Fig. 4.9a. We observe that for $^9\mathrm{Be}^+$ ions in a $\omega = 2\pi \times 4$ MHz trap with the detection laser beam direction oriented 45° to the trap axis with half of the saturation intensity, the on-resonance scattering rate drops to half of its original value after the ion heats up to a motional occupation number of $\langle n \rangle \simeq 420$. The dashed curve in Fig. 4.9a was obtained by calculating the expectation value of the scattering rate for a statistical mixture of momentum space wave functions based on a thermal distribution with mean phonon occupation number $\langle n \rangle$. We truncated the sum of expectation values for Fock state momentum space wave functions at $n = 500$, hence the two plots disagree for $\langle n \rangle \gtrsim 200$. We observe that the two approaches agree well for $\langle n \rangle \lesssim 200$ which was the region where we were originally unsure that the gaussian distribution of momentum was valid. Recall from § 2.5.1 that the measured heating rate for John Jost's trap was $\langle \dot{n} \rangle \simeq 0.25\ \mathrm{ms}^{-1}$. Naively assuming the heating rate is constant over this temperature range, we expect the ion to obtain a temperature $\langle n \rangle \simeq 500$ after 2 seconds in the dark causing the on-resonance scattering rate to drop to approximately half. This appears consistent with the data in Fig. 4.8.

The appropriate method for dealing with detection loss is sympathetic cooling (see [Barrett 03]). However, for the long coherence time measurements, we handled this problem using data analysis. For each Ramsey interval T_R, we collected histograms of photon counts for each phase point. In general, these histograms were bimodal with one mode near zero (the dark distribution mean) and the other near 10 (the bright distribution mean). Because of detection loss induced by ion heating during the Ramsey interval, the bright mean would drop for the longer Ramsey intervals. We desired to extract the means of the bright and dark distributions so that we could fit the histograms to a sum of two poisson reference histograms, one for the bright distribution and one

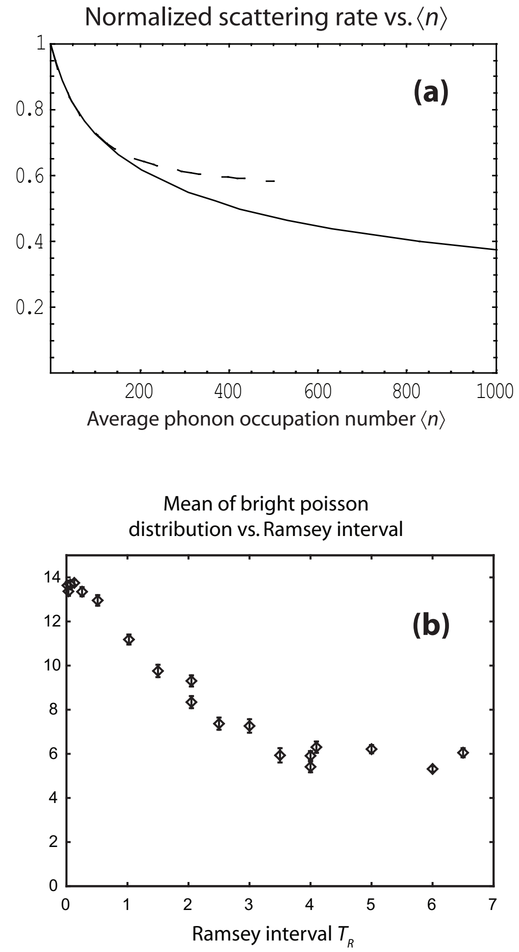

Figure 4.9: **(a)** Detection loss induced by ion heating—theory. Solid curve is calculated using Eq. (4.18). Dashed curve is calculated by taking the expectation value of the scattering rate for a statistical mixture of momentum space wave functions based on a thermal distribution with mean phonon occupation number $\langle n\rangle$. The sums in the wave function calculation are truncated at $n = 500$, hence the departure of the two curves near $\langle n\rangle \simeq 200$. **(b)** Mean of the poisson distribution for the bright state as a function of Ramsey interval T_R. The mean is determined by fitting a sum of two poisson distributions with variable means to the sum of all histograms with same T_R for the data in Fig. 4.4a.

for the dark distribution (see method of maximum likelihood in Appendix C). Since the means of the reference histograms would vary as a function of Ramsey interval, using the same means for the reference poisson distributions would yield bad fit results. Therefore, we determined the means for the bright and dark reference poisson distributions by summing the histograms for all phase points for an individual Ramsey interval T_R and fit this histogram to a sum of two poisson distributions with variable means using the method of maximum likelihood (see Appendix C). Then, the histograms for each phase point were fit to a weighted sum of two poisson distributions with fixed mean given by the previous step. The weight parameter determined the fraction of experiments for each phase point where the bright state was inferred. We then plotted the probability of measuring the bright state as a function of phase and fit it to the phase scan function as described in § 4.1 to obtain the contrast. The mean of the bright distribution as a function of Ramsey interval extracted in this manner was similar to the data in Fig. 4.8 and is shown in Fig. 4.9b.

4.5 Systematics at the Field-Independent Point

Fluctuating systematic frequency shifts of the qubit transition can be a source of phase noise in QIP experiments. Therefore, we performed a simple study of the systematic frequency shifts in our system. In regards to long coherence times, we only concerned ourselves with systematic frequency shifts on the order of 1 Hz or larger. Therefore, I do not do a full systematics study in this section. Rather, I cover only those shifts which were detectable on the 1 Hz level or higher and those which caused problems on the way to the 15 seconds coherence time.

The second largest frequency shift was due to the second order AC Zeeman effect. Recall that field independent transitions have a second order dependence on the magnetic field and can be expressed by a Taylor series expansion about the magnetic field extremum:

$$\omega(B) = \omega_0 + c_2 \Delta B^2 \tag{4.19}$$

where ΔB is the deviation of the magnetic field from the field-independent point, ω_0 is the qubit transition frequency at $\Delta B = 0$, and c_2 is the second-order coefficient (see Table 2.1 in § 2.2). From Eq. (4.19) we find that an oscillating magnetic field will induce a frequency shift in the amount of $c_2\langle \Delta B^2 \rangle = c_2 \langle B^2 \rangle$. We note that this shift is proportional to the square of the amplitude of an oscillating magnetic field; it is independent of the oscillation frequency, and its sign is given by the sign of c_2.

The largest source of oscillating magnetic field was RF currents in the trap's RF electrodes. We characterized the frequency shift induced by these currents by measuring the qubit transition frequency for different RF input power levels to the resonator. Because the RF power stored in the resonator is proportional to both the input power and the average of the square of the magnetic field, the systematic frequency shift is linear in the input RF power. For Brian DeMarco's trap, the qubit frequency shift vs. RF power is shown in Fig. 4.10. We find the slope of the shift vs. RF input power to be 2.27(2) Hz/W. For the data in Fig. 4.3, the trap was operated at 0.80 W inducing an AC Zeeman shift of 1.81 Hz. This shift was removed from the data in Fig. 4.3.

Because strong RF electric fields are required for trapping, we could not eliminate AC Zeeman shift induced by the trap completely. However, we were able to operate the trap at the weakest strength allowable to minimize the AC Zeeman shift. Fortunately, only fluctuations in frequency shifts cause decoherence. At the trap's weakest point, the AC Zeeman shift was approximately 0.5 Hz. We estimated the RF power stored in the resonator to be more stable than 1%. Therefore, the estimated uncertainty in the qubit frequency due to the trap's RF currents was roughly 5 mHz.

The third largest systematic frequency shift was the AC Stark shift of near resonant leakage light from the detuned BD laser beam. The reason for BD detuned leakage

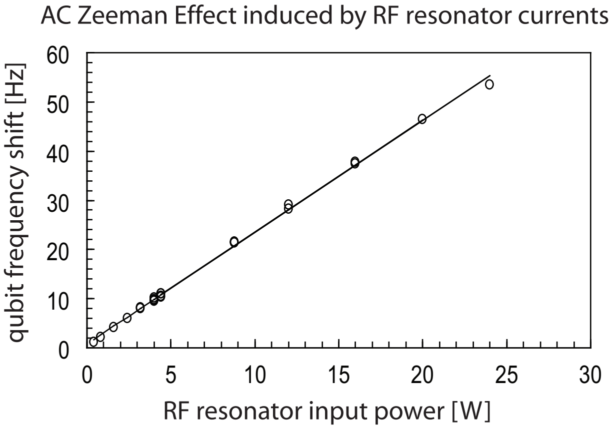

Figure 4.10: Systematic AC Zeeman shift in Brian DeMarco's trap. Data was taken on June 29, 2004. Open circles are measurement data; solid line is a linear best fit. The slope of the shift is 2.27(2) Hz/W.

light was the existence of a single-pass AOM switch used to block the beam (see § 3.3.2 Fig. 3.5). Using a double-pass AOM configuration as a switch may have mediated this problem somewhat. The detuned BD laser beam had a few hundred μW of optical power focused to a spot size of roughly 30 μm when turned on and was tuned approximately 400 MHz to the red of the detection cycling transition (see § 3.3.2). The shift induced by leakage light from this beam was measured to be as high as 30 Hz. We reduced this shift by attenuating the laser beam by 26 dB with a neutral density filter. The differential AC Stark shift of the qubit transition is linear in the optical power. Therefore, we estimated this shift to be approximately 80 mHz. In principle, optical shutters can be used to reduce this shift even further.

In addition to leakage light shifts and second order Zeeman shifts, we checked for Stark shifts of the ^{24}Mg^{+} laser, spatial dependence of the second order Zeeman effect along the trap axis, and shifts induced by the room lights. None of these had any measurable shift detectable at the 1 Hz level.

Chapter 5

Off-Resonant Spontaneous Photon Scattering

In Ch. 2 I showed how to implement the requirements for quantum computation with ions. In particular, the universal quantum gate set (single qubit rotations and a two-qubit entangling gate) is implemented by interacting the ions with off-resonant laser beams. Therefore, it is necessary to consider the decoherence of quantum information stored in ions due to the presence of off-resonant laser light.

For laser sources, the quantum description of the light is closely approximated by a coherent state of the quantum electro-magnetic field [Loudon 00, § 7.4 pp. 304–310]. Furthermore, a coherent state of light is equivalent to a classical field plus a quantum field originally in the vacuum state [Mollow 75, Cohen-Tannoudji 92, pp.597–601]. The decohering mechanisms then can be broken up into two parts: (1) decoherence induced by the classical field and (2) decoherence induced by the quantum vacuum field. The decoherence of the classical field is easily described by classical noise. Common classical laser noise sources are due to fluctuations of the intensity, frequency, and phase. Fault-tolerant quantum computation will require classical noise sources to be small enough such that the errors imparted to the quantum information carriers are well below the fault tolerance threshold. However, I will show in this chapter that we were able to control in certain experiments the errors induced by classical noise sources to levels below the fault-tolerance threshold. This involved a handful of experimental techniques such as refocusing slow-timescale coherent errors (i.e. over-rotations or accumulated phase). In principle, classical noise is classically controllable (via feedback) and can be eliminated. In practice, all experimental techniques for eliminating classical noise must be used to achieve fault-tolerance including classical controllers and other techniques such as refocusing and composite pulse techniques [Vandersypen 04].

The interaction of the ion with the quantum electro-magnetic vacuum, however, is a fundamental source of decoherence. Physically, the quantum vacuum is responsible for excited state decay, i.e. spontaneous emission, and in our experimental setup, the vacuum is responsible for the spontaneous scattering of photons from an off-resonant laser beam. The question then arises, "what are the decohering effects of spontaneous photon scattering?" This question we experimentally answer in this chapter [Ozeri 05]. In the context of quantum information, we are interested in decoherence of quantum information, i.e. qubit coherence, and in our experimental system, the qubit eigenstates are two hyperfine ground states of ^{9}Be$^+$. Therefore, we experimentally study the decohering effects of off-resonant laser light on coherent superpositions of hyperfine ground states [Ozeri 05].

Previous experiments with neutral atoms have studied the coherence of hyperfine superpositions in the presence of laser light [Andersen 03, Kuhr 03]. In these experiments, the dominant source of decoherence was classical noise such as laser intensity noise or ambient magnetic fields. The coherence of Zeeman ground states in the presence of resonant spontaneous scattering was investigated by Cohen-Tannoudji [Cohen-Tannoudji 62]. In these experiments, coherence was shown to be preserved when the Zeeman splitting of the ground states was small compared to the excited state line width. Here, we study the coherence of hyperfine states separated in energy much more than the excited state line-width in the presence of off-resonant spontaneous photon scattering [Ozeri 05].

5.1 Raman Inelastic vs. Rayleigh Elastic Photon Scattering

The photon scattering process for an atomic ion (or neutral atom) can be broken into two separate types: (1) Rayleigh elastic scattering and (2) Raman inelastic scattering. These two different types of scattering are depicted in Fig. 5.1. Rayleigh elastic scattering describes events where the post-scattering state of the atom is unchanged. Consequently, the scattered photon has the same frequency and polarization of the incoming laser [Mollow 69, Höffges 97]. No information about the state of the atom is carried away by the scattered photon. Directly after the scattering process and prior to measurement, the atom and the scattered photon are in a product state. Therefore, any measurement of the scattered photon will not collapse the state of the atom. Theoretically, if we trace over the degrees of freedom of the scattered photon, the reduced density matrix of the atom is unaffected and remains in a pure state. In particular, if the atom was in a coherent superposition prior to scattering, it remains so after the scattering process.

The situation is quite different for the case of Raman inelastic scattering. Here, the atom changes state after the scattering process. If the two ground states are separated in energy as they are in Fig. 5.1, then the scattered photon can have a different frequency than the incoming laser. Hence, the frequency of the scattered photon is entangled with the state of the atom. Consider an atom prepared in an equal superposition of the two ground states in Fig. 5.1 prior to scattering. After scattering, if the scattered photon frequency is larger than that of the laser, then the post-scattering state of the atom is the lower state (by energy conservation), no longer a superposition state (see right-most diagram in Fig. 5.1b). Similarly, if the scattered photon frequency is smaller than that of the laser, then the post-scattering state of the atom is the higher ground state, also not a superposition (see left-most diagram in Fig 5.1b). In both cases, Raman scattering projects the state of the atom. In terms of quantum informa-

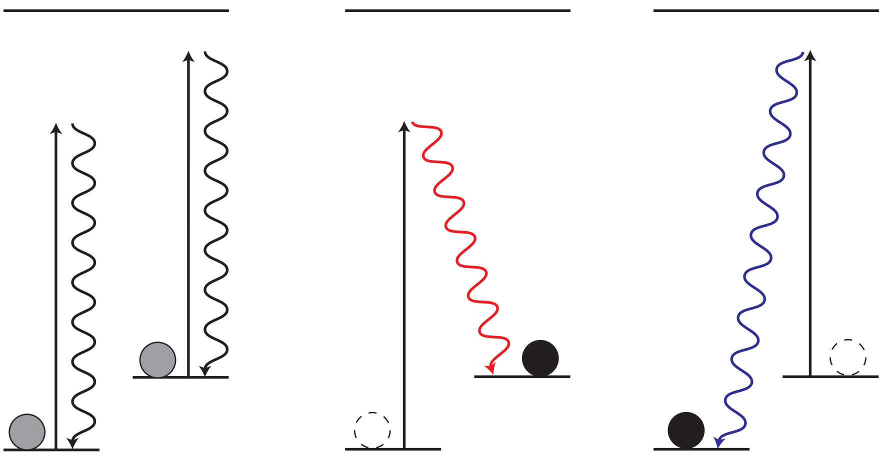

(a) Rayeigh elastic scattering

(b) Raman inelastic scattering

Figure 5.1: Rayleigh and Raman scattering of a coherent superposition by an off-resonant laser (straight vertical arrows). Curvy arrows represent scattered photons. Rayleigh scattered photons have the same frequency and polarization of the incoming laser and do not decohere superposition states. A Raman scattered photon's frequency and/or polarization is entangled with the state of the atom and measures the atom's state collapsing the superposition to one of the atom's eigenstates.

tion theory, the scattered photon carries away information (i.e. in its frequency) about the quantum state of the atom and hence acts like a projective measurement operator. In terms of quantum theory, the state of the atom is entangled with the state of the scattered photon, and upon tracing over the degrees of freedom of the scattered photon, the reduced density matrix for the atom is in a mixed state. The same arguments apply to the polarization state of the scattered photon. If the two ground states of the atom are eigenstates with different z-projection of angular momentum, then the scattered photon's polarization is also entangled with the state of the atom [Blinov 04].

Generally, if the scattered photon(s) reveal information as to the quantum state of the atom, then the scattering process causes decoherence. For example, the Raman scattering process measures the state of the atom after a single scattering event. In the case of Rayleigh scattering of a single photon as in Fig. 5.1a, there is no way for the experimenter to infer the state of the atom based on a measurement of the scattered photon. However, it may be possible to collect many Rayleigh scattered photons and infer the rate of Rayleigh scattering within some uncertainty based on counting statistics. If the two ground states have different Rayleigh scattering rates, then the collection of Rayleigh scattered photons acts as a measurement, and the quantum state of the atom will collapse if the Rayleigh scattered photons provide enough information to distinguish between the two ground states. This process is a measurement which occurs over an interval [Geremia 04] where the atomic state collapses over time as the uncertainty in the measurement of the scattering rates reduces over time. For the experiments in this chapter, we used magnetic field insensitive hyperfine states which have the same total scattering rates within 1% for the range of detunings used.[1] Therefore, in order to have the atomic state collapse due to the information leaked from the atom by the difference in scattering rates, the atom would have to scatter more than 10^4 photons.[2]

---

[1] The reason for the difference in scattering rates is dominated by the different detunings for the two states which differ by ~1 GHz out of ~100 GHz.

The extreme example of different scattering rates performing measurement and hence collapsing the atomic state is in the case of state dependent resonance fluorescence (see § 2.4). Here, the laser is tuned on resonance such that one ground state has a large scattering rate (tens of MHz), and the other has a very small scattering rate (few kHz). In this case, the state of the atom is projected in a few 10's of nanoseconds as these scattering rates are very distinguishable.

We consider scattering from an off-resonant laser of intensity I and polarization $\hat{\epsilon} \equiv \epsilon_+ \hat{\sigma}_+ + \epsilon_0 \hat{\pi} + \epsilon_- \hat{\sigma}_-$ where $\hat{\pi}$ is parallel to the quantizing magnetic field and $\hat{\sigma}_+$ ($\hat{\sigma}_-$) is right (left) circularly polarized with respect to the magnetic field direction. The polarization is normalized such that $\sum_{k\in\{+,-,0\}} \epsilon_k^2 = 1$. The rate of photon scattering for an atom originally in state $|i\rangle$ scattering into state $|f\rangle$ is given by the Heisenberg-Kramers relation (see [Loudon 00] and § 2.4.3)

$$\Gamma_{i\to f} = |g|^2 \gamma \left| \sum_k \frac{a_{i\to f}^{(k)}}{\Delta_k} \right|^2 \tag{5.1}$$

$$a_{i\to f}^{(k)} = \frac{1}{\mu^2} \sum_q \langle f|\mathbf{d}\cdot\hat{\sigma}_q|k\rangle\langle k|\mathbf{d}\cdot\hat{\epsilon}|i\rangle \tag{5.2}$$

where $g = \frac{E\mu}{2\hbar}$, $E = \sqrt{2I/c\epsilon_0}$ is the laser-beam electric field amplitude, c is the speed of light, ϵ_0 is the vacuum dielectric constant (in the expression for the electric field amplitude, everywhere else, ϵ_0 is the $\hat{\pi}$ polarization component), and $\mu = |\langle P_{3/2}, F = 3, m_F = 3|\mathbf{d}\cdot\hat{\sigma}_+|S_{1/2}, F = 2, m_F = 2\rangle|$ is the magnitude of the cycling transition electric-dipole moment. Here, $\mathbf{d}$ is the electric dipole operator, and γ is the natural line-width. The amplitude $a_{i\to f}^{(k)}$ is the normalized second-order coupling from state $|i\rangle$ to state $|f\rangle$ through the excited state $|k\rangle$, and Δ_k is the detuning of the laser from the $|i\rangle \leftrightarrow |k\rangle$ transition frequency. The sum over k in Eq. (5.1) is over all intermediate excited states $|k\rangle$. Raman inelastic scattering describes state-changing events where $i \neq f$, and Rayleigh elastic scattering describes events where $i = f$ leaving the state

---

[2] The uncertainty in a measurement of the scattering rate is proportional to the square root of the number of photons collected. Therefore, to distinguish between two scattering rates which fractionally differ by 10^{-2}, a minimum of 10^4 photons would need to be scattered.

unchanged. The Raman scattering rate out of state $|i\rangle$ is $\Gamma_i^{\text{Raman}} = \sum_{f\neq i}\Gamma_{i\to f}$, and the Rayleigh scattering rate is $\Gamma_i^{\text{Rayleigh}} = \Gamma_{i\to i}$. It should be noted that the final state $|f\rangle$ is the final state of the atom-scattered-photon system, and scattered photons with different modes (including different polarizations) are distinguishable. Therefore, the $\mathbf{d}\cdot\hat{\epsilon}$ operator in Eq. (5.2) must be constrained so that non-zero matrix elements only occur for scattered photon polarizations consistent with the final state $|f\rangle$.

We will consider detunings near the first excited state fine structure levels ${}^2P_J$ accessible via the electric-dipole interaction where $J \in \{\frac{1}{2}, \frac{3}{2}\}$ for alkali-like atoms such as ${}^9\text{Be}^+$. It is convenient to introduce the effective amplitude $a_{i\to f}^{(J)} = \sum_{k\in J} a_{i\to f}^{(k)}$ for scattering through all levels in the J fine-structure manifold. For detunings Δ_k large compared to hyperfine and Zeeman splittings in the ${}^2P_J$ manifolds[3] , the scattering rate from atomic state $|i\rangle$ to state $|f\rangle$ simplifies to

$$\Gamma_{i\to f} = |g|^2\gamma\left|\frac{a_{i\to f}^{(J=1/2)}}{\Delta} + \frac{a_{i\to f}^{(J=3/2)}}{\Delta - \Delta_F}\right|^2 \qquad (5.3)$$

where Δ is the detuning of the laser from the $|i\rangle \leftrightarrow |{}^2P_{1/2}\rangle$ transition frequency, and Δ_F is the fine structure splitting between ${}^2P_J$ manifolds ($J \in \{\frac{1}{2}, \frac{3}{2}\}$) (see Fig. 5.2). In Eq. (5.3), the final state of the system $|f\rangle$ represents the final atomic state as well as the final polarization state of the scattered photon. The integration over the final density of states of the scattered photon is contained in γ in Eq. (5.3).

For ground hyperfine states of the form (see § 2.2)

$$|l\rangle \equiv \alpha_l|m_J = -\frac{1}{2}, m_I = m_F^{(l)} + \frac{1}{2}\rangle + \beta_l|m_J = +\frac{1}{2}, m_I = m_F^{(l)} - \frac{1}{2}\rangle, \qquad (5.4)$$

---

[3] The hyperfine splitting of the ${}^2P_{3/2}$ manifold at zero magnetic field is less than 1 MHz; the hyperfine splitting of the ${}^2P_{1/2}$ manifold at zero magnetic field is 237 MHz. At $B = 0.0119$ T, the field-independent point, the Zeeman splitting of the ${}^2P_J$ levels is of order a few hundred MHz.

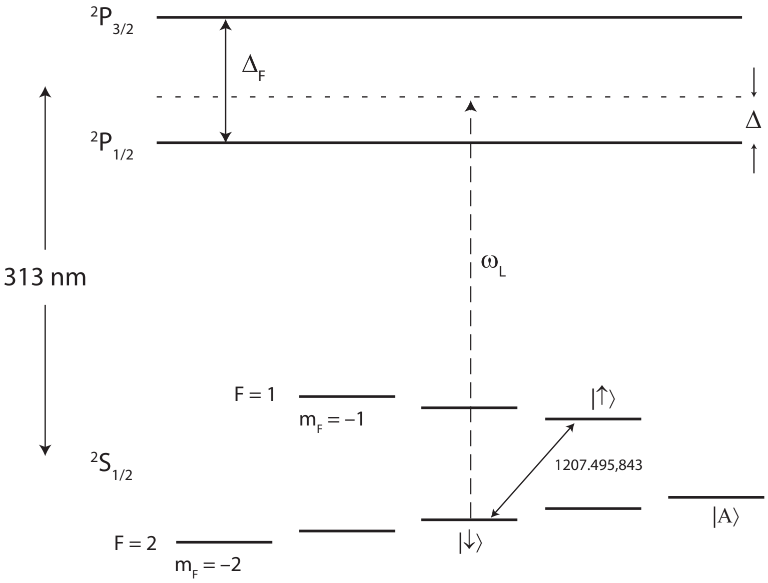

Figure 5.2: The relevant energy levels of $^9\mathrm{Be}^+$ for the spontaneous scattering experiment. ω_L is the frequency of the decohering laser beam and is detuned Δ from the $|\downarrow\rangle \leftrightarrow |^2P_{1/2}\rangle$ transition frequency.

the scattering amplitudes can be written as

$$\begin{aligned} a_{i\to f}^{(J=1/2)} &= \epsilon_+ \left[\frac{2}{3}\alpha_i\alpha_f^*\delta_{m_F^{(i)},m_F^{(f)}}\delta_{\hat{\epsilon}_s,\hat{\sigma}_+} - \frac{\sqrt{2}}{3}\alpha_i\beta_f^*\delta_{m_F^{(i)}+1,m_F^{(f)}}\delta_{\hat{\epsilon}_s,\hat{\pi}}\right] \\ &+\epsilon_0 \left[\frac{1}{3}\delta_{i,f}\delta_{\hat{\epsilon}_s,\hat{\pi}} - \frac{\sqrt{2}}{3}(\alpha_i\beta_f^*\delta_{m_F^{(i)}+1,m_F^{(f)}}\delta_{\hat{\epsilon}_s,\hat{\sigma}_-} + \beta_i\alpha_f^*\delta_{m_F^{(i)}-1,m_F^{(f)}}\delta_{\hat{\epsilon}_s,\hat{\sigma}_+})\right] \\ &+\epsilon_- \left[\frac{2}{3}\beta_i\beta_f^*\delta_{m_F^{(i)},m_F^{(f)}}\delta_{\hat{\epsilon}_s,\hat{\sigma}_-} - \frac{\sqrt{2}}{3}\beta_i\alpha_f^*\delta_{m_F^{(i)}-1,m_F^{(f)}}\delta_{\hat{\epsilon}_s,\hat{\pi}}\right] \end{aligned} \tag{5.5}$$

$$\begin{aligned} a_{i\to f}^{(J=3/2)} &= \epsilon_+ \left[\left(\frac{1}{3}\delta_{i,f} + \frac{2}{3}\beta_i\beta_f^*\delta_{m_F^{(i)},m_F^{(f)}}\right)\delta_{\hat{\epsilon}_s,\hat{\sigma}_+} + \frac{\sqrt{2}}{3}\alpha_i\beta_f^*\delta_{m_F^{(i)}+1,m_F^{(f)}}\delta_{\hat{\epsilon}_s,\hat{\pi}}\right] \\ &+\epsilon_0 \left[\frac{2}{3}\delta_{i,f}\delta_{\hat{\epsilon}_s,\hat{\pi}} + \frac{\sqrt{2}}{3}(\alpha_i\beta_f^*\delta_{m_F^{(i)}+1,m_F^{(f)}}\delta_{\hat{\epsilon}_s,\hat{\sigma}_-} + \beta_i\alpha_f^*\delta_{m_F^{(i)}-1,m_F^{(f)}}\delta_{\hat{\epsilon}_s,\hat{\sigma}_+})\right] \\ &+\epsilon_- \left[\left(\frac{1}{3}\delta_{i,f} + \frac{2}{3}\alpha_i\alpha_f^*\delta_{m_F^{(i)},m_F^{(f)}}\right)\delta_{\hat{\epsilon}_s,\hat{\sigma}_-} + \frac{\sqrt{2}}{3}\beta_i\alpha_f^*\delta_{m_F^{(i)}-1,m_F^{(f)}}\delta_{\hat{\epsilon}_s,\hat{\pi}}\right] \end{aligned} \tag{5.6}$$

where we have used the orthonormality condition $\alpha_i\alpha_f^* + \beta_i\beta_f^* = \delta_{i,f}$ for states with the same m_F throughout Eqs. (5.5) and (5.6); $\delta_{n,m}$ is the Kronecker delta function defined as $\delta_{n,m} = 1$ for $n = m$, 0 otherwise. The scattered photon polarization is represented by $\hat{\epsilon}_s$, and the Kronecker delta function on the polarization $\delta_{\hat{\epsilon}_s,\hat{\sigma}_k}$, $k \in \{+,-,0\}$ ensures that the final state of the system is consistent with conservation of angular momentum ($\hat{\sigma}_0 \equiv \hat{\pi}$). We note that every individual term is distinguishable in the amplitudes of Eqs. (5.5) and (5.6). This is because each term represents a different distinguishable final state whether it is a different atomic state or a different polarization state of the scattered photon. In practice, for a particular final state, the amplitude $a_{i\to f}^{(J)}$ will only have one non-zero term. It is convenient to define the scattering amplitude for a single term given the polarization of the laser and the polarization of the scattered photon. We define $a_{i_k\to f_q}^{(J)}$ as the scattering amplitude from the initial atomic state $|i\rangle$ scattering into the final atomic state $|f\rangle$ via photon scattering from a laser with polarization $\hat{\sigma}_k$ where the scattered photon has polarization $\hat{\sigma}_q$. The scattering amplitudes then simplify to

$$a_{i\to f}^{(J)} = \sum_{k,q} \epsilon_k a_{i_k\to f_q}^{(J)}\delta_{\hat{\epsilon}_s,\hat{\sigma}_q}. \tag{5.7}$$

For example, $a^{(J=1/2)}_{i_+\to f_+} = \frac{2}{3}\alpha_i\alpha_f^*\delta_{m_F^{(i)},m_F^{(f)}}$. Examining Eqs. (5.5) and (5.6) we observe that $a^{(J=3/2)}_{i_k\to f_q} + a^{(J=1/2)}_{i_k\to f_q} = \delta_{i,f}$; that is, for each polarization component of the laser and the scattered photon, the Raman scattering amplitudes through the ${}^2P_{1/2}$ and the ${}^2P_{3/2}$ are equal in magnitude and opposite in sign. Consequently, the Raman scattering rate [see Eq. (5.3)] is proportional to $\left|\frac{1}{\Delta} - \frac{1}{\Delta-\Delta_F}\right|^2$, and for detunings much larger than the fine structure ($\Delta \gg \Delta_F$), the Raman scattering amplitudes destructively interfere. For large detunings, the Raman scattering rate scales as $\sim \Delta^{-4}$, whereas the Rayleigh scattering rate scales as $\sim \Delta^{-2}$.

The Raman scattering rate for an initial state $|i\rangle$ is calculated by summing over all final states to which the initial state can scatter. Because the scattering amplitude through the ${}^2P_{3/2}$ level is equal in magnitude and opposite in sign to that through the ${}^2P_{1/2}$ manifold, the Raman scattering rate is straight forward to calculate. Using the orthonormality of hyperfine states with the same m_F, we obtain

$$\begin{aligned}\Gamma_i^{\text{Raman}} &= |g|^2\gamma\left|\frac{1}{\Delta} - \frac{1}{\Delta-\Delta_F}\right|^2 \sum_k \epsilon_k^2 \sum_{f\neq i,q} |a^{(J=1/2)}_{i_k\to f_q}|^2 \\ &= \frac{2}{9}|g|^2\gamma\left|\frac{1}{\Delta} - \frac{1}{\Delta-\Delta_F}\right|^2 \left[\epsilon_+^2\alpha_i^2(1+2\beta_i^2) + \epsilon_0^2 + \epsilon_-^2\beta_i^2(1+2\alpha_i^2)\right].\end{aligned} \tag{5.8}$$

Similarly, the Rayleigh scattering rate is given by

$$\begin{aligned}\Gamma_i^{\text{Rayleigh}} = \frac{1}{9}|g|^2\gamma\Bigg[&\epsilon_+^2\left|\frac{2\alpha_i^2}{\Delta} + \frac{1+2\beta_i^2}{\Delta-\Delta_F}\right|^2 \\ &+ \epsilon_0^2\left|\frac{1}{\Delta} + \frac{2}{\Delta-\Delta_F}\right|^2 \\ &+ \epsilon_-^2\left|\frac{2\beta_i^2}{\Delta} + \frac{1+2\alpha_i^2}{\Delta-\Delta_F}\right|^2\Bigg],\end{aligned} \tag{5.9}$$

and the total scattering rate is given by the sum $\Gamma_i^{\text{total}} \equiv \Gamma_i^{\text{Raman}} + \gamma_i^{\text{Rayleigh}}$. These expressions are valid when the detunings Δ and $\Delta - \Delta_F$ are large compared to the hyperfine and zeeman splittings in the excited ${}^2P_{1/2}$ and ${}^2P_{3/2}$ manifolds.

The suppression of Raman scattering with large detuning can be physically understood by considering the fine structure interaction. The fine structure couples the electron spin to the electron's orbital angular momentum; the electron spin does not couple to the electric field of the light directly. The electric field does couple to the electron's orbital angular momentum, however, and the spin-orbit coupling then gives an effective coupling between electron spin and the light field. When the detuning is large compared to the fine structure splitting, the ^2P_J levels are less distinguishable to the scattering laser, and the laser scatters from an atom with an effective P level without fine structure. Therefore, Raman scattering events, which involve the reorientation of the electron spin, are suppressed for detunings large compared to the fine structure splitting. The suppression of Raman scattering events relative to Rayleigh scattering for large detunings has been observed by Cline *et al.* [Cline 94] by observing population changes due to scattering. The same reasons apply to the suppression of stimulated Raman transitions for detunings large compared to the fine structure splitting. The two-photon Rabi frequency scales as $\sim \Delta^{-2}$ for $\Delta \gg \Delta_F$ compared to $\sim \Delta^{-1}$ when the laser is tuned near a single fine-structure transition.

In the context of quantum information processing, we are interested in the spontaneous scattering error during quantum gate operations. We can quantify this error by considering the probability of Raman scattering during a π pulse, for example. Both the two-photon Rabi frequency (see § 2.5.2) and the spontaneous scattering rate are functions of the laser intensity and the detuning. The duration of a π pulse τ_π is defined by the relation $|\Omega|\tau_\pi = \frac{\pi}{2}$ where Ω is the two-photon Rabi frequency. For small probabilities of photon scattering, the probability of scattering a single Raman photon during a π pulse is given by $\frac{1}{2}\left(\Gamma_\downarrow^{\text{Raman}} + \Gamma_\uparrow^{\text{Raman}}\right)\tau_\pi = \frac{\pi}{2}\frac{1}{2}\left(\Gamma_\downarrow^{\text{Raman}} + \Gamma_\uparrow^{\text{Raman}}\right)/|\Omega|$. During a π pulse, the qubit spends an equal amount of time in both the $|\uparrow\rangle$ and $|\downarrow\rangle$ states, hence we average the scattering rates of the two qubit eigenstates. To simplify the analysis, we consider forming a qubit out of a $\Delta m_F = 0$ hyperfine transition. Results for different pairs of hyperfine states which are suitable for use as qubits will differ by factors close to unity. However, the functional form of the Raman scattering error vs. detuning will be similar.

In § 2.5.2 we calculated the stimulated Raman two-photon Rabi frequency between a pair of ground state levels which were coupled by two lasers to a single excited state. Generalizing this result, the Rabi frequency for two lasers b and r with polarizations $\epsilon_l = l_+\hat{\sigma}_+ + l_0\hat{\pi} + l_-\hat{\sigma}_-$ with $l \in \{b, r\}$ for stimulated Raman transitions through the multiple excited states is given by

$$\Omega = \frac{\mu^2 E_b E_r^*}{4\hbar^2} \sum_k \frac{\langle \uparrow |\mathbf{d} \cdot \hat{\epsilon}_r | k\rangle \langle k | \mathbf{d} \cdot \hat{\epsilon}_b | \downarrow\rangle}{\Delta_k \mu^2} \tag{5.10}$$

where E_l is the electric field amplitude for laser $l \in \{b, r\}$ and the sum in Eq. (5.10) is over the intermediate excited states $|k\rangle$. Using the excited states in the ${}^2P_{1/2}$ and ${}^2P_{3/2}$ manifolds, the Rabi frequency becomes

$$\begin{aligned} \Omega = {} & \frac{\mu^2 E_b E_r^*}{4\hbar^2} \left\{ \frac{1}{\Delta} \left[\frac{2}{3}\alpha_\downarrow \alpha_\uparrow^* b_+ r_+^* + \frac{1}{3}(\alpha_\downarrow \alpha_\uparrow^* + \beta_\downarrow \beta_\uparrow^*) b_0 r_0^* + \frac{2}{3}\beta_\downarrow \beta_\uparrow^* b_- r_-^* \right] \right. \\ & + \frac{1}{\Delta - \Delta_F} \left[(\frac{1}{3}\alpha_\downarrow \alpha_\uparrow^* + \beta_\downarrow \beta_\uparrow^*) b_+ r_+^* \right. \\ & \left. \left. + \frac{2}{3}(\alpha_\downarrow \alpha_\uparrow^* + \beta_\downarrow \beta_\uparrow^*) b_0 r_0^* + (\alpha_\downarrow \alpha_\uparrow^* + \frac{1}{3}\beta_\downarrow \beta_\uparrow^*) b_- r_-^* \right] \right\} \\ = {} & \frac{\mu^2 E_b E_r^*}{4\hbar^2} \frac{2}{3} \left[\frac{1}{\Delta} - \frac{1}{\Delta - \Delta_F} \right] \alpha_\downarrow \alpha_\uparrow^* (b_+ r_+^* - b_- r_-^*) \end{aligned} \tag{5.11}$$

where we have used the orthogonality condition $\alpha_\uparrow \alpha_\downarrow^* + \beta_\uparrow \beta_\downarrow^* = 0$ for states with the same m_F to simplify the second line of Eq. (5.11). We observe that $\hat{\pi}$ polarized light does not contribute to the Rabi frequency. Furthermore, using linearly polarized light requires that the polarizations of the b and r beams be orthogonal to maximize $b_+ r_+^* - b_- r_-^*$. Linearly polarized light has the additional advantage that differential Stark shifts between non-field independent transitions is suppressed. For field independent transitions, the differential Stark shift is suppressed independent of polarization. We let $b_+ = b_- = r_+ = -r_- = \frac{1}{\sqrt{2}}$ resulting in $b_+ r_+^* - b_- r_-^* = 1$. Using these polarizations for the b and r beams, the Raman spontaneous scattering rate (Eq. (5.8)) for atomic state $|i\rangle$ from both beams is

$$\Gamma_i^{\text{Raman}} = \frac{(E_b^2 + E_r^2)\mu^2}{4\hbar^2} \frac{2}{9} \gamma \left| \frac{1}{\Delta} - \frac{1}{\Delta - \Delta_F} \right|^2 (1 + 4\alpha_i^2 \beta_i^2) \tag{5.12}$$

Simplifying the analysis, we specialize to the case of the $|F, m_F = 0\rangle \leftrightarrow |F', m'_F = 0\rangle$ clock transition at low magnetic fields where $\alpha_i^2 = \beta_i^2 = \frac{1}{2}$ for $i \in \{\uparrow, \downarrow\}$, and we let the electric field amplitude for the two Raman laser beams be equal $E_b = E_r = E$. Under these conditions, the Raman scattering rate (Eq. (5.12)) is the same for the two qubit states $|\downarrow\rangle$ and $|\uparrow\rangle$; that is $\Gamma_{\downarrow}^{\text{Raman}} = \Gamma_{\uparrow}^{\text{Raman}} \equiv \Gamma^{\text{Raman}}$. Comparing Ω to the spontaneous scattering rate (Eq. (5.8)), we find the probability of Raman spontaneous scattering during a π pulse to be

$$P_{\text{Raman}-\pi} = \frac{\pi}{2}\frac{\Gamma^{\text{Raman}}}{|\Omega|} = \frac{2\pi\gamma}{3}\left|\frac{\Delta_F}{\Delta(\Delta - \Delta_F)}\right|. \tag{5.13}$$

Similarly, the probability of Rayleigh scattering during a π pulse on the clock transition is given by ($\Gamma_{\downarrow}^{\text{Rayleigh}} = \Gamma_{\uparrow}^{\text{Rayleigh}} \equiv \Gamma^{\text{Rayleigh}}$)

$$P_{\text{Rayleigh}-\pi} = \frac{\pi}{2}\frac{\Gamma^{\text{Rayleigh}}}{|\Omega|} = \frac{\pi\gamma}{3\Delta_F}\left|\frac{(3\Delta - \Delta_F)^2}{\Delta(\Delta - \Delta_F)}\right|. \tag{5.14}$$

Finally, the probability of scattering *any* photon, Rayleigh or Raman, is given by the sum of Eqs. (5.13) and (5.14) ($\Gamma_{\downarrow}^{\text{total}} = \Gamma_{\uparrow}^{\text{total}} \equiv \Gamma^{\text{total}}$):

$$P_{\text{total}-\pi} = \frac{\pi}{2}\frac{\Gamma^{\text{total}}}{|\Omega|} = \frac{\pi\gamma}{\Delta_F|\Delta(\Delta - \Delta_F)|}\left[(\Delta - \Delta_F)^2 + 2\Delta^2\right]. \tag{5.15}$$

We note that in deriving the relations in Eqs. (5.13), (5.14), and (5.15) we used the approximation that the detunings $\Delta, \Delta - \Delta_F$ are much greater than the hyperfine splitting, zeeman splittings, and the power-broadened line width $\gamma\sqrt{s_0 + 1}$ of the excited ${}^2P_J$ manifolds ($J \in \{\frac{1}{2}, \frac{3}{2}\}$) where s_0 is the on-resonance saturation parameter.

A plot of the Raman spontaneous scattering error probability vs. detuning (Eq. (5.13)) is shown in Fig 5.3 along with the total scattering probability (Eq. (5.15)) for comparison. We find that the Raman spontaneous scattering probability during a π pulse drops quadratically to zero when the detuning Δ is much larger than the fine structure splitting Δ_F. In contrast, the total scattering probability asymptotically approaches the finite non-zero value of $\frac{3\pi\gamma}{\Delta_F}$. The global minimum in the total spontaneous scattering rate of $P_{\text{total}-\pi} = \frac{4\pi\gamma}{\Delta_F}\left(\frac{3-2\sqrt{2}}{3\sqrt{2}-4}\right) \simeq (2.83)\frac{\pi\gamma}{\Delta_F}$ occurring at a detuning of

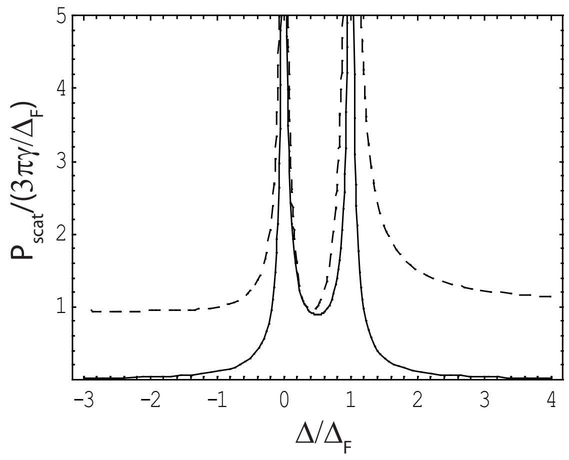

Figure 5.3: Solid curve is the calculated probability of inelastic Raman scattering during a π pulse. The dashed curve is the probability of total scattering during a π pulse. The detuning (x-axis) is in units of the fine structure splitting Δ_F. The probability (y-axis) is in units of the limiting probability of scattering at large detunings $\frac{3\pi\gamma}{\Delta_F}$; $\frac{3\pi\gamma}{\Delta_F} = 9.3 \times 10^{-4}$ for $^9\mathrm{Be}^+$.

$\Delta = \left(\sqrt{2} - 1\right) \Delta_F$ between the two fine-structure manifolds is slightly lower than the asymptotic value. If it were the case that all spontaneously scattered photons would cause decoherence, then it would appear that an ion with a large fine structure splitting Δ_F would be advantageous to reduce the probability of photon scattering. For $^9\text{Be}^+$, the saturated probability of photon scattering is 9.3×10^{-4}, considerably high when compared to Steane's fault-tolerance threshold [Steane 03]. We note that according to Knill [Knill 05], having errors below fault-tolerance thresholds is not necessary to perform useful quantum computation. However, it is desirable to push the errors in our system to very low levels, and we use the 10^{-4} threshold of Steane as a benchmark to which we can compare all of our errors. Even though it may be possible to perform useful quantum computing with errors above this threshold [Knill 05], certainly if we can push our errors well below this threshold, then we are at a good starting point for building a large scale quantum computer.

By increasing the detuning Δ, we can suppress Raman spontaneous scattering and hence reduce the error during quantum gates. However, as we see from Eq. (5.11), as the detuning becomes large compared to the fine structure splitting Δ_F, both the probability of spontaneous Raman scattering during a π pulse and the Rabi frequency decrease quadratically. That is to say, reducing the error comes at a cost. If we are to maintain the same Rabi frequency and reduce the error due to spontaneous scattering by an order of magnitude, we would require an order of magnitude more laser power. From a different perspective, if we keep the laser power constant, then reducing the spontaneous scattering by an order of magnitude will slow the gate speed by an order of magnitude.

We can quantify the laser power requirements for a given probability of spontaneous scattering error as follows [Ozeri 06]. Examining Eqs. (5.11) and (5.13), we can write the probability of Raman scattering during a π pulse as

$$P_{\text{Raman}-\pi} = \frac{8\hbar^2\pi|\Omega|}{E^2}\frac{\gamma}{\mu^2}. \tag{5.16}$$

The natural line width γ and the dipole moment squared μ^2 are proportional, and the ratio is a function of atomic constants, namely

$$\frac{\gamma}{\mu^2} = \frac{\omega_{3/2}^3}{3\hbar\pi\epsilon_0 c^3} \tag{5.17}$$

where $\omega_{3/2}$ is the $|^2S_{1/2}\rangle \leftrightarrow |^2P_{3/2}\rangle$ transition frequency, ϵ_0 is the vacuum dielectric constant, and c is the speed of light. Furthermore, for a gaussian laser spatial mode with waist w_0 at the ion, the electric field amplitude can be expressed in terms of the waist and the laser power P_{laser}:

$$E^2 = \frac{4P_{\text{laser}}}{\pi w_0^2 c\epsilon_0}. \tag{5.18}$$

Using these expressions, the probability of Raman photon scattering during a π pulse can be written in terms of the Rabi frequency, waist, laser power, and atomic constants:

$$P_{\text{Raman}-\pi} = \frac{2}{3}\frac{|\Omega|}{P_{\text{laser}}}\frac{\hbar\pi w_0^2\omega_{3/2}^3}{c^2}. \tag{5.19}$$

We find that the probability of error induced by spontaneous scattering during a π pulse is proportional to the Rabi frequency and inversely proportional to the laser power. As was mentioned previously, speed and laser power are trade-offs if the probability of error is kept constant. From a different perspective, given a required gate speed, the laser power must be greater than

$$P_{\text{laser}} \geq \frac{2}{3}\frac{|\Omega|}{P_{\text{Raman}-\pi}}\frac{\hbar\pi w_0^2\omega_{3/2}^3}{c^2}. \tag{5.20}$$

Furthermore, ions with longer wavelengths have lower spontaneous scattering error for the same laser power. This results from the fact that the natural line width is proportional to $\omega_{3/2}^3$ resulting from the fact that higher energy states have shorter lifetimes

Ion	λ [nm]	P_{laser} [mW]
$^{9}\text{Be}^{+}$	313	3.36
$^{43}\text{Ca}^{+}$	393	1.69
$^{113}\text{Cd}^{+}$	215	10.5
$^{199}\text{Hg}^{+}$	165	23.0
$^{25}\text{Mg}^{+}$	280	4.72
$^{87}\text{Sr}^{+}$	408	1.52
$^{137}\text{Ba}^{+}$	456	1.09

Table 5.1: Laser power requirements to achieve 10^{-4} spontaneous scattering error during a π pulse for different ion species.

because of the larger density of states for the electromagnetic vacuum at higher frequencies.

In principle, the waist w_0 when diffraction limited can be as small as the wavelength. However, the waist size in practice is set by other experimental parameters such as the inter-ion spacing when performing two-qubit gates. In the former, the Raman spontaneous scattering error probability would scale linearly with the frequency $\omega_{3/2}$ whereas in the latter, the error probability scales with the frequency cubed $\omega_{3/2}^3$.

The probability of spontaneous scattering error can be compared across different ion species using Eq. (5.20). In Tbl. 5.1 we show the laser power required in each Raman beam for different ion species to achieve an error during a π pulse of 10^{-4}. We assume a waist of $w_0 = 20\ \mu$m and a Rabi frequency of $\Omega = 2\pi \times 250$ kHz corresponding to a π pulse duration of 1 μs. For $^{9}\text{Be}^{+}$, a minimum laser power of 3.4 mW is required to reach a probability of error below 10^{-4}. For the set of ions under consideration for use in quantum information processing, the range of $\omega_{3/2}$ frequencies spans approximately an octave making the laser power requirements for the different ions fall within an order of magnitude. This makes the decision of which ion to use for QIP more a function of technical parameters such as which ion has a wavelength where high power readily available laser sources exist rather than physical reasons such as which ion has the largest fine structure splitting. When considering the laser power requirements for fault-tolerant two-qubit gates, the ion mass in addition to the frequency $\omega_{3/2}$ is another physical parameter which plays a role into which ion has the lowest laser power requirements [Ozeri 06]. The reason for this is that the two-qubit gate speed is proportional to the Lamb-Dicke parameter η which is inversely proportional to the square root of the mass (see § 2.6). The largest contribution to the two-qubit gate error is Raman spontaneous scattering [Ozeri 06], and the probability of error is $\sim 2/\eta$ larger than the one-qubit gate. The ability of two ions to scatter Raman photons gives the factor of 2, and the gate speed is $1/\eta$ slower. A more detailed discussion of the spontaneous scattering error during two-qubit gates can be found in [Ozeri 06].

5.2 Experimental Verification

In the previous section I gave arguments why elastic Rayleigh spontaneous scattering does not cause decoherence of superposition states. In this section, I describe the experiment we performed to verify these claims [Ozeri 05]. The Raman spontaneous scattering rate is measured and compared to the measured decoherence rate of prepared superposition states. It is shown that Raman spontaneous photon scattering is responsible for coherence decay, and that Rayleigh scattering does not cause decoherence.

In the experiment, a single $^9\text{Be}^+$ ion is confined in a single zone of the linear Paul trap (see § 3.1). The ion is Doppler cooled and prepared in the stretched $|A\rangle \equiv |F = 2, m_F = 2\rangle$ state. Coherent superpositions are then prepared in the $|\uparrow\rangle \equiv |F = 1, m_F = 1\rangle$ and $|\downarrow\rangle \equiv |F = 2, m_F = 0\rangle$ hyperfine ground states (see Fig. 5.2). At a magnetic field of 0.01194 T, these two states form a qubit with a transition frequency which has zero first-order dependence on small changes in the magnetic field, and long coherence times have been observed (see Ch. 4 and [Langer 05]). Both z-basis eigenstates ($|\uparrow\rangle$ and $|\downarrow\rangle$) and coherent superpositions of the qubit states are prepared by first performing a π rotation on the $|A\rangle \leftrightarrow |\uparrow\rangle$ transition using a stimulated Raman pulse (see § 2.5.2) followed by a qubit rotation of the form

$$R(\theta, \phi) = \cos(\theta/2)\mathbf{I} - i \sin(\theta/2)(\cos\phi\sigma_x + \sin\phi\sigma_y) \tag{5.21}$$

where θ is the rotation angle about an axis in the xy-plane at an angle ϕ from the x-axis. Here, σ_x and σ_y are Pauli matrices, and $\mathbf{I}$ is the identity matrix. The $|\downarrow\rangle$ state is prepared by first preparing $|\uparrow\rangle$ followed by a π qubit rotation. Qubit measurements are performed via state-dependent resonance fluorescence (see § 2.4). A $\hat{\sigma}_+$ polarized laser resonant with the $|A\rangle \leftrightarrow |^2P_{3/2}, F = 3, m_F = 3\rangle$ transition frequency applied to the ion causes the state $|A\rangle$ fluoresce strongly whereas the other hyperfine states do not. To measure the probability of the ion to be in a particular qubit eigenstate, the particular qubit eigenstate is transferred to the state $|A\rangle$ prior to measurement through a sequence of π rotations. For example, to measure the state $|\downarrow\rangle$, we apply a π rotation on the qubit transition transferring $|\downarrow\rangle \rightarrow |\uparrow\rangle$ followed by a π rotation on the $|\uparrow\rangle \leftrightarrow |A\rangle$ transition transferring the population now in $|\uparrow\rangle$ to $|A\rangle$. The $|A\rangle$ state is measured, which effectively measures the population in $|\downarrow\rangle$ prior to the transfer sequence. Similarly, to measure $|\uparrow\rangle$, we first transfer $|\uparrow\rangle$ to $|A\rangle$ through a π rotation on the $|\uparrow\rangle \leftrightarrow |A\rangle$ transition prior to $|A\rangle$ measurement.

5.2.1 Measurement of the Raman Scattering Rate

The Raman scattering rate is measured by performing the experimental sequence in Fig. 5.4a. The eigenstate $|i\rangle \in \{|\uparrow\rangle, |\downarrow\rangle\}$ is prepared as described above. The ion is then illuminated with the decohering laser beam detuned from the $|^2S_{1/2}, F = 2, m_F = 0\rangle \leftrightarrow |^2P_{1/2}\rangle$ transition frequency by Δ with polarization $\hat{\sigma}_+$. The population remaining in state $|i\rangle$ is then measured. The application of the decohering laser beam causes Raman spontaneous scattering which, by definition, causes the population in the state $|i\rangle$ to optically pump to other states. By measuring the population remaining in state $|i\rangle$ as a function of the duration of the decohering beam, we can extract the

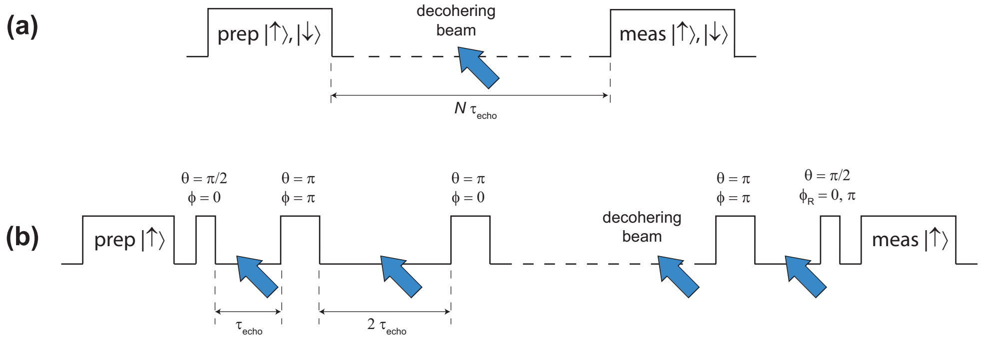

Figure 5.4: **(a)** Experimental sequence for population relaxation measurement. The eigenstate $|i\rangle$ ($i \in \{\uparrow, \downarrow\}$) is prepared followed by application of the decohering laser beam (thick arrow). The population of state $|i\rangle$ is measured as a function of decohering beam duration $N\tau_{\text{echo}}$. **(b)** Experimental sequence for coherence decay measurement. An equal superposition of $|\uparrow\rangle$ and $|\downarrow\rangle$ is prepared with the first $\theta = \pi/2$ pulse. A spin-echo sequence follows where $\theta = \pi$ pulses are applied with alternating phase $\phi = 0, \pi$ such that slow rotation angle errors are refocused as well as slow Stark shifts and Zeeman shifts. The final $\theta = \pi/2$ pulse at phases $\phi = 0, \pi$ followed by measurement interrogates the superposition. The decohering beam is applied in the Ramsey intervals. Coherence vs. τ_{echo} is measured. The number of intervals τ_{echo} is N for simple comparison with the population relaxation rate measurement.

rate of population decay. Rayleigh elastic scattering also occurs with application of the decohering laser beam; however, because Rayleigh scattering, by definition, does not change the atomic state of the ion, the population remaining in the $|i\rangle$ state is unaffected. Typical data for population decay is shown in Fig. 5.5. The grey-filled squares are proportional to the population remaining in the state $|\uparrow\rangle$ after application of the decohering laser beam to the prepared $|\uparrow\rangle$ state. For the data in Fig. 5.5, the detuning was $\Delta = 2\pi \times 227.5$ GHz.

The dynamics of population decay can be described using an analysis similar to that in § 2.4.2. Recall from § 2.4.2 that a $\hat{\sigma}_+$ polarized near-resonant laser beam caused optical pumping of the dark state to the bright state during state-dependent resonance fluorescence measurements. The dynamics of optical pumping was solved using Laplace transforms. For application to measurement, we were concerned with the population optically pumped into the bright state $|A\rangle$, whereas here, we are concerned with the population remaining in the prepared state $|i\rangle \in \{|\uparrow\rangle, |\downarrow\rangle\}$. In both cases, the optical pumping rates from state $|i\rangle$ to state $|f\rangle$ are given by the Heisenberg-Kramers relation with a slight modification in the near-resonant case (see § 2.4.3). We were able to obtain a closed-form solution because $\hat{\sigma}_+$ polarized light optically pumps only in one direction of angular momentum, namely increasing m_F. Since we are concerned only with the population remaining in the prepared state $|i\rangle$, we can simplify the analysis. We let $|i\rangle \equiv |F, m_F\rangle$ and define F' to be the total angular momentum quantum number other than F such that $F' \neq F$. The possible states to which $|i\rangle$ can optically pump under the application of $\hat{\sigma}_+$ polarized light are $|F, m_F+1\rangle$, $|F', m_F+1\rangle$, and $|F', m_F\rangle$. Because $|F, m_F+1\rangle$ and $|F', m_F+1\rangle$ cannot optically pump back to $|F, m_F\rangle$ due to the polarization of the decohering laser beam, population optically pumped to these states is lost from $|F, m_F\rangle$ forever. However, population optically pumped to $|F', m_F\rangle$ may repump back to $|F, m_F\rangle$.

We define $v_F(t)$ and $v_{F'}(t)$ to be the population in the states $|F, m_F\rangle$ and $|F', m_F\rangle$

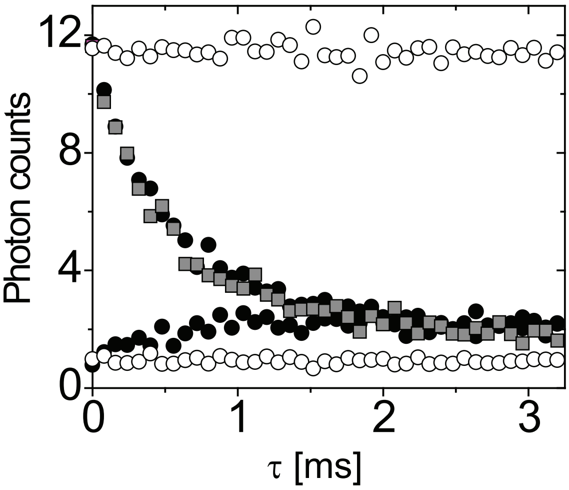

Figure 5.5: Coherence and population relaxation data for a decohering beam detuning of $\Delta = 2\pi \times 227.5$ GHz. The difference between the open (closed) circles is proportional to the coherence of a prepared hyperfine superposition state in the absence (presence) of the decohering laser for duration τ (x-axis) in each arm of the Ramsey spin-echo sequence. The gray-filled squares are proportional to the population remaining in the prepared $|\uparrow\rangle$ state after the decohering laser has been applied for the duration τ in each arm of the Ramsey spin-echo sequence. It is clear from the data that the timescales for coherence relaxation and population relaxation are similar.

respectively at time t, and we define $\mathbf{v} \equiv \begin{pmatrix} v_F \\ v_{F'} \end{pmatrix}$ to be the two-dimensional vector of these populations. Given the arguments above concerning the angular momentum directionality of optical pumping with $\hat{\sigma}_+$ polarized light, the rate equation for the optical pumping process can be written as follows:

$$\dot{\mathbf{v}} = \mathbf{\Gamma} \cdot \mathbf{v} \tag{5.22}$$

where

$$\mathbf{\Gamma} \equiv \begin{pmatrix} -\Gamma_{F \to F'} - \Gamma_{F \to (m_F+1)} & \Gamma_{F \to F'} \\ \Gamma_{F' \to F} & -\Gamma_{F' \to F} - \Gamma_{F' \to (m_F+1)} \end{pmatrix}. \tag{5.23}$$

The terms in Eq. (5.23) are defined as follows: $\Gamma_{F \to F'}$ is the optical pumping rate from state $|F, m_F\rangle$ to state $|F', m_F\rangle$ and $\Gamma_{F \to (m_F+1)}$ is the optical pumping rate from $|F, m_F\rangle$ to both $|F, m_F + 1\rangle$ and $|F', m_F + 1\rangle$ states. Similarly, the rates $\Gamma_{F' \to k}$ are defined as the optical pumping rates from $|F', m_F\rangle$ to states $k \in \{F, (m_F + 1)\}$ in an analogous fashion. The Raman scattering rate out of state $|F, m_F\rangle$ is the upper-left term in the matrix (5.23). We define the hyperfine states in terms of their m_J and m_I components as in Eq. (5.4). Due to the orthonormality condition $\alpha_i \alpha_j^* + \beta_i \beta_j^* = \delta_{i,j}$ for hyperfine states $|i\rangle$ and $|j\rangle$ with the same m_F, the terms in the matrix (5.23) are constrained, namely: $\Gamma_{F \to F'} = \Gamma_{F' \to F}$ and $\Gamma_{F \to (m_F+1)} + \Gamma_{F' \to (m_F+1)} = 1$ ($\delta_{i,j}$ is the Kronecker delta function).

Using the Heisenberg-Kramers relation [Eq. (5.3)], the matrix $\mathbf{\Gamma}$ can be written as $\mathbf{\Gamma} \equiv \Gamma_0 \mathbf{M}$ where

$$\Gamma_0 \equiv \frac{2}{9} g^2 \gamma \left| \frac{1}{\Delta} - \frac{1}{\Delta - \Delta_F} \right|^2, \tag{5.24}$$

$$\mathbf{M} \equiv \begin{pmatrix} -\alpha^2(1 + 2\beta^2) & 2\alpha^2\beta^2 \\ 2\alpha^2\beta^2 & -\beta^2(1 + 2\alpha^2) \end{pmatrix}, \tag{5.25}$$

and the symbols in the definition of Γ_0 are defined in the previous section (§ 5.1); α and β are the coefficients of the $|m_J, m_I\rangle$ components for the $|F, m_F\rangle$ state as defined in Eq. (5.4). It is evident from Eq. (5.25) that $\Gamma_{F\to F'} = \Gamma_{F'\to F}$. Similarly, because $\Gamma_{F\to(m_F+1)}$ ($\Gamma_{F'\to(m_F+1)}$) is proportional to α^2 (β^2), it is also clear that $\Gamma_{F\to(m_F+1)} + \Gamma_{F'\to(m_F+1)} = 1$. With these definitions, the Raman scattering rate out of state $|F, m_F\rangle$ is given by

$$\Gamma_F^{\text{Raman}} = \Gamma_0[\alpha^2(1+2\beta^2)]. \tag{5.26}$$

We desire to extract the Raman scattering rate of state $|F, m_F\rangle$ from the data in Fig. 5.5. The coefficients α and β are known from the Breit-Rabi solution (see § 2.2), and the only free parameter which we would like to extract from the data in Fig. 5.5 is Γ_0. Once Γ_0 is known, we can calculate the Raman scattering rate using Eq. (5.26). The functional form to which we fit the data to extract Γ_0 is given by the dynamics of optical pumping which we now derive.

The dynamics of population relaxation can be solved similar to § 2.4.2 using Laplace transforms. Taking the Laplace transform of Eq. (5.22) and solving for $\mathbf{V}(s) \equiv \mathcal{L}(\mathbf{v}(t))$ where $\mathcal{L}(f(t))$ is the Laplace transform of $f(t)$ and s is the Laplace transform variable, we obtain the solution (in s) $\mathbf{V}(s) = -(\Gamma_0\mathbf{M} - s\mathbf{I})^{-1}\mathbf{v}(0)$ where $\mathbf{I}$ is the identity matrix. After some simplification, the matrix $-(\Gamma_0\mathbf{M} - s\mathbf{I})^{-1}$ can be written as

$$-(\Gamma_0\mathbf{M} - s\mathbf{I})^{-1} = \frac{1}{q(s)}\begin{pmatrix} s+\Gamma_0(a+\beta^2) & -a\Gamma_0 \\ -a\Gamma_0 & s+\Gamma_0(a+\alpha^2) \end{pmatrix} \tag{5.27}$$

where $a \equiv 2\alpha^2\beta^2 \in [0,1]$, $q(s) = (s+\omega_+)(s+\omega_-)$, and

$$\omega_\pm = \frac{\Gamma_0}{2}\left(1+2a \pm \sqrt{4a^2-2a+1}\right). \tag{5.28}$$

The frequencies $\omega_\pm$ are non-negative real numbers. We are concerned with the dynamics of $v_F(t)$ with the initial conditions $v_F(0) = 1$ and $v_{F'}(0) = 0$. Therefore, we only consider the upper-left term in Eq. (5.27). This term can be written as a sum of partial fractions:

$$V_F(s) = \frac{s+\Gamma_0(a+\beta^2)}{\Gamma_0\sqrt{4a^2-2a+a}}\left(\frac{1}{s+\omega_-} - \frac{1}{s+\omega_+}\right), \tag{5.29}$$

and the time-domain solution is given by the inverse Laplace transform of Eq. (5.29):

$$v_F(t) = (4a^2 - 2a + 1)^{-1/2} \left[e^{-\omega_- t} \left(a + \beta^2 - \frac{\omega_-}{\Gamma_0} \right) - e^{-\omega_+ t} \left(a + \beta^2 - \frac{\omega_+}{\Gamma_0} \right) \right]. \quad (5.30)$$

The terms $\omega_\pm/\Gamma_0$ are independent of Γ_0; Γ_0 only enters in the exponential terms $e^{-\omega_\pm t}$ in Eq. (5.30) as a linear scaling factor of the frequencies.

The population decay data in Fig. 5.5 (grey-filled squares) is fit to Eq. (5.30) by varying Γ_0, and the Raman scattering rate is determined by Eq. (5.26).

5.2.2 Coherence in the Presence of Spontaneous Photon Scattering

The coherence remaining in a prepared superposition state after application of the decohering beam is measured in a similar fashion to the population decay. The experimental sequence is shown in Fig. 5.4b. A coherent superposition of qubit states $|\Psi_1\rangle = \frac{1}{\sqrt{2}}(|\uparrow\rangle - i|\downarrow\rangle)$ is prepared by first preparing $|\uparrow\rangle$ followed by the rotation $R(\theta = \pi/2, \phi = 0)$ [see Eq. (5.21)]. After a spin echo sequence with delay, the superposition is interrogated with a final $R(\theta = \pi/2, \phi = 0)$ pulse followed by measurement of the state $|\uparrow\rangle$. Because the spin echo sequence refocuses any detuning of the local oscillator with respect to the qubit transition frequency, the measurement of the $|\uparrow\rangle$ state always yields either the bright or dark extremum of the equivalent Ramsey phase scan experiment depending on whether or not there are an odd or even number of spin echo pulses respectively (see Fig. 4.4a in Ch. 4). The experiment is repeated with the final $\pi/2$ pulse having a phase $\phi = \pi$ yielding the opposite extremum. In the absence of the decohering beam, the measurement record for this experiment yields the open circles data in Fig. 5.5. The difference between the bright data and the dark data is directly proportional to the coherence of the superposition state at the time of measurement. We see from Fig. 5.5 that in the absence of the decohering laser, the coherence is constant as a function of time indicating we have a good quantum memory, consistent with the results of Ch. 4.

The application of the decohering laser in the intervals between the spin echo pulses did cause decoherence of the prepared superposition, and data for these measurements are shown as filled circles in Fig. 5.5. The difference between the upper and lower filled circles is a measure of the coherence, and fitting the difference between these two curves as a function time to an exponential yields the decoherence rate in the presence of light. It is notable that the population relaxation measurement (filled-grey squares) decays on the same time-scale as the coherence. This implies that the rate of coherence decay is similar to the rate of population decay at the particular detuning where this data was taken ($\Delta = 2\pi \times 227.5$ GHz in Fig. 5.5).

In order to prove that the decoherence rate is the same as the Raman scattering rate, we repeated the coherence and population decay measurements for different detunings Δ of the decohering laser. The differential Stark shift of the qubit transition frequency was also measured at each detuning. The measured decoherence rate and the measured Raman scattering rate were normalized by the measured differential Stark shift to remove any dependence on the laser intensity. The differential Stark shift is measured rather than the total scattering rate because the total scattering rate is too small to measure directly. In Fig. 5.6 we plot the normalized measured Raman scattering rate (open circles) and the normalized measured decoherence rate (filled circles) as a function of laser detuning. Also plotted in Fig. 5.6 are the calculated total scattering rate (dashed curve) and calculated Raman scattering rate (solid curve) both normalized by the calculated differential Stark shift for comparison. There are no fit parameters in the calculated total scattering rate or the calculated Raman scattering rate normalized by the calculated differential Stark shift. Both these rates are a function of atomic parameters, namely the fine-structure splitting $\Delta_F = 197.2$ GHz, the excited state linewidth $\gamma = 19.4$ MHz, and the hyperfine state coefficients α and β derived from the Breit-Rabi formula (see § 2.2). It is clear from Fig. 5.6 that both the measured Raman scattering rate and the measured decoherence rate are in good agreement with the

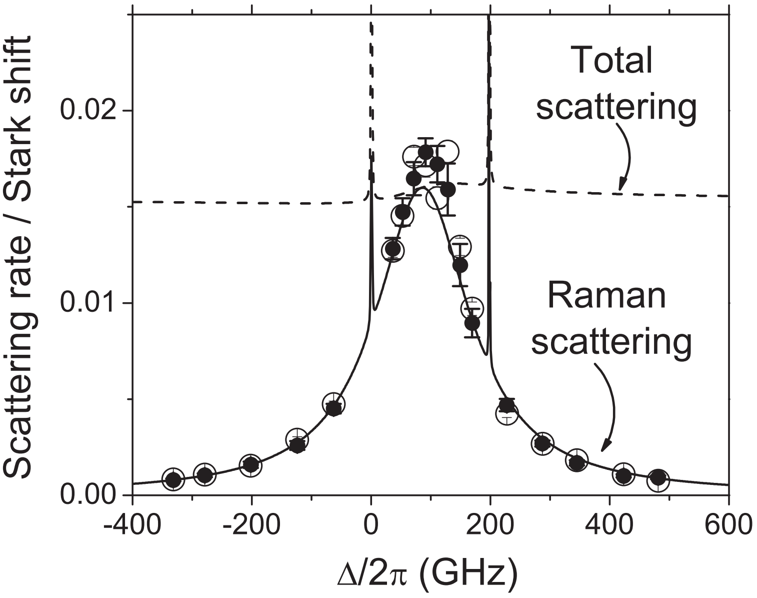

Figure 5.6: The measured decoherence rates (filled circles) and population relaxation rates (open circles) normalized by the measured differential Stark shift are plotted vs. the detuning of the decohering laser beam. The dashed curve is the calculated total scattering rate normalized by the calculated differential Stark shift. The solid curve is the calculated Raman scattering rate normalized by the calculated differential Stark shift. Similar to Fig. 5.3, the total scattering rate normalized by the differential Stark shift asymptotically approaches a finite non-zero value of $\simeq 0.0154$ whereas the Raman scattering rate normalized by the differential Stark shift quadratically approaches zero for detunings large compared to the fine structure splitting. Both the measured normalized decoherence rates (filled circles) and population decay rates (open circles) are in good agreement with the calculated normalized Raman scattering rate curve (solid line) indicating that Raman spontaneous scattering is responsible for both population relaxation and decoherence of superposition states and that elastic Rayleigh scattering does not cause decoherence.

calculated Raman scattering rate curve implying that Raman spontaneous scattering is responsible for coherence decay. In addition, Rayleigh elastic scattering does not cause decoherence of superposition states. In particular, at a detuning of $\Delta = -331.8$ GHz, the measured decoherence rate is more than a factor of 19 below the calculated total scattering rate implying that coherence is maintained in the presence of spontaneous photon scattering.

The measured Raman scattering rate and the measured decoherence rate are compared directly in Fig. 5.7. Fig. 5.7 plots the measured decoherence rate (y-axis) against the measured Raman scattering rate (x-axis), both which are normalized by the measured Stark shift. The solid curve is a weighted least squares fit to the power law $y = x^{\alpha}$ yielding the best-fit parameter $\alpha = 0.997(4)$. This comparison implies that the Raman scattering rate and the decoherence rate are the same. From a different perspective, the scattering of one Raman photon is sufficient to destroy coherence. We recall from the study of two-level atoms that the decoherence rate is bounded below by half of the excited state decay rate [Metcalf 99] which is a population relaxation process. Here, we find that the decoherence rate is bounded below by the Raman scattering rate, also a population relaxation process. The reason that the two-level atom has a lower bound to the decoherence rate half of the excited state decay rate and not the excited state decay rate itself is because only one of the two states of the two-level atom decays, namely the excited state. The ground-state does not decay in the two-level atom model. However, in the presence of an off-resonant decohering laser, both hyperfine states decay due to spontaneous scattering which makes the lower bound to the decoherence rate the Raman scattering rate itself and not half. If in some model of the two-level atom the ground state also decayed to other levels at some rate, then the decoherence would be bounded below by the average of the two rates—the excited state decay rate and the ground state decay rate. If the ground state decay rate is the same as the excited state decay rate, then the decoherence rate is the same as the population decay rate.

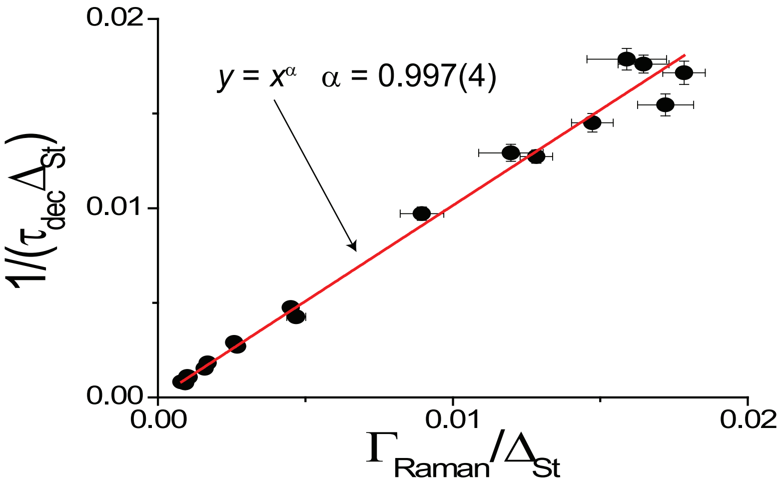

Figure 5.7: The measured coherence decay rate (y-axis) is plotted against the measured population relaxation rate (x-axis), both normalized by the measured differential Stark shift. The filled circles are measured data; the solid line is a weighted least squares fit to the power law $y = x^{\alpha}$ yielding the best-fit parameter $\alpha = 0.997(4)$ indicating that 1 Raman scattered photon is sufficient to destroy the coherence of a superposition state.

The decoherence rates we measured were very low for the larger detunings, and successful measurement of the decoherence rate limited by spontaneous scattering required suppression of all other decohering mechanisms below that of Raman spontaneous scattering. In particular, laser intensity noise induces phase noise due to the differential Stark shift of the qubit transition frequency. The total scattering rate normalized by the differential Stark shift asymptotically approaches the value of 0.0154. Consequently, in order to measure decoherence rates dominated by Raman spontaneous scattering, the phase noise induced by the differential Stark shift had to be suppressed to well below this value. For the particular detuning of $\Delta = -331.8$ GHz where we measured a decoherence rate over a factor of 19 below the total scattering rate, the phase noise induced by the differential Stark shift was below 10^{-3}.

Multiple experimental techniques were used to suppress Stark shift phase noise. First the laser beam propagated through a short 30 cm section of optical fiber close to the trap to reduce beam pointing fluctuations after the output of the fiber. Beam pointing fluctuations into the fiber remained a problem, and fluctuating beam position on the entrance to the fiber translated into laser power noise at the fiber exit. This was overcome by sampling the laser power after the fiber and feeding back on the RF power level of an acousto-optic modulator before the fiber. The bandwidth of the laser power servo was limited to less than 100 kHz; therefore, fast noise was not controlled. However, the phase noise induced by the differential Stark shift is the integrated Stark shift frequency noise, and high frequency noise averages to very low phase noise levels upon integration. The limited servo bandwidth was more of a problem when switching the decohering laser on as the control system would require ~ 10 μs to lock after turning on the laser. The spin-echo arm length τ_{echo} (see Fig. 5.4b) was typically in the few milliseconds range before spontaneous scattering decohering effects would manifest themselves, and the ~ 10 μs Stark shift noise, after integration on the ion, was undetectable. The final experimental technique we used to suppress Stark shift phase noise was the spin-echo sequence in Fig. 5.4b. Stark shift noise with frequencies much lower than $1/\tau_{\mathrm{echo}}$ would refocus under the spin-echo sequence as would any slowly changing systematic frequency shift, occurring from magnetic field drift, for example. We found that we could not tolerate spin-echo intervals τ_{echo} longer than a few milliseconds. At the time of the experiment, we speculated that the laser must have some 60 Hz intensity noise which limited the spin-echo technique to durations shorter than the 17 ms period of the 60 Hz cycle even though we could not detect laser power noise at 60 Hz. Our speculations were that the photo detector used to servo the laser power may have had some 60 Hz noise which it injected into the laser via the feedback circuit. In hindsight we realized that the $\hat{\sigma}_+$ polarized decohering laser beam shifted the location of the magnetic field independent point, and that magnetic field noise at 60 Hz was limiting the spin-echo arm duration τ_{echo} to much less than 17 ms (see § 5.3).

Because the spin-echo duration τ_{echo} was limited to on the order of a few milliseconds, a large number of spin-echo pulses were added to semi-continually refocus systematic frequency shifts induced by Stark shifts and Zeeman shifts. For the larger detunings, we used 18 spin-echo pulses. This made the measurement more susceptible to rotation angle errors induced by intensity noise on the Raman lasers. We circumvented this problem by alternating the phase of subsequent spin-echo pulses. This had the effect that if the Rabi frequency drifted at a rate much slower than $1/\tau_{\mathrm{echo}}$, then rotation angle errors on a spin-echo pulse would be automatically corrected on the next pulse. For example, if the first spin-echo pulse over-rotated by an angle ϵ about the x-axis, because the phase ϕ of rotation on the next spin-echo pulse was π, the rotation of the subsequent spin-echo pulse, about the $-x$-axis would undo the over-rotation so long as the Rabi frequency did not change dramatically between application of the two pulses. This is effectively a refocussing scheme for the rotation about the x-axis whereas the usual spin-echo sequence refocuses phase rotation about the z-axis.

The techniques outlined in the previous two paragraphs were necessary to suppress phase noise induced by differential Stark shifts to levels below that of Raman spontaneous scattering. In principle, the same techniques can be used when performing quantum gates or quantum algorithms. In conclusion, by detuning the laser far from the fine structure, we should be able to perform quantum gates below the fault-tolerance threshold. In particular, at the detuning $\Delta = -331.8$ GHz used in Fig. 5.6, the probability of Raman scattering during a π pulse is $\sim 1 \times 10^{-5}$ (see Eq. (5.13)). Two-ion gates require application of the laser for a duration $1/\eta$ longer than the π-pulse one-qubit gate where η is the Lamb-Dicke parameter, and the presence of a second ion increases the probability of Raman scattering during a two-qubit gate to be $2/\eta$ times larger than the one-qubit gate [Ozeri 06]. For the typical Lamb-Dicke parameter used in the laboratory of $\eta \simeq 0.3$, the probability of Raman scattering during a two-qubit gate is approximately $\sim 6 \times 10^{-5}$ for $\Delta = -331.8$ GHz. Both the one-qubit gate error probability and the two-qubit gate error probability due to spontaneous photon scattering are below Steane's fault-tolerance threshold [Steane 03], and we have experimentally measured decoherence induced by spontaneous Raman scattering at this level.

5.3 Field-Independent Point Shift due to the Light Shift

For circularly polarized light propagating along the magnetic field direction, the differential Stark shift of the qubit transition is dependent on the magnetic field strength. The Stark shift turn modifies the magnetic field at which first-order sensitivity of the qubit transition frequency vanishes. The experiments described in this chapter used a $\hat{\sigma}_+$ polarized laser beam as the decohering beam, and consequently we could not simultaneously work at the field-independent point for both situations where the decohering beam was on and when the decohering beam was off. We did not realize this at the time, and we tuned the magnetic field such that the ion was at the field-independent point in the absence of light. When the decohering beam was on, the qubit transition frequency picked up an linear dependence on the magnetic field, and the qubit became more susceptible to magnetic field noise. In hind-sight, we believe that the reason we could not use spin-echo arms longer than a few milliseconds was because 60 Hz magnetic field noise was causing significant decoherence. In this section, I derive the field-independent point shift induced by the differential Stark shift dependence on the magnetic field.

Hyperfine states labeled $|l\rangle = \alpha_l|m_J = -1/2, m_I = m_F + 1/2\rangle + \beta_l|m_J = +1/2, m_I = m_F - 1/2\rangle$ in the presence of an off-resonant laser beam with polarization $\hat{\epsilon} = \epsilon_\pi\hat{\pi} + \epsilon_-\hat{\sigma}_- + \epsilon_+\hat{\sigma}_+$ will have an AC Stark shift given by:

$$\begin{aligned}\delta_s &= \frac{1}{3}g^2\epsilon_\pi^2\left(\frac{1}{\Delta} + \frac{2}{\Delta - \Delta_F}\right) + \frac{2}{3}\frac{g^2}{\Delta}\left(\alpha^2\epsilon_+^2 + \beta^2\epsilon_-^2\right) \\ &\quad + \frac{g^2}{\Delta - \Delta_F}\left[\epsilon_+^2\left(\frac{1}{3}\alpha^2 + \beta^2\right) + \epsilon_-^2\left(\alpha^2 + \frac{1}{3}\beta^2\right)\right] \\ &= \left\{\frac{g^2}{3\Delta}\left[\epsilon_\pi^2 + 2\epsilon_-^2\right] + \frac{g^2}{3(\Delta - \Delta_F)}\left[2\epsilon_\pi^2 + \epsilon_-^2\right]\right\} \\ &\quad + \frac{2}{3}g^2\alpha^2\left(\epsilon_+^2 - \epsilon_-^2\right)\left[\frac{1}{\Delta} - \frac{1}{\Delta - \Delta_F}\right]\end{aligned} \tag{5.31}$$

where the bracketed {} term in Eq. (5.31) is not a function of the magnetic field. The magnetic field dependence enters Eq. (5.31) through the coefficient α (see Eq. (2.9) in § 2.2). We have replaced β^2 with $1-\alpha^2$ in the last line of Eq. (5.31) by the normalization condition. We note that the Stark shift induced by linearly polarized light ($\epsilon_+^2 = \epsilon_-^2$) has no magnetic field dependence. Therefore, we need not worry about memory decoherence induced by magnetic fields when performing quantum gates with laser beams as the laser beams are linearly polarized.

The differential Stark shift of the qubit transition can be calculated using Eq. (5.31) and the fact that α^2 is nearly the same[4] for both states of a field-independent qubit (see § 2.2). We label the states of the qubit as $|0\rangle$ and $|1\rangle$ with corresponding coefficients α_0

---

[4] The coefficients actually differ by roughly 10^{-4} due to the nuclear Zeeman effect. See § 2.2.

and α_1 respectively. The differential Stark shift between these states is:

$$\begin{aligned}\Delta\delta_s &= \text{const.} - \frac{2}{3}g^2\left(\epsilon_+^2 - \epsilon_-^2\right)\left[\alpha_0^2\omega_0\left(\frac{1}{\Delta^2} - \frac{1}{(\Delta-\Delta_F)^2}\right)\right. \\ &\qquad \left. - \Delta\alpha_1^2\left(\frac{1}{\Delta} - \frac{1}{\Delta-\Delta_F}\right)\right] \qquad (5.32) \\ &\simeq \text{const.} + c_s\Delta\alpha_1^2\end{aligned}$$

where $\Delta\alpha_1^2 \equiv \alpha_1^2 - \alpha_0^2$, $c_s \equiv \frac{2}{3}g^2\left(\epsilon_+^2 - \epsilon_-^2\right)\left(\frac{1}{\Delta} - \frac{1}{\Delta-\Delta_F}\right)$, and we have used the fact that the qubit transition frequency $\omega_0 \ll \Delta_{1/2}, \Delta_{3/2}$. We absorbed the $\alpha_0^2\omega_0\left(\frac{1}{\Delta^2} - \frac{1}{(\Delta-\Delta_F)^2}\right)$ term into the constant term because its dependence on the magnetic field is suppressed compared to $c_s\Delta\alpha_1^2$ by a factor of $\sim \omega_0/\Delta, \omega_0/(\Delta-\Delta_F)$. The qubit transition frequency in the presence of a Stark shifting laser beam can now be described as

$$\omega(B) = \omega_0 + c_2\Delta B^2 + c_s^{(1)}\Delta B + c_s^{(2)}\Delta B^2 \qquad (5.33)$$

where the constant term in Eq. (5.32) has been absorbed into ω_0. The constant c_2 is the second order coefficient calculated using the Breit-Rabi formula (see § 2.2), and the coefficients $c_s^{(1)}$ and $c_s^{(2)}$ are the first and second order coefficients from a Taylor expansion of $\Delta\delta_s$, namely: $c_s^{(1)} \equiv c_s\frac{\partial\Delta\alpha_1^2}{\partial\Delta B}|_{B_0}$ and $c_s^{(2)} \equiv \frac{1}{2}c_s\frac{\partial^2\Delta\alpha_1^2}{\partial\Delta B^2}|_{B_0}$. We recall from § 2.2 that $\Delta\alpha_1^2(B_0) = 0$, and the magnetic field dependence of $\Delta\alpha_1^2$ can be determined from Eq. (2.9). We minimize Eq. (5.33) by differentiating, setting to zero, and solving for ΔB to find the new location of the magnetic field independent point:

$$\Delta B_0 = -\frac{1}{2}\frac{c_s^{(1)}}{c_2 + c_s^{(2)}}. \qquad (5.34)$$

For the $|F=2, m_F=0\rangle \leftrightarrow |F=1, m_F=1\rangle$ qubit used in this and the previous chapters, $c_s^{(1)} = 0.485\ c_s\frac{\partial x}{\partial B}$ and $c_s^{(2)} = -0.0141\ c_s\left(\frac{\partial x}{\partial B}\right)^2$ where $\frac{\partial x}{\partial B} = -\frac{\mu_B g_J(1-g_I')}{A\hbar^2} = -4.483\times10^{-5}\ \mu\text{T}^{-1}$ is obtained from the x definition in § 2.2 following Eq. (2.9). The magnetic field independent point offset can be re-expressed using these numbers as:

$$\Delta B_0 = -\frac{1}{2}\frac{s_0}{(-8.53\times10^{-3})\left[\left(\epsilon_+^2 - \epsilon_-^2\right)\left(\frac{\gamma}{\Delta} - \frac{\gamma}{\Delta-\Delta_F}\right)\right]^{-1} + (1.3\times10^{-6})s_0}\ [\mu\text{T}] \qquad (5.35)$$

We find from Eq. (5.35) that the deviation of the magnetic field independent point saturates near 0.5 T. However, for typical detunings in the tens of GHz range, saturation does not occur until the on-resonance saturation parameter is on the order of 10^6 ($\sim$1 W laser power in $\sim$30 μm waist). The spontaneous scattering experiments in this chapter used detunings in the hundreds of GHz range with an on-resonance saturation parameter of $s_0 \sim 10^5$ causing a deviation of the magnetic field independent point by 1 mT. This is quite far away from the optimal point. The qubit transition acquires a linear magnetic field dependence with slope of 600 Hz/μT. With a 0.1 μT step in the magnetic field, we would expect the qubit to dephase by 1 radian in 17 ms.

Bibliography

[Acton 05] M Acton, K A Brickman, P C Haljan, P J Lee, L Deslauriers & C Monroe. Near-perfect simultaneous measurement of a qubit register. quant-ph/0511257, 2005.

[Allen 87] L Allen & J H Eberly. Optical resonance and two-level atoms. Dover, Mineola, N.Y., 1987.

[Andersen 03] M. F. Andersen, A. Kaplan & N. Davidson. Echo spectroscopy and quantum stability of trapped atoms. Phys. Rev. Lett., vol. 90, no. 2, page 023001, 2003.

[Bardroff 96] P J Bardroff, C Leichtle, G Schrade & W P Schleich. Endoscopy in the Paul trap: measurement of the vibratory quantum state of a single ion. Phys. Rev. Lett., vol. 77, no. 11, pages 2198–2201, 1996.

[Barenco 95] A Barenco, C H Bennett, R Cleve, D P DiVincenzo, N Margolus, P Shor, T Sleator, J Smolin & H Weinfurter. Elementary gates for quantum computation. Phys. Rev. A, vol. 52, no. 5, pages 3457–3467, 1995.

[Barrett 03] M D Barrett, B DeMarco, T Schaetz, V Meyer, D Leibfried, J Britton, J Chiaverini, W M Itano, B Jelenković, J D Jost, C langer, T Rosenband & D J Wineland. Sympathetic cooling of ^{9}Be^{+} and ^{24}Mg^{+} for quantum logic. Phys. Rev. A, vol. 68, no. 4, pages 042302–1–8, 2003.

[Barrett 04] M D Barrett, J Chiaverini, T Schätz, J Britton, W M Itano, J D Jost, E Knill, C Langer, D Leibfried, R Ozeri & D J Wineland. Deterministic quantum teleportation of atomic qubits. Nature, vol. 429, no. 6993, pages 737–739, 2004.

[Bergquist 86] J C Bergquist, R G Hulet, W M Itano & D J Wineland. Observation of quantum jumps in a single atom. Phys. Rev. Lett., vol. 57, no. 14, pages 1699–1702, 1986.

[Bergquist 87] J C Bergquist, W M Itano & D J Wineland. Recoilless optical absorption and Doppler sidebands of a single trapped ion. Phys. Rev. A, vol. 36, no. 1, pages 428–430, 1987.

[Blinov 02] B B Blinov, L Deslauriers, P Lee, M J Madsen, R Miller & C Monroe. Sympathetic cooling of trapped Cd^+ isotopes. Phys. Rev. A, vol. 65, no. 4, pages 040304–1–4, 2002.

[Blinov 04] B B Blinov, D L Moehring, L M Duan & C Monroe. Observation of entanglement between a single trapped atom and a single photon. Nature, vol. 428, no. 6979, pages 153–157, 2004.

[Bollinger 85] J. J. Bollinger, J. S. Wells, D. J. Wineland & Wayne M. Itano. Hyperfine structure of the $2p\ ^2P_{1/2}$ state in $^9Be^+$. Phys. Rev. A, vol. 31, no. 4, pages 2711–2714, 1985.

[Bollinger 91] J J Bollinger, D J Heinzen, W M Itano, S L Gilbert & D J Wineland. A 303-MHz frequency standard based on trapped $^9Be^+$ Ions. IEEE Trans. Instr. Meas., vol. 40, no. 2, pages 126–128, 1991.

[Bollinger 96] J J Bollinger, W M Itano, D J Wineland & D J Heinzen. Optimal frequency measurements with maximally correlated states. Phys. Rev. A, vol. 54, no. 6, pages R4649–R4652, 1996.

[Brickman 05] K A Brickman, P C Haljan, P J Lee, M Acton, L Deslauriers & C Monroe. Implementation of Grover's quantum search algorithm in a scalable system. Phys. Rev. A, vol. 72, no. 5, pages 050306–1–4, 2005.

[Britton 06] J Britton, D Leibfried, J Beall, R B Blakestad, J J Bollinger, J Chiaverini, R J Epstein, J D Jost, D Kielpinski, C Langer, R Ozeri, R Reichle, S Seidelin, N Shiga, J H Wesenberg & D J Wineland. A microfabricated surface-electrode ion trap in silicon. quant-ph/0605170, 2006.

[Brown 91] Lowell S. Brown. Quantum motion in a Paul trap. Phys. Rev. Lett., vol. 66, no. 5, pages 527–529, 1991.

[Cahill 69] K E Cahill & R J Glauber. Ordered expansions in boson amplitude operators. Phys. Rev., vol. 177, no. 5, pages 1857–1881, 1969.

[Chiaverini 04] J Chiaverini, D Leibfried, T Schaetz, MD Barrett, RB Blakestad, J Britton, WM Itano, JD Jost, E Knill, C Langer, R Ozeri & DJ Wineland. Realization of quantum error correction. Nature, vol. 432, no. 7017, pages 602 – 605, 2004.

[Chiaverini 05] J Chiaverini, J Britton, D Leibfried, E Knill, M D Barrett, R B Blakestad, W M Itano, J D Jost, C Langer, R Ozeri, T Schaetz & D J Wineland. Implementation of the semiclassical quantum Fourier transform in a scalable system. Science, vol. 308, no. 5724, pages 997–1000, 2005.

[Cirac 95] J I Cirac & P Zoller. Quantum computation with cold, trapped ions. Phys. Rev. Lett., vol. 74, no. 20, pages 4091–4094, 1995.

[Cline 94] R A Cline, J D Miller, M R Matthews & D J Heinzen. Spin relaxation of optically trapped atoms by light scattering. Opt. Lett., vol. 19, no. 3, pages 207–209, 1994.

[Cohen-Tannoudji 62] C Cohen-Tannoudji. Ph.D. Thesis. Ann. Phys., vol. 7, no. 2, page 423, 1962.

[Cohen-Tannoudji 92] C Cohen-Tannoudji, J Dupont-Roc & G Grynberg. Atom-photon interactions. John Wiley & Sons, New York, 1992.

[Dehmelt 75] H Dehmelt. Proposed 1O NU greater than NU laser fluorescence spectroscopy on T1+mono-ion oscillator II. Bull. Am. Phys. Soc., vol. 20, no. 1, pages 60–60, 1975.

[Deslauriers 06] L Deslauriers, S Olmschenk, D Stick, W K Hensinger, J Sterk & C Monroe. Scaling and suppression of anomalous quantum decoherence in ion traps. quant-ph/0602003, 2006.

[Dicke 53] R H Dicke. The effect of collisions upon the doppler width of spectral lines. Physical Review, vol. 89, no. 2, pages 472–473, 1953.

[Diddams 04] S A Diddams, J C Bergquist, S R Jefferts & C W Oates. Standards of time and frequency at the outset of the 21st century. Science, vol. 306, no. 5700, pages 1318–1324, 2004.

[Diedrich 89] F Diedrich, J C Bergquist, W M Itano, & D J Wineland. Laser cooling to the zero point energy of motion. Phys. Rev. Lett., vol. 62, no. 4, pages 403–406, 1989.

[DiVincenzo 98] D P DiVincenzo & D Loss. Quantum information is physical. Superlattices Microstruct., vol. 23, no. 3-4, pages 419–432, 1998.

[Feynman 82] R P Feynman. Simulating physics with computers. Int. J. Th. Phys., vol. 21, no. 6/7, pages 467–488, 1982.

[Fisk 95] P T H Fisk, M J Sellars, M A Lawn, C Coles, A G Mann & D G Blair. Very high Q microwave spectroscopy on trapped $^{171}\text{Yb}^{+}$ ions: application as a frequency standard. IEEE Trans. Instrum. Meas., vol. 44, no. 2, pages 113–116, 1995.

[Freund 92] J E Freund. Mathematical statistics. Prentice Hall, Upper Saddle River, NJ, 5th edition, 1992.

[Galleani 03] L Galleani, L Sacerdote, P Tavella & C Zucca. A mathematical model for the atomic clock error. Metrologia, vol. 40, no. 2003, pages S257–S264, 2003.

[García-Ripoll 03] J J García-Ripoll, P Zoller & J I Cirac. Speed optimized two-qubit gates with laser coherent control techniques for ion trap quantum computing. Phys. Rev. Lett., vol. 91, no. 15, pages 157901–1–4, 2003.

[Geremia 04] J M Geremia, J K Stockton & H Mabuchi. Real-time quantum feedback control of atomic spin-squeezing. Science, vol. 304, no. 5668, pages 270–273, 2004.

[Gheorghe 92] V. N. Gheorghe & F. Vedel. Quantum dynamics of trapped ions. Phys. Rev. A, vol. 45, no. 7, pages 4828–4831, 1992.

[Gheorghe 00] V. N. Gheorghe & G. Werth. Quasienergy states of trapped ions. Eur. Hys. Journal D, vol. 10, no. 2, pages 197–203, 2000.

[Ghosh 95] P K Ghosh. Ion traps. Clarendon Press, Oxford, 1995.

[Goldstein 80] H Goldstein. Classical mechanics. Addison-Wesley, Reading, Massachusetts, 2nd edition, 1980.

[Haffner 05] H Haffner, W Hansel, C F Roos, J Benhelm, D Chek al kar, M Chwalla, T Korber, U D Rapol, M Riebe, P O Schmidt, C Becher, O Gunhe, W Dur & R Blatt. Scalable multiparticle entanglement of trapped ions. Nature, vol. 438, no. 7068, pages 643–646, 2005.

[Haljan 05a] P C Haljan, K-A Brickman, L Deslauriers, P J Lee & C Monroe. Spin-dependent forces on trapped ions for phase-stable quantum gates and engangled states of spin and motion. Phys. Rev. Lett., vol. 94, no. 15, page 153602, 2005.

[Haljan 05b] P C Haljan, P J Lee, K-A Brickman, M Acton, L Deslauriers & C Monroe. Entanglement of trapped-ion clock states. Phys. Rev. A, vol. 72, no. 6, page 062316, 2005.

[Hansch 80] T W Hansch & B Couillaud. Laser frequency stabilization by polarization spectroscopy of a reflecting reference cavity. Opt. Comm., vol. 35, no. 3, pages 441–444, 1980.

[Harber 02] D M Harber, H J Lewandowski, J M McGuirk & E A Cornell. Effect of cold collisions on spin coherence and resonance shifts in a magnetically trapped ultracold gas. Phys. Rev. A, vol. 66, no. 5, pages 053616–1–6, 2002.

[Hensinger 06] W K Hensinger, S Olmschenk, D Stick, D Hucul, M Yeo, M Acton, L Deslauriers, C Monroe & J Rabchuk. T-junction ion trap array for two-dimensional ion shuttling, storage, and manipulation. App. Phys. Lett., vol. 88, no. 3, pages 034101–1–3, 2006.

[Höffges 97] J T Höffges, H W Baldauf, T Eichler, S R Helmfrid & H Walther. Heterodyne measurement of the fluorescent radiation of a single trapped ion. Opt. Commun., vol. 133, no. 1–6, pages 170–174, 1997.

[James 98] D F V James. Quantum dynamics of cold trapped ions with applications to quantum computing. Appl. Phys. B, vol. 66, no. 2, pages 181–190, 1998.

[Jaynes 63] E T Jaynes & F W Cummings. Comparison of quantum and semiclassical radiation theories with application to the beam maser. Proceedings of the IEEE, vol. 51, pages 89–109, 1963.

[Jefferts 95] S R Jefferts, C Monroe, E Bell & D J Wineland. Coaxial-resonator driven rf (Paul) trap for strong confinement. Phys. Rev. A, vol. 51, no. 4, pages 3112–3116, 1995.

[Jones 01] J A Jones. NMR quantum computation. Prog. Nucl. Mag. Res. Spec., vol. 38, no. 4, pages 325–360, 2001.

[Keller 04] M Keller, B Lange, K Hayasaka, W Lange & H Walther. Continuous generation of single photons with controlled waveform in an ion-trap cavity system. Nature, vol. 431, no. 7012, pages 1075–1078, 2004.

[Kielpinski 00] D Kielpinski, B E King, C J Myatt, C A Sackett, Q A Turchette, W M Itano, C Monroe & D J Wineland. Sympathetic cooling of trapped ions for quantum logic. Phys. Rev. A, vol. 61, no. 3, pages 032310–1–8, 2000.

[Kielpinski 01] D Kielpinski. Entanglement and decoherence in a trapped-ion quantum register. PhD thesis, Univ. Colorado, Dept. of Physics, Boulder, 2001.

[Kielpinski 02] D Kielpinski, C Monroe & D J Wineland. Architecture for a large-scale ion-trap quantum computer. Nature, vol. 417, no. 6890, pages 709–711, 2002.

[King 98] B E King, C S Wood, C J Myatt, Q A Turchette, D Leibfried, W M Itano, C Monroe & D J Wineland. Cooling the Collective Motion of Trapped Ions to Initialize a Quantum Register. Phys. Rev. Lett., vol. 81, no. 7, pages 1525–1528, 1998.

[King 99] B E King. Quantum state engineering and information processing with trapped ions. PhD thesis, Univ. Colorado, Dept. of Physics, Boulder, 1999.

[Knill 05] E Knill. Quantum computing with realistically noisy devices. Nature, vol. 434, no. 7029, pages 39–44, 2005.

[Kuhr 03] S Kuhr, W Alt, D Schrader, I Dotsenko, Y Miroshnychenko, W Rosenfeld, M Khudaverdyan, V Gomer, A Rauschenbeutel & D Meschede. Coherence properties and quantum state transportation in an optical conveyor belt. Phys. Rev. Lett., vol. 91, no. 21, pages 213002–1–4, 2003.

[Langer 05] C Langer, R Ozeri, J D Jost, J Chiaverini, B DeMarco, A Ben-Kish, R B Blakestad, J Britton, D B Hume, W M Itano, D Leibfried, R Reichle, T Rosenband, T Schaetz, P O Schmidt & D J Wineland. Long-lived qubit memory using atomic ions. Phys. Rev. Lett., vol. 95, no. 6, pages 060502–1–4, 2005.

[Leibfried 03] D Leibfried, B DeMarco, V Meyer, D Lucas, M Barrett, J Britton, W M Itano, B Jelenković, C Langer, T Rosenband & D J Wineland. Experimental demonstration of a robust, high-fidelity geometrical two ion-qubit phase gate. Nature, vol. 422, no. 6930, pages 412–415, 2003.

[Leibfried 04] D Leibfried, M D Barrett, T Schätz, J Britton, J Chiaverini, W M Itano, J D Jost, C Langer & D J Wineland. Toward Heisenberg-limited spectroscopy with multiparticle entangled states. Science, vol. 304, no. 5676, pages 1476–1478, 2004.

[Leibfried 05] D Leibfried, E Knill, S Seidelin, J Britton, R B Blakestad, J Chiaverini, D Hume, W M Itano, J D Jost, C Langer, R Ozeri, R Reichle & D J Wineland. Creation of a six atom Schrödinger cat state. Nature, vol. 438, no. 7068, pages 639–642, 2005.

[Loudon 00] R Loudon. The quantum theory of light. Oxford University Press, New York, NY, 3rd edition, 2000.

[Major 05] F G Major, V N Gheorghe & G Werth. Charged particle traps. Springer, Berlin, Heidelberg, 2005.

[Metcalf 99] H J Metcalf & P van der Straten. Laser cooling and trapping. Springer, New York, NY, 1999.

[Milburn 01] G J Milburn, S Schneider & D F V James. Ion trap quantum computing with warm ions. In S L Braunstein, H -K Lo & P Kok, editeurs, Scalable Quantum Computers, pages 31–40, Berlin, 2001. Wiley-VCH.

[Mintert 01] F Mintert & C Wunderlich. Ion-trap quantum logic using long-wavelength radiation. Phys. Rev. Lett., vol. 87, no. 25, pages 257904–1–4, 2001.

[Mollow 69] B. R. Mollow. Power spectrum of light scattered by two-level systems. Phys. Rev., vol. 188, no. 5, pages 1969–1975, 1969.

[Mollow 75] B R Mollow. Pure-state analysis of resonant light scattering: Radiative damping, saturation, and multiphoton effects. Phys. Rev. A, vol. 12, no. 5, pages 1919–1943, 1975.

[Mølmer 99] K Mølmer & A Sørensen. Multiparticle entanglement of hot trapped ions. Phys. Rev. Lett., vol. 82, no. 9, pages 1835–1838, 1999.

[Monroe 95a] C Monroe, D M Meekhof, B E King, W M Itano & D J Wineland. Demonstration of a fundamental quantum logic gate. Phys. Rev. Lett., vol. 75, no. 25, pages 4714–4717, 1995.

[Monroe 95b] C Monroe, D M Meekhof, B E King, S R Jefferts, W M Itano, D J Wineland & P Gould. Resolved-sideband Raman cooling of a bound atom to the 3D zero-point energy. Phys. Rev. Lett., vol. 75, no. 22, pages 4011–4014, 1995.

[Morigi 01] G Morigi & H Walther. Two-species Coulomb chains for quantum information. Eur. Phys. J. D, vol. 13, no. 2, pages 261–269, 2001.

[Nagourney 86] W Nagourney, J Sandberg & H G Dehmelt. Shelved Optical Electron Amplifier: Observation of Quantum Jumps. Phys. Rev. Lett., vol. 56, no. 26, pages 2797–2799, 1986.

[Nallatech 03] Nallatech. XtremeDSP Development Kit Users Guide, 9th edition, 2003.

[Nieto 00] M. M. Nieto & D. R Truax. Coherent states sometimes look like squeezed states and vice versa: the Paul trap. New J. Physics, vol. 2, pages 18.1–18.9, 2000.

[Ozeri 05] R Ozeri, C Langer, J D Jost, B L DeMarco, A Ben-Kish, B R Blakestad, J Britton, J Chiaverini, W M Itano, D Hume, D Leibfried, T Rosenband, P Schmidt & D J Wineland. Hyperfine coherence in the presence of spontaneous photon scattering. Phys. Rev. Lett., vol. 95, no. 3, pages 030403–1–4, 2005.

[Ozeri 06] R Ozeri & *et al.* Infidelity of trapped-ion quantum gates due to spontaneous scattering. in preparation, 2006.

[Pathria 96] R K Pathria. Statistical mechanics. Butterworth-Heinemann, Woburn, MA, 2nd edition, 1996.

[Perry 02] D L Perry. Vhdl: programming by example. McGraw-Hill, New York, 4 edition, 2002.

[Poulsen 75] O Poulsen, T Andersen & N Skouboe. Fast-beam, zero-field level-crossing measurements of radiative lifetimes, fine and hyperfine structures in excited-states of ionic and neutral beryllium. J. Phys. B: Atom. Mol. Phys., vol. 8, no. 9, pages 1393–1405, 1975.

[Preskill 97] J Preskill. Reliable quantum computers. quant-ph/9705031, 1997.

[Press 03] W H Press, S A Teukolsky, W T Vetterling & B P Flannery. Numerical recipes in c++. Cambridge University Press, New York, 2nd edition, 2003.

[Preston 96] D W Preston. Doppler-free saturated absorption: Laser spectroscopy. Am. J. Phys., vol. 64, no. 11, pages 1432–1436, 1996.

[Raizen 93] M G Raizen, J M Gilligan, J C Bergquist, W M Itano & D J Wineland. Ionic crystals in a linear Paul trap. Phys. Rev. A, vol. 45, no. 9, pages 6493–6501, May 1993.

[Ramsey 63] N F Ramsey. Molecular beams. Oxford University Press, London, 1963.

[Reichle 06] R Reichle, D Leibfried, E Knill, J Britton, R B Blakestad, J D Jost, C Langer, R Ozeri, S Seidelin & D J Wineland. Experimental purification of two-atom entanglement. Nature (in press), 2006.

[Reif 65] F Reif. Statistical and thermal physics. McGraw-Hill, 1965.

[Riebe 04] M Riebe, H Häffner, C F Roos, W Hänsel, J Benhelm, G P T Lancaster, T W Körber, C Becher, F Schmidt-Kaler, D F V James & R Blatt. Deterministic quantum teleportation with atoms. Nature, vol. 429, no. 6993, pages 734–737, 2004.

[Rohde 01] H Rohde, S T Gulde, C F Roos, P A Barton, D Leibfried, J Eschner, F Schmidt-Kaler & R Blatt. Sympathetic ground-state cooling and coherent manipulation with two-ion crystals. J. Opt. B: Quantum Semiclass. Opt., vol. 3, no. 1, pages S34–S41, 2001.

[Rowe 02] M A Rowe, A Ben-Kish, B DeMarco, D Leibfried, V Meyer, J Beall, J Britton, J Hughes, W M Itano, B Jelenković, C Langer, T Rosenband & D J Wineland. Transport of quantum states and separation of ions in a dual RF ion trap. Quant. Inform. Comp., vol. 2, no. 4, pages 257–271, 2002.

[Sackett 00] C A Sackett, D Kielpinski, B E King, C Langer, V Meyer, C J Myatt, M Rowe, Q A Turchette, W M Itano, D J Wineland & C Monroe. Experimental entanglement of four particles. Nature, vol. 404, no. 6775, pages 256–258, 2000.

[Sakurai 94] J. J. Sakurai. Modern quantum mechanics. Addison-Wesley, New York, NY, 1994.

[Sauter 86] Th Sauter, W Neuhauser, R Blatt & P E Toschek. Observation of quantum jumps. Phys. Rev. Lett., vol. 57, no. 14, pages 1696–1698, 1986.

[Schaetz 04] T Schaetz, M D Barrett, D Leibfried, J Chiaverini, J Britton, W M Itano, J D Jost, C Langer & D J Wineland. Quantum dense coding with atomic qubits. Phys. Rev. Lett., vol. 93, no. 4, pages 040505–1–4, 2004.

[Schaetz 05] T Schaetz, M D Barrett, D Leibfried, , J Britton, J Chiaverini, W M Itano, J D Jost, E Knill, C Langer & D J Wineland. Enhanced quantum state detection efficiency through quantum information processing. Phys. Rev. Lett., vol. 94, no. 1, pages 010501–1–4, 2005.

[Schmidt-Kaler 03] F Schmidt-Kaler, H Häffner, M Riebe, S Gulde, G P T Lancaster, T Deuschle, C Becher, C Roos, J Eschner & R Blatt. Realization of the Cirac-Zoller controlled-NOT quantum gate. Nature, vol. 422, no. 6930, pages 408–411, 2003.

[Schrade 95] G. Schrade, V. I. Man'ko, W. Schleich & R. J. Glauber. Wigner functions in the Paul trap. Quantum Semiclass. Opt., vol. 7, no. 3, pages 307–325, 1995.

[Schrader 04] D Schrader, I Dotsenko, M Khudaverdyan, Y Miroshnychenko, A Rauschenbeutel & D Meschede. Neutral atom quantum register. Phys. Rev. Lett., vol. 93, no. 15, pages 150501–1–4, 2004.

[Seidelin 06] S Seidelin, J Chiaverini, R Reichle, J J Bollinger, D Leibfried, J Britton, J H Wesenberg, R B Blakestad, R J Epstein, D B Hume, J D Jost, C Langer, R Ozeri, N Shiga & D J Wineland. A microfabricated surface-electrode ion trap for scalable quantum information processing. Phys. Rev. Lett., vol. 96, no. 25, pages 253003–1–4, 2006.

[Shor 94] P W Shor. Algorithms for quantum computation: discrete logarithms and factoring. In S Goldwasser, editeur, Proceedings of the 35th Annual Symposium on the Foundations of Computer Science, volume 35, page 124, Los Alamitos, CA, 1994. IEEE Computer Society Press.

[Solano 99] E Solano, R L de Matos Filho & N Zagury. Deterministic Bell states and measurement of the motional state of two trapped ions. Phys. Rev. A, vol. 59, no. 4, pages 2539–2542, 1999.

[Sørensen 99] A Sørensen & K Mølmer. Quantum computation with ions in thermal motion. Phys. Rev. Lett., vol. 82, no. 9, pages 1971–1974, 1999.

[Sørensen 00] A Sørensen & K Mølmer. Entanglement and quantum computation with ions in thermal motion. Phys. Rev. A, vol. 62, no. 2, pages 02231–1–11, 2000.

[Steane 03] A M Steane. Overhead and noise threshold of fault-tolerant quantum error correction. Phys. Rev. A, vol. 68, no. 4, pages 042322–1–19, 2003.

[Stenholm 92] S. Stenholm. Quantum motion in a Paul trap. J. Mod. Optics, vol. 39, no. 2, pages 279–290, 1992.

[Stick 06] D Stick, W K Hensinger, S Olmschenk, M J Madsen, K Schwab & C Monroe. Ion trap in a semiconductor chip. Nature Physics, vol. 2, no. 1, pages 36–39, 2006.

[Stockton 02] J Stockton, M Armen & H Mabuchi. Programmable logic devices in experimental quantum optics. J. Opt. Soc. Am. B, vol. 19, no. 12, page 3019, 2002.

[Treutlein 04] P Treutlein, P Hommelhoff, T Steinmetz, T W Hänsch & J Reichel. Coherence in microchip traps. Phys. Rev. Lett., vol. 92, no. 20, pages 203005–1–4, 2004.

[Turchette 00] Q A Turchette, D Kielpinski, B E King, D Leibfried, D M Meekhof, C J Myatt, M A Rowe, C A Sackett, C S Wood, W M Itano, C Monroe & D J Wineland. Heating of trapped ions from the quantum ground state. Phys. Rev. A, vol. 61, no. 6, pages 063418–1–8, 2000.

[Vandersypen 01] L M K Vandersypen, M Steffen, G Breyta, C S Yannoni, M H Sherwood MH & I L Chuang. Experimental realization of Shor's quantum factoring algorithm using nuclear magnetic resonance. Nature, vol. 414, no. 6866, pages 833–837, 2001.

[Vandersypen 04] L. M. K. Vandersypen & I. L. Chuang. NMR techniques for quantum control and computation. Rev. Mod. Phys., vol. 76, no. 4, page 1037, 2004.

[Walls 94] D F Walls & G J Milburn. Quantum optics. Springer, Berlin, 1st edition, 1994.

[Wineland 79] D J Wineland & W M Itano. Laser cooling of atoms. Phys. Rev. A, vol. 20, no. 4, pages 1521–1540, 1979.

[Wineland 80] D J Wineland, J C Bergquist, W M Itano & R E Drullinger. Double-resonance and optical-pumping experiments on electromagnetically confied, laser-cooled ions. Opt. Lett., vol. 5, no. 6, pages 245–247, 1980.

[Wineland 83] D J Wineland, J J Bollinger & W M Itano. Laser-fluorescence mass spectroscopy. Phys. Rev. Lett., vol. 50, no. 9, pages 628–631, 1983.

[Wineland 98] D J Wineland, C Monroe, W M Itano, D Leibfried, B E King & D M Meekhof. Experimental issues in coherent quantum-state manipulation of trapped atomic ions. J. Res. Nat. Inst. Stand. Tech., vol. 103, no. 3, pages 259–328, 1998.

[Wineland 03] D J Wineland, M Barrett, J Britton, J Chiaverini, B DeMarco, W M Itano, B. Jelenković, C Langer, D Leibfried, V Meyer, T Rosenband & T Schätz. Quantum information processing with trapped ions. Phil. Trans. R. Soc. Lond. A, vol. 361, no. 1808, pages 1349–1361, 2003.

[Woodgate 92] G K Woodgate. Elementary atomic structure. Oxford University Press, Walton Street, Oxford OX2 6DP, 2nd edition, 1992.

Appendix A

Glossary of Acronyms

AC: Alternating current—generic term for describing electronic signals which vary in time.

ADC: Analog to digital converter—integrated circuit which converts analog signals to digital signals.

DAC: Digital to analog converter—integrated circuit which converts digital signals to analog signals.

DC: Direct current—generic term for describing electronic signals which are constant in time.

DDS: Direct digital synthesis—frequency synthesis technique where output is a sampled sinusoid generated by a digital frequency.

DIP: Dual-inline package—a type of electronics package where there are two parallel rows of pins.

FPGA: Field programmable gate array—reconfigurable programmable logic device.

HDL: Hardware description language—language used to describe digital logic circuits. Most common HDLs are VHDL and Verilog.

I/O: Input/output.

kB: kilobyte—1024 bytes.

LSB: Least significant bit.

LVTTL: Low voltage TTL (transistor-transistor logic)—logic family where logic '1' is represented by 3.3 V and logic '0' is represented by 0 V.

LVDS: Low voltage differential signal—differential digital communications specification for 100 Ω transmission lines. Communications speeds can reach hundreds of MHz. Differential voltage swing is 350 mV.

MSB: Most significant bit.

MSPS: Mega-samples per second.

NIST: National Institute off Standards and Technology

PCI: Peripheral component interconnect—local bus standard for connecting peripherals to computers. Clock speeds are 33 or 66 MHz, and the data word is 32 bits wide.

PLL: Phase-locked loop—feedback control loop used to lock the phase of one oscillator to another.

PMT: Photo-multiplier tube—photon counting detector used for detecting single photons in low-light conditions.

QIP: Quantum information processing.

RF: Radio frequency.

SSB: Single side band—frequency modulation technique which suppresses one sideband in favor of another.

TTL: Transistor-transistor logic—logic family where logic '1' is represented by 5 V and logic '0' is represented by 0 V.

USB: Universal serial bus—serial communications standard common in most modern computers.

VHDL: VHSIC (very high speed integrated circuit) hardware description language.

VHSIC: Very high speed integrated circuit.

Appendix B

Daughter Board Schematics

B.1 FPGA Daughter Board

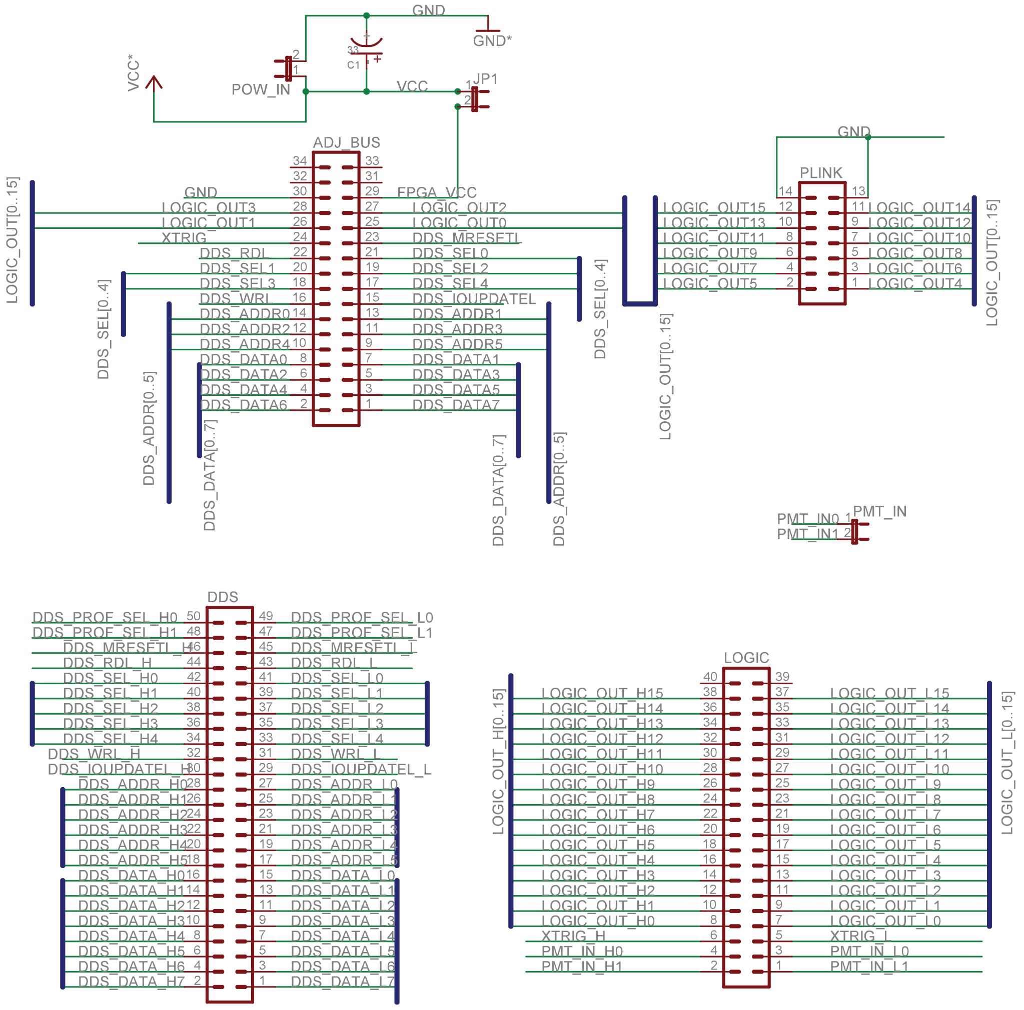

FPGA daughter board schematic page 1/3.

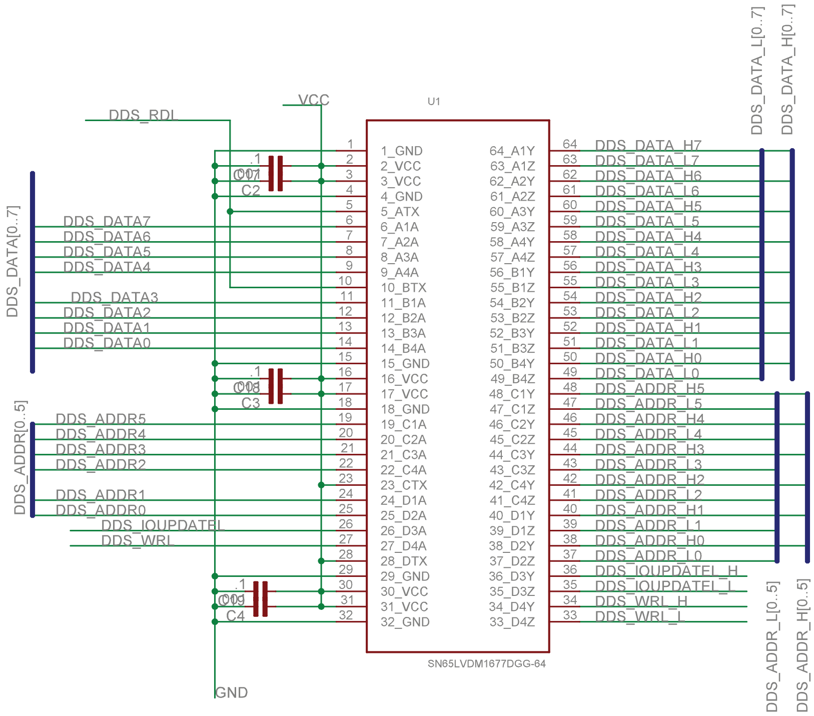

FPGA daughter board schematic page 2/3.

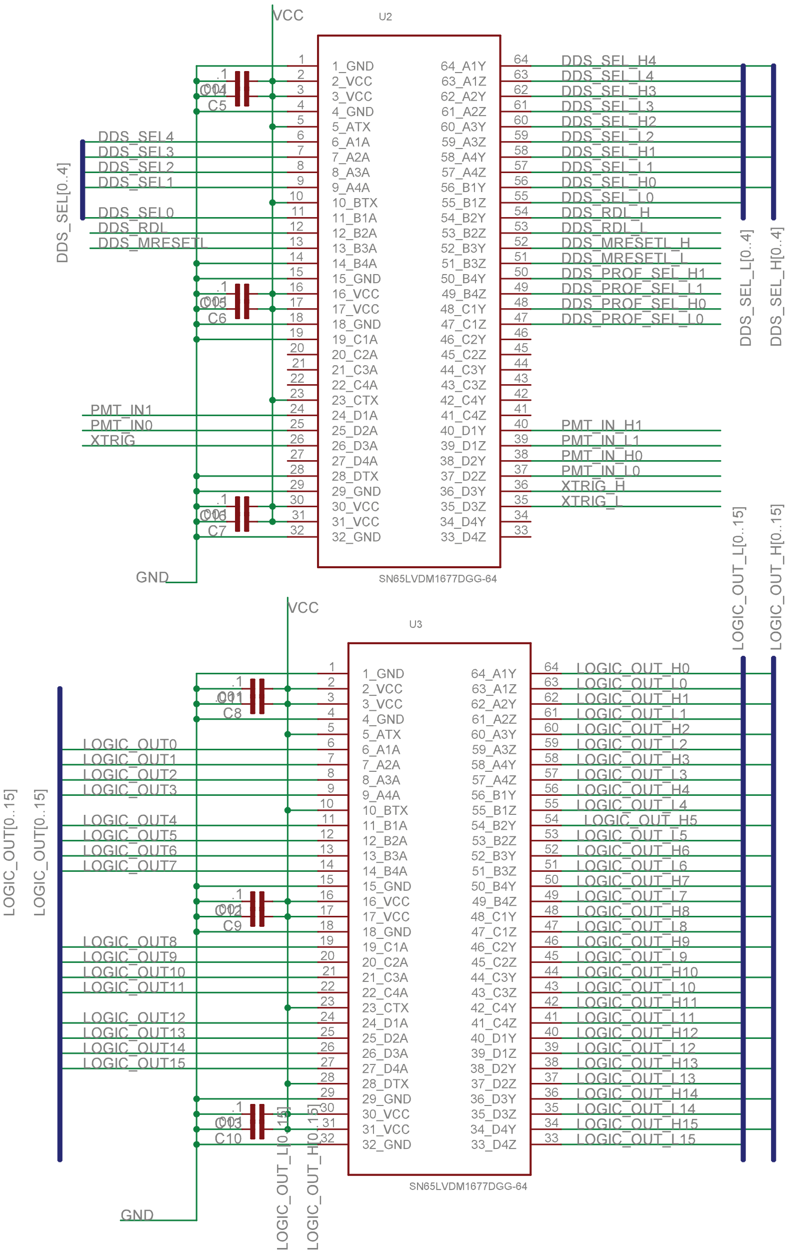

FPGA daughter board schematic page 3/3.

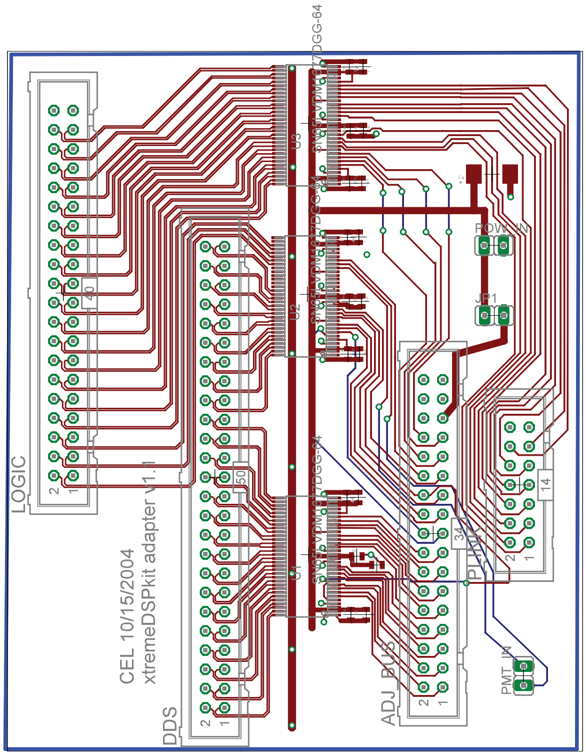

FPGA daughter board layout.

B.2 DDS Daughter Board

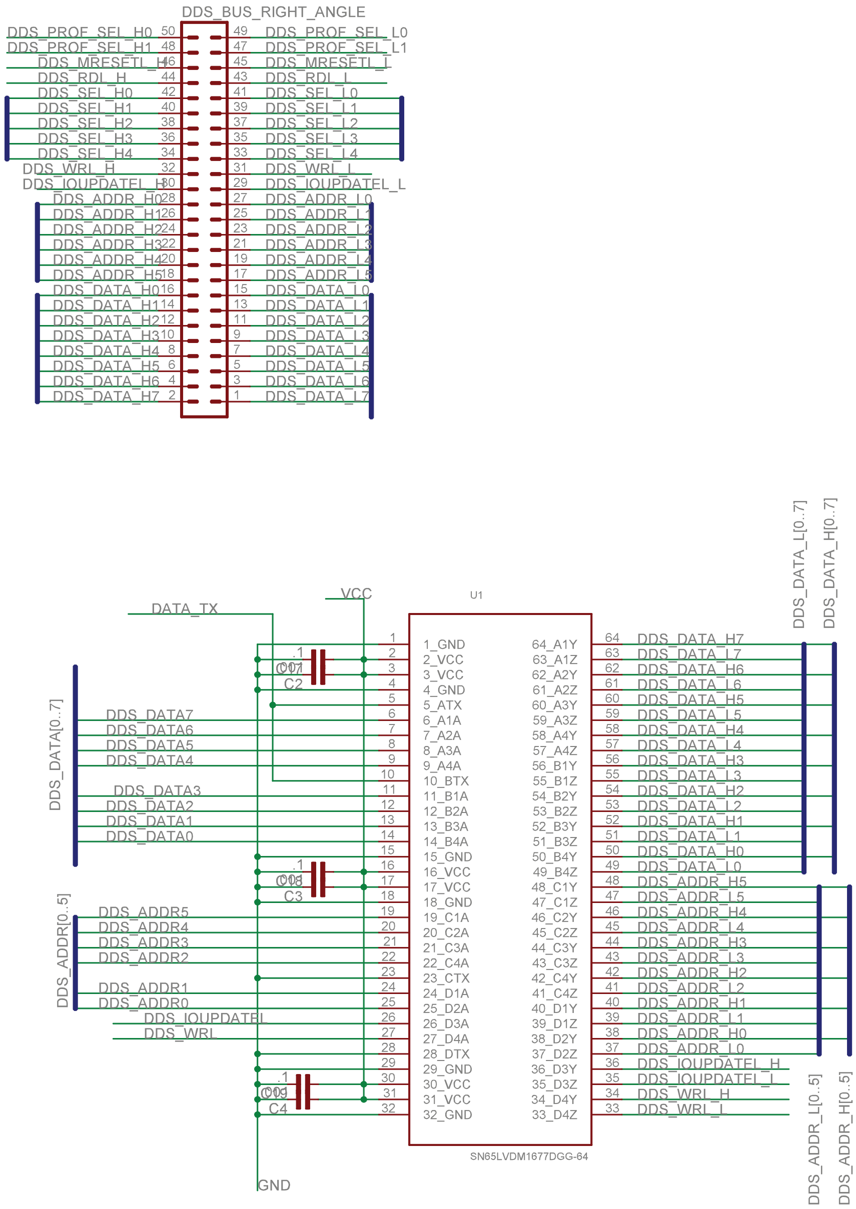

DDS daughter board schematic page 1/3.

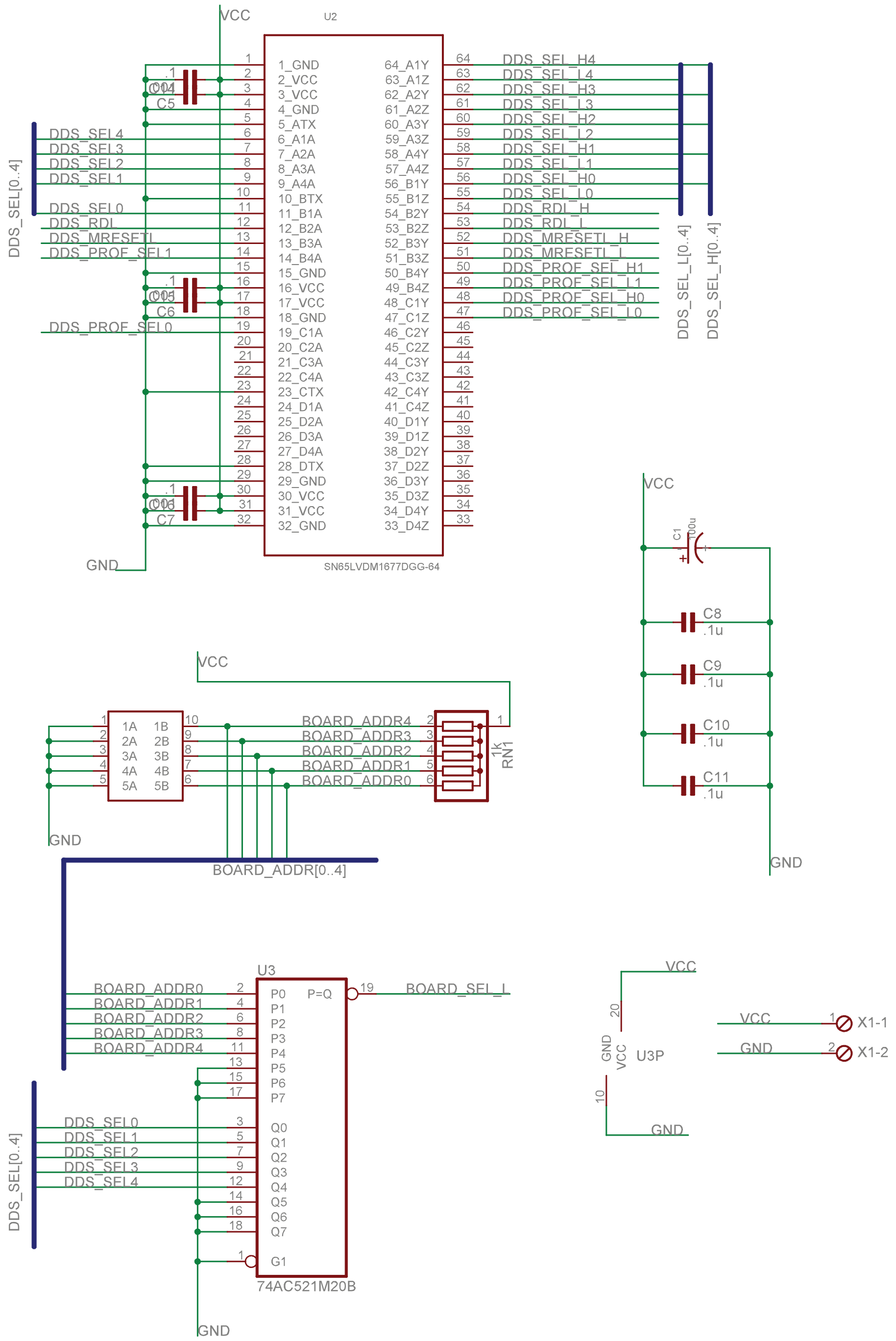

DDS daughter board schematic page 2/3.

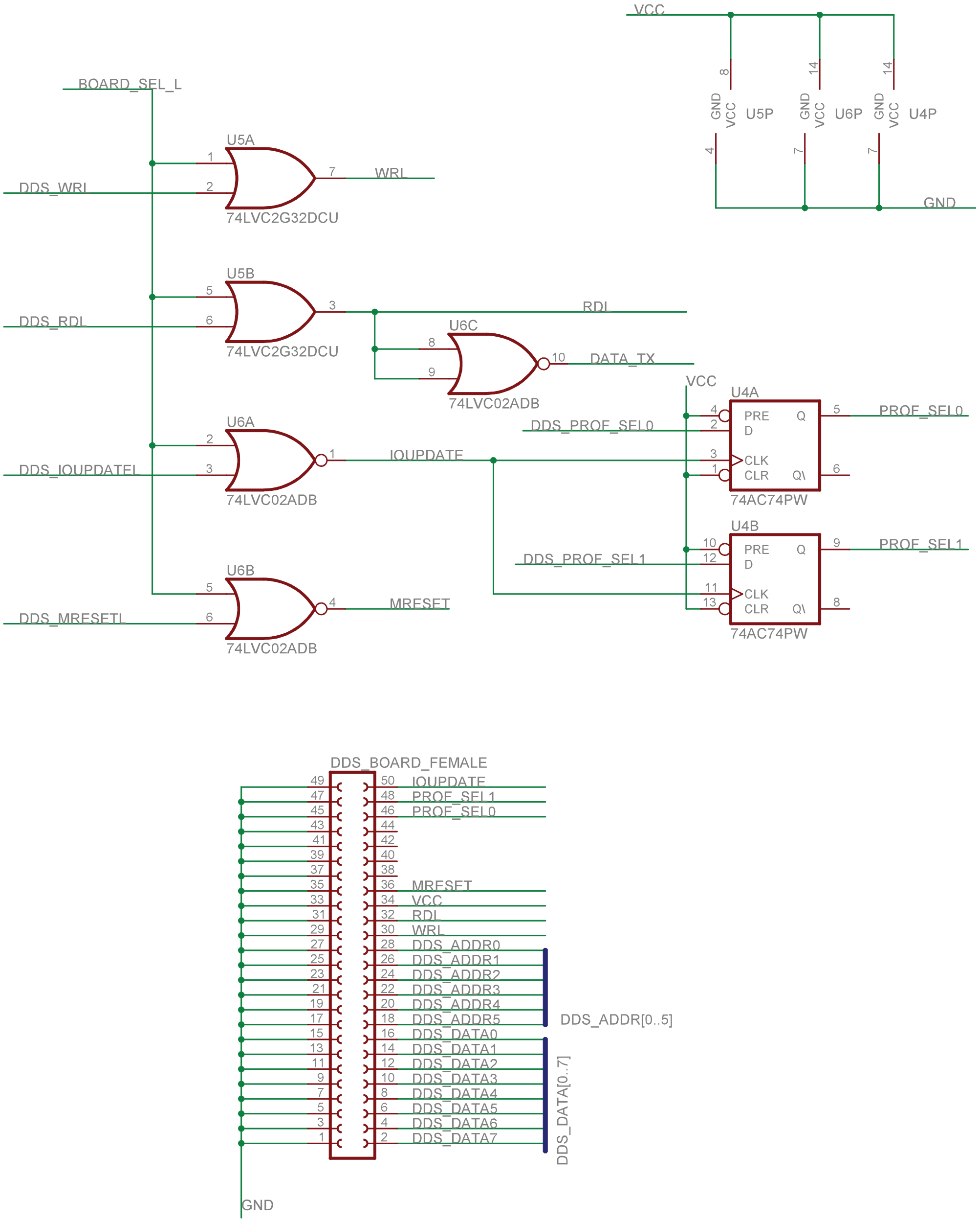

DDS daughter board schematic page 3/3.

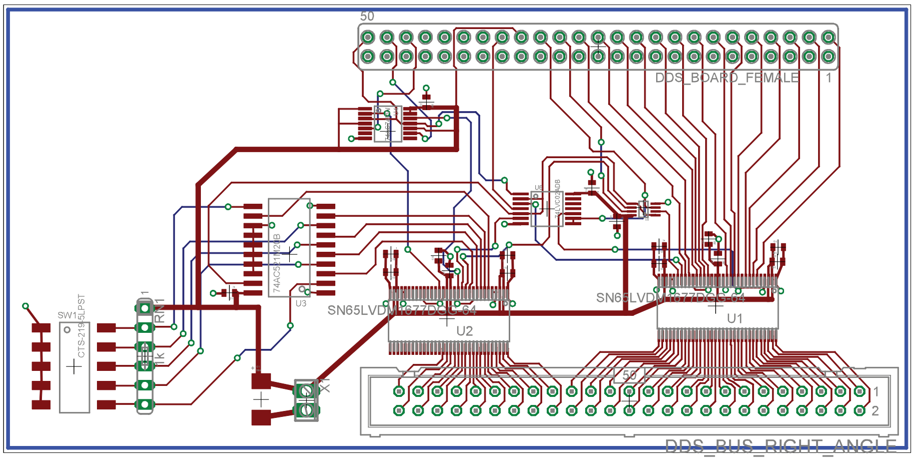

DDS daughter board layout.

Appendix C

Histogram Data Analysis using Maximum Likelihood

The measurement process for ion-trap quantum information processing (QIP) experiments typically involves collecting a number of photons on a detector for a fixed detection interval. Many experiments are performed for the same set of experimental parameters resulting in a histogram of photon counts (see § 2.4). From this histogram, we would like to know what fraction of the total experiments are M out of N ions fluorescing. I demonstrate the maximum likelihood method to determine this fraction.

C.1 The Problem

Given: (1) a histogram $h(n)$ of photon counts in a fixed detection interval where n is the number of photon counts and $N \equiv \sum_n h(n)$ is the total number of experiments and (2) a parameterized model probability distribution $P(n; \mathbf{a})$ from which these events were selected where $\mathbf{a}$ is a vector of parameters for the distribution, find the parameters $\mathbf{a}$ which maximize the likelihood function $L(\mathbf{a})$. In practice, the parameters $\mathbf{a}$ are the statistical weights and means of bright and dark photon count distributions.

C.2 Background—Least Squares Fit as a Maximum Likelihood Estimator

For data $(x_i, y_i), i \in \{1, 2, \cdots, N\}$ which are assumed to fit a parameterized model $y(x; \mathbf{a})$, the method of weighted least squares is commonly used to determine the "best fit" parameters $\mathbf{a}$. In this method, the χ^2 statistic,

$$\chi^2 = \sum_{i=1}^{N} \left(\frac{y_i - y(x_i; \mathbf{a})}{\Delta y_i} \right)^2, \tag{C.1}$$

is minimized where Δy_i is the measurement error on y_i.

Minimizing χ^2 is equivalent to maximizing the likelihood function where the data (x_i, y_i) are normally distributed about the model $y(x; \mathbf{a})$ with variance for point (x_i, y_i) given by Δy_i^2 [Press 03]. The likelihood function $L(\mathbf{a})$ is defined as the probability of measuring data (x_i, y_i) given parameters $\mathbf{a}$, namely:

$$L(\mathbf{a}) \propto \prod_{i=1}^{N} \exp\left(-\frac{1}{2} \left(\frac{y_i - y(x_i; \mathbf{a})}{\Delta y_i} \right)^2 \right). \tag{C.2}$$

Maximizing L is equivalent to minimizing its negative logarithm, which is equivalent to minimizing χ^2 in Eq. (C.1).

The problem we are trying to solve is not one of finding the best fit parameters $\mathbf{a}$ of a model $y(x; \mathbf{a})$ where x is an independent variable and y is a dependent variable. Rather, we have a set of photon counts $\{x_i\}$ all of which are independent; the data are not paired data (x_i, y_i) as is the case with least squares fitting, and we want to determine from which probability distribution (parameterized by $\mathbf{a}$) the data $\{x_i\}$ came. Thus, it would be incorrect to attempt to fit the histogram of counts $h(n)$ to a parameterized distribution using minimum least squares. As an example, suppose $N = 10^5$ experiments were performed measuring the photon counts from a single ion that is initially prepared in a superposition of bright and dark states. The data is a histogram of counts with maximum photon number no more than 40. If we blindly use least squares fitting we would make the association $x_i = n$ and $y_i = h(n)$ where $i \in \{0, 1, \cdots, 40\}$ effectively give the fitting routine ~40 data points even though we performed 10^5 experiments. Some questions naturally arise which we must answer if we attempt to use least squares fitting: (1) What is the error Δy_i? (2) How do you handle zero counts [$h(n) = 0$ for some n]? (3) What is the error for zero counts?

A natural guess for the error Δy_i is 1 for all i because if we happened to perform $N-1$ experiments instead, one of the $h(n)$ would have 1 less experiment. However, we know $h(n)$ exactly, thus we should expect to have zero error. We might think about estimating the error in x_i or n, but this is also discrete which makes it difficult to estimate. I propose there is a better way to determine the parameters $\mathbf{a}$, namely the method of maximum likelihood [Freund 92].

C.3 Method of Maximum Likelihood

Suppose we have a probability distribution $P(n;\mathbf{a})$ parameterized by the vector $\mathbf{a}$ of measuring n photons, and we have a measured histogram of counts $h(n)$. The likelihood function is:

$$L(\mathbf{a}) \propto \prod_{i=1}^{N} P(x_i;\mathbf{a}) \tag{C.3}$$

where x_i is the number of photons counted for experiment $i \in \{1, 2, \cdots, N\}$. The histogram $h(n)$ is defined as the multiplicity of events where n photons were measured, thus the likelihood function can also written as

$$L(\mathbf{a}) = \prod_{n=0}^{\infty} C(n, h(n)) P(n;\mathbf{a})^{h(n)}, \tag{C.4}$$

where $C(n, h(n))$ is a combinatorial factor and $N = \sum_n h(n)$. The maximum likelihood estimate $\mathbf{a_0}$ is calculated by maximizing the likelihood (or equivalently and more simply $\ln L$):

$$\ln L = \text{const.} + \sum_{n=0}^{\infty} h(n) \ln P(n;\mathbf{a}) \tag{C.5}$$

which is equivalent to solving the system of equations:

$$\frac{\partial \ln L}{\partial a_k} = \sum_{n=0}^{\infty} \frac{h(n)}{P(n;\mathbf{a})} \frac{\partial P(n;\mathbf{a})}{\partial a_k} = 0. \tag{C.6}$$

In practice, $h(n) = 0$ for $n > n_{\max}$ for some $n_{\max}$ relatively small (for one ion, $n_{\max} \sim 50$), and we can safely truncate the sum in Eq. (C.6) at $n = n_{\max}$ as each term contains a factor of $h(n)$.

Even for linear models $P(n;\mathbf{a}) = \sum_k a_k f_k(n)$, L and $\ln L$ are non-linear, thus non-linear root finding or non-linear minimization is required to find $\mathbf{a_0}$. In general, non-linear minimization is numerically easier than non-linear root finding [Press 03]. Once $\mathbf{a_0}$ is determined, error estimates on $\mathbf{a_0}$ are straight forward. For the number of experiments N relatively large, the likelihood function is strongly peaked about $\mathbf{a_0}$. We can approximate the likelihood function as a multivariate gaussian:

$$L(\mathbf{a}) \simeq \exp\left(\text{const.} + \frac{1}{2}\delta\mathbf{a}^T\mathbf{A}\delta\mathbf{a} + \cdots\right) \tag{C.7}$$

where $\delta\mathbf{a} \equiv \mathbf{a} - \mathbf{a_0}$ and

$$\begin{aligned} A_{ij} \equiv & \frac{\partial^2}{\partial a_i \partial a_j} \ln L(\mathbf{a})\bigg|_{\mathbf{a_0}} \\ = & -\sum_n h(n)\left[\frac{\partial P(n;\mathbf{a})}{\partial a_i}\frac{\partial P(n;\mathbf{a})}{\partial a_j}\frac{1}{P(n;\mathbf{a})^2}\right. \\ & \left.- \frac{\partial^2 P(n;\mathbf{a})}{\partial a_i \partial a_j}\frac{1}{P(n;\mathbf{a})}\right]\Bigg|_{\mathbf{a_0}} \end{aligned} \tag{C.8}$$

are the negative inverse elements of the covariance matrix.

This approximation is valid for large N; however, a more robust method for determining the error is to construct synthetic data sets of the same size (N) from the newly found fitted parameters, perform the fitting procedure for these synthetic data sets, and calculate the sample variance on the best fit parameters for the synthetic data sets. This method of resampling is robust and can be used to analyze any bias in the fitted parameters [Press 03].

For linear models,

$$P(n;\mathbf{a}) \equiv \sum_k f_k(n) a_k, \tag{C.9}$$

the equation for maximum likelihood [Eq. (C.6)] and the $\mathbf{A}$ matrix have a simpler form:

$$\frac{\partial \ln L}{\partial a_k} \propto \sum_n h(n)\frac{f_k(n)}{P(n;\mathbf{a})} \tag{C.10}$$

$$A_{ij} = -\sum_n h(n)\frac{f_i(n) f_j(n)}{P(n;\mathbf{a_0})^2} \tag{C.11}$$

Notice that A_{ii} is negative indicating that the maximum likelihood occurs at $\mathbf{a_0}$ rather than the minimum likelihood.

C.4 Examples

C.4.1 Single Poisson Distribution

Suppose we assume the photon counts are distributed according to the Poisson distribution. Then, $\mathbf{a} = \nu$ and $P(n; \mathbf{a}) = P(n; \nu)$ where

$$P(n;\nu) \equiv \frac{\nu^n e^{-\nu}}{n!} \tag{C.12}$$

From Eq. (C.6) using Eq. (C.12), we must solve:

$$\begin{aligned} 0 &= \sum_n h(n) \frac{\partial}{\partial \nu} \ln P(n;\nu) \\ &= \sum_n h(n) \frac{\partial}{\partial \nu} \Big(n \ln \nu - \nu - \ln n! \Big) \\ &= \frac{1}{\nu} \sum_n h(n) n - \sum_n h(n) \\ &= N \left(\frac{\bar{n}}{\nu} - 1 \right), \end{aligned} \tag{C.13}$$

indicating $\nu = \bar{n}$, the sample mean $[\bar{n} \equiv \frac{1}{N} \sum_n h(n) n]$.

The error $\sigma_\nu = 1/\sqrt{-A_{\nu\nu}}$ is evaluated as follows.

$$\begin{aligned} -A_{\nu\nu} &= -\frac{\partial^2}{\partial \nu^2} \ln L = -\frac{\partial}{\partial \nu} \sum_n h(n) \left(\frac{n}{\nu} - 1 \right) \\ &= \sum_n h(n) \frac{n}{\nu^2} \bigg|_{\nu_0} = \frac{N}{\bar{n}} \end{aligned} \tag{C.14}$$

We find $\sigma_\nu = \sqrt{\bar{n}/N}$ is the distribution error ($\sqrt{\bar{n}}$) averaged down by $1/\sqrt{N}$ as expected.

C.4.2 Weighted Poisson Distribution

When performing repeated measurements of identically prepared states of M ions, the expected histogram of measured photon counts is a weighted sum of the photon count distributions of having $k \in \{0, 1, \cdots, M\}$ ions bright. The photon count distribution of k ions bright is a Poisson distribution with mean ν_k. We let $P(n;\mathbf{a})$ be defined as follows:

$$P(n;\mathbf{a}) \equiv \left(1 - \sum_{k=1}^{M} b_k\right) g(n;\nu_0) + \sum_{k=1}^{M} b_k g(n;\nu_k) \tag{C.15}$$

where $\mathbf{a} = \mathbf{a}(b_1, b_2, \cdots, b_M)$, ν_k are defined positive constants, and $g(n;\nu_k)$ is a poisson distribution with mean ν_k. Here, $b_k \geq 0$ is the weight of the k-ions bright poisson distribution with mean ν_k, and $\sum_{k=1}^{M} b_k \leq 1$. Alternatively, b_k is the probability that k ions are bright. We would like to maximize the likelihood by varying b_k for $k \in \{1, 2, \cdots, M\}$ and hence determine from the data the probability that k ions are bright. We can use non-linear minimization routines to minimize:

$$-\ln L = -\sum_{n} h(n) \ln P(n;\mathbf{a}) \tag{C.16}$$

and the errors can be calculated as

$$\sigma_{b_k} = \left(\sum_{n} h(n) \frac{g_k(n)^2}{P(n;\mathbf{a_0})^2}\right)^{-1/2} \tag{C.17}$$

This treatment assumes ν_k are fixed. However, ν_k may as well be varied, and $\mathbf{a}$ would be a function of these as well. In this case, $P(n;\mathbf{a})$ is no longer linear in a_k; however, it is still linear in the weights b_k. In this case, Eq. (C.17) is valid for the errors in the b_k, but it is not valid for errors in the ν_k. For errors in ν_k, Eq. (C.8) must be used instead.

C.5 Experimental Data Fitting in Practice

In practice, we collect a large number of histograms $h(n)$ for different experimental parameters. If the detection interval is the same for these histograms, then the different histograms can be summed together to generate a single large histogram $h_r(n)$. This histogram can be fit letting both the weights b_k and means ν_k vary to determine the reference poisson distributions defined by the set $\{\nu_k\}$. The means $\{\nu_k\}$ may have constraints such as $\nu_k(\nu_0, \nu_1) = \nu_0 + k\nu_1$. Once $\{\nu_k\}$ are determined, we can fit individual histograms $h(n)$ varying only the weights b_k. The errors in b_k would then be given by Eq. (C.17).